Third-order Nonlinear Optical Response and Ultrafast Carrier Dynamics of 2D Materials

Gaozhong Wang

A thesis submitted for the degree of Doctor of Philosophy

Supervised by Prof. Werner Blau

School of Physics and the Centre for Research on Adaptive Nanostructures and Nanodevices (CRANN)

Trinity College Dublin

2018

To my Dad, Mum, Yueming, Zhongzheng, and Bangzheng

DECLARATION

I declare that this thesis has not been submitted as an exercise for a degree at this or any other university and it is entirely my own work.

I agree to deposit this thesis in the University's open access institutional repository or allow the library to do so on my behalf, subject to Irish Copyright Legislation and Trinity College Library conditions of use and acknowledgement.

Elements of this work that have been carried jointly with others and collaborators have be duly acknowledged in the text wherever included

Gaozhong Wang

Abstract

Two dimensional (2D) materials have been in the spotlight of scientific researchers in the last decade due to their outstanding chemical, physical, electronic, mechanical and optical properties in comparison to their bulk. Strong photoluminescence was observed in 2D materials because of the transition from indirect bandgap semiconductor in bulk limit to direct bandgap in monolayer limit. 2D materials have also attracted tremendous interest due to their quantum confinement which results in intriguing physical phenomenon at room temperature, such as optical Stark effect, stable exciton, trion formation and exciton-exciton annihilation etc. These make them promising candidates for applications in the field of spintronics, valleytronics, optoelectronics and nano-electronics. However, the optical and physical performance of many 2D materials are still under questions and their excited carrier dynamics remains unclear. Therefore it is interesting and necessary to study their nonlinear optical performance and ultrafast carrier dynamics relative to the above mentioned field.

In this thesis, the nonlinear optical behaviors and ultrafast exaction carrier dynamics of several 2D materials, including graphene saturable absorption mirror (GSAM), layered antimony, $PtSe_2$, transition metal dichalcogenides (TMDs, e.g., WS_2, MoS_2 and $MoSe_2$), and their polymer composites (e.g. $MoSe_2$/PVA composites), were investigated from visible to infrared range. The GSAM was fabricated through a vacuum-filtrated transfer of liquid-phase-exfoliated graphene onto a silver-coated mirror. Liquid-phase-exfoliation technique was also employed to prepare layered TDMs. Meanwhile, Chemical vapor deposition (CVD) method was utilized to fabricate layered $PtSe_2$ by direct selenization of previously deposited Pt atom layer on substrate. The layer structure and high quality of these 2D materials was verified by scan electron microscopy (SEM), transmission electron microscopy (TEM), atomic force microscopy (AFM) and Raman spectrum. In terms of optics, nonlinear optical response of the above 2D materials were systematically studied by spatial self-phase modulation (SSPM), Z-scan and I-scan, while their ultrafast excitation carrier dynamics was characterized by time-resolved degenerate femtosecond pump-probe technique and spectra-resolved transient absorption spectroscopy.

Firstly, SSPM technique based on continuous wavelength lasers in the visible range was utilized to study the coherent nonlinear optical behaviors of the above TMDs and layered antimony. From SSPM experiments, one is able to calculate the nonlinear refractive index and third-order nonlinear optical susceptibility ($\chi^{(3)}$), which are two of the important parameters in nonlinear optics. By

changing the incident laser intensity to tune the distortion of SSPM pattern, the relative effective nonlinear refractive index can be modulated.

Secondly, saturable absorption behavior, one of most important nonlinear response, was observed in layered antimony, $PtSe_2$ and $MoSe_2$/PVA composites using the Z-scan technique. By applying a typical nonlinear theory and slow-absorber model to analyze the Z-scan data in the visible regime, the key nonlinear parameters such as nonlinear absorption coefficients were extracted.

Thirdly, the photonic performance of a graphene saturable absorption mirror (GSAM) based on liquid-phase-exfoliation at mid-infrared regime was compared with a commercial semiconductor saturable absorption mirror (SESAM, BATOP, SAM-2000-44-10ps) using a reflective I-scan method. The linear reflection of the GSAM was designed to be similar to that of the commercial SESAM (~64%). A reflective slow-absorber mirror model modified from slow-absorber theory was applied to analyze I-scan data and the results show that the GSAM has a comparable non-saturable loss 9.9% and modulation depth of ~13%. By subtracting the 13.8% surface scattering of GSAM, the theory calculation indicated that GSAM have better nonlinear optical performance than the commercial SESAM. The cross-section ratio of excited-state over ground state σ_e/σ_g is fitted to be 0.442 and 0.615 for graphene and SESAM respectively, implying graphene based SAM would have less loss and heat than SEAM in a laser cavity.

Finally, transient absorptive mapping and degenerate femtosecond pump-probe results signify that layered $PtSe_2$ crystals exhibit broadband excited-stated absorption and the excited carriers exhibited three decays. By employing a three-dimensional (3D) triexponential and biexponential decay models to fit the differential transmission traces, the carrier life times of layered $PtSe_2$ crystalline were figured out. The first fast decay process was attributed to carrier-carrier scattering while the second fast relaxation was dominated by intraband carrier-phonon and carrier-carrier scattering. The slowest relaxation is attributable to the indirect recombination of electron-hole pairs.

These results offer systemic insights into photophysical properties like nonlinear optical response and ultrafast excitation carrier dynamics of 2D materials in question, with their applications for photonic, photovoltaic, optoelectronic and nano-electronic devices.

Key words: 2D Materials, Layered $PtSe_2$, Polymer Composites, Nonlinear Optics, SSPM, Saturable Absorption, Z-scan, Slow-absorber, Mode-locker, I-scan, GSAM, SESAM, Carrier Dynamics, Pump-probe, Transient Absorption Spectroscopy

LIST OF ABBREVIATIONS

2D: Two-dimensional

$PtSe_2$: Platinum Diselenide

WS_2: Tungsten Disulfide

$MoSe_2$: Molybdenum Diselenide

ML: Mode-Locking

CVD: Chemical Vapor Deposition

TEM: Transmission Electron Microscopy

SPM: Self-phase Modulation

SAM: Saturable Absorption Mirror

NLO: Nonlinear Optical

SA: Saturable Absorption

BN: Boron Nitride

BBO: β-Barium Borate

CCD: Charge-couple Device

UV-vis: Ultraviolet-visible

CHP: cyclohexylpyrrolidone

SRH: Shockley-Read-Hall

SSE: The Sum of Squares Due to Error

XPS: X-ray Photoelectron Spectroscopy

GSAM: Graphene Saturable Absorption Mirror

TMDs: Transition Metal Dichalcogenides

MoS_2: Molybdenum Disulfide

PVA: Poly(vinyl alcohol)

DOS: Density of States

SEM: Scan Electron Microscopy

AFM: Atomic Force Microscopy

SESAM: Semiconductor Saturable Absorption Mirror

3D: Three-dimensional

THG: Third-harmonic Generation

TPA: Two-photon Absorption

RSA: Reverse Saturable Absorption

OPA: Optical Parametric Amplifier

TA: Transient Absorption

CW: Continuous Wavelength

NMP: N-Methyl-2-pyrrolidone

NIR: Near-infrared

GoM: Graphene on Mirror

PMMA: Poly(methyl methacrylate)

MY PUBLICATIONS

---

1. **Wang, G.**; Wang, K.; Szydłowska, B. M.; Baker‐Murray, A. A.; Wang, J. J.; Feng, Y.; Zhang, X.; Wang, J.; Blau, W. J. Ultrafast Nonlinear Optical Properties of a Graphene Saturable Mirror in the 2 μm Wavelength Region. *Laser & Photonics Reviews* **2017**. 11, 1700166-1700175.

2. **Wang, G.**; Zhang, S.; Zhang, X.; Zhang, L.; Cheng, Y.; Fox, D.; Zhang, H.; Coleman, J. N.; Blau, W. J.; Wang, J. Tunable nonlinear refractive index of two-dimensional MoS_2, WS_2, and $MoSe_2$ nanosheet dispersions. *Photonics Research* **2015**, 3, A51-A55.

3. **Wang, G.**; Zhang, S.; Umran, F. A.; Cheng, X.; Dong, N.; Coghlan, D.; Cheng, Y.; Zhang, L.; Blau, W. J.; Wang, J. Tunable effective nonlinear refractive index of graphene dispersions during the distortion of spatial self-phase modulation. *Applied Physics Letter* **2014**, 104, 141909.

4. Wang, K.; Szydłowska, B. M.; **Wang, G.**; Zhang, X.; Wang, J. J.; Magan, J. J.; Zhang, L.; Coleman, J. N.; Wang, J.; Blau, W. J. Ultrafast nonlinear excitation dynamics of black phosphorus nanosheets from visible to mid-infrared. *ACS nano* **2016**, 10, 6923-6932.

5. Feng, Y.; Dong, N.; **Wang, G.**; Li, Y.; Zhang, S.; Wang, K.; Zhang, L.; Blau, W. J.; Wang, J. Saturable absorption behavior of free-standing graphene polymer composite films over broad wavelength and time ranges. *Optic Express* **2015**, 23, 559-569.

6. Bai, Z.; Tao, G.; Li, Y.; He, J.; Wang, K.; **Wang, G.**; Jiang, X.; Wang, J.; Blau, W.; Zhang, L. Fabrication and near-infrared optical responses of 2D periodical Au/ITO nanocomposite arrays. *Photonics Research* **2017**, 5, 280-286.

ACKNOWLEDGEMENTS

I would like to express my two millions thanks to my supervisor, Prof. Werner Blau, who is, objectively, the nicest person I have ever met up until now. More importantly, Prof. Blau is proficient in nonlinear optics and nano-materials. He is always able to point out the key to the difficulties that I met during my three years of academic study and research. I must thank Government of Ireland International Education Scholarship and TCD postgraduate research award, without which I couldn't finish my PhD study and research. Massive thanks to Dr Kangpeng Wang, whom I have been working with and he gave me a lot of professional suggestions and help. I would also like to thank Dr JingJing Wang, who provides technical and timely support in regard to lasers. Dr Niall McEvoy, Dr Xiaoyan Zhand and Prof Jun Wang also provide massive instruction on the material fabrication and characterization. I appreciate it. I also thank Jian-Yao, Sean, Conor, Zhengyuan, Chuan, Mr Niall McGroarty, Dr Niamh McGoldrick, Prof. Louise Bradley, Dr Colm Stephens, Ms Helen O'Halloran and other members from our group, for their kind help in not only research but also daily life. A special thanks to good John James Magan and gentle Brian David Jennings, who make my TCD life and study beautiful and enjoyable like a football. One million thanks to Nina for helping to improve my academic reading and writing skills, and making my Dublin more attractive. This is particularly important. I would also like to thank my friends Lichao and Zhihai, who took care of me when I was sick after longtime experiments. Last but not least, I must thank my parents, sister and brothers for their love and support all this time.

CONTENTS

1. Introduction

In 1666, a ray of white light was divided by a prism into a series of constituent colors: red, orange, yellow, green, blue and violet. [1] This famous Isaac Newton's optical experiment opened a new page of Spectrum, helping to understand the world of light and the molecular and atomic structure via the study on the interaction of light and matter. This kind of study went to a large step thanks to the advent of the world's first working laser based on a ruby built by T. H. Maiman and his colleagues in 1960. [2] Even though the pulse duration of this ruby laser was only in the magnitude of second, the high light intensity of the laser allows for the new optical study that require high-density photon fluence. This leads to the development of a new brand of optics: Nonlinear Optics, which focuses on the phenomenon that result from modifying the optical properties of a material by intense light.[3] Commonly, the discovery of Second harmonic generation (SHG) in crystalline quartz in 1961, *i.e.*, two photons with the same energy are converted to one photon with double energy through the interaction with nonlinear materials, was seen as the start of Nonlinear Optics.[4]

In the last 6 decades, a great number of nonlinear optical (NLO) phenomenon have been discovered and verified in different nonlinear mediums, such as Third-harmonic generation (THG), Saturable Absorption (SA), two- and multi- photon absorption etc. Similar to SHG, THG describes an optical phenomenon where three photons are combined into one photon with the sum energy of the initial three photons after the interaction of light and materials. Saturable Absorption is a NLO property of many materials which results from Pauli-blocking. Under the irradiation of an intense laser, electrons are pumped to the conduction band and fill it. Due to Pauli-blocking, the conduction band no longer accepts more incoming electrons, *i.e.*, saturable. SA materials are widely used in passive-mode locking lasers to generate laser pulses. Two-photon absorption (TPA) is a nonlinear optical process in which the electrons in the ground state absorb two photons and then are pumped to the excited states. In a TPA configuration, as the incident laser intensity increases, more and more photons are absorbed and hence resulting in a decrease in the transmitted laser intensity. Therefore it can be used as optical limiters for laser safety.

Another intriguing research area that benefits from the advent of pulse lasers is excited carrier dynamics. In 1980s, lasers with pulse duration ranges from picosecond to femtosecond based on titanium-sapphire were developed by Peter F. Moulton in MIT's Lincoln Laboratory.[5, 6] Up until now femtosecond lasers have been widely used and the laser pulse duration goes up to the order of attosecond (10^{-18} s).[7-9] Thanks to these ultrafast pulse lasers, investigation on ultrafast physical processes of carriers in the femtosecond time domain became experimentally possible. One of the advanced methods is the pump-probe technique based on pulse lasers, in which one laser beam is utilized to inject excited carrier and another relatively weak beam is employed to probe the excited carrier. By converting the time domain to spatial regime, this technique can demonstrate that the carrier population in different energy levels of excited states changes with time. Hence one is able to develop a clear insight on the excited carrier relaxing process, charge transfer, energy transfer etc. [10-13]

1.1 Nonlinear optics

Nonlinear optics is a subsection of optics that explains the interaction of light and nonlinear materials.[3] Light is an electromagnetic wave with both optical electric field and magnetic field. When light travels through a medium, charges inside the materials move under the optical electric force. For example, electrons and holes separate and move in an opposite direction under the optical electric force. This results in polarizability, which is described using $\boldsymbol{P}(\boldsymbol{r},t)$ in spatial and time domain:

$$\boldsymbol{P}(\boldsymbol{r},t) = \varepsilon_0 \chi \boldsymbol{E}(\boldsymbol{r},t) \tag{1.1}$$

Here ε_0 is the permittivity of free space, χ is the optical susceptibility and $\boldsymbol{E}(\boldsymbol{r},t)$ represents the optical induced electric field. In conventional optics, χ is independent to $\boldsymbol{E}(\boldsymbol{r},t)$ and $\boldsymbol{P}(\boldsymbol{r},t)$ is proportional to $\boldsymbol{E}(\boldsymbol{r},t)$. In nonlinear optics, the polarization ($\boldsymbol{P}(\boldsymbol{r},t)$) is not simply linear to $\boldsymbol{E}(\boldsymbol{r},t)$, which can be described by a general format:

$$\boldsymbol{P}(\boldsymbol{r},t) = \varepsilon_0 \boldsymbol{\chi}^{(1)} \cdot \boldsymbol{E} + \varepsilon_0 \boldsymbol{\chi}^{(2)} : \boldsymbol{EE} + \varepsilon_0 \boldsymbol{\chi}^{(3)} \vdots \boldsymbol{EEE} + \cdots\cdots \tag{1.2}$$

Here $\chi^{(n)}$ is the n-th order optical susceptibility of the nonlinear medium. The second-order nonlinear optical susceptibility $\chi^{(2)}$ is utilized to characterize the second-order optical effect such as second-harmonic generation. The third-order nonlinear optical susceptibility $\chi^{(3)}$ is referred to third-harmonic generation, Kerr effect, saturable absorption, two-photon absorption and coherent

anti-Stokes Raman scattering etc.[14] As saturable absorption is strongly relevant to the content of my thesis, a detailed introduction on this nonlinear optical phenomenon is given as the following sections.

1.1.1 Mode-locking

This section is going to introduce the mode-locking technique which is relevant to the saturable absorption. According to the principle of lasers, many longitudinal modes are commonly oscillating inside a laser resonant cavity.[15] The oscillation and the initial phase of these modes are random under ordinary circumstances and no interference occurs among these longitudinal modes. Hence the output is the average values of all these modes. A laser with fixed-phase relation between the longitudinal modes in the resonant cavity is referred to as the mode-locked laser.[16] The corresponding technique to induce the definite phase relationship between modes is called mode-locking. For simplicity, I initially introduce a special case of a two longitudinal modes, whose electric fields $E_1(z,t)$ and $E_2(z,t)$ are expressed as:[17]

$$E_1(z,t) = E_1 \cos\left[\omega_1\left(t - \frac{z}{v}\right) + \varphi_1\right] \tag{1.3}$$

$$E_2(z,t) = E_2 \cos\left[\omega_2\left(t - \frac{z}{v}\right) + \varphi_2\right] \tag{1.4}$$

Here z is the propagation position, E, ω and φ represent the amplitude, angular frequency and initial phase of the longitudinal modes. Both initial phases φ_1 and φ_2 are assumed to be 0 and the electric fields $E_1(0,t)$ and $E_2(0,t)$ as a function of time can be seen as Figure 1.1 (a) and (b) respectively. At $t = 0$, the electric field strengths of both modes reach the maximum values and corresponding output intensity, I, can be calculated as:

$$I = (E_1 + E_2)^2 \tag{1.5}$$

As the initial phases of both modes are fixed to be 0, the phase difference of the two modes can be 2π at $t = T_0$, which satisfies the following equation:

$$(\omega_2 - \omega_1)T_0 = 2\pi \tag{1.6}$$

The two modes interfere at $t = T_0$ and the intensity arrives the maximum values, which can also be calculated by Equation (1.5). The intensity as a function of time is plotted as Figure 1.1 (c).

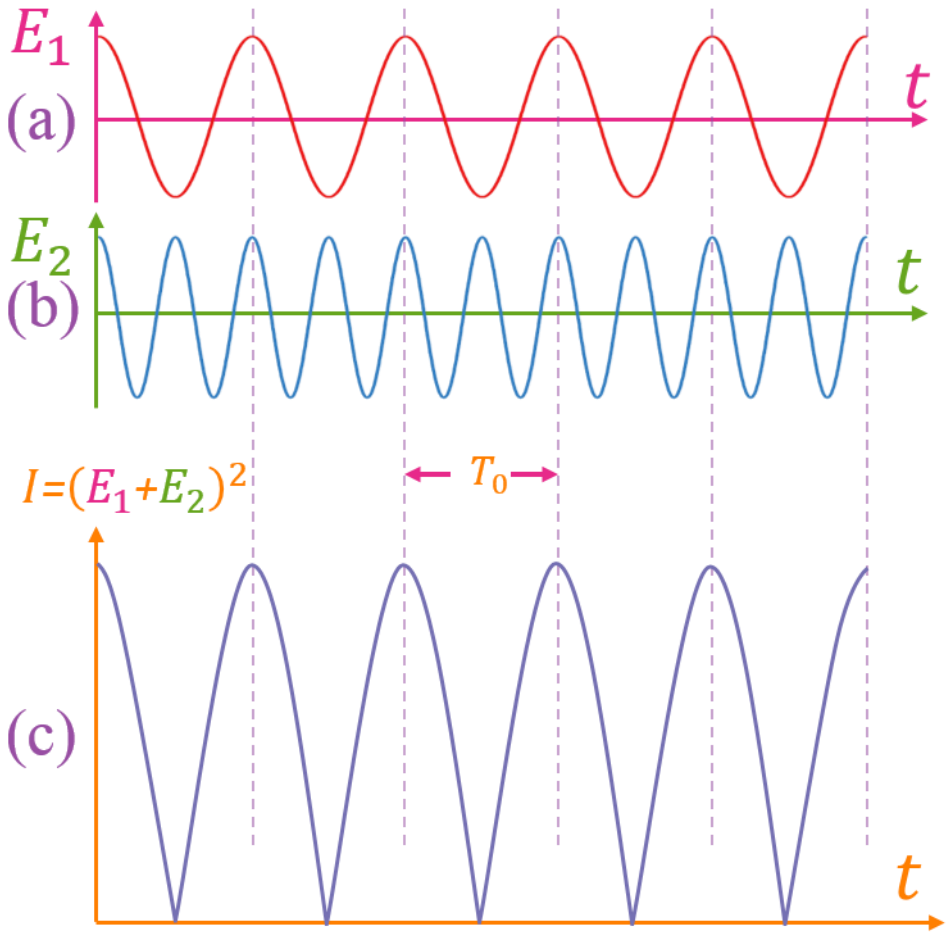

Figure 1.1 Two longitudinal modes oscillating at z=0. (a)-(b) The electric field strengths, (E_1), (E_2), of the two modes and (c) interfered intensity as a function of time.

Based on the above particular case, a more general case of $2N+1$ oscillating modes in a laser resonant cavity with, for simplicity, the same electric field amplitude (E_0) is considered. The q-th electric filed strengths at z=0 can be expressed as:[18]

$$E_q(t) = E_0 \exp\left[j\left(\omega_q t + \varphi_q\right)\right] \tag{1.7}$$

Here ω_q and φ_q represent the angular frequency and initial phase of the q-th longitudinal mode. Under the ordinary circumstance, there is no definite relationship among these initial phases and hence the output from the resonant cavity is composed by the random sum of the longitudinal modes, as seen in figure 1.2 (a).

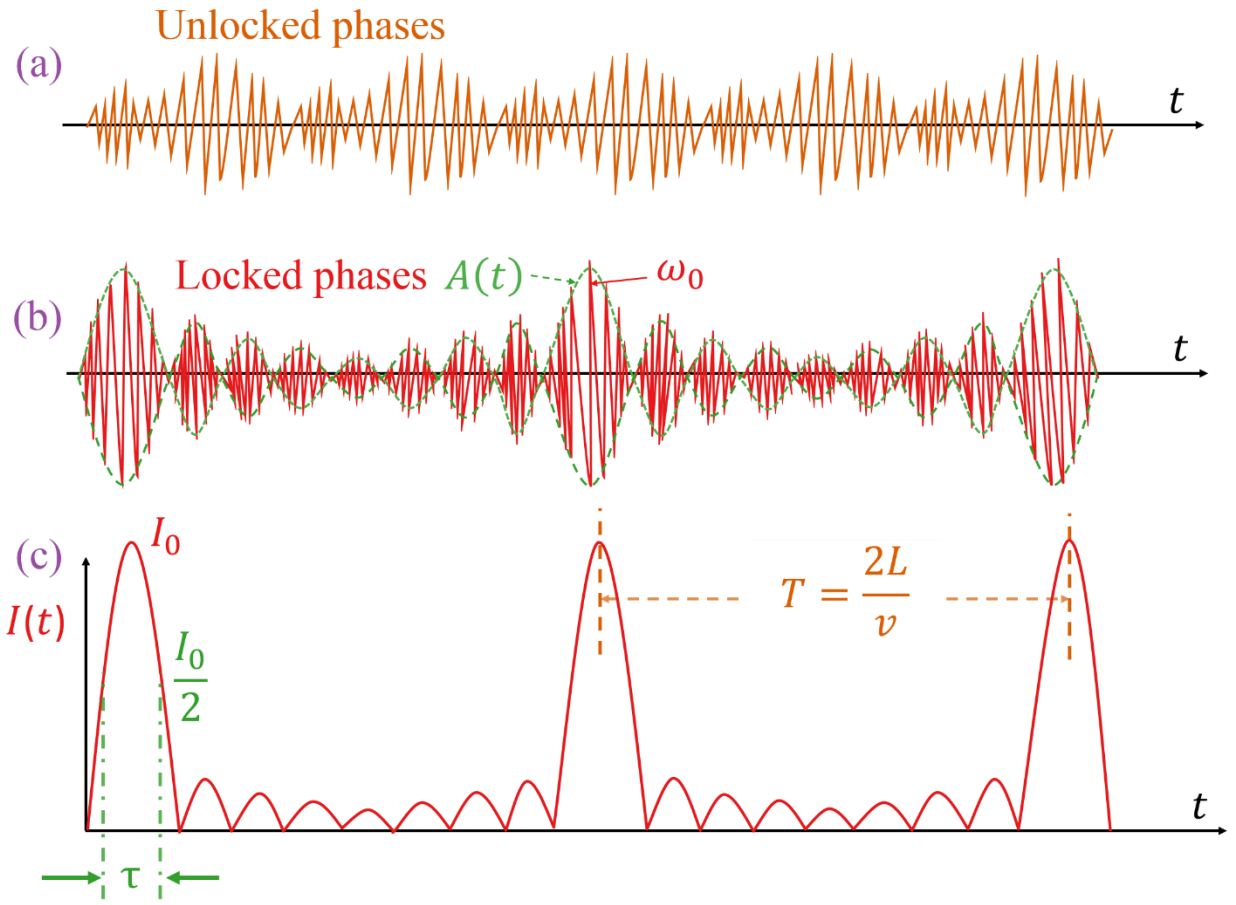

Figure 1.2. Electric field strength and laser intensity as functions of time domain when 2N+1=9. The laser intracavity electric fields with (a) random (unlocked) phases and (b) fixed phases among the longitudinal modes. (c) Mode-locked laser pulses.

In contrast, the output will be dramatically enhanced when the phases φ_q of the longitudinal modes are fixed to the following relationship:

$$\varphi_q = \varphi_{q-1} + \Delta\varphi \tag{1.8}$$

$$i.e., \varphi_q = \varphi_0 + \mathrm{q}\Delta\varphi \tag{1.9}$$

Here $\Delta\varphi$ is a constant. According to Equation (1.7) and $\omega_q = \omega_0 + \mathrm{q}\Delta\omega$, the total electric field, $E(t)$, at z=0 can be calculated as: [19]

$$E(t) = \sum_{q=-N}^{q=N} E_q \exp\left[j\left(\omega_q t + \varphi_q\right)\right]$$

$$= \sum_{q=-N}^{q=N} E_0 \exp\{j[(\omega_0 + \mathrm{q}\Delta\omega)t + \varphi_0 + q\Delta\varphi]\}$$

$$= E_0 \exp[j(\omega_0 t + \varphi_0)] \sum_{q=-N}^{q=N} \exp[j(q\Delta\omega t + q\Delta\varphi)]$$

$$= E_0 \exp[j(\omega_0 t + \varphi_0)] \sum_{q=-N}^{q=N} \cos[q(\Delta\omega t + \Delta\varphi)]$$

$$= A(t)\exp[j(\omega_0 t + \varphi_0)] \tag{1.10}$$

Here $A(t) = E_0 \sum_{q=-N}^{q=N} \cos[q(\Delta\omega t + \Delta\varphi)]$ represents the amplitude of the total electric field:[18]

$$A(t) = E_0 \frac{\sin\left[\frac{1}{2}(2N+1)(\Delta\omega t+\Delta\varphi)\right]}{\sin\left[\frac{1}{2}(\Delta\omega t+\Delta\varphi)\right]} \tag{1.11}$$

Equation (1.11) indicates that $A(t)$ is a periodic function. Based on this equation, the synthesis of a pulse train by adding 9 ($2N + 1 = 9$) longitudinal modes oscillating with fixed-phases can be plotted as Figure 1.2 (b). The peak intensity of the corresponding mode-locked laser pulses can be expressed as:

$$I \propto A^2(t) = E_0^2 \frac{\sin^2\left[\frac{1}{2}(2N+1)(\Delta\omega t+\Delta\varphi)\right]}{\sin^2\left[\frac{1}{2}(\Delta\omega t+\Delta\varphi)\right]} \tag{1.12}$$

It should be pointed out that $\frac{\sin(\Delta\omega t+\Delta\varphi)}{\sin(\Delta\omega t+\Delta\varphi)} \to 1$ as $\Delta\omega t + \Delta\varphi \to 2m\pi$, ($m = 0, 1, 2, \cdots\cdots$). One can therefore obtain the output peak intensity, I_p, at $\Delta\omega t + \Delta\varphi = 2m\pi$:

$$I_p = (2N + 1)^2 E_0^2 = (2N + 1)^2 I_0 \tag{1.13}$$

It can be easily seen from Equation (1.13) that the peak intensity of mode-locked laser pulse is $(2N + 1)^2$ times as the one with random phases of longitudinal modes. Figure 1.2 (c) plots a train of mode-locked laser pulses with 9 ($2N + 1 = 9$) longitudinal modes. Equation (1.12) also indicates that the separation time between two successive peaks, T, *i.e.*, the period of the laser pulses is calculated as:

$$\mathrm{T} = \frac{2\pi}{\Delta\omega} = \frac{2L}{c} = \frac{1}{\Delta v} \tag{1.14}$$

Where L is the separation distance of two sides of the resonant cavity and Δv represents the repetition rate of laser pulses. From Equation (1.13) one can also calculate that the separated time between the maximum and minimum of a pulse by:

$$\tau' = \frac{2\pi}{(2N+1)\Delta\omega} \tag{1.15}$$

Therefore, the pulse duration of a mode-locked laser, *i.e.*, FWHM of I (Equation (1.12)) can be calculated as:[18]

$$\tau \approx \tau' = \frac{2\pi}{(2N+1)\Delta\omega} \tag{1.16}$$

1.1.2 Passive mode-locking

As introduced in chapter 1.1.1, mode-locking (ML) is an important technique in the laser cavity to generate ultrafast laser pulses, in which the pulse duration can go up to femtosecond. The methods of mode-locking mainly consists of active, Fourier-domain, Hybrid and passive mode-locking.[20-22] In general, active mode-locking requires an external signal, like a wave electro optic modulator in the laser cavity, to generate a sinusoidal amplitude modulation.[23] For passive mode-locking, no external signal is needed but a device, *i.e.*, a saturable absorber, inside the laser cavity is required to modulate the intracavity light to obtain laser pulses.[20]

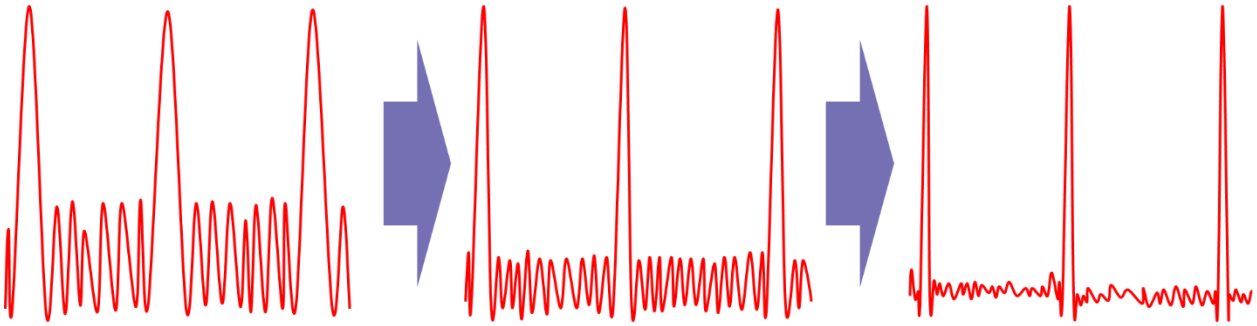

Figure 1.3. The schematic of producing ultrashort laser pulses by passive mode-locking.

During saturable absorption, the majority of the low-intensity light is absorbed by NLO materials while most of the high-intensity passes through the materials.[24] That is to say, as the intensity of the incident light increases, the transmission increases, as illustrated in Figure 1.3. Saturable absorber is including fast- and slow- absorbers. Fast-saturable absorber is referred to as an absorber of which the relaxation time of the excited carrier is much shorter than the mode-locked pulse duration, while the case of an slow-saturable absorber is opposite.[25] A train of pulses are assumed to be already doing a round-trip in a laser resonant cavity with a fast-saturable absorber. Initially, the loss is roughly equal to the unsaturated loss, as seen in Figure 1.4 (a). After interacting with the fast saturable absorber, the intense pulses saturate the absorption and result in a reducing loss and the saturated loss is smaller than the gain.[17] This leads to a time window of net gain, as seen the

brown area in Figure 1.4 (a). As a result, the intensity of the intense pulses increases in comparison to the un-locked case. As the recovery time is sufficient short in a fast-saturable absorber, the loss at the two sides of the pulses can be larger than the gain and hence trailing wing of the pulses can be attenuated, *i.e.*, shorten the pulse duration. That is to say, passive mock-locking is a method to obtain ultrafast laser pulses.[26] In contrast, the pulses with low intensity suffer from loss during the circulating in the resonator as the loss is larger than the gain. A train of passive mode-locked pulses by a fast-saturable absorber are plotted in Figure 1.4 (a). The case is similar for a slow-saturable absorber except for that the net gain still exist for a short time after the pulse, which results from the slow recovery time of the absorber, as seen in Figure 1.4 (b).

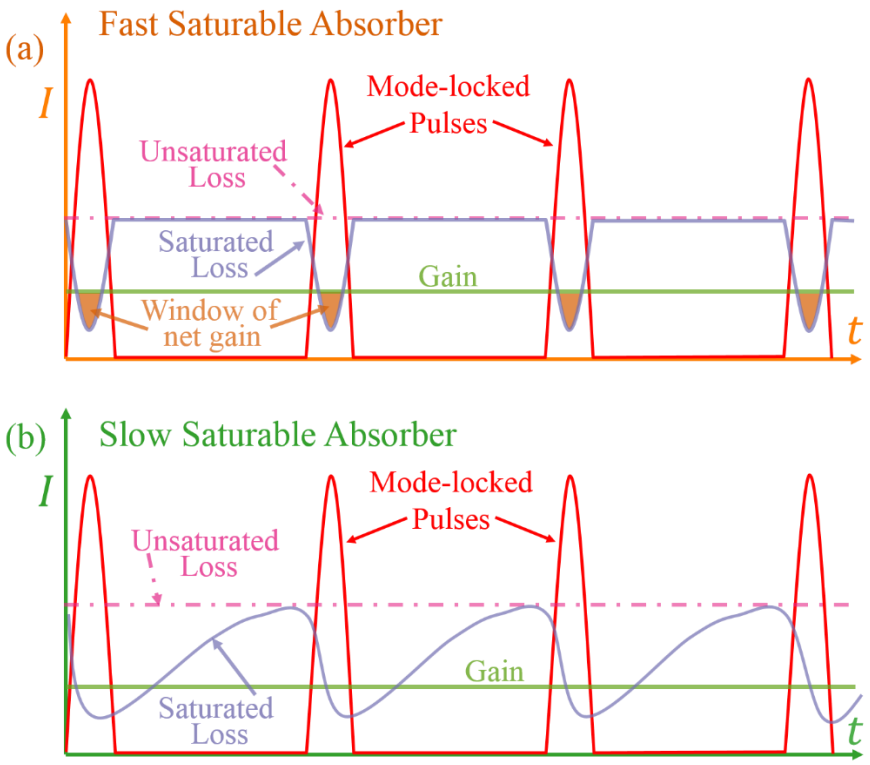

Figure 1.4 Passive mode-locking by a (a) fast- and (b) slow-absorbers.

1.1.3 Saturable absorption

As discussed in last section, saturable absorber is a significant component in a passive mode-locking laser.[20] Saturable absorption is one optical property of NLO materials which occurs under the intense light such as lasers. It is caused by the Pauli-blocking effect, where a transition state is fully occupied and can no longer accept more incoming electrons.[27] When a ray of light interacts with the NLO materials, the electrons in the valence band absorb incident photons and

then are excited to the conduction band. At a low incident intensity case as seen in Figure 1.5(a), most of the photons are absorbed and results in a low transmission. In contrast, if the intensity of the incident laser beam is relatively high, a large number of electrons are excited to the conduction band which is then filled and cannot accept any more incoming electrons. Consequently, most of the incident laser are not absorbed and transverse the material, *i.e.*, high transmission, as seen in Figure 1.5 (b).

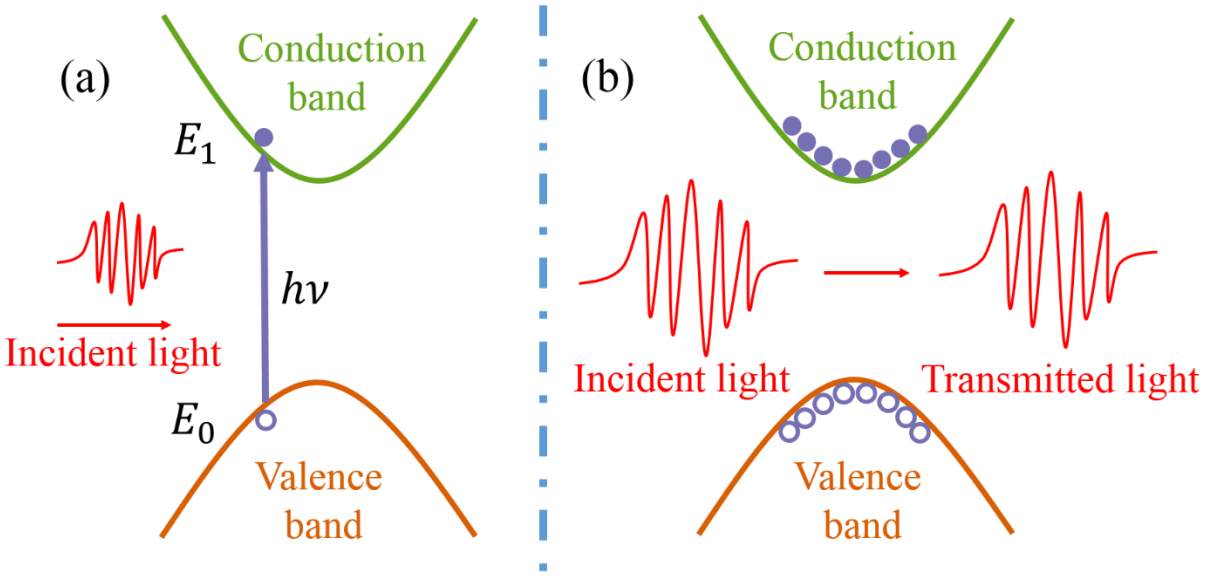

Figure 1.5. The principle of saturable absorption due to the Pauli-blocking. (a) A low-intensity incident laser beam passes through a nonlinear optical material with a low transmission, while the high intensity one results in high intensity. The blue solid circles stand for electrons while the open circles for holes.

1.2 Excitation carrier dynamics

The study on excited carrier relaxation is important for developing both optoelectronic and photonics devices including NLO devices. Because the excited carrier lifetime limits the response time of the devices and determines some of their performance. For example, in a mode-locked laser, the shortest pulse duration is approximately limited to the carrier recovery time for a fast-absorber, and to the recovery time divided by 30 for a slow-absorber.[28] Hence it is necessary to obtain a clear understanding of the excited carrier relaxing processes and mechanisms.

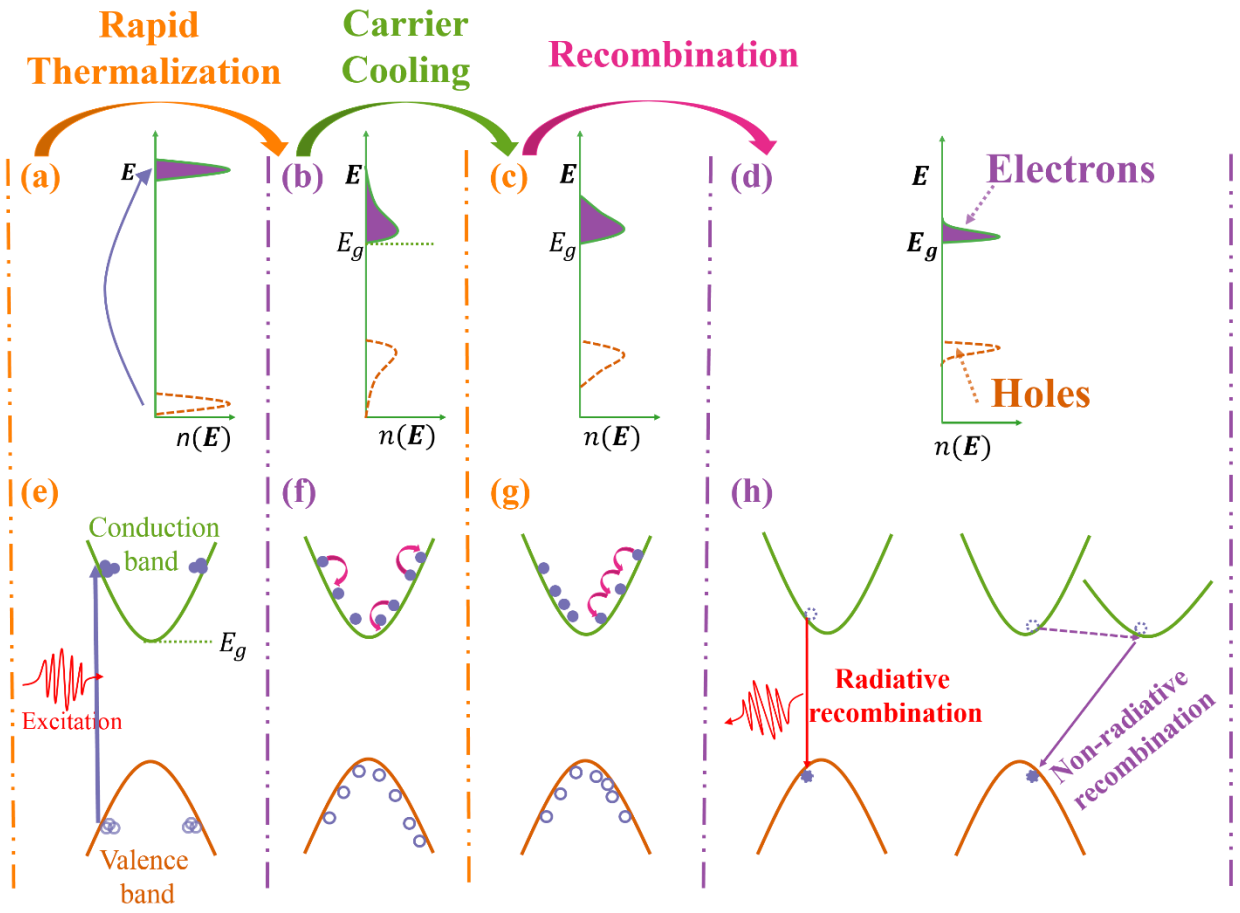

Figure 1.6. A schematic showing the possible excitation, rapid thermalization, cooling and recombination processes of carrier (e)-(h) and corresponding carrier distribution (a)-(d). Excited carrier is injected to the conduction band (e) and stay in a non-thermal state (a). Non-equilibrium carriers are rapidly thermalized to a quasi-thermal state via carrier-carrier scattering path, see (f). Carrier cool down via intraband carrier-phonon scattering, see (g). Electrons recombine with holes in the valence band via radiative or non-radiative recombination until returning to an equilibrium distribution, see (h) and (d).

Figure 1.6 provides a direct view on the possible excitation, rapid thermalization, cooling and recombination processes of carrier (e)-(h) and corresponding carrier distribution (a)-(d). Under the irradiation of the intense laser, electron-hole pairs are generated and the electrons are excited to the conduction band, see Figure 1.6 (e). The energy distribution of these carriers in the early time regime after excitation is shown in Figure 1.6 (a). They do not follow any standard thermal distribution function and cannot be characterized by a temperature.[29] These non-equilibrium carriers will be subsequently thermalized to a quasi-thermal state via carrier-carrier scattering in a very short time regime within ~10 - 200 fs, see Figure 1.6 (f).[30] In the quasi-thermal state, the electron energy distribution follows a Fermi-Dirac distribution:[31]

$$f_n(E) = f_0(E) = \frac{1}{e^{(E-E_f)/k_BT}+1} \tag{1.17}$$

And the holes energy distribution in the valence band follows:

$$f_p(E) = 1 - f_n(E) \tag{1.18}$$

Here E_f is the Fermi energy, k_B is the Boltzmann constant and T is the absolute temperature of the carrier. The distribution of quasi-thermal equilibrium carrier is shown in Figure 1.6 (b) and Figure 1.7 (c). This quasi-thermal carrier distribution is the product of density of states (DOS) and Fermi-Dirac distribution. DOS is referred to as the number of electron states available per unit energy and volume, giving the information where the carrier can occupy. DOS for electrons in the conduction band and holes in valence, respectively, can be expressed as:[32]

$$g_n(E) = 4\pi \left(\frac{2m_e^*}{h^2}\right)^{3/2} \sqrt{\left(E - E_g\right)} \tag{1.19}$$

$$g_p(E) = 4\pi \left(\frac{2m_p^*}{h^2}\right)^{3/2} \sqrt{(E_v - E)} \tag{1.20}$$

Here m_e^* and m_p^* represent the effective mass of an electron and hole respectively, E_g is the bandgap and E_v is the maximum energy of the valence band. $g_n(E)$ and $g_p(E)$ are plotted in Figure 1.7 (a). The carrier concentration is proportional to DOS (The number of electron states available per unit energy and volume) over the interval between E and $E + dE$ and Fermi-Dirac function. Electrons are occupying the energy states above E_g while holes bellow E_v, as seen in Figure 1.6 (e)-(h) and Figure 1.7 (b). Hence the total number of electrons in the conduction band and holes in the valence band can be, respectively, calculated by:[33, 34]

$$n_n(E) = \int_{E_g}^{+\infty} g_n(E) f_n(E) dE \tag{1.21}$$

$$n_p(E) = \int_{+\infty}^{E_v} g_p(E) f_p(E) dE \tag{1.22}$$

Equations (1.21) and (1.22) indicate the total number of carriers that follow the Fermi-Dirac distribution.

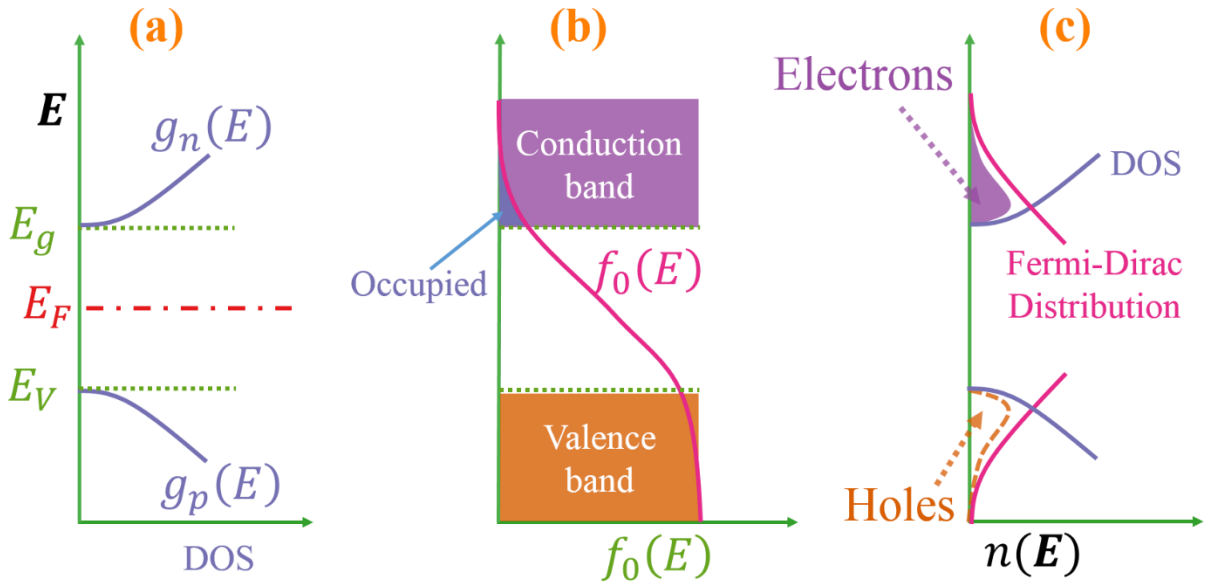

Figure 1.7. (a) DOS of conduction and valence bands as a function of energy for semiconductors. (b) Fermi-Dirac distribution. (c) Carrier distribution resulting from DOS and Fermi-Dirac distribution.

In general, the temperature (T_e for electrons and T_h for holes) of quasi-thermal equilibrium carriers are much higher than that of the lattice, T_L. These carriers are further cooled and thermalized via intraband carrier-photon scattering, [29] as seen in Figure 1.6 (g), with less population in the high energy states, which is shown in Figure 1.6 (c). This process commonly occurs within several picoseconds. Finally the electrons and holes recombine via radiative or non-radiative recombination until returning to an equilibrium distribution, see Figure 1.6 (h) and (d).

The radiative recombination is very likely to be observed in direct bandgap materials instead of indirect bandgap structure. Without the phonon assistance, radiative recombination cannot occur in an indirect semiconductor.[35] In radiative recombination, the excited electrons interact with the lattice by the emission of phonons, including acoustic and optical phonons (Longitudinal and Transverse Optical Phonon), following by recombination with holes with the emission of photons.[36-38] That is to say, one part of the energy of excited electrons is transferred to lattice via phonons and another part releases as photoluminescence.[39] This finally results in a thermal equilibrium between carrier and lattice, *i.e.*, $T_e = T_h = T_L$.

Non-radiative recombination includes Shockley-Read-Hall (SRH) recombination and Auger recombination. SRH recombination is also called trap-assisted recombination, in which electrons and holes recombine through an extra energy state, *i.e.*, a trap state.[40] As shown in Figure 1.8 (a),

an electron or a hole is trapped to an extra energy state followed by recombination with a hole or an electron. The trap state can be generated by defects of the crystal lattice. Hence the SRH recombination can be tuned deliberately by controlling the dopants to change the trap state. Auger recombination is a three-body behavior involving two electrons and one hole.[41] As seen in Figure 1.8 (b), an electron and a hole annihilate with giving energy to another electron in the conduction band. The electron that obtained energy is then excited to higher energy level. Therefore, no phonon emission or photoluminescence is observed in this recombination.

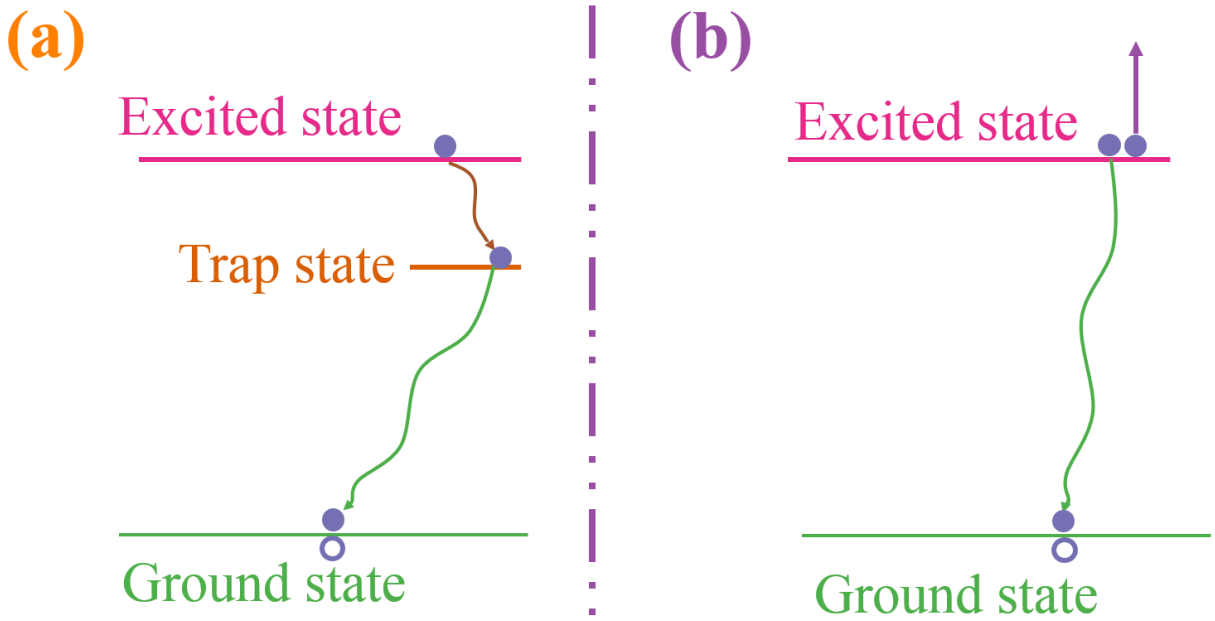

Figure 1.8. Non-radiative recombination: (a) Shockley-Read-Hall recombination and (b) Auger recombination.

1.3 Optical nonlinearities and carrier dynamics of 2D materials

1.3.1 2D materials

As the most typical two-dimensional (2D) material, graphene has been in the spotlight of research for a long time due to its outstanding optical, mechanical, chemical, electronic, thermal and structural properties since it was experimentally fabricated in 2004.[42-47] Graphene is a single layer of hexagonal carbon atoms that are bonded sp^2 hybridized orbitals, see Figure 1.9 (a).[42] Each carbon atom consists of three in-plane covalent carbon-carbon bonds of 0.14 nm and one out-plane *p* orbital.[48]

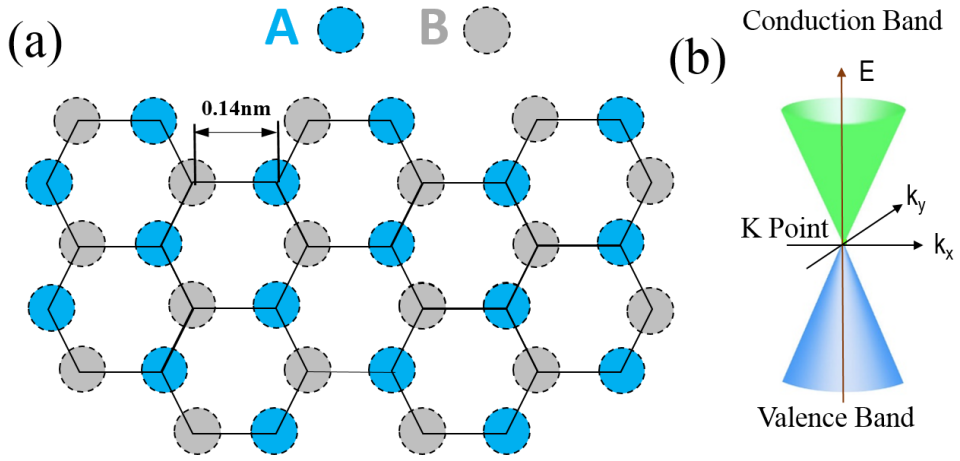

Figure 1.9. (a) Hexagonal carbon atom crystal structure whose lattices are composed of two equivalent carbon atoms A and B. (b) Cosine-like band structure of graphene.

Based on its atom structure, graphene's band structure was modelled to be like two cones, as seen Figure 1.9 (b). In a band structure, the Dirac equation is used to describe the spin $^1/_2$ relativistic quantum particles like electrons and quarks. [49] In conventional semiconductors, for Dirac particles with mass m, there is a band gap ($2mc^2$) between the maximum energy of holes ($E_0 = -mc^2$) and the minimum energy of electrons (E_0). When the energy of electrons, E_e, is far larger compared to its minimum energy, it is proportional to the wave vector k:

$$E_e = \hbar ck \tag{1.23}$$

The massless Dirac fermions of graphene imply that it has a zero-gap in which the fermions near the Dirac point (K point) is described by the Dirac-like Hamiltonian:[42]

$$H = \hbar v_F \begin{pmatrix} 0 & k_x - ik_y \\ k_x + ik_y & 0 \end{pmatrix} = \hbar v_F \boldsymbol{\sigma} \cdot \boldsymbol{k} \tag{1.24}$$

Here the fermi velocity, $v_F = c/300$, takes the place of the role of the light speed in Equation (1.23), $\boldsymbol{\sigma}$ is the 2D Pauli matrix, $\boldsymbol{k}$ is the momentum of the quasiparticle. Similar to the case in conventional semiconductors, two-component spinor wave functions are needed to describe the electronic states contributed by the different carbon sublattices, A and B (See Figure 1.9 (a)). This gives rise to the Cosine-like band structure with zero bandgap, see Figure 1.9 (b). Thanks to this band structure, graphene possess optical response in a super wide spectral range from ultraviolet to radio-wave.

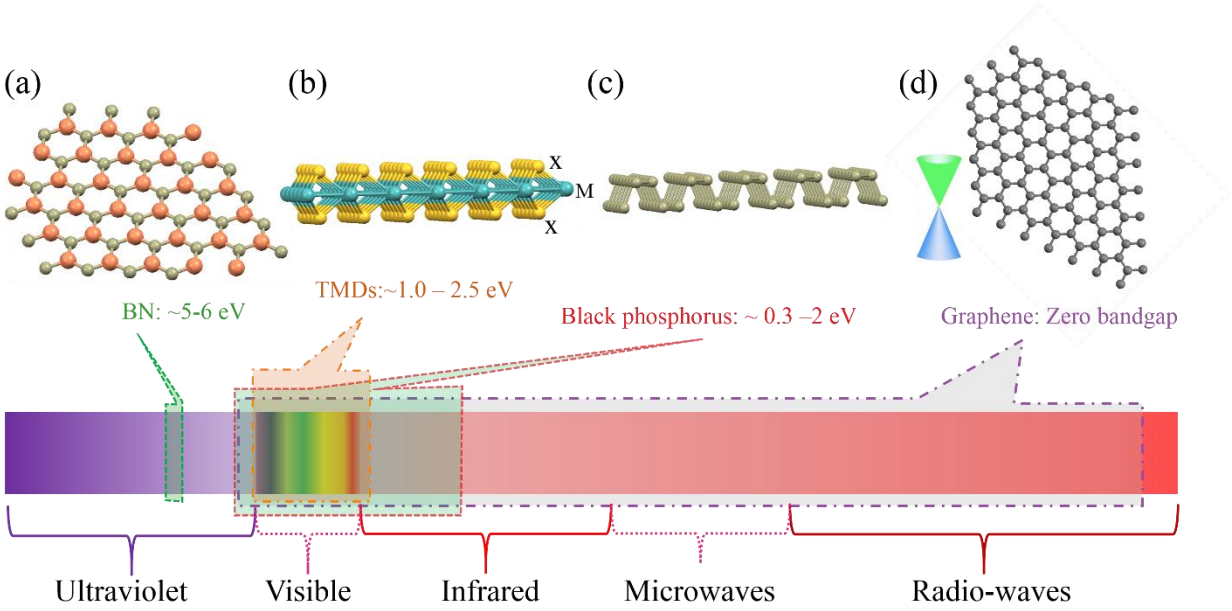

Figure 1.10. The spectral region that is covered by BN, layered TMDs, black phosphorus and graphene.

Follow the similar vein of graphene preparation, a range of graphene analogues, such as 2D transition metal dichalcogenides (TMDs), black phosphorus and boron nitride (BN), were experimentally obtained.[50-53] Layered TMDs are a large 2D material ilk whose form of chemical composition is expressed as MX_2, where M stands for transition metal atoms such as Mo, W, Ti, Ta, Nb, etc., and X for the dichalcogenides atom like S, Se, Ru, Te, etc.[54, 55] As shown in Figure 1.10(b), in a MX_2 monolayer, the transition metal atom layer is sandwiched by two dichalcogenides atom layers.[55, 56] In the majority of these TDMs, a transition from the indirect bandgap in bulk limit to the direct bandgap in their monolayer forms was observed. For example, $MoSe_2$ and MoS_2 monolayers have direct bandgap of 1.55 eV and 1.89 eV while its bulk was proved to be an indirect semiconductor with a bandgap of 1.1 eV and 1.54 eV respectively.[57] Hence, 2D TMDs mainly interact with light in the visible wavelength regime, see Figure 1.10 (b).[58] Layered boron nitride with the bandgap of ~5 - 6 eV shows a narrow optical response in the ultraviolet wavelength region, see Figure 1.10 (a).[59] In contrast, layered black phosphorus with large bandgap transition from ~0.3 eV - 2 eV possessed a broadband optical properties from visible to mid infrared region, as shown in Figure 1.10 (c).[60]

The advent of these two-dimensional materials brings forth great excitation to searchers in the field of optics due to their novel photonics properties such as NLO performance. These novel NLO properties of some 2D materials include large nonlinear optical coefficient, broadband SA from

visible to mid-infrared wavelength region, giant TPA and broadband optical limiting etc.[43, 61-68] 2D materials are also of tremendous interest due to their quantum confinement that leads to intriguing physical phenomenon at room temperature, such as optical Stark effect, Bloch-Siegert shift, exciton formation, trion dynamics and exciton-exciton annihilation etc.[69-73]

1.3.2 NOL properties of 2D materials

As the most typical 2D material, graphene possesses novel NLO properties. In 2009, Prof. Blau's group for the first time reported the broadband optical limiting, *i.e.*, the transmission decreases with the incident intensity, of liquid-phase-exfoliated graphene at the wavelength of 532 nm and 1064 nm.[43] A large resonant 2PA coefficient of bilayer graphene was theoretically calculated to be to∼0.2 cm/W and the giant TPA was experimentally observed in bilayer graphene at 780 and 1100 nm by Z-scan.[61] Graphene was also found to possess SA property and then utilized as a saturable absorber in a mode-locked fiber laser to generate ultrashort laser pulses with duration of 756 fs at the wavelength of 1565nm.[62, 63] This is a popular telecommunication wavelength, implying promising applications of graphene in optical communications.

Some of these layered TMDs were even experimentally demonstrated to have better NLO properties then graphene. Layered Molybdenum Disulfide (MoS_2) was reported to have stronger SA than graphene with an imaginary part of third-order nonlinear optical susceptibility of -1.56 $\times 10^{-14}$ esu.[74] Based on this performance, an ytterbium-doped mode-locking fiber laser using layered MoS_2 as saturable absorber obtained an output with power of 210 mW, a repetition rate of 6.74 MHz and pulse duration of 656 ps at the center wavelength of 1042.6 nm.[64] Intense SHG was observed in odd-layer MoS_2 from 680 to 1080 nm and 810 nm independently.[65, 66] Giant TPA was probed in 1-3 layer Tungsten Disulfide (WS_2) with a larger TPA coefficient up to (1.0+0.8) $\times 10^4$ cm/GW at the wavelength of 1030 nm.[67] Layered black phosphorus was found to have SA properties in a wide wavelength regime from visible to mid-infrared thanks to its large bandgap transition, and utilized to generate ultrafast laser pulse with 272 fs duration at 1550 nm telecommunication wavelength.[60, 68, 75]

1.3.2 Carrier dynamics of 2D materials

Except for the excellent NLO properties, 2D materials are also of tremendous interest in the field of photonics due to their quantum confinement that leads to intriguing physical phenomenon at

room temperature, such as stable exciton, trion formation, exciton-exciton annihilation and optical Stark effect, etc.[70, 71, 76-79]

An exciton is an electron and a hole held together through the Coulomb force.[80] Thanks to the intense coulomb interaction that might results in very high binding energy of excitons, stable excitons can be observed in layered TMDs even at room temperature. [70, 81] Excitons were experimentally observed in monolayer WS_2 and its exciton binding energy was measured to be as large as 0.71 $\pm$0.01 eV.[76] Excitons were also observed to form in the interlayer of MoS_2/WS_2 heterojunctions.[82] When an exciton interacts with a nearby charge due to the existence of free electrons, a trion is generated. Obviously, a trion is a kind of charged quasiparticle consisting of three carriers (two electrons and one hole for negative charged trion, two holes and one electrons for positive charged trion). The formation of trion was directly observed in some TMDs monolayers such as MoS_2, $MoSe_2$ and WSe_2.[70, 78, 79] Exciton-exciton annihilation is a four-body dynamic behavior where two electrons from two excitons recombine with two holes from the two excitons.

The study on these carrier dynamics and NOL properties provides key photophysical insight into the requirements and strategies for developing a saturable absorber, optical limiter and NOL phase modulator based on 2D materials for future optical applications. As the very likely basic material ilk for next generation of optoelectronic and photonic devices, 2D nano- and micro-sheets have been shown, as introduced above, to possess novel optical properties. Even though, some NOL performance and carrier dynamics of many 2D materials used as practical devices remain unclear, leaving large room for the investigation in the crossing field of photonic and 2D materials. Recently, the antimonene monolayer was predicted to be a direct bandgap semiconductor and it is very likely to possess intriguing photonic properties.[83, 84] Liquid-phase exfoliation is an effective way to produce 2D materials in low-cost, high quality and yield.[85] However, 2D nanosheets in solution are not stable for a long time and then generate a difficulty in the practical applications based on liquid-phase-exfoliated 2D materials. Polymer as a host to embody 2D nanosheets might be a way to solve this problem. As the carrier relaxation plays an important role in the photonic behaviours, it is necessary to study the relative excited carrier dynamics.

In light of these, the third-order nonlinear optical response and ultrafast excitation carrier dynamics of some 2D Materials (Including antimonene, molybdenum diselenide, *i.e.*, $MoSe_2$, platinum diselenide, *i.e.*, $PtSe_2$), and their polymer composites are systematically studied based on home-

made spatial self-phase modulation, Z-scan, I-scan, degenerate pump-probe and transient absorptive spectroscopy using continuous wavelength, nanosecond and femtosecond lasers from visible infrared regions (See Figure 1.11). After these basic NOL properties study, a practical photonic device, graphene saturable absorption mirror (GSAM) was fabricated and its NOL performance was compared with a commercial semiconductor saturable absorption mirror (SESAM).

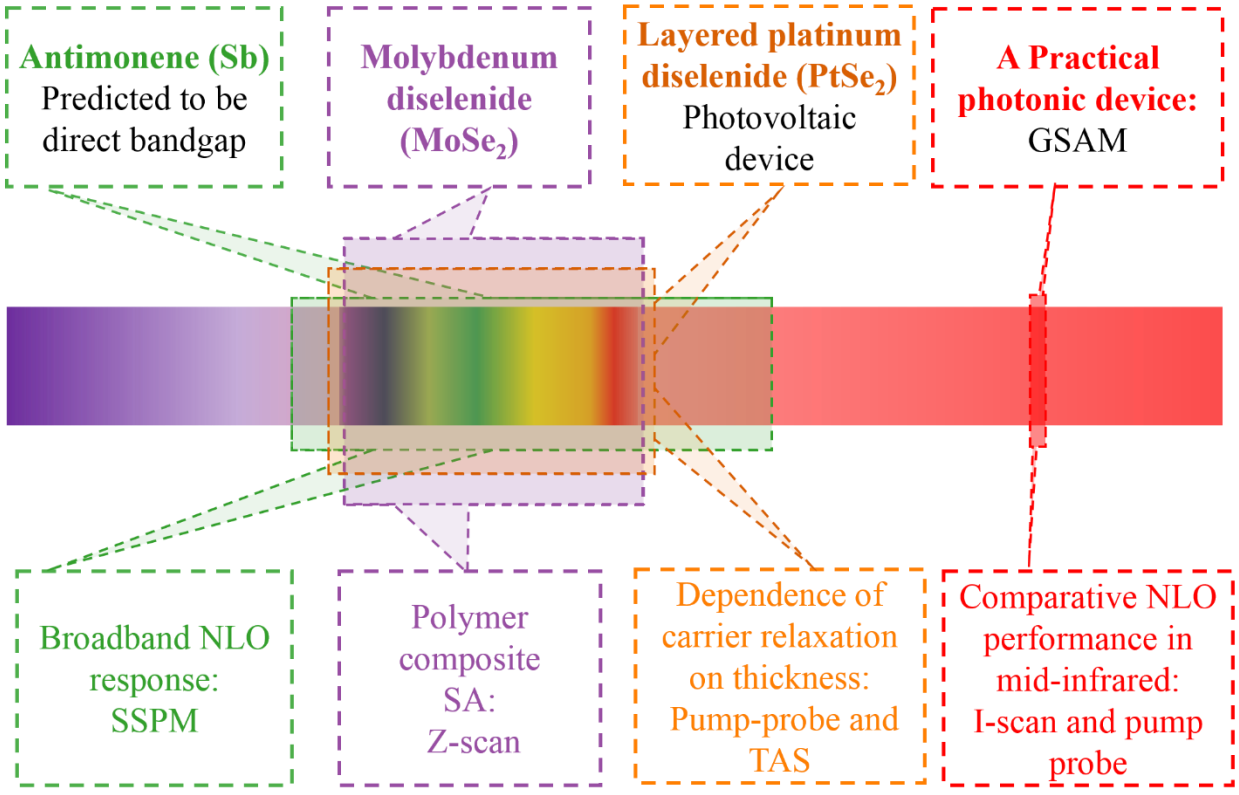

Figure 1.11. The schematic of the main structure of this thesis. The NOL response of liquid-phase-exfoliated antimonene has be studied in a wide wavelength range from 405 nm to 1064 nm. Molybdenum diselenide ($MoSe_2$) nanosheets was utilized to fabricate polymer composite thin films and their sturable absorption (SA) was proven by an open-aperture Z-scan method in the visible range. The dependence of the excited carrier relaxation processes on the thickness of layered platinum diselenide ($PtSe_2$) has been investigated using the degenerate pump-probe technique and transient absorption spectroscopy (TAS). After these basic NOL properties study, a practical photonic device, graphene saturable absorption mirror (GSAM) was fabricated and its NOL performance was compared with a commercial semiconductor sturable absorption mirror (SESAM) at mid-infrared region based on I-scan and pump-probe techniques.

2. Nonlinear optical techniques

2.1 Spatial self-phase modulation

2.1.1 Mechanism of SSPM

Spatial self-phase modulation (SSPM) is a typical nonlinear optical phenomenon of the interaction of light and matter that is induced by the optical Kerr effect: $n = n_0 + In_2$, where n, n_0 and n_2 represent the refractive index, linear and nonlinear refractive index of nonlinear mediums respectively. I is the incident laser intensity.[86, 87] SSPM has be observed as a transmitted concentric cone diffraction rings pattern (see Figure 2.1 (b)) in the far field in many nonlinear optical materials such as liquid crystal, carbon nanotube, graphene dispersion, and dye solutions etc.[86-89] Its mechanism can be explained through reorienting and aligning the vector of molecule or nanosheets of nonlinear optical materials by the laser electromagnetic field.[86, 87, 90] Under the irradiation of the laser, electron-hole pairs are produced and they move oppositely parallel to the direction of optical electric field, resulting a polarization of the molecular or nanosheets.[86, 87] This initial polarization are very likely not to be parallel to the optical electric field and hence exist an interaction energy, which leads to the reorientation and alignment of the molecule or nanosheets.[86] A change of local refractive index, Δn, is then induced with a corresponding laser phase shift:[87]

$$\Delta\psi(r) = \frac{2\pi n_{0e}}{\lambda}\int_{-L_e/2}^{L_e/2} n_2 I(r,z)dz \qquad (2.1.1)$$

Here r is the radial coordinate of laser beam and λ represent the laser wavelength in the vacuum. $L_e = \int_{L_1}^{L_2}(1 + z^2/{z_0}^2)^{-1}\,dz$ is the effective optical path length contributing to SSPM, where L_1 and L_2 are the on-axis coordinates of sample, and $L = L_2 - L_1$ is the sample thickness. $z_0 = \pi w_0^2/\lambda$ (w_0 is the $1/e^2$ laser beam waist) is the diffraction length the focus point of the laser. For a laser with Gaussian profile, the phase shift can be also expressed as:[87]

$$\Delta\psi(r) \approx \Delta\psi(0)\exp\left(-\frac{2r^2}{w_0^2}\right) \tag{2.1.2}$$

Here $\Delta\psi(0)$ stands for the phase shift at $r = 0$. Based on Equation (2.1.2), the profile of the phase shift is plotted in Figure 2.1 (a). Since $\Delta\psi(0)$ is a constant for one sample, there will always be two r values, r_1 and r_2, satisfying the Equation:[87]

$$\left(\frac{d\Delta\psi}{dr}\right)_{r=r_1} = \left(\frac{d\Delta\psi}{dr}\right)_{r=r_2} \tag{2.1.3}$$

Here $d\Delta\psi/dr$ is the slope of the curves of the phase shift profile, which represents the wave vector. Therefore Equation (2.1.3) proves that the light fields from the region r_1 and r_2 possess the same wave vector and then interfere.[87] One can observe the maximal destructive and constructive interference appears in the far field when $\Delta\psi(R_1) - \Delta\psi(R_1) = M\pi$, where M is an integer.[87] This results in the typical SSPM diffraction rings patterns, as seen in Figure 2.1 (b). From Equation (2.1.1), it is clear that the phase shift is relative to the nonlinear refraction of the materials. Hence, the nonlinear optical response can be studied by analyzing their SSPM phenomenon.

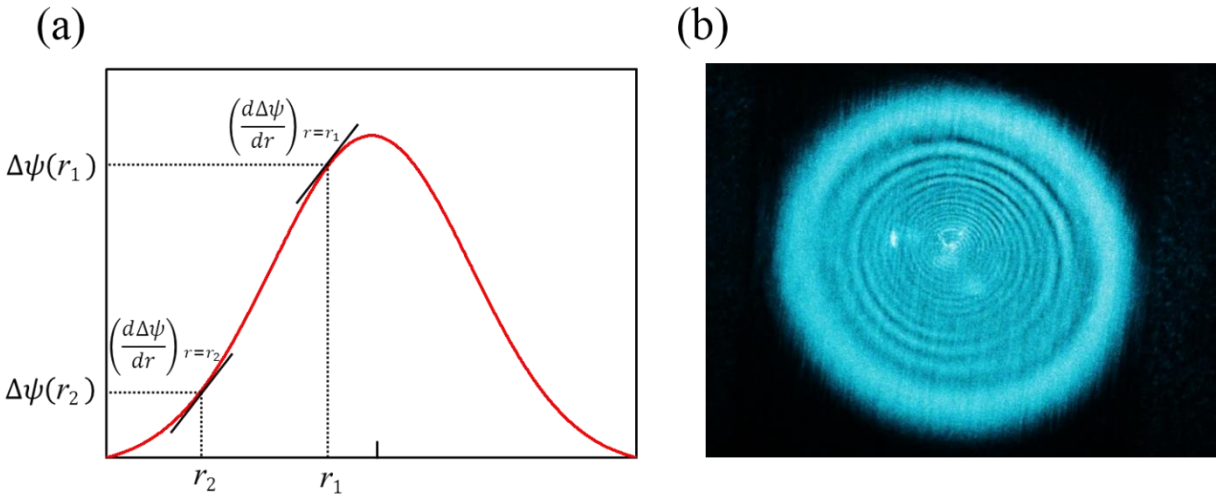

Figure 2.1 (a). The profile of the phase shift. (b) A typical SSPM diffraction rings patterns captured in the far field from a 488 nm laser.

2.1.2 Kirchhoff's diffraction integral

The diffraction rings (Figure 2.1 (b)) can be further confirmed to be induced by SSPM using Kirchhoff's diffraction integral. In general, intensity distribution of a focused laser beam follows the Gaussian function, which can be described by: [91]

$$I(r,z) = I_0(1 + z^2/{z_0}^2)^{-1} exp(-2r^2/{w_z}^2) \quad (2.1.4)$$

where *r* is the radial distance, $z_0 = \pi {w_0}^2/\lambda$ is the diffraction length of the beam at the focal point $z = 0$, w_0 is the radius of beam waist, λ is the wavelength of the laser in vacuum, w_z is the radius of beam at a given *z*, and I_0 is the on-axis intensity, which is the twice of *I*. For a Gaussian beam transmitted through a nonlinear material, the Kirchhoff's diffraction integral for the diffraction intensity distribution can be expressed as [92-95]

$$I(R,D) = \left(\frac{k_0}{D}\right)^2 I_0 \left| \int_0^\infty \left\{ r J_0\left(\frac{k_0 R r}{D}\right) exp\left(-\frac{2r^2}{w_0^2}\right) exp[-i(\phi_L + \phi_{NL})] \right\} dr \right|^2 \quad (2.1.5)$$

where *R* is the radius of the rings in the pattern, $k_0 = 2\pi n_0/\lambda$ is the wave vector, *D* is the distance from the sample to the diffraction rings pattern, and J_0 is the zeroth-order Bessel function of the first kind. The linear and nonlinear phases (ϕ_L and ϕ_{NL}) are given by $\phi_L = k_0 r^2(1/D + 1/\rho)/2$ and $\phi_{NL} = k_0 n_2 L I_0 exp(-2r^2/w_0^2)$, where L is the sample thickness, and ρ is the radius of wavefront curvature of the incident beam in the nonlinear optical medium. The calculated radial intensity distribution based on Equation (2.1.5) is shown in Figure 2.2 (b). The intensity distribution is symmetrical, and the outmost is highest and decrease toward the center. This trend is in good agreement with the experimental intensity distribution that is shown Figure 2.2 (a)

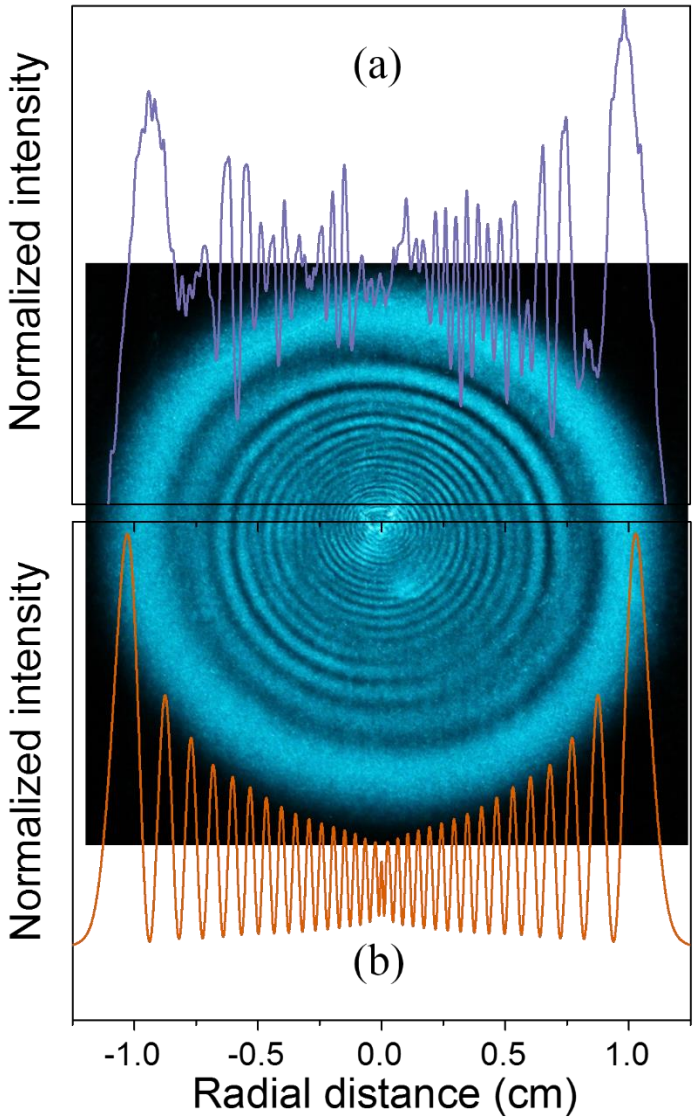

Figure 2.2. Experimental (a) and theoretical (b) and radial intensity distributions of a typical SSPM diffraction rings. The blue concentric circles are the SSPM diffraction rings pattern generated by a 488 nm laser.

2.2 Z-scan

2.2.1 Closed- and open-aperture Z-scan

Z-scan technique was invented and reported for the first time in 1989 and used to measure the nonlinear refractive index n_2 by Sheik-Bahae et al,[96], it was later utilized to measure the nonlinear absorption in 1990 by David J. Hagan et al.[97] This technique involves open-aperture and closed-aperture Z-scans, which can be used to measure the third-order nonlinear susceptibility

and nonlinear refractive index respectively (see Figure 2.3(a) and (b)).[24, 98] The main principle is to obtain the nonlinear optical parameters by analyzing the transmission of nonlinear materials as a function of the incident laser intensity. A lens is used to focus the laser beam to achieve continuously variable laser intensity. The sample is placed after the lens, in the direction of travel of the laser, and is translated in the Z-direction. In the open-aperture Z-scan, all the transmitted signal is collected by a lens into a detector. In the closed-aperture configuration, an aperture is placed in the center of the laser beam before the detector (See Figure 2.3(b)). This makes sure that only a small part of the light from the center of the transmitted beam can arrive at the detector. By recording the position of the sample on the Z-axis, the transmission as a function of incident laser intensity can be acquired.

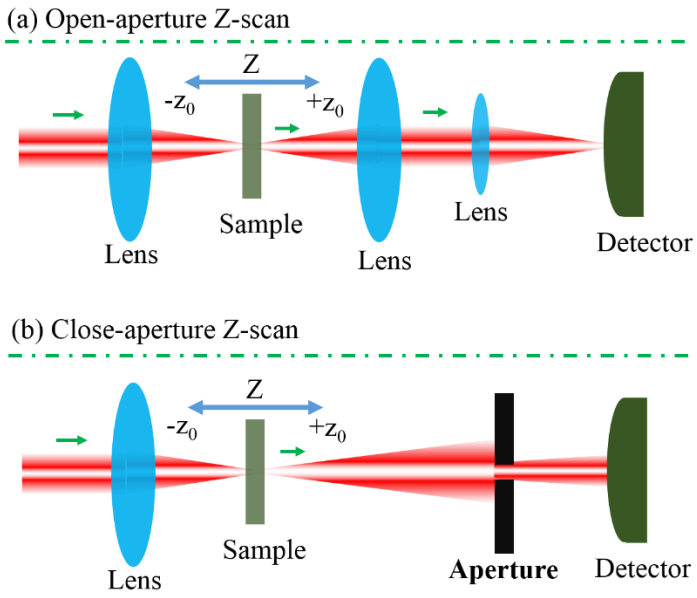

Figure 2.3. Schemes showing the principle of open-aperture (a) and (b) closed-aperture Z-scan.

Closed-aperture Z-scan can be utilized to measure the nonlinear refractive index (n_2) of materials and the typical results were seen in Figure 2.4 (a).[96, 97] The change of the normalized transmittance is due to the self-focus effect induced by the Kerr effect in nonlinear optical materials. For positive-refractive-index materials, a positive self-focusing can be observed under high-intensity lasers.[97] As the sample moves from $-z_0$ toward the focus point (z = 0), the incident intensity increases and results in a larger dispersion angle of the laser beam in the far-field due to the larger positive self-focusing (See Figure 2.5 (a)). That is to say, less and less light can reach the detector. Consequently, the normalized transmittance decreases with the movement of the sample.

When the sample is moved from focus point toward $+z_0$ direction, a positive self-focusing is also induced. But this leads to smaller dispersion of the laser beam in the far field and more light arriving at the detector, which means an increase in the normalized transmittance (See the orange solid line in Figure 2.4(a)).

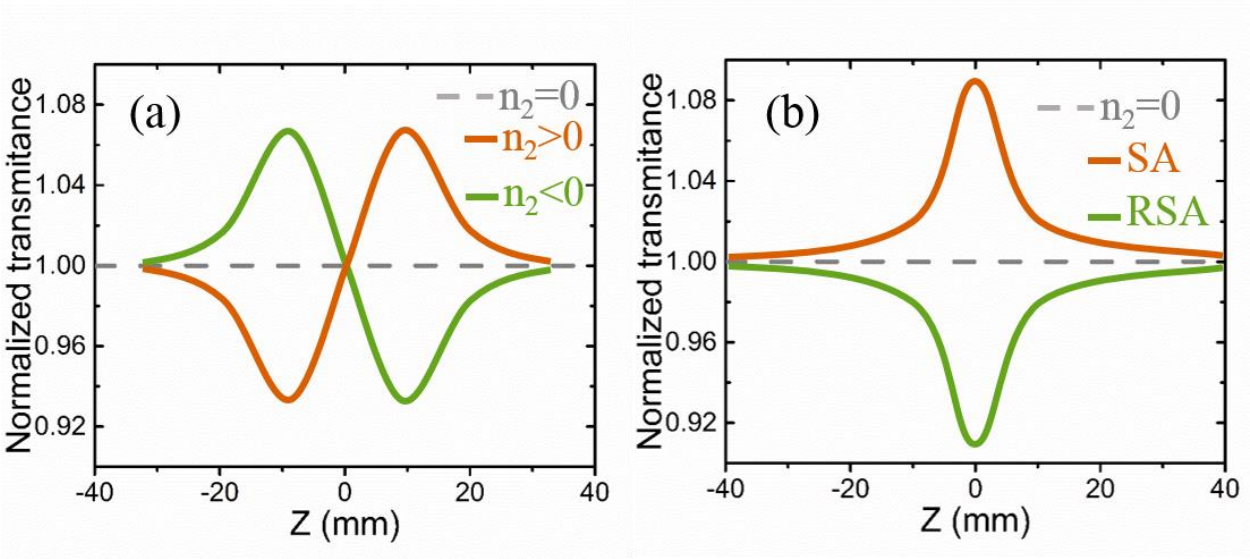

Figure 2.4. A typical (a) closed-aperture and (b) open-aperture Z-scan curves. The curves of linear optical materials are straght lines and their normalized tansmitance are equal to 100% at all incident intensity in both configurations.

In contrast, a negative self-focusing would be induced in negative-refractive-index materials, which is akin to a concave lens.[99] Therefore the cases are opposite to that of positive-refractive-index materials. The results are seen in the green solid line in Figure 2.4(a) and the schematics showing the principle are seen in Figure 2.5(c) and (d). A photo of the Z-scan set-up used in this thesis is shown in Figure 2.6.

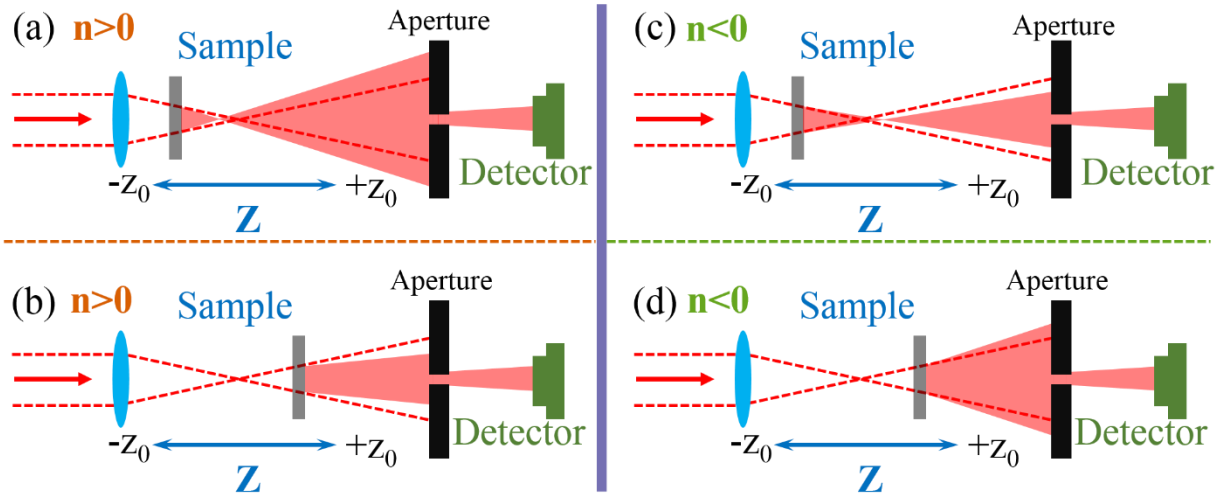

Figure 2.5. The principle of closed-aperture Z-scan measurement. (a) and (b) show the schematics of self-focus effect in positive-refractive-index materials, which is akin to a convex lens. (c) and (d) are the cases in negative-refractive-index materials, but akin to a concave lens.

Open-aperture Z-scan is a more common nonlinear optical tool which has been widely utilized to study the third-order optical effects and scatterings. These effects are mainly observed as saturable absorption (SA) and reverse saturable absorption (RSA) in the open-aperture Z-scan measurements.[100, 101] SA is caused by the electron-filling effect, *i.e.*, Pauli-blocking principle, which is related to the cross-sections of the ground state and the excited states.[102] Take a two-level system for instance, as the sample is moved toward the focus point, *i.e.*, increasing the intensity, more electrons are excited from the ground-state to the excited state. When the cross-section of the ground state is smaller than that of excited state, no more electrons can be filled to the excited state once the incident intensity reaches a saturable threshold. Hence the transmittance increases with the incident laser intensity, *i.e.*, the movement of the sample toward the focus point (See the orange solid line in Figure 2.4(b)). In contrast, the transmittance at the focus point ($z = 0$) is smallest for RSA (see the green solid line Figure 2.4(b)), where the cross-section of excited state is generally larger than that of the ground state.[103-105] For example, in the two-photon absorption where the electrons in the valence band absorb two photons and jump to the conduction band, the transmittance decreases with increasing intensity of the incident laser which pumps more electrons to the excited state.[67]

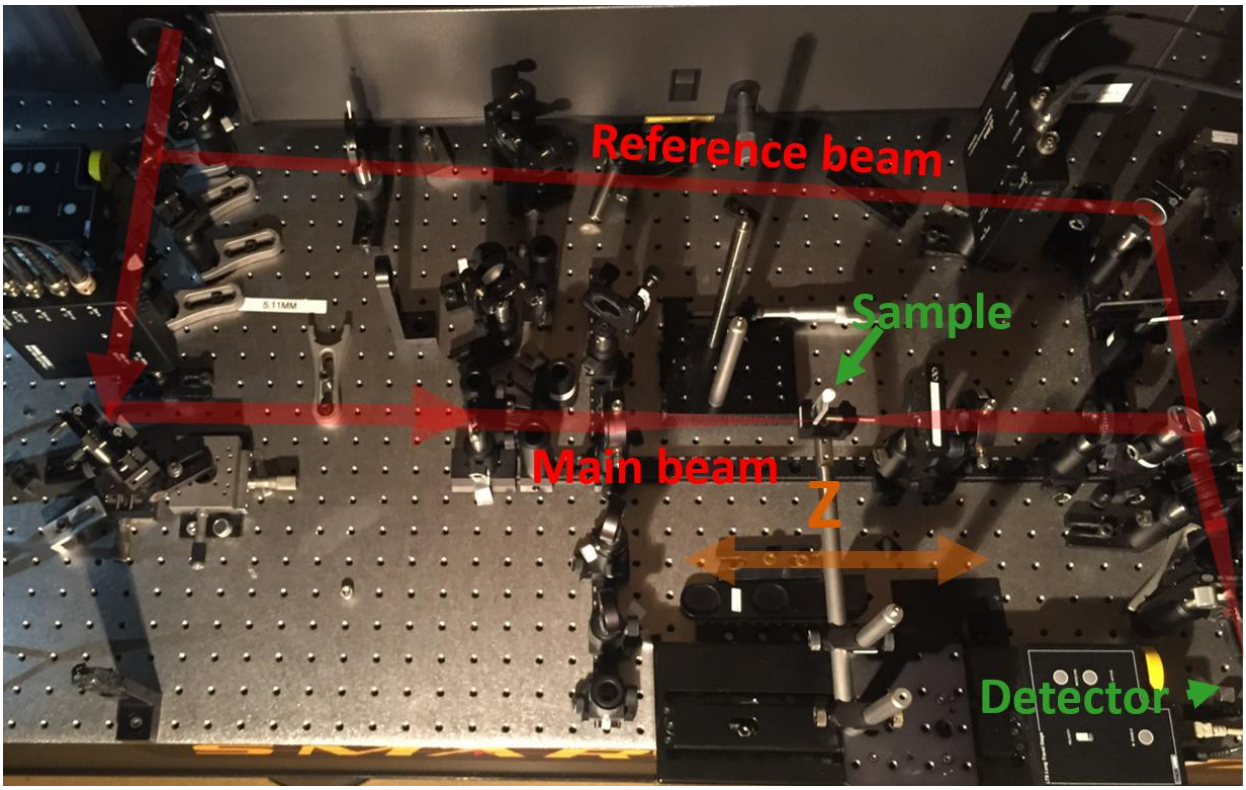

Figure 2.6. A photo of an open-aperture Z-scan set-up used in this thesis.

2.2.2 NLO theory of Z-scan

To analyze the nonlinear optical (NLO) behaviors based on Z-scan measurements, nonlinear optical theories and models are necessary. When the light is propagating along the z direction inside the nonlinear optical medium, the corresponding equation can be written as:[74]

$$\frac{dI}{dz} = -\alpha(I) \cdot I \tag{2.2.1}$$

where I is the laser intensity, z is the propagating distance in the medium and $\alpha(I)$ is the total absorption which can be expressed using linear absorptive and nonlinear absorptive coefficients (α_0 and α_{NL} respectively):[24, 51]

$$\alpha(I) = \alpha_0 + \alpha_{NL} \cdot I \tag{2.2.2}$$

This equation indicates that the total absorption originates from both linear and nonlinear parts, of which α_0 can be measured directly under a lower incident intensity. By applying Equations (2.2.1) and (2.2.2) to fit the open-aperture Z-scan trace, the nonlinear absorption coefficient can be

obtained.[24] As α_{NL} is related to the imaginary part of the third nonlinear optical susceptibility $\mathrm{Im}(\chi^{(3)})$, one can study the third-order optical effects:[24, 51, 74]

$$\mathrm{Im}(\chi^{(3)}) = (1.04 \times 10^{-9} c\lambda n^2/\pi^2) \cdot \alpha_{NL} \quad (2.2.3)$$

where c is the light speed, λ represents the incident laser wavelength in vacuum and n is the effective refractive index of materials.

In a case where both saturable and reversible saturable absorption exist, the total absorption can be written as:[61]

$$\alpha(I) = \frac{\alpha_0}{1+I/I_S} + \beta I \quad (2.2.4)$$

where I_S saturable absorption intensity, which is defined as the intensity where the transmittance reaches half of the maximum. The first term of Equation (2.2.4) is utilized to describe the saturable absorptive behavior while the second term (βI) is related to the reversible saturable absorption such as two-photon absorption (TPA). By combining Equation (2.2.1) and (2.2.4), one can have the general nonlinear propagation equation for modeling Z-scan traces:[61]

$$\frac{dI}{dz} = -\left[\frac{\alpha_0}{1+I/I_S} + \beta I\right] \cdot I \quad (2.2.5)$$

In TPA, β is the TPA coefficient. On one hand, if β was fitted to be zero, the total absorption in Equation (2.3.4) can be written as $\alpha(I) = \alpha_0/(1 + I/I_S)$ which is a simple saturable model. That is to say, the total absorption is dominated by saturable absorption, and TPA does not contribute to it. On the other hand, if I_S was fitted to be much larger than I, *i.e.*, $1 + I/I_S \approx 1$, the total absorption is only contributed by TPA. From this point of view, the general open-aperture Z-scan modeling Equation (2.3.4) can be utilized to distinguish SA and RSA behaviors.

2.3 I-scan

2.3.1 Principle of I-scan

I-scan is another effective method to study nonlinear optical behaviors of materials, particularly for the solid samples. A typical I-scan set-up is shown in Figure 2.7. The intensity of an initial laser beam is tuned by a variable filter which is moved via a linear motorised stage. After the variable filter, the laser beam is split into two beams: a reference beam and a main one. The

reference beam is collected by a convex lens into a detector directly. Another convex lens is employed to focus the main beam into the sample which is placed at the focus point. Another convex lens and detector are used to measure the transmitted (reflective) signal. By moving the variable filter to change the incident intensity, the transmittance (reflection) as a function of the intensity can be obtained. As the laser spot is focused at a single position of the sample, I-scan possesses an obvious advantage of avoiding the noise created by moving samples when comparing to similar NLO techniques. This is particularly significant for the solid sample whose surface is not uniform.

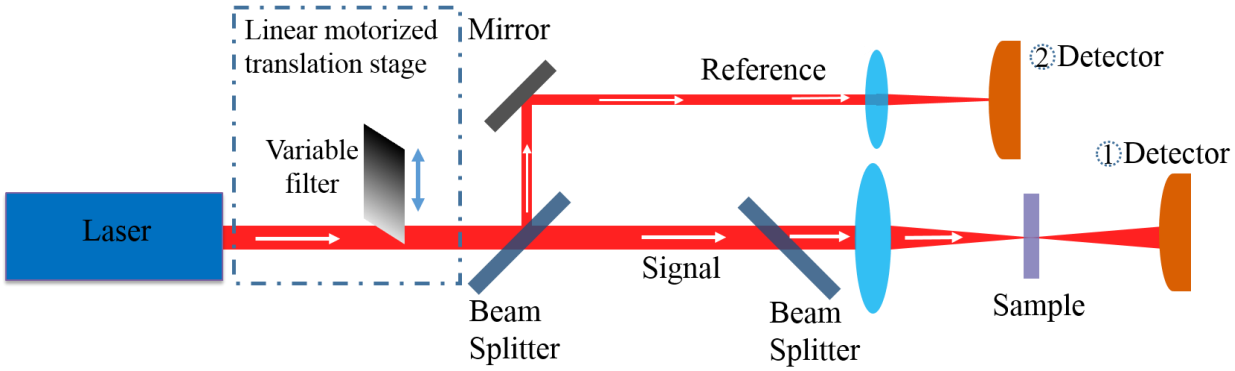

Figure 2.7. The schematic of a typical I-scan set-up.

2.3.2 Knife-edge measurement of the beam diameter

In I-scan measurements, it is necessary to figure out the beam profile to calculate the laser intensity. This is also one part of the pump-probe measurements. A typical method is to calculate a beam diameter by measuring the integral of Gaussian beam intensity from $-\infty$ to the position of a razor blade edge which is moving through the laser beam perpendicularly.[106-109] A Gaussian beam with a xyz coordinate axes is shown in Figure 2.8(a). Z-axis is the laser propagation direction and a razor blade moves along y-axis direction in the x-y plane (See Figure 2.8(b)).

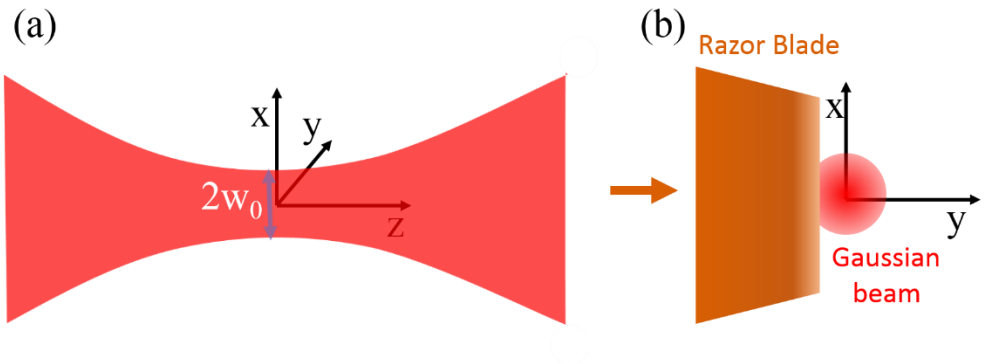

Figure 2.8. (a) The scheme of a typical Gaussian beam that propagates along Z-axis direction. (b)The knife-edge method to measure the diameter of a Gaussian beam. The razor blade is translating along x-axis in the x-y plane which is perpendicular to the laser propagating direction.

A typical curve that measured Gaussian beam intensity as a function of the razor blade edge position is shown in Figure 2.8(a). To obtained the diameter of the Gaussian beam from this experimental data, one can analyze its spatial profile in the x-y plane, which is expressed as:[108]

$$I(x,y) = I_0 exp[r^2(x,y)] \tag{2.3.1}$$

where I_0 is the peak intensity and $r^2(x,y) = -2\left[\frac{(x-x_0)^2}{w_x^2} + \frac{(y-y_0)^2}{w_y^2}\right]$, in which w_x and w_y are the x- and y-axis radius respectively where the intensity drops to $1/e$ times the peak intensity I_0. (x_0, y_0) is the center of the beam profile. The total intensity of the laser beam can be calculated by:[108, 109]

$$I_{Total} = \int_{-\infty}^{+\infty}\int_{-\infty}^{+\infty} I_0 exp\left\{-2\left[\frac{(x-x_0)^2}{w_x^2} + \frac{(y-y_0)^2}{w_y^2}\right]\right\} dxdy \tag{2.3.2}$$

To simply the calculation, the center of the beam is defined to be the zero point of both the x and y axes, see Figure 2.8. (b). Equation (2.3.2) can be expressed as:

$$I_{Total} = \int_{-\infty}^{+\infty}\int_{-\infty}^{+\infty} I_0 exp\left[-2\left(\frac{x^2}{w_x^2} + \frac{y^2}{w_y^2}\right)\right] dxdy \tag{2.3.3}$$

From Equation (2.3.2), the total intensity was calculated via the Gaussian integral ($\int_{-\infty}^{+\infty} e^{-x^2} = \sqrt{\pi}$) to be $I_{Total} = \frac{\pi}{2} I_0 w_x w_y$. As the razor blade was moved to the Y position, the area of the laser beam from $-\infty$ to Y was blocked and the corresponding intensity ($I_{Y.B}$) can be calculated via the Gaussian integral:[108]

$$I_{Y.B} = \int_{-\infty}^{+Y}\int_{-\infty}^{+\infty} I_0 exp\left[-2\left(\frac{x^2}{w_x^2}+\frac{y^2}{w_y^2}\right)\right]dxdy = \frac{\pi}{4}I_0 w_x w_y + \sqrt{\frac{\pi}{2}}I_0 w_y \int_0^Y exp\left(-\frac{2y^2}{w_y^2}\right)dy \quad (2.3.4)$$

Therefore the transmitted intensity is written as:

$$I_{T,Y} = I_{Total} - I_{Y.B} = \frac{I_{Total}}{2} - \frac{I_{Total}}{2}\frac{2}{\sqrt{\pi}}\int_0^{\sqrt{2}Y/w_y}\left[\exp(-\frac{2y^2}{w_y^2})\right]d\left(\sqrt{2}\,y/w_y\right) \quad (2.3.5)$$

By combining the standard error function: $\mathrm{erfc}(y) = \frac{2}{\sqrt{\pi}}\int_0^y \exp(-u^2)du$ and take the $u = \sqrt{2}\,y/w_y$, Equation (2.3.5) is then written as:[108]

$$I_{T,Y} = \frac{I_{Total}}{2}\left[1 - erfc\left(\frac{\sqrt{2}Y}{w_y}\right)\right] \quad (2.3.6)$$

$I_{T,Y}$ is the measured intensity when the razor blade edge is sitting at Y position. Therefore, Equation (2.3.6) can be utilized to fit the experimental data obtained from the configuration of Figure 2.8. An experimental data is shown in Figure 2.9 (a) and the corresponding fitting results obtained from Equation (2.3.6) is plotted in Figure 2.9 (b).

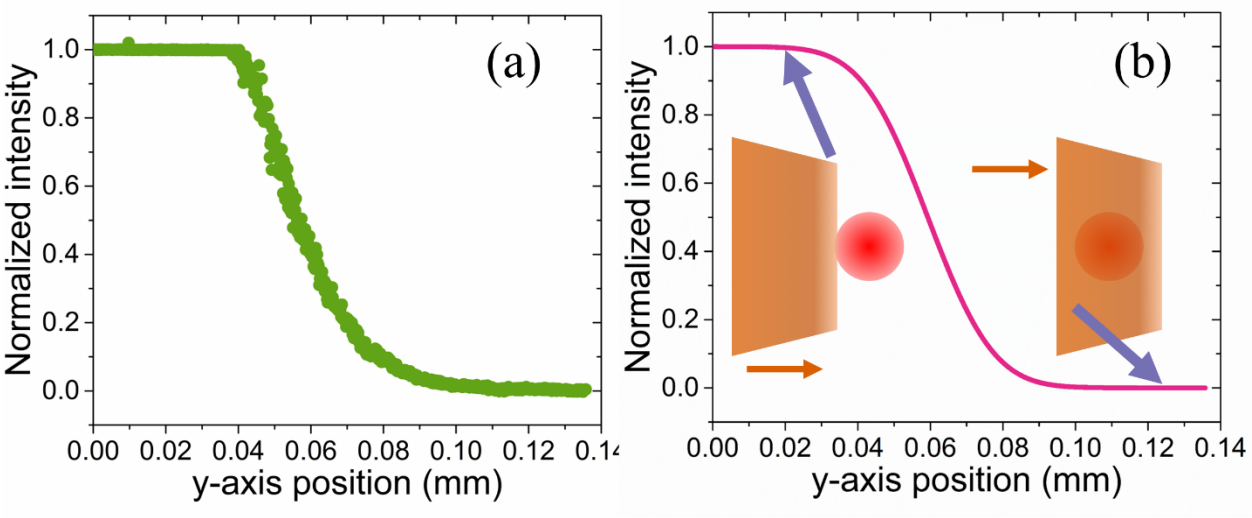

Figure 2.9. Normalized (a) experimental and (b) fitting integrated Gaussian beam intensity as a function of the razor blade edge position. Insets in (b) show schemes of the razor blade and beam cross-section at different position.

Another method is to employ the first differential to convert the measured transmitted intensity (Figure 2.10(a)) into an initial beam intensity, with a Gaussian distribution (See green solid scatters in Figure 2.10(b)). The Gaussian function is then utilized to fit the converted data and the width at $1/e$ of peak intensity is the beam diameter.

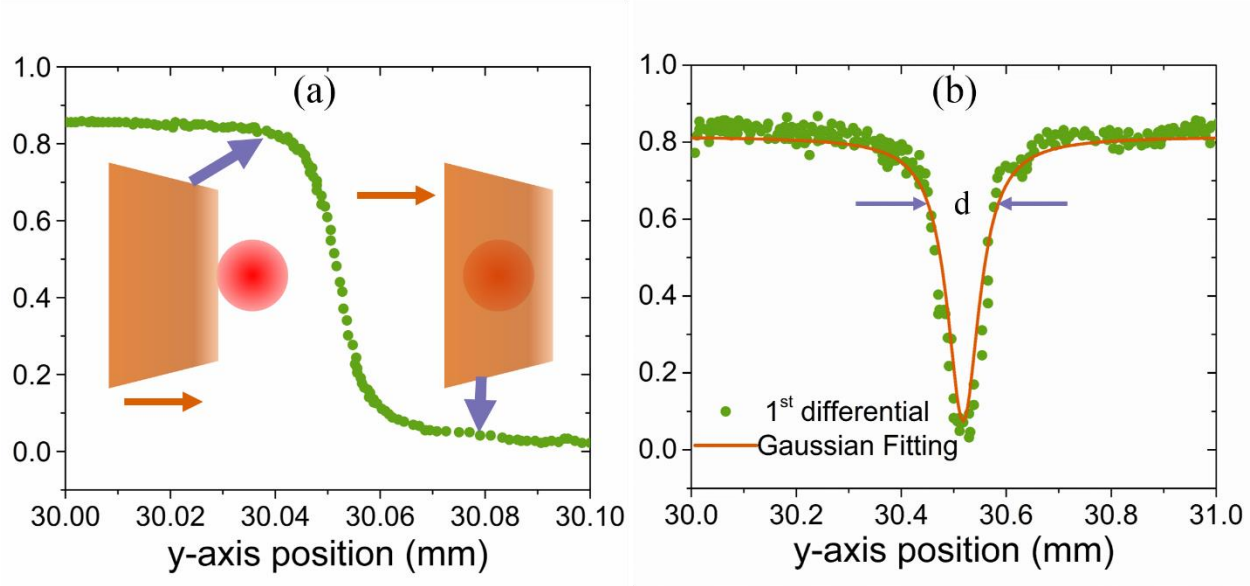

Figure 2.10. (a) Experimental transmitted intensity of a Gaussian beam versus the razor blade edge position. (b) The result after applying 1st-order differential on (a). Solid line stands for Gaussian fitting.

2.4 Time-resolved femtosecond pump-probe

2.4.1 Pump-probe principle and set-up

The pump-probe measurement is a significant scientific technique which has been employed in the field of valleytronics,[110, 111] spintronics,[112, 113] photocatalysis,[114, 115] biomedicine[116] and thermology[117], etc. It is mainly utilized to investigate the carrier dynamics of materials based on ultrafast lasers. In this experiment, a pump beam is utilized to excite materials to generate excited carriers, which are detected by a delayed probe beam.[118] As shown in Figure 2.11, both pump and probe beams are focused onto the sample and two spots center of the beams are made sure to overlap inside the sample. The spot size of the probe beam is commonly set to be smaller than that of the pump beam to probe a relatively uniform carrier density.[119] After passing through the sample, the pump beam was blocked by an aperture while probe beam was measured by a detector.

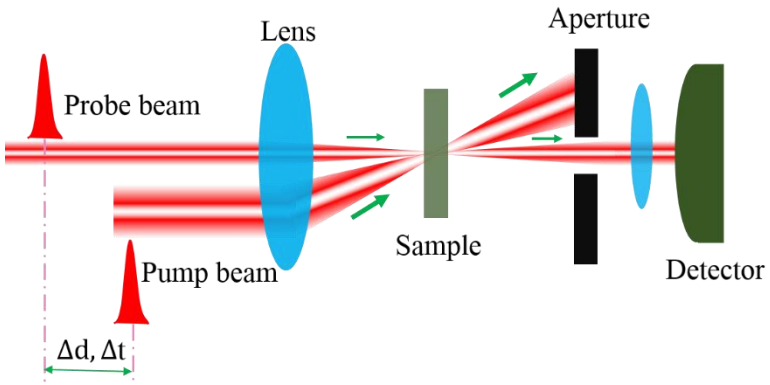

Figure 2.11. A typical schematic showing the pump-probe principle. The pump beam is usually chosen to be of higher intensity than that of the probe. The two beams are focused by a lens and their centers overlap at the position of the sample.

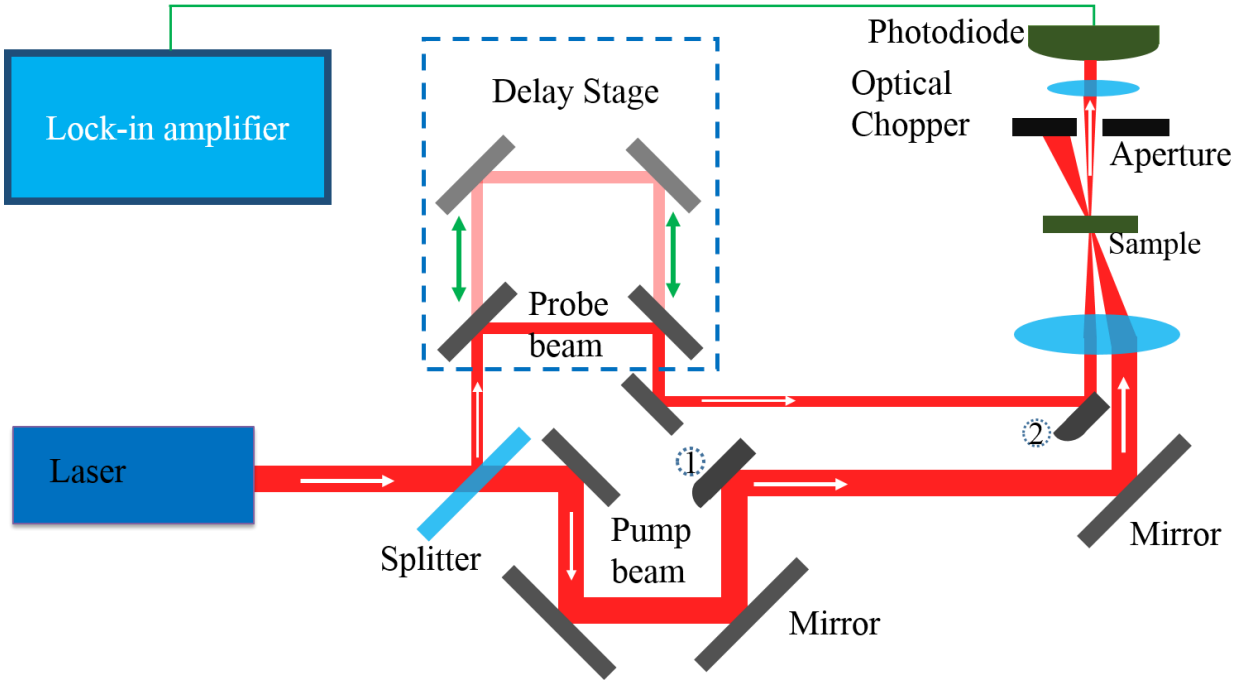

Figure 2.12. A scheme of a degenerate pump-probe based on a lock-in amplifier.

In general, the delay of the probe beam is controlled by a linear motorized translation stage. A typical degenerate pump-probe scheme, *i.e.*, both pump and probe beams have the same wavelength, is shown in Figure 2.12. In the experiment of this thesis, the laser source from Rage 9000 (coherent) was split into two beams, of which one main beam was used for pumping and another for probing. The probe pulses were delayed by a motorized stage and their polarization was rotated by 90-degrees with respect to the pump pulses to eliminate coherent artefacts. The

pump and probe beams were modulated by a chopper at different frequencies. Then both beams were non-collinearly combined and focused on the samples. The light transmitted through the sample was filtered by a polarizer to block the pump beam. The final signal was detected by a single Si photodiode with a lock-in amplifier. The photo of a pump-probe set-up is shown in Figure 2.13.

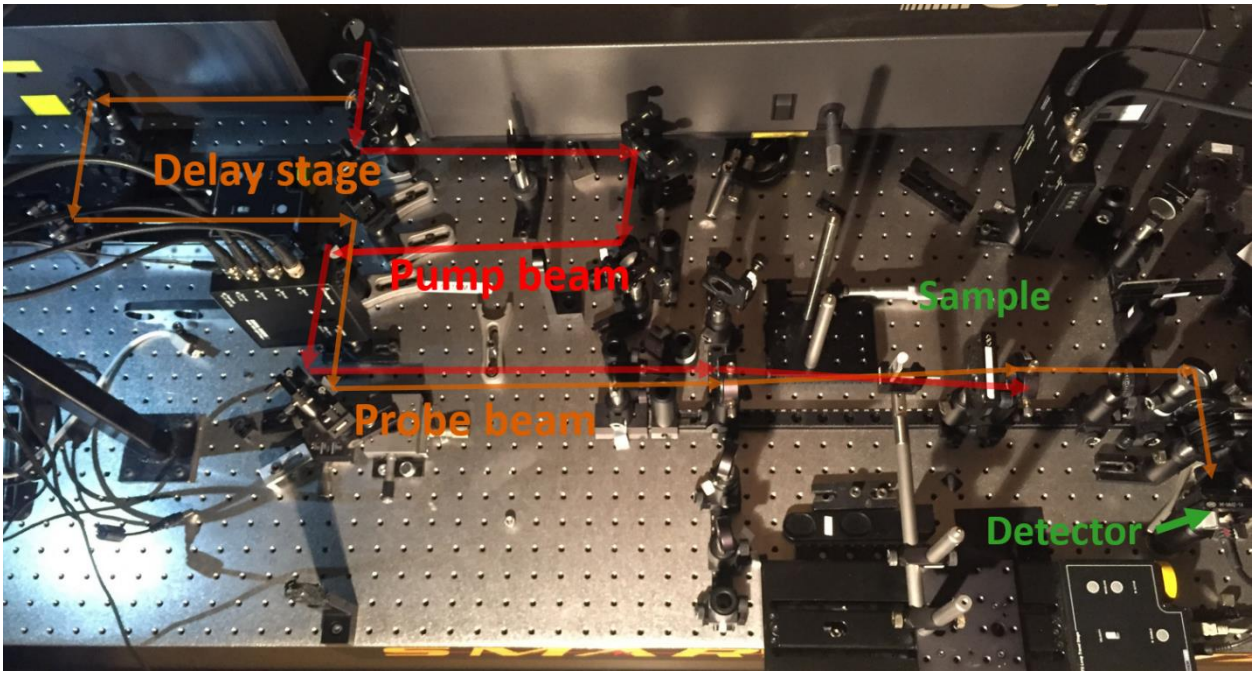

Figure 2.13. The photo of a transmitted degenerate pump-probe set-up used in this thesis.

The optical path of probe beam was tuned by a linear motorized translation stage, *i.e.*, the delay of the probe beam. Therefore the temporal resolution (Δt_{min}) of a pump-probe set-up depends on the minimum step of delayed stage:

$$\Delta t_{min} = \frac{\Delta d}{2c} \tag{2.4.1}$$

where c is the light speed and Δd is the minimum achiveable incremental movement of the delayed stage. The pump-probe technique is to measure the differential transmission or reflection of probe beam, *i.e.*, the relative change of probe beam due to the pump beam.[120] In the time-resovled pump-probe configuration, the differential transmission ($\Delta T/T$) or reflection ($\Delta R/R$) of probe beam as a function of the delay time, t,[118] can be expressed as:

$$\frac{\Delta T}{T} = \frac{T_P - T_0}{T_0} \tag{2.4.2}$$

Where T_P and T_0 is the transmission of probe beam with and without pump beam respectively. In the reflective configuration, Equation (2.4.2) can be written as:

$$\frac{\Delta R}{R} = \frac{R_P - R_0}{R_0} \qquad (2.4.3)$$

To obtain ($\Delta T/T$) or ($\Delta R/R$) signal, an optical choper is employed to modulate the pump beam.[51, 121] Figure 2.14 shows an example in which, to be brief, the frequency of the pump optical chopper is chosen to be half of the repeat rate of initial laser pulses.The initial laser pules with high repeat rate is shown in red on top. The square wave signal in the second row (Green) is the output signal of an optical chopper modulating the pump beam. As a concequence, the pump pulses after modulation are seen in the third row (red pulses). It is obvious that the intensity of probe pulses with pump signal (p_p) is different from that without pump signal (p_0). Hence one can obtain the differential transmission/reflection ($\Delta T/T$/ $\Delta R/R$) from p_p and p_0 with the assumption that the probe beam is stable, *i.e.*, the intensity of all the probe pulses before passing through a sample are equivalent. This assumption is true for most lasers and experimental enviorenments. To achieve high signal-to-noise ratio, a series of probe pulses with and without pump signal are collected to calculate their average values in the experiments.

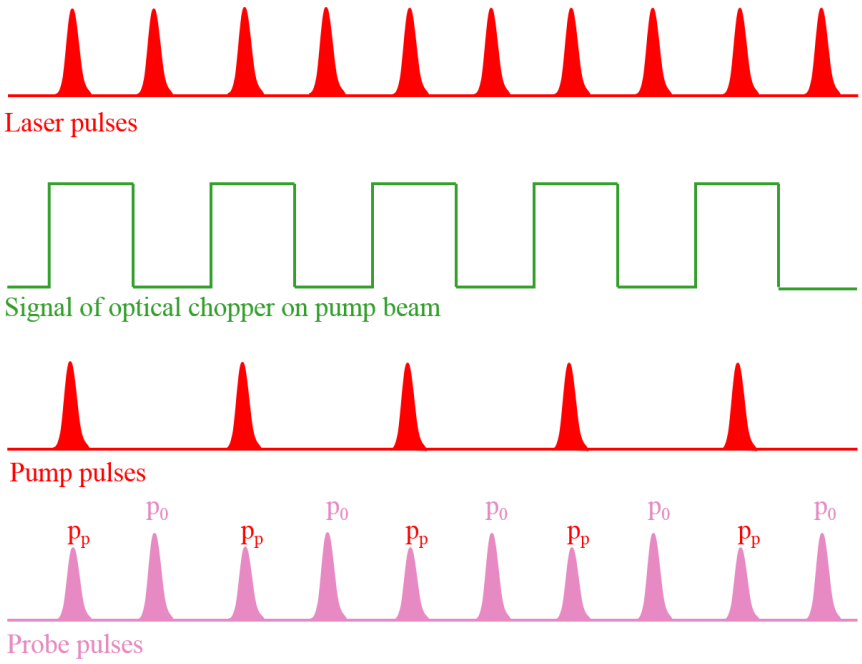

Figure 2.14. Pulses of lasers before optical choppers (on the top), output signal of optical chopper modulating pump beam (Green), pump (The third one) and probe pulses (The last one).

In time-resolved pump-probe spectrum, both photoinduced bleaching and photoinduced absorption are likely to be observed. The differential transmission/reflection ($\Delta T/T$/ $\Delta R/R$) is negative in photoinduced bleaching while positve in the photoinduced absorption.[122, 123] They originate from three major physical progresses: ground-state bleaching, excite-state absorption and stimulated emission (See Figure 2.15). [122-128]

The first positive $\Delta T/T$/ $\Delta R/R$ signal are from ground-state bleaching.[122] A pump beam is utilized to excite materials, resulting in the generation of electron-hole pairs. The electrons are pumped to the excited-states while holes remain in the ground state. This leads to lower carrier population in the ground state in comparison to that without excitation by pump pulses.[125] Consequently, the ground-state absorption of the probe beam in excited material is smaller than that in the material without excitation, *i.e.*, $\Delta T = T_P - T_0 > 0$/ $\Delta R = R_P - R_0 > 0$.

The second positive $\Delta T/T$/ $\Delta R/R$ signal results from the stimulated emission, which occurs only when the probe photon energy ($h\nu$) is equivalent to the bandgap between excited state and ground state (ΔE).[126, 129] In stimulated emission, the excited carriers interact with the probe photons and relax to the ground stage. Since the newly emitted photon has the same frequency, phase, polarization and travel direction as the probe photon, the transmission of probe beam is increased.[127] Therefore ΔT/ ΔR originating from stimulated emission is positive.

Excited-state absorption occurs when the probe beam is absorbed by the carrier in excited-states. The pump beam is used to inject the excited-state carriers, which subsequently interact with the probe photons. This leads to a decrease in the transmission of probe beam, *i.e.*, $\Delta T = T_P - T_0 < 0$/ $\Delta R = R_P - R_0 < 0$.[128]

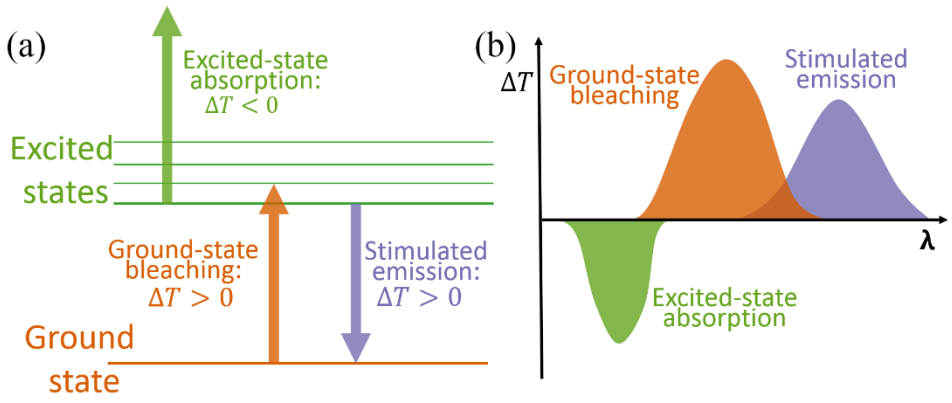

Figure 2.15. (a) The origins of the pump-probe signal: ground-state bleaching, excite-state absorption and stimulated emission. (b) Both ground-state bleaching and stimulated emission contribute to positive differential transmission/reflection signal while the excited-state absorption offers a negative signal.

Additionally, the absorption is relative to the cross-sections of the ground-state and the excited states, which play a significant role in the time-resolved pump-probe traces.[130] Take a two-level system for instance, a photoinduced bleaching signal is observed when the cross section of the excited state is larger than that of the ground state.[131] In contrast, photoinduced absorption shows up when the cross section of the excited state is smaller than that of the ground state.[123]

Here I should mention that the two-color time-resolved pump-probe technique is also commonly utilized to investigate carrier dynamics.[132, 133] The main difference between this technique and the degenerate pump-probe is that its pump and probe beams use laser pulses with different wavelength. The probe pulses can be set to resonate with the carrier that is going to be studied through changing the wavelength of the probe beam. Since it is the same as the degenerate pump-probe except for the different wavelength of probe beam and it is not going to be used in my study, further discussion of two-color pump-probe technique will be omitted here.

2.4.2 Zero delay point

It should be pointed out that one of the difficulties in designing pump-probe experiments is to determine the zero delay point. The zero delay point is defined at the position where pump and probe pulses overlap in both spatial and temporal regime. One method in the degenerate and non-collinear pump-probe experiment is to observe the second harmonic generation using a beta barium borate (BBO) crystal. This method requires that the pump and probe beams are non-collinear. As seen in Figure 2.16, the parallel pump and probe beams with the same wavelengths are focused

into a BBO crystal by a lens. Firstly, the two beams are aligned to overlap at the focus point. Next step is to move the delay stage freely around the zero delay point, *i.e.*, a come-and-go of the probe pulses nearby the zero point. The probe and pump pulses arrive at the BBO crystal at the same time and inferere, leading to a high intensity. This results in a second harmonic generation,[134] *i.e.*, a frequency doubling, a flashing beam spot can be observed on the screen behind the BBO crystal. In my degenerate pump-probe experiments where the central wavelength of pump and probe beams are at 800 nm, a blue (400 nm) flash is visible between pump and probe spot on the screen. (See Figure 2.16). One can also use this method to do the alignment to overlap the center of pump and probe beams by finding out the strongest flash.

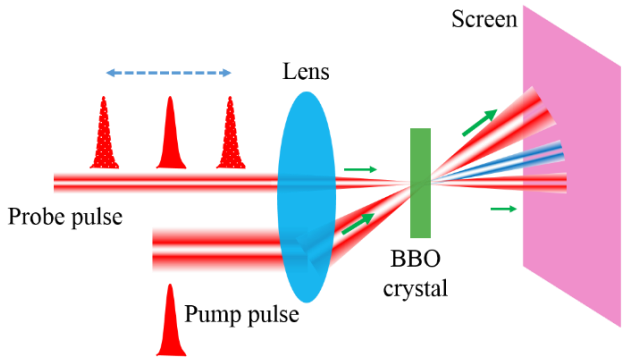

Figure 2.16. A method to find the zero delay point based on second harmonic generation.

2.4.3 Coherence spike

One may has noticed that pump-probe measurements might give rise to a coherent spike around zero pump-probe delay point due to the same polarization of pump and probe beams. It is also called coherent spike or coherence artifact.[51, 135, 136] Coherence spike is harmful for extracting the real pump-probe traces. To eliminate the coherent spike, the polarizations of the pump beam and the probe beam are commonly set to be orthogonal to each other using a half wavelength plate and a polarizer.

In my degenerate pump-probe experiment, a strong coherence spike was observed around the zero delay point, see the shadow area in Figure 2.17(b). In the regime of coherence spike, the pump-probe trace fluctuated frequently and strongly, and therefore covered the real signal. Since the probe and pump beams originated from the same linear polarized laser, their polarization were parallel to each other. A half wavelength plate was used to rotate the probe polarization by 90º, *i.e.*,

perpendicular to that of pump beam. Consequently, the coherence spike was eliminated and the real pump-probe trace was observed, see Figure 2.17 (a) and the green curve in Figure 2.17(b).

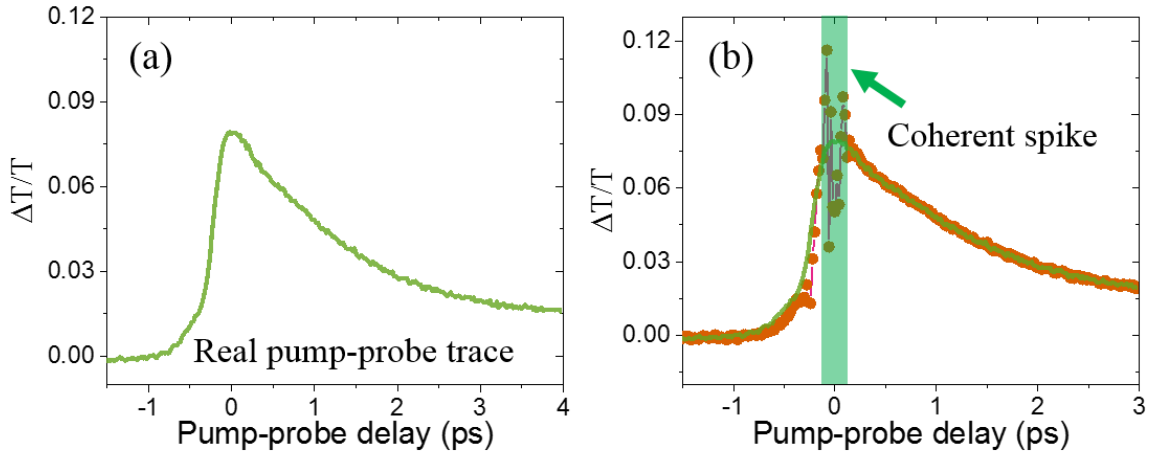

Figure 2.17. (a) The coherence-spike-free pump-probe trace obtained from a degenerate pump-probe set-up where the polarizations of pump and probe beams are orthogonal to each other. (b) The circle scatters represent the pump-probe trace with coherence spike the light green solid line is pump-probe trace without coherence spike. The shadow area shows the coherence spike regime.

2.4.4 Exponential decay model

The relaxation process of excited carriers are generally assumed to follow exponential decays. Double exponential decays with two corresponding characteristic lifetime (τ_1 and τ_2, $\tau_1 < \tau_2$) are very common and I take them as an example. The pump-probe signal in time domain, $g(t)$, is consist of two exponential components. When the excitation process is assumed to be "instantaneous", *i.e.*, the rise time is zero, and laser pulse duration is neglected, $g(t)$ can be written as:[137]

$$g_0(t) = u(t)\left[A_1 \exp\left(-\frac{t}{\tau_1}\right) - A_2 \exp\left(-\frac{t}{\tau_2}\right)\right] \tag{2.4.4}$$

where $u(t)$ represents the unit step function, which is equivalent to 0 for $0 <$ t and 1 for $0 \geq$ t. A_1 and A_2 are the relative amplitudes of the double temporal components. Based on Equation (2.4.4), a biexponential decay trace is simulated as Figure 2.18(a). However, the real measured differential transmitted/reflective signals are more complicated due to the finite pulse duration and excitation time which cause a rise signal during relaxation of the excited carriers (see the shadow region in

Figure 2.18(b)). Consequently, a finite pulse width and excitation time must be taken into account to analyze the real pump-probe traces.

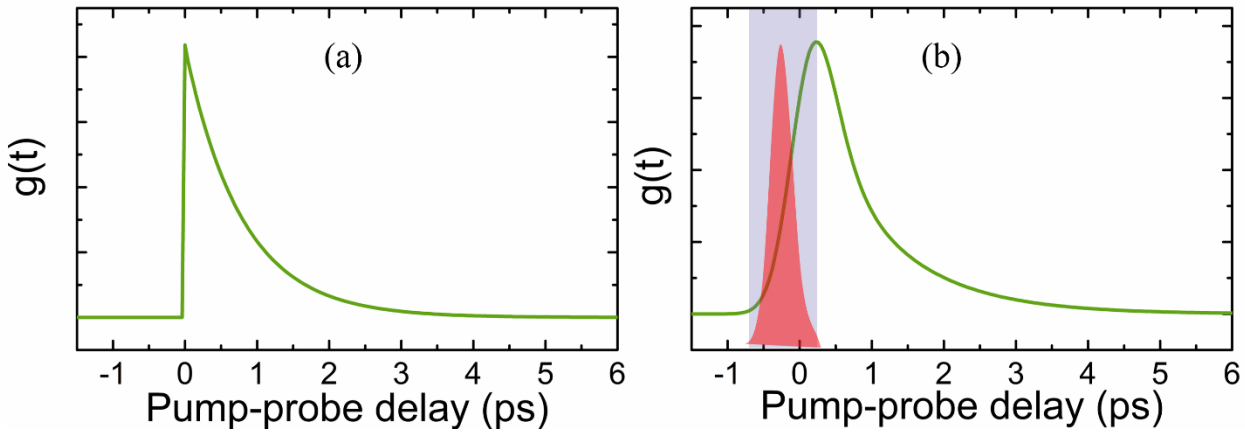

Figure 2.18. The instantaneous (a) and non-instantaneous (b) pump-probe curves without and with infinite rise time respectively. Both are related to a biexponential decay and can be simulated from Equation (2.4.4) and respectively. The shadow area shows the excitation region and the light red part represents a laser pulse.

The pulse of an ultrafast laser generally has a Gaussian temporal profile with a pulse duration of σ and a central wavelength of λ_0. It can be described by:[138]

$$P = \text{Bexp}\left(-\frac{t^2}{\sigma}\right)\sin(\frac{2\pi ct}{\lambda_0}) \tag{2.4.5}$$

Here B is the amplitude and c is the light speed. In a degenerate pump-probe, both pump (P_{pump}) and probe (P_{probe}) pulses are generated from the same laser and therefore their temporal profiles are the same as that of the laser:[138]

$$P_{pump} = P_{probe} = P = \text{Bexp}\left(-\frac{t^2}{\sigma}\right)\sin(\frac{2\pi ct}{\lambda_0}) \tag{2.4.6}$$

The rise signal in pump-probe traces in practice is not instantaneous and it should be considered. From mathematical point of view, a finite rise time can be added to the pump-probe traces via two convolution integrals which result from the temporal profiles of pump and probe pulses:[138]

$$g_1(t) = \int_{-\infty}^{+\infty}\left[\int_{-\infty}^{+\infty} g_0(T)P_{pump}\,(T-t)P_{probe}(T'-t)dT\right]dT' \tag{2.4.7}$$

In Equation (2.4.7), an autocorrelation integral ($\text{C}(\tau)$) can be obtained by exchange the integral order:[139]

$$\mathrm{C}(\tau) = \int_{-\infty}^{\infty} P_{pump}(T'')P_{probe}(T'' - \tau)dT'' = \mathrm{B}^2 \exp\left[-\left(\frac{\tau}{\sqrt{2}\sigma}\right)^2\right] \quad (2.4.8)$$

$\mathrm{C}(\tau)$ reflects the temporal overlap of profiles of pump and probe pules, which can be measured independently. The measured differential transmission/reflection can be expressed as (From Equation $(2.4.7)$ and $(2.4.8)$):

$$g_1(t) = \mathrm{B}^2 \int_{-\infty}^{\infty} g_0(T) \exp\left[-\left(\frac{T-t}{\sqrt{2}\sigma}\right)^2\right] d\,T \quad (2.4.9)$$

According to Equation $(2.4.5)$, Equation $(2.4.9)$ can be expressed as:[140]

$$g_1(t) = \mathrm{B}^2 \int_{-\infty}^{\infty} \left[A_1 \exp\left(-\frac{t}{\tau_1}\right) - A_2 \exp\left(-\frac{t}{\tau_2}\right)\right] \exp\left[-\left(\frac{T-t}{\sqrt{2}\sigma}\right)^2\right] d\,T \quad (2.4.10)$$

Based on the error function, *i.e.*, $\mathrm{erfc}(y) = \frac{2}{\sqrt{\pi}} \int_0^y \exp(-u^2)du$, an end signal can be achieved after integrals:[140]

$$g_1(t) = \left\{D_1 \exp\left(-\frac{t-t_0}{\tau_1}\right)\left[1 + \mathrm{erfc}\left(\frac{\sigma}{\sqrt{2}\tau_1} - \frac{t-t_0}{\sqrt{2}\sigma}\right)\right] + D_2 \exp\left(-\frac{t-t_0}{\tau_2}\right)\left[1 + \mathrm{erfc}\left(\frac{\sigma}{\sqrt{2}\tau_2} - \frac{t-t_0}{\sqrt{2}\sigma}\right)\right]\right\} + y_0 \quad (2.4.11)$$

In this equation, $D_1 = A_1\mathrm{B}^2$ and $D_2 = A_2\mathrm{B}^2$ are the relative amplitudes of the two exponential components. t_0 and y_0 are utilized to reset the initial values of the differential transmission or reflection signal ($\Delta T/T$ or $\Delta R/R$) to zero. Basically, a standard pump-probe trace rises from zero delay point and the values of $\Delta T/T$ or $\Delta R/R$ without pump signal are zero, and so the t_0 and y_0 can be ignored in Equation (2.4.11). Additionally, $D_1 \exp\left(-\frac{t}{\tau_1}\right) + D_2 \exp\left(-\frac{t}{\tau_2}\right)$ is one part of the initial exponential decay where the rise is instantaneous (see Equation$(2.4.5)$). Consequently, the differential transmission/reflection signal ($\Delta T/T$ or $\Delta R/R$) can be expressed as:[51]

$$g(t) = \left\{D_1 \exp\left(-\frac{t}{\tau_1}\right) \mathrm{erfc}\left(\frac{\sigma}{\sqrt{2}\tau_1} - \frac{t}{\sqrt{2}\sigma}\right) + D_2 \exp\left(-\frac{t}{\tau_2}\right) \mathrm{erfc}\left(\frac{\sigma}{\sqrt{2}\tau_2} - \frac{t}{\sqrt{2}\sigma}\right)\right\} \quad (2.4.12)$$

This is an equation to describe a typical two exponential decay pump-probe trace with two characteristic decay times. By employing this equation to simulate a biexponential pump-probe trace with a finite rise time, a curve that implys both excitation and decay processes can be achieved. (See Figure 2.18(b)).

In many other studies of carrier dynamics, excited carriers in different materials were reported to possess not only biexponential decay but also single, tri- and multi-exponential decays.[70, 114, 124, 141-148] Based on Equation (2.4.12), a general from with auto-correlation for fitting pump-probe differential transmittance/reflection trace can be written as:

$$g(t) = \sum_{i=1}^{N} D_i \exp\left(-\frac{t}{\tau_i}\right) erfc\left(\frac{\sigma}{\sqrt{2}\tau_i} - \frac{t}{\sqrt{2}\sigma}\right) \quad (2.4.13)$$

Here, N is the number of exponential decays which depends on the number of actual decays, and the other symbols represent the same as that in Equation (2.1.11). This equation with autocorrelation can be utilized to fit all the pump-probe traces with exponential decays to figure out the characteristic carrier lifetimes.

2.5 Transient absorption spectroscopy

The time-resolved pump-probe technique was introduced in section 2.4 in great detail including the working principle. Based on a similar principle, time- and spectra-resolved pump-probe technique, *i.e.*, transient absorption spectroscopy, was designed to study carrier dynamics using a supercontinuum light as a probe beam.[149] It is relatively easy to obtain a supercontinuum laser beam in visible range, so the probe beams in most transient absorption spectroscopies are white light. Meanwhile, the photon energies of while light cover the resonance region of excitons in many materials, and therefore can be employed to study the exciton behaviors such as exciton formation, exciton-exciton annihilation, and trion dynamics *etc*.[125, 149-159] This is one of the main advantage of the transient absorption spectroscopy in comparison to the degenerate or two-color pump probe measurements.

2.5.1 Transient absorption set-up and principle

The schematic in Figure 2.19 shows the basic principle of a typical collinear transient absorption spectroscopy based on a spectrometer. A laser beam with relatively higher intensity and larger spot size is employed for pumping materials. A white light with a series of different wavelengths is utilized to probe the carriers excited by the pump beam. This supercontinuum white light can be achieved by focusing a high power laser beam into either a BBO crystal[160, 161], quartz,[160, 162] or distilled water [163]contained in a quartz cuvettes. A white light generated from the BBO crystal is relatively stable but with a narrow photon range.[161] White light generated from distilled water is broadband but the stability is relatively poor, while the quality of the white light obtained

from quartz is not as good as the previous two.[160-162] The two beams are then combined by a beam splitter or a dichroic filter. In a collinear configuration as seen in Figure 2.19, both collinear beams are focused into the sample, which is usually placed at the focal point to obtain higher intensity. After the sample, the pump beam is blocked by a certain long pass filter which allows the probe beam passing through. The transmitted probe beam is finally corrected by a lens into a fiber and analyzed by a spectrometer.

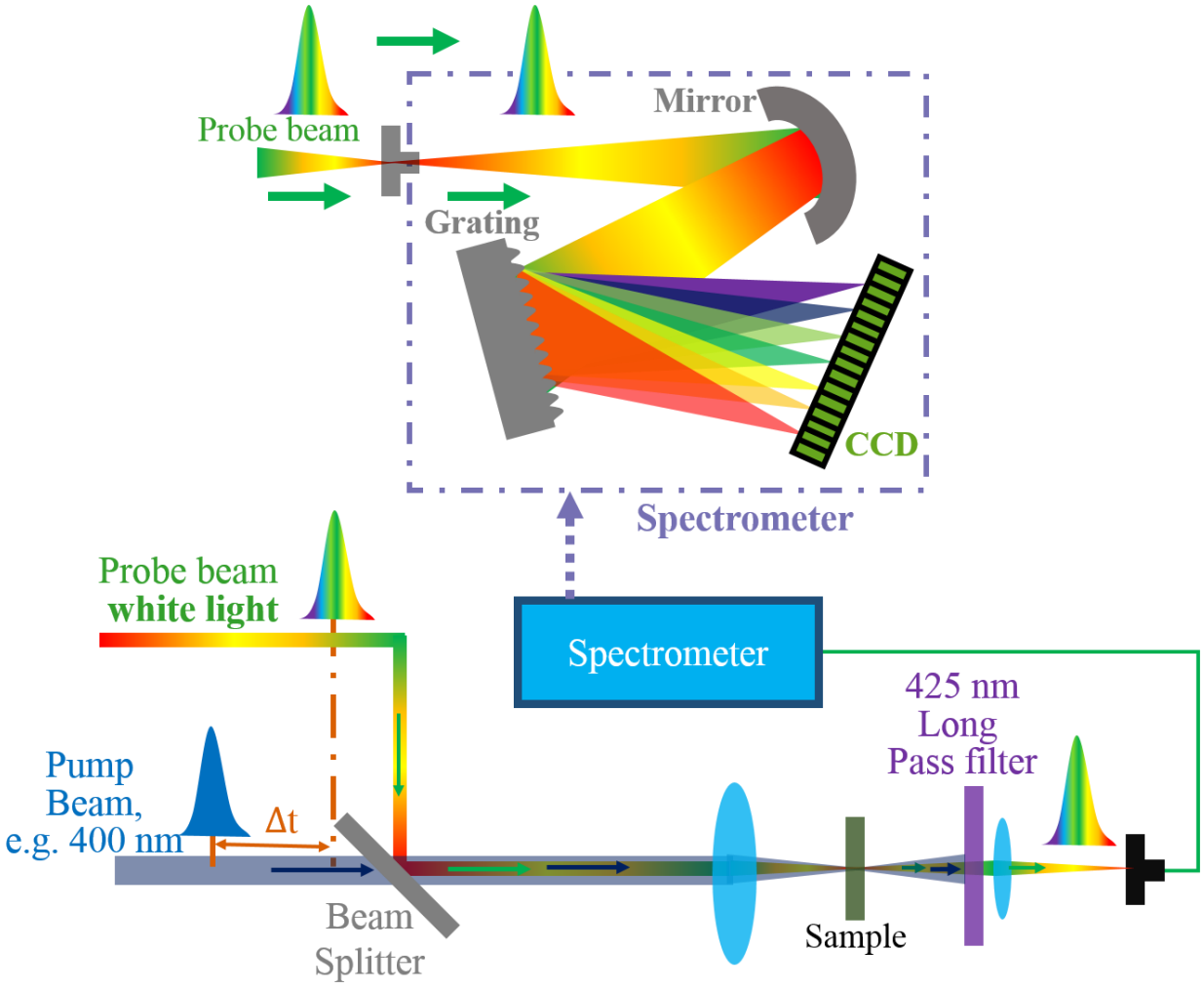

Figure 2.19. A schematic showing the principle of a collinear transient absorption spectroscopy. The top part shows the working principle of a spectrometer where an optical diffraction grating is utilized to divide the supercontinuum light into quasi-monochromatic lights with different wavelengths. These lights are then detected by a CCD inside the spectrometer. The lower part indicates the pump and probe beams paths which are collinear. Both are focused into a sample, and the pump beam is blocked with a chosen filter while the probe beam passes through it and detected by a spectrometer.

From the above, it is very clear that the main difference of spectra-resolved transient absorption spectroscopy from time-resolved pump-probe technique is using a white light as probe beam. This white light consists of a series lights with different photon energies which are able to carry different information about carriers. In order to distinguish between these different wavelengths, a spectrometer with an optical diffraction grating is employed to detect the transmitted probe white light. The optical diffraction grating plays a key role in dividing the supercontinuum white light into quasi-monochromatic lights, see the top part in Figure 2.19. The diffraction grating equation can be expressed as:[164, 165]

$$d\sin\theta_m = m\lambda \tag{2.5.1}$$

Here d is the diffraction grating constant, *i.e.*, the distance between the center of two nearest slits, $m = 0, \pm1, \pm2, \pm3, \pm \cdots\cdots$ is an integer, which indicates the propagation-mode of interest, and θ_m is the diffraction angle. When the incident angle of the light is θ_i, the diffraction grating equation can be written as: [164]

$$d(\sin\theta_m + \sin\theta_i) = m\lambda \tag{2.5.2}$$

Since the incident angle of the white light in a spectrometer is the same, the diffraction angles, θ_m, are different for the different wavelength according to Equation (2.5.2) Consequently, the probe supercontinuum light is divided into many quasi-monochromatic lights which are recognized and recorded by a CCD inside the spectrometer (see the top part of Figure 2.19). Finally, the differential transmission as a function of both pump-probe delay time and probe wavelength can be mapped.

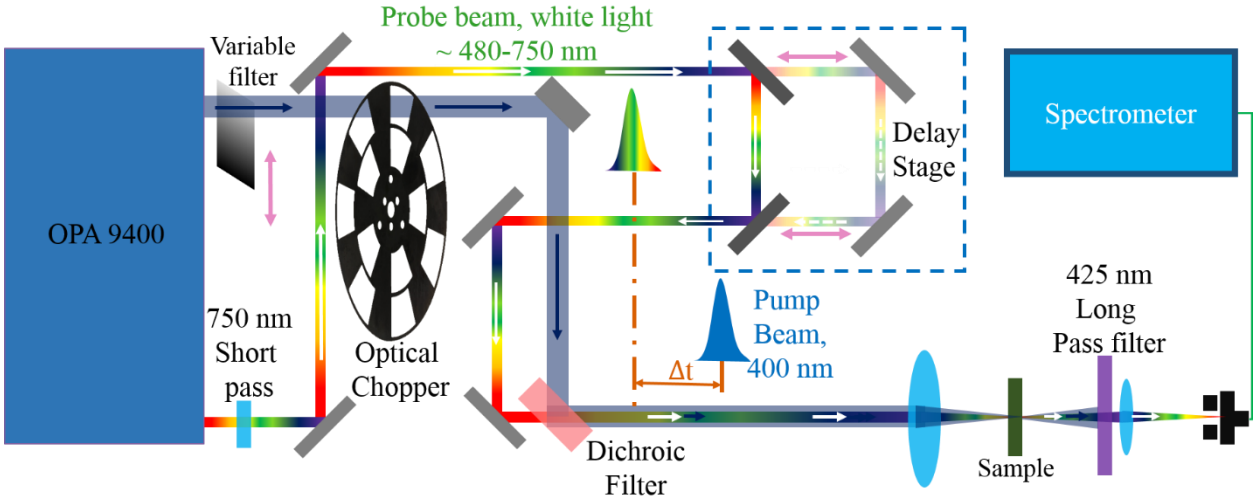

Figure 2.20. A typical spectra-and time-resolved transient absorption spectroscopy.

The transient absorption spectroscopy used in my thesis is based on a modified optical parametric amplifier (Coherent OPA 9400), which is drove by a series of laser pulses with duration of ~100 fs, wavelength of 800 nm and repetition rate of 100 kHz from a mode-locked Ti:sapphire laser (Coherent RegA 9000, repetition rate 10-200 kHz). The initial 800 nm beam was split into two, one of which was focused into a BBO crystal to produce 400 nm femtosecond pulses for pumping. As seen in Figure 2.20, the 400 nm beam was firstly tuned by a linear continuously variable filter to obtain different intensities of pumping pulses, followed by modulation via an optical chopper. The other 800 nm beam was then focused into a sapphire with a thickness of 3 mm to generate a supercontinuum white light, which covered a wavelength region from ~480 to ~1100 nm. This is done inside the OPA and so the output from the OPA signal port is a ray of white light. However, this white light contained a 800 nm beam with high intensity since not all the initial 800 nm pulses were absorbed and transformed by the sapphire crystal. To obtain a relatively uniform white light, a 750 nm short pass filter was placed after the OPA signal port to block the strong 800 nm beam. As a result, I achieved a probe pulses with wavelength spanning from ~480 to ~750 nm. The obtained white light was then delayed by a linear motorized translation stage. A dichroic mirror was employed to combine the pump and probe beam in question to be collinear. Here one should make sure that the center of two beams overlap spatially. Two collinear beams were then focused into a sample which was placed at the focal point. The pump pulses were then blocked via a 425 nm long-pass filter, while the transmitted probe white light was corrected by a lens into a CCD spectrometer. This was then processed to extract the signal at the chopper frequency from the noisy background via a computer program to obtain the transient absorptive spectra, *i.e.*, the differential absorption transmission as a function of both pump-probe delay time and probe wavelength.

2.5.2 Differential optical density

In the Transient absorption mapping experiment, the measured results are commonly characterized via a differential optical density, also called optical density change (ΔOD), which is given by:[166, 167]

$$\Delta OD = A(\lambda, t)_p - A(\lambda, t)_0 \tag{2.5.3}$$

Here $A(\lambda,t)_p$ and $A(\lambda,t)_0$ represent the absorbance with and without pump excitation respectively at probe wavelength λ and pump-probe delay time t. According to the Lambert-Beer law, $I_{out}(\lambda) = I_{in}(\lambda) \cdot exp[-A(\lambda,)]$, the absorbance, $-A(\lambda,)$, can be written as: [168]

$$A(\lambda,t) = log\left[\frac{I_{in}(\lambda,t)}{I_{out}(\lambda,t)}\right] \tag{2.5.4}$$

where $I_{in}(\lambda,t)$ and $I_{out}(\lambda,t)$ are the incident and transmitted intensities respectively. As the transmission is defined as $T(\lambda,t) = \frac{I_{out}(\lambda,t)}{I_{in}(\lambda,t)}$, Equation (2.5.4) can be written as:

$$A(\lambda,t) = -log\, T(\lambda,t) \tag{2.5.5}$$

From Equation (2.5.3) and (2.5.5), one can have:

$$\Delta OD = log\, T(\lambda,t)_0 - logT(\lambda,t)_p = log\frac{T(\lambda,t)_0}{T(\lambda,t)_p} \tag{2.5.6}$$

Here $T(\lambda,t)_p$ and $T(\lambda,t)_0$ are the transmissions with and without pump excitation respectively at probe wavelength λ and pump-probe delay time t. After some simple derivations, Equation (2.6.6) can be expressed as:

$$\Delta OD = log\left(1 - \frac{\Delta T}{T}\right) \tag{2.5.7}$$

This is the general relationship between the differential optical change and differential transmission, which can be utilized to transform the data in transient absorptive measurement or analysis.

Additionally, the transmission $T(\lambda,t)$ can be expressed as:

$$T(\lambda,t) = exp(-\alpha L) \tag{2.5.8}$$

Here α is the total absorption coefficient and L represents the sample thickness that contributes to the absorptions. Hence the differential transmission can be expressed as:

$$-\frac{\Delta T}{T} = 1 - exp\left(\alpha_0 L - \alpha_p L\right) \tag{2.5.9}$$

Here α_0 and α_p represent the absorption coefficient with and without pump excitation respectively. According to Taylor' Formula, the second term of Equation (2.5.9) can be expresses via Taylor series:

$$exp(\alpha_0 L - \alpha_p L) = 1 + (\alpha_0 L - \alpha_p L) + \frac{(\alpha_0 L - \alpha_p L)^2}{2!} + \cdots \frac{(\alpha_0 L - \alpha_p L)^n}{n!} + Rn(\alpha_0 L - \alpha_p L) \quad (2.5.10)$$

In most cases, the value of $\alpha_0 L - \alpha_p L$ is small and the high order terms can be neglected. Therefore, Equation (2.5.10) can be approximately equal to:

$$exp(\alpha_0 L - \alpha_p L) \cong 1 + (\alpha_0 L - \alpha_p L) \quad (2.5.11)$$

By combining Equation (2.5.9) and (2.5.11), one can have:

$$\frac{\Delta T}{T} = -(\alpha_0 L - \alpha_p L) \quad (2.5.12)$$

Additionally, based on Equation (2.5.3) and (2.5.5), the differential optical density can be derived into: [166]

$$\Delta OD = log\left[exp(\alpha_p L - \alpha_0 L)\right] = (\alpha_p L - \alpha_0 L) \cdot log(e) \quad (2.5.13)$$

Therefore the differential optical density is linear to the differential transmission:[166]

$$\Delta OD = -log(e) \cdot \frac{\Delta T}{T} \quad (2.5.14)$$

Equation (2.5.14) shows the linear relationship between differential optical density and transmission. Both Equation (2.5.7) and (2.5.14) offer a bridge between differential optical density and differential transmission. This is helpful for both the design of the transient absorptive set-up and corresponding data analysis.

2.5.3 Three-dimensional exponential decay model

Since the transient absorptive results are characterized by the differential optical density or differential absorption transmission as a function of both pump-probe delay time and probe wavelength, Equation (2.4.13) cannot be employed to directly fit the transient absorptive mapping. Based on Equation (2.4.13), a three-dimensional exponential decay model, *i.e.*, the differential transmission/reflection as a function of both probe wavelength and pump-probe delay time, was developed to analyse the time- and spectra-resolved pump-probe experimental results:

$$g(t,\lambda) = \sum_{i=1}^{N} D_{\lambda i} \exp\left(-\frac{t}{\tau_{\lambda i}}\right) erfc\left(\frac{\sigma}{\sqrt{2}\tau_{\lambda i}} - \frac{t}{\sqrt{2}\sigma}\right) \quad (2.5.15)$$

Here, N is the number of exponential decays which depends on the number of actual decays, $\tau_{\lambda i}$ stands for the i-th carrier lifetime at a wavelength of λ, and other symbols represent the same

expression as that in Equation (2.4.11). It is a three-dimensional exponential decay model where wavelength, $\tau_{\lambda i}$, and pump-probe decay time, t, are independent variables and differential transmission or optical density is the dependent variable. This Equation with autocorrelation can be utilized to fit any time- and spectra- resolved pump-probe traces with exponential decays, while figuring out the corresponding characteristic lifetimes.

3. Broadband SSPM of antimonene dispersions

Antimonene is a new member of the group of two-dimensional (2D) materials that have attracted tremendous research interests due to outstanding electronic, mechanical and optical properties. Antimonene was theoretically predicted to possess a narrow bandgap which will results in a broadband absorption from the infrared to the ultraviolet region.[83, 84, 169] The calculation of electron energy loss and optical reflection showed that its absorption peaks are located in the ultraviolet regime and hence it is likely to be exploited as ultraviolet optical devices.[169] In the visible region, antimonene and its quantum dots were experimentally proved to possess a continuous-wave third-order nonlinear optical response at 532 nm and 633 nm.[170] Overall, however, the optical properties of antimonene remain largely unexploited.

Recent reports have demonstrated the liquid-phase exfoliation of antimonene [171] and its stability under ambient environments[172]. As introduced in Chapter 1, for most layered materials, the monolayer limit exhibits excellent photonic performances in comparison to their bulk limit, such as strong photoluminescence in $MoSe_2$, [57, 173] MoS_2 [174, 175] and black phosphorus [52] single layers due to their direct band gap. These 2D nano-sheets also reveal excellent nonlinear optical behavior such as optical limiting,[176] saturated absorption,[177, 178] two-photon absorption [67, 179] and broadband spatial self-phase modulation,[180] etc. Interestingly, the transformation of antimony from an indirect semimetal in its bulk limit to a direct semiconductor in its monolayer form under small biaxial strain was also theoretically proven by density functional theory (DFT) calculations.[181] This indicates the huge potential for photonics of antimony nano-sheets.[182] To date there have been very few experimental optical measurements of the optical/nonlinear optical/photonic properties of antimonene.[183] It is important to investigate these optical performance of antimonene in order to exploit its applications like optical modulator and switchers.

In this chapter, the nonlinear optical properties of antimony nanosheets was investigated over a wide wavelength range using the spatial self-phase modulation (SSPM) technique with 405 nm, 785 nm and 1064 nm continuous wavelength (CW) lasers. The antimonene nanosheets were

exfoliated from bulk to few-layers by liquid phase exfoliation in cyclohexylpyrrolidone (CHP). The optical properties and morphology of these nanosheets were characterized by UV-visible spectroscopy, Raman spectroscopy and transmission electron microscopy (TEM). From SSPM results, the nonlinear refractive index and the third-order nonlinear optical susceptibility of the antimony monolayer were obtained. Furthermore, the effective nonlinear refractive index of the dispersion can be tuned by changing the incident intensity of the laser. This property can be utilized to exploit devices such as nonlinear optical modulator and all-optical switch.[55, 90, 184]

3.1 Antimonene dispersion and its characterizations

Antimonene dispersions were prepared by liquid-phase exfoliation (LPE) from bulk antimony to nanosheets in CHP. 50 mg antimony powder (Sigma Aldrich) was added to 20 ml CHP and then sonicated (Sonics VX-750) for 5 hours with 4 seconds on/off and 40% amplitude to avoid overheating. This process creates a dispersion mixing with bulk, few- and mono-layered materials. To remove non-exfoliated bulk particles, the dispersion was centrifuged for 90 mins at 1000 rpm and the top 3/4 of the dispersion was carefully extracted. The centrifugation was repeated twice to reach a desired separation and stable dispersion. The exfoliation quality of antimony nanosheets was then characterized using transmission electron microscopy (TEM), Raman and UV-Vis spectroscopy.

Figure 3.1(a) gives an overview TEM image of the antimony nanosheets produced by the liquid-phase-exfoliation. These nanoflakes were deposited on the TEM grid using drop-casting method. It is shown that most of the nanoflakes are about tens of nanometers while only a few are as large as ~100 nm. It is obvious that the smaller nanoflakes exhibited less number of layers than that of larger ones. Figure 3.1 (b) shows a high magnified image of a typical antimonene nano-flake in the dispersion. Like the nanoflakes produced from other 2D materials by LPE method,[24, 51, 55, 185] The antimonene nano-flake also looks to be a stack of different layers. The upper edge of the flakes seems to be as thin as mono-layer or bi-layer, while the middle thick part is obviously multi-layered. Raman spectroscopy is a very useful way for identifying allotropes and characterize properties of 2D materials. The antimonene has two major Raman vibration modes, *i.e.*, in-plane (E_g) and out-plane A_{1g}, as the inset of Figure 3.1(c) shows. The theoretical calculation predicted that both E_g and A_{1g} modes will red shift from bulk to monolayer because of the contraction of the lattice constant.[171] The E_g and A_{1g} peak locate at 88 cm^{-1} and 137 cm^{-1} respectively in Sb bulk

material while they shift to 167 cm^{-1} and 208 cm^{-1} in monolayer.[171] In the dispersion, the E_g and A_{1g} mode are measured to be 115.8 cm^{-1} and 153 cm^{-1} respectively. Both peaks sit between the values of Sb bulk and those of monolayer. These results imply that the antimonene dispersions are composed of a large number of different few-layers, which is in agreement with the TEM images.

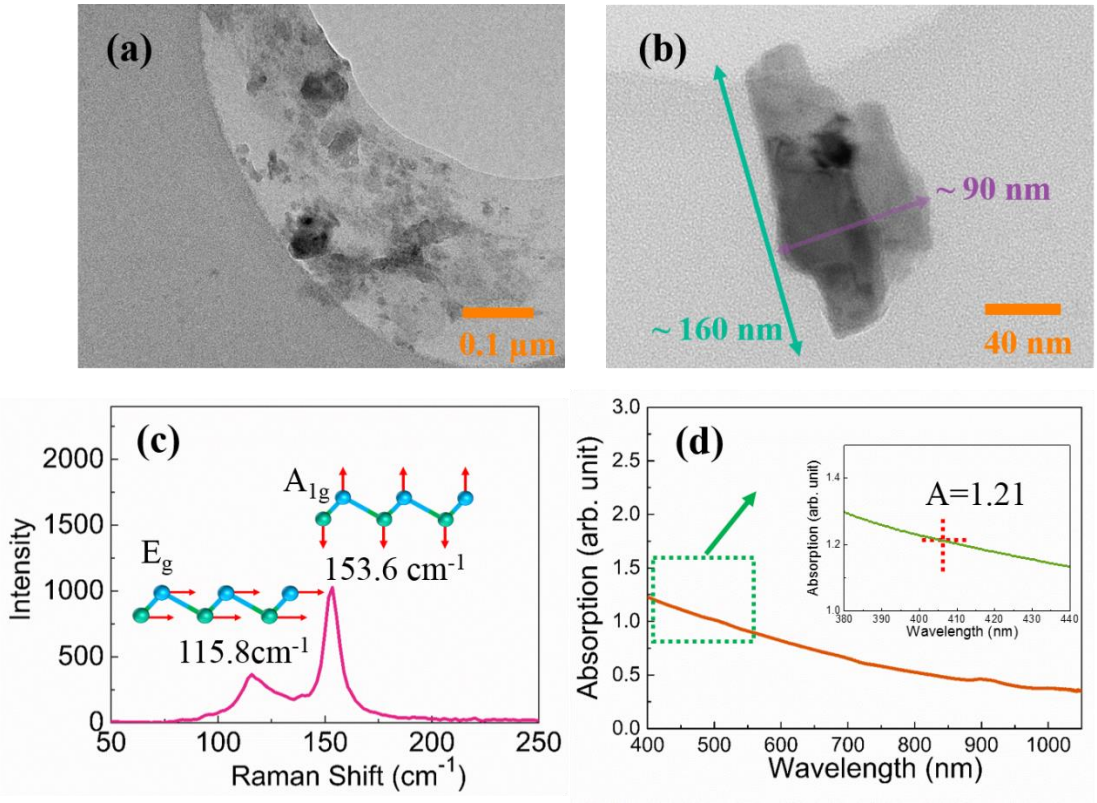

Figure 3.1. TEM images in low (a) and relatively high (b) magnification. (c) Raman spectrum of the antimony nanosheets. (d) UV-vis absorption spectra of the antimonene dispersion in a quartz cuvette. The inset zoom-in in the absorption spectra goes from 380 nm to 440 nm.

3.2 Nonlinear refraction and CW third-order susceptibility

Spatial self-phase modulation (SSPM) is a third-order nonlinear optical phenomenon induced by the optical Kerr effect.[87] The strong electrical field produced by a high power laser leads to a corresponding local variation of the optical refractive index, which also changes the phase of the laser. The optical refractive index in the nonlinear regime can be expressed as $n_e = n_{0e} + n_{2e}I$, where n_{0e} and n_{2e} are the linear and nonlinear parts of the refractive index and I stands for the incident laser intensity.[90] A corresponding local variation of the refractive index would give rise to spatial self-phase modulation. This results in a series of diffraction rings in the far field. By

investigating this SSPM pattern, the nonlinear refractive coefficients of the material can be calculated.

In my SSPM measurements, focused CW laser beams were applied on the as-prepared antimonene nanosheets dispersion. After the sample, a screen was employed to show the SSPM patterns. For 1064 nm, a fluorescent card (Thorlabs VRC2) was used to convert the infrared pattern to the visible range. For the other wavelengths, a standard black screen was applied. Figure 3.2 shows the SSPM diffraction rings induced by 1064 nm, 785 nm, and 405 nm lasers. As the laser intensity increases from ~7.5W/cm^2 to ~60 W/cm^2, the SSPM pattern appears from the background and becomes larger and larger. It can be also found that each pattern was composed by many small rings. The intensity of the outmost ring is strongest and that of inner ones become lower and lower as the rings approach the center of the pattern. This phenomenon was also observed in carbon nanotube, graphene and TMDs dispersions.[55, 86]

The SSPM effect has been shown to originate from the electronic properties in materials such as graphite, C_{60}, graphene and liquid crystals.[86, 87, 186] The electrons are excited to the conduction band from the valence band when the antimony flakes dispersions are irradiated by a CW laser with enough intensity. The excited electrons will transfer to the ground states from the conduction band, and the corresponding holes move in the opposite direction; *i.e.* parallel and antiparallel to the laser-induced electric field; *i.e.,* the antimony nanosheets become polarized. The initial angle between this polarization and the laser-induced electric field tend to be zero, and therefore the antimony nanosheets will be aligned and reoriented. [86, 187]

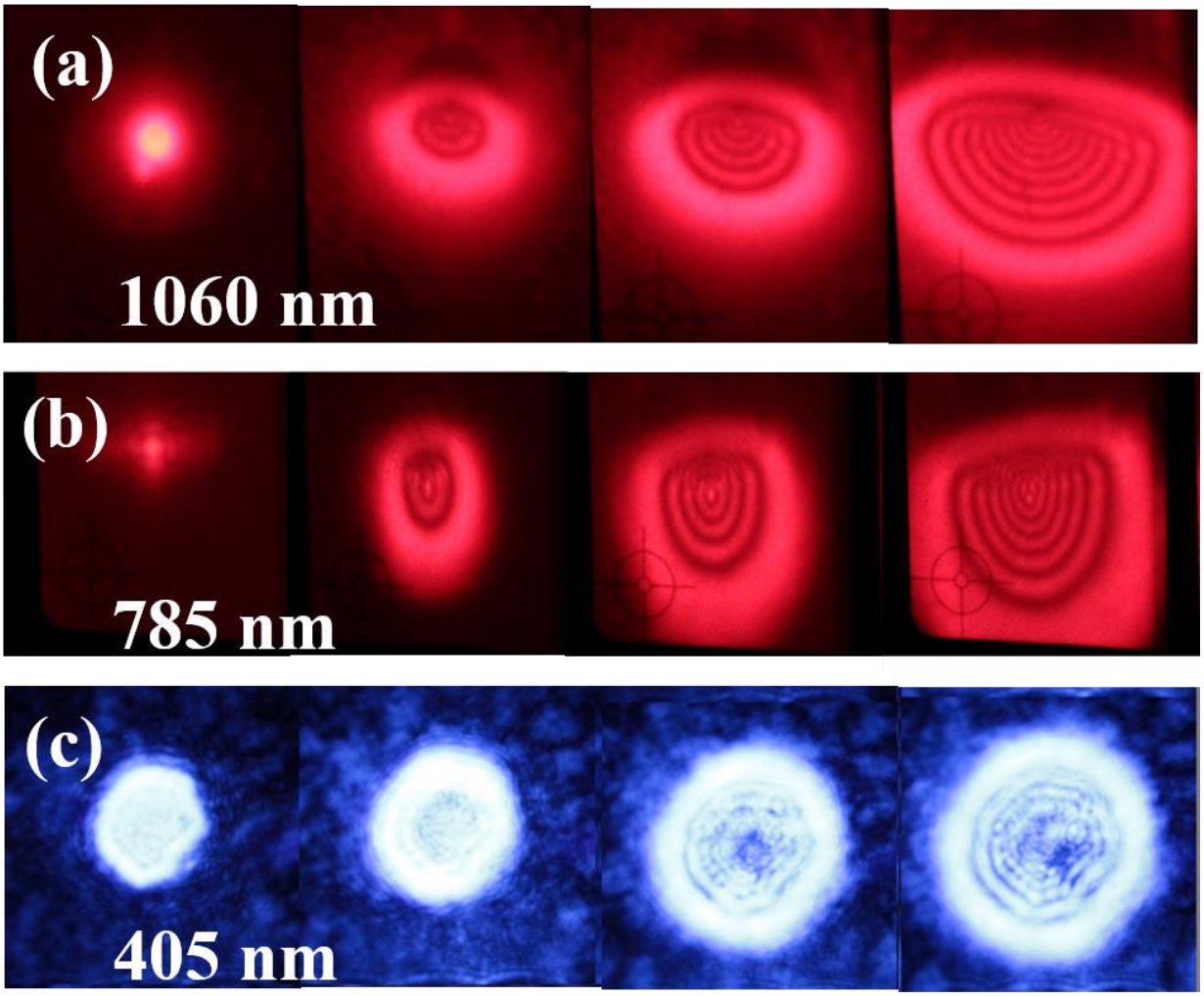

Figure 3.2. SSPM diffraction rings induced by 1064, 785, and 405 nm lasers under increasing incident intensity.

As a powerful nonlinear optical characterization method, the SSPM effect can be utilized to measure the effective nonlinear refractive index of the antimony nano-flake dispersions and the third-order nonlinear optical susceptibility of the effective monolayer,[86, 90] which are two of the significant parameters in nonlinear optics. The local refractive index change Δn_e mentioned above came along with a corresponding phase shift [87]: $\Delta\psi(r) = \frac{2\pi n_{0e}}{\lambda}\int_{-L_e/2}^{L_e/2}\Delta n_e(r,z)dz$, where λ is the laser wavelength in vacuum and r is the radial coordinate of the laser beam. $L_e = \int_{L_1}^{L_2}(1+z^2/{z_0}^2)^{-1}\,dz$ is the effective length for generating SSPM, where w_0 (33.87, 17.49 and 12.89 μm for 1064, 785 and 405 nm lasers respectively) is the beam radius at $1/e^2$ and $z_0 =$

$\pi w_0^2/\lambda$ is the diffraction length at $z = 0$, and $L = L_2 - L_1 = 10\,mm$ is the cuvette thickness(L_2 and L_1 are the on-axis coordinates of the dispersions). And L_e were respectively calculated to be 4.21, 1.77 and 1.29 mm for 1064, 785 and 405 nm lasers. According to the Bruggeman effective medium theory,[90] the change of linear refractive index n_{0e} can be ignored. Then it can be seen clearly from the Kerr effect equation that the change of refractive index Δn_e is equal to $\Delta n_{2e} I(r,z)$, where $I(r,z)$ is the intensity distribution of the laser beam in the medium. Therefore the phase shift of the laser beam can be written as:

$$\Delta\psi(r) = \frac{2\pi n_{0e}}{\lambda}\int_{-L_e/2}^{L_e/2} \Delta n_{2e} I(r,z)dz \tag{3.1}$$

The phase shift can be also expressed as[87]:

$$\Delta\psi(r) = \Delta\psi_0 \exp(-2r^2/w_0^2) \tag{3.2}$$

This equation shows that there must exist two points r_1 and r_2, at which the slopes are equal($(\frac{d\Delta\psi(r)}{dr})_{r_1} = (\frac{d\Delta\psi(r)}{dr})_{r_2}$), *i.e.*, the electromagnetic fields at these two points have the same vectors and hence the light from these two points interfere in the far field.

This results in a series of diffraction rings, which can be captured by a black screen perpendicular to the laser propagating direction. The total number of the SSPM diffraction rings (N) can be calculated from Equation $\psi(0) - \Delta\psi(+\infty) = 2N\pi$.[87]

By combining Equation (3.1) and (3.2), one can deduce the effective nonlinear refractive index: [86]

$$n_{2e} = \frac{\lambda}{2n_{0e}L_e} \cdot \frac{N}{I}\,, \tag{3.3}$$

Where *I* is the average incident intensity. In the experiments, *N* is proved to be proportional to *I* in all cases, as seen in Figure 3.3. As a result, the effective nonlinear refractive index of the antimony nano-flake dispersions can be estimated by linear fitting to find out the slopes ($\frac{N}{I}$).

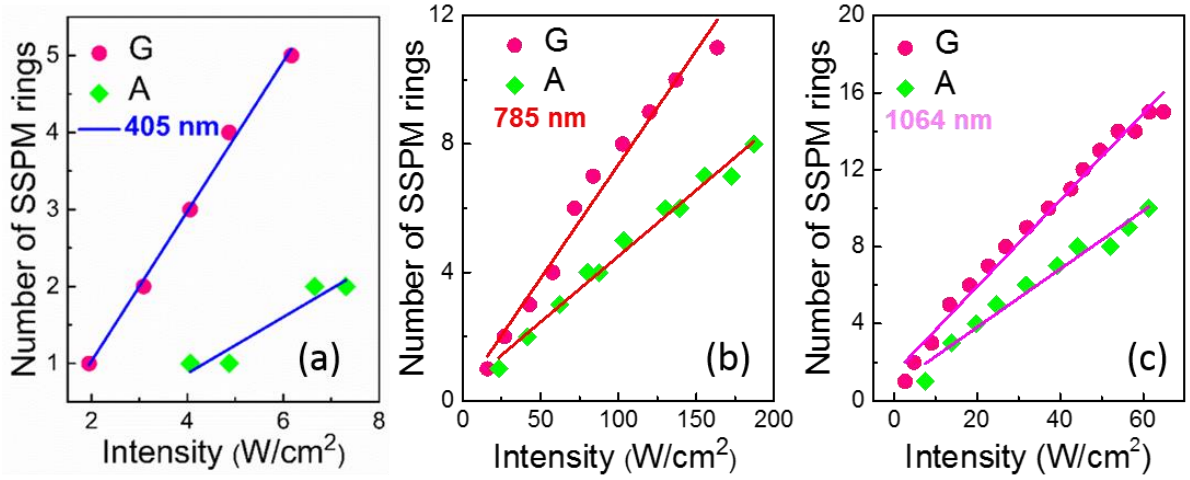

Figure 3.3. Number of SSPM diffraction rings as a function of intensity in antimony nanosheets (Green dot) and graphene (Pink dot) dispersions at 405, 785 and 1064 nm.

Since the third-order nonlinear optical susceptibility $\chi^{(3)}_{total}$ is relative to the nonlinear refractive index ($n_{2e}(cm^2/W) = 0.0395\chi^{(3)}_{total}(esu)/n^2_{0e}$,) and $\chi^{(3)}_{total} = N_e^2\chi^{(3)}_{monolayer}$, where N_{eff} is the effective number of monolayer, the third-order nonlinear optical susceptibility of effective antimony monolayer can be obtained: [55]

$$\chi^{(3)}_{monolayer}(esu) = \frac{n^2_{0e}n_{2e}(cm^2/W)}{0.0395\times N_e^2} \quad (3.4)$$

$\frac{N}{I}$ was already measured from Figure 3.3. The effective number of antimony monolayer can be calculated by $T^{N_e}_{monolayer} = T_{total}$,[55, 86] where $T_{monolayer}$ is the transmittance of an antimony monolayer, which was calculated to be 97.08%.[188] T_{total} is the transmittance of the antimony dispersion in a quartz cuvette. This was obtained by measuring UV-vis spectra of the dispersions, as shown in Figure 3.1(d), from which the absorption was measured to be 1.21 and based on Lambert-Beer law and transmittance was then calculated to be 6.165%. Hence the effective number of antimony monolayers was then calculated to be ~94. The linear refractive index (n_{0e}) of the antimonene dispersion is closed to that of the CHP (1.50).[55] Consequently, the nonlinear refractive index (n_{2e}) of the antimonene dispersion can be obtained from Equation (3.3) and the third-order nonlinear optical susceptibility ($\chi^{(3)}_{monolayer}$) of antimonene monolayer from Equation (3.4). As shown in Table 3.1, antimonene monolayer possesses third-order nonlinear optical

susceptibility up to ~ 10^{-8} esu. This indicates that it has huge potential applications in nonlinear optics.

Table 3.1. The effective nonlinear refractive index and third-order nonlinear susceptibility of graphene, antimonene, WS_2 and BN.

		405 nm	785 nm	1064 nm	Average
Antimonene	$n_{2e}\ (cm^2/W)$	3.72×10^{-5}	0.61×10^{-5}	1.30×10^{-5}	1.88×10^{-5}
	$\chi^{(3)}$ (esu)	15.8×10^{-8}	3.90×10^{-8}	8.07×10^{-8}	9.26×10^{-8}
Graphene	$n_{2e}\ (cm^2/W)$	7.07×10^{-5}	1.05×10^{-5}	1.93×10^{-5}	3.35×10^{-5}
	$\chi^{(3)}$ (esu)	1.97×10^{-7}	0.91×10^{-7}	0.52×10^{-7}	1.13×10^{-7}
WS_2	$n_{2e}\ (cm^2/W)$	6.02×10^{-7}	–	–	6.02×10^{-7}
	$\chi^{(3)}$ (esu)	5.12×10^{-9}	–	–	5.12×10^{-9}
BN	$n_{2e}\ (cm^2/W)$	–	–	–	–
	$\chi^{(3)}$ (esu)	–	–	–	–

'–' means no SSPM diffraction for the wavelength.

The SSPM experiments were also carried on graphene, WS_2 and boron nitride (BN) using 405, 785 and 1064 nm lasers. As seen in Table 3.1, the effective nonlinear refractive index of WS_2 dispersion was calculated to be $6.02 \times 10^{-7}\ cm^2/W$ and the third-order nonlinear optical susceptibility was 5.12×10^{-9} esu at 405 nm, while no SSPM was observed using the 785 nm or 1064 nm lasers. For BN, since it has a large bandgap (up to ~5-6 eV), which is larger than the photon energy of our laser (*i.e.*, 3.08eV or 405 nm),[189] the electrons in the valance band cannot be excited to the conduction band through single-photon absorption. Meanwhile, no two-photon absorption or multi-photon process was observed in the SSPM experiments.[86, 184] Consequently, there is no SSPM response in the BN sample for all the three wavelengths, which is in good agreement with the experimental results seen in Table 3.1. On the other hand, both graphene and antimonene show a SSPM response to 405, 785 and 1064 nm lasers, as shown in Table 3.1. The broadband nonlinear optical response of graphene is due to its large-energy-scale band structure.[43, 86] The band gap of monolayer antimonene with different phases ranged from 0.3 eV to 1.5 eV[84] and the few-layer antimonene has the zero band gap. As a result, the sample shows a response to all the three wavelengths (1064 nm: 1.17 eV; 785 nm: 1.59 eV; 405 nm: 3.08 eV) and broadband SSPM diffraction patterns were observed in the experiments for all the three wavelengths.

3.3 Tuneable nonlinear refractive index

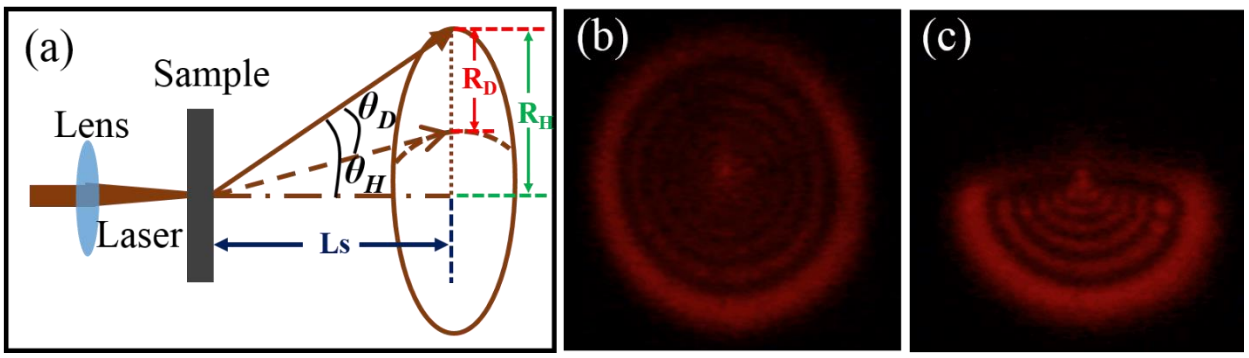

Figure 3.4. (a) Schematic of half-cone angle and distortion angle. The initial perfect circular (b) at 0.35 s and distorted (c) SSPM diffraction rings pattern until its stabilization.

It takes a few seconds for the SSPM diffraction rings to form (due to the polarizing of the 2D material) which they do in two stages – first they expand circularly to a maximum diameter as in Figure 3.4(b), then thermal effects take over and the upper half of the rings distorts as in Figure 3.4(c). This phenomenon was observed in many other materials such as dye solutions[190], liquid crystals,[87] carbon nanotubes[89], graphene [86, 191] and some TMDs dispersions.[55] The mechanism of this distortion is similar to the case of graphene dispersions, which has experimentally shown that the deviation of the upper half of the rings is due to non-axis-symmetrical thermal convections[191, 192]. As introduced in section 2.1, SSPM is a nonlinear optical phenomenon induced by the optical Kerr effect: $n = n_0 + In_2$. This indicates that the distortion could result from the variation of linear refractive index (Δn_0) and/or nonlinear refractive index (Δn_2). The most possible factor to induce the change in the linear refractive index of a dispersion is the possible bubbles produced by the laser heating. To investigate this possibility, a series of SSPM experiments were carried out at different atmospheric pressure in graphene dispersion.[191] The results in Figure 3.5 (a) show that there were no observable change in the distortion properties, including distortion time, distortion angle and half-cone angle, when the air pressure changed from 1.00 atm to 0.02 atm. This proves that the possible variation of linear refractive index plays negligible role in the distortion of the SSPM rings pattern.

Next is to discuss the passible contribution of the variation nonlinear refractive index to the distortion. For simplicity, θ_H is defined as the half-cone angle and θ_D as the distortion angle, as seen in Figure 3.4 (a). The half-cone angle θ_H can be written as: [87, 90]

$$\theta_H \approx \frac{\lambda}{2\pi}\left(\frac{d\Delta\psi}{dr}\right)_{max} \tag{3.5}$$

By imposing Equation (3.1) into Equation (3.5), one can have

$$\theta_H \approx n_{2e}\left[-\frac{8IrL_{eff}}{w_0^2}exp\left(-\frac{2r^2}{w_0^2}\right)\right]_{max}, r\in[0,+\infty) \tag{3.6}$$

Since the last part of Equation (3.6) ($\left[-\frac{8IrL_{eff}}{w_0^2}exp\left(-\frac{2r^2}{w_0^2}\right)\right]_{max}, r\in[0,+\infty) = C$) is a constant, Equation (3.6) can be written as: $\theta_H \approx n_{2e}C$. After a few simple derivations from this equation, the relationship between half-cone angle θ_H and distortion angle θ_D can be expressed as:[55]

$$\Delta n_{2e}/n_{2e} = \theta_D/\theta_H \tag{3.7}$$

Equation (3.7) shows that the distortion angle is proportional to Δn_2. That is to say, the distortion of SSPM rings pattern results from the variation of nonlinear refractive index. This variation is very likely to be caused by the thermal convections induced by laser heating. The case is similar to the onset of convection around a horizontal wire that is suddenly heated. [192] As the inset of Figure 3.5(c) illustrates, a temperature gradient along the vertical direction would be generated by the heating of a laser beam with enough intensity. This leads to a thermal convection surrounding the laser beam inside the dispersion. The thermal convection is stronger in the upper part of the beam while weaker in the downer part, resulting in corresponding lower and higher density of nanosheets. Figure 3.5 (b) implies that the more nanosheets contributing to the SSPM, the larger of the SSPM rings' diameter. Consequently, obvious distortion was observed in the upper part of the SSPM ring pattern. This was supported by a thermal experiment, as seen in Figure 3.5 (c).[191] As the temperature of the dispersion increases, *i.e.*, stronger thermal convection, the differential nonlinear refractive index increases.

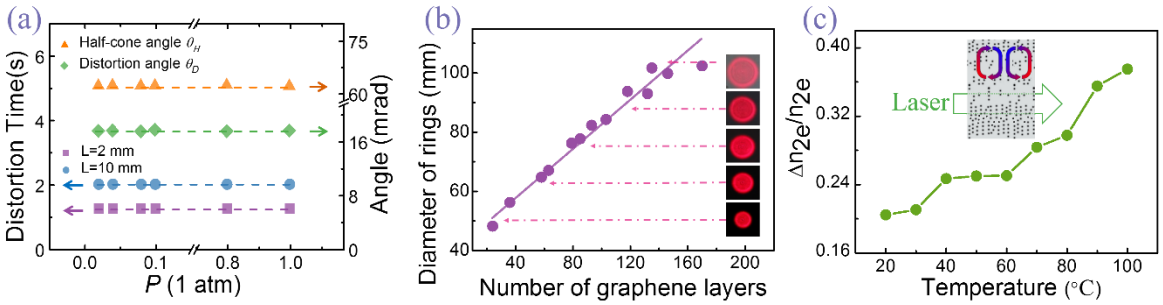

Figure 3.5 (a) The distortion time, distortion angle (θ_D) and half-cone angle (θ_H) at different atmospheric pressure (P). (b) The diameter of outmost diffraction ring versus the number of nanosheets layers that contribute to SSPM. Inset: Photos of the corresponding SSPM rings. (c)Differential change of nonlinear optical refractive index ($\Delta n_{2e}/n_{2e}$) as a function of the temperature of dispersions. The inset shows the thermal convections in the dispersion induced by laser heating.[191]

To furtherly support this argument, a comparable experiment on the incident directions of the focused laser beam was carried out at Figure 3.6. In horizontal incident geometry (Figure 3.6 (a)-(c)), a series of perfect concentric circles were generated at 0.5 s after the dispersion was irradiated by the laser. From ~0.5 s to ~2.8 s, the upper half of this rings bends toward to the centre of the pattern while no observable change was seen in the lower half. The distortion pattern would be stable after ~2.8 s. In another experiment when the dispersion was irradiated by a laser along the vertical direction (Figure 3.6(d)-(f)), the perfect concentric circles were also formed at ~0.5 s after the irradiation of the laser. However, this rings remained the same and no distortion was observed even after 30 min. These imply that the distribution of the dispersion along the vertical direction is the same while different along horizontal direction. This is in agreement of the distribution of the temperature gradient that induced the distortion of the SSPM diffraction rings pattern.

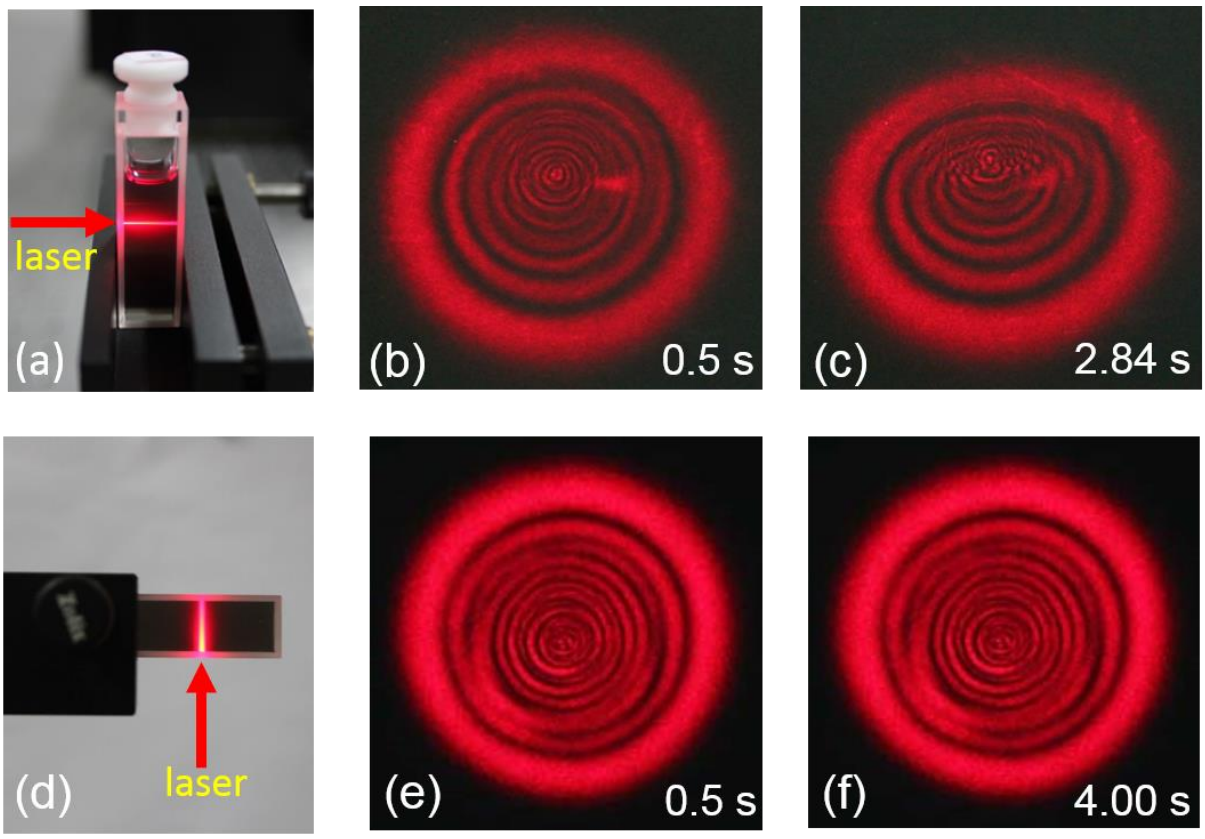

Figure 3.6. (a) The dispersion was irradiated by a focused laser along horizontal direction. (b) The corresponding perfect-circle SPM diffraction ring pattern at 0.5 s and (c) the stable distorted rings pattern at 2.84 s. (c)-(f) The case of vertical incident laser irradiating the dispersion.[191]

It can be seen from Equation (3.7) that these results are used here to investigate the change in the nonlinear refractive index of the dispersions. From Figure 3.4 (a) it can be seen that $\theta_H = \csc(R_H/L_S) \approx R_H/L_S$ and $\theta_D \approx R_D/L_S$ since distance from the samples to center of the circular diffraction rings pattern (L_S) is far larger than the radius of the outmost diffraction rings. Therefore the relative change in the nonlinear refractive index ($\Delta n_{2e}/n_{2e}$) of the antimony nano-sheet dispersions can be easily obtained by measuring R_H, R_D and L_S. The graphene and antimony nano-sheet samples were tested using the 1064 nm laser from ~8 W/cm^2 to ~63 W/cm^2. As seen in Figure 3.7, the half-cone angle and distortion angle increased with the intensity in both cases, but the half-cone angle of the antimony nano-sheet dispersions increased slightly slower than the distortion angle. Consequently, $\Delta n_{2e}/n_{2e}$ increased dramatically from 8 W/cm^2 to 40 W/cm^2 there tends to be a maximum at ~63% after 40 W/cm^2, *i.e.*, the nonlinear refractive index can be tuned from ~14% to ~63%, while $\Delta n_{2e}/n_{2e}$ of graphene dispersion in the experiment can span from ~28% to ~75%.

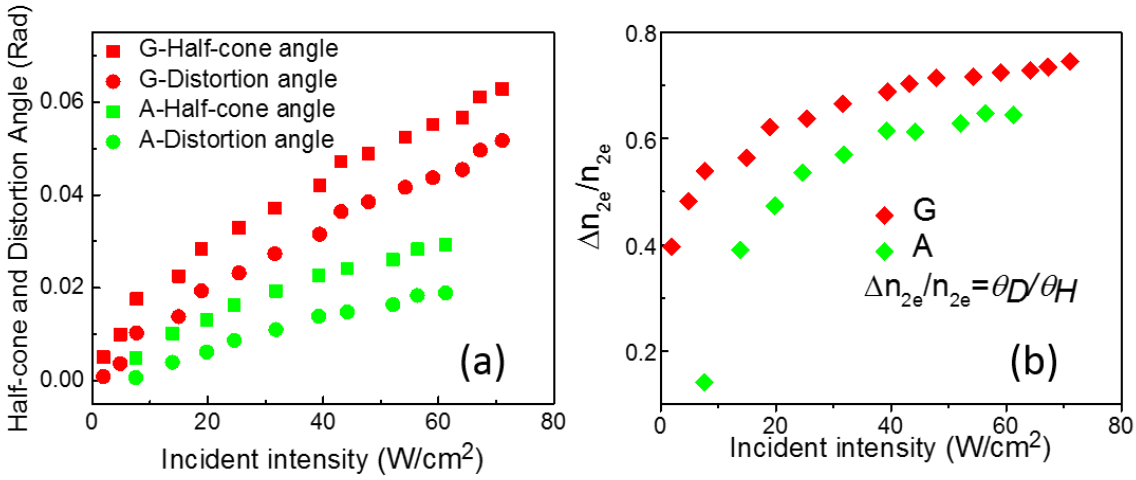

Figure 3.7. (a) Half-cone angle and distortion angle as functions of incident intensity in antimony nanosheets (green dot) and graphene (red dot). (b)The relative change of nonlinear refractive index of antimony nanosheets (Green dot) and graphene (red dot) vs incident intensity.

3.4 Conclusion

In this chapter, the spatial self-phase modulation and its distortion based on 405, 785 and 1064 *nm* CW lasers were carried out on liquid-phase-exfoliated antimony nano-sheet dispersions. The third-order nonlinear susceptibility of effective antimony monolayer is calculated to be $\chi^{(3)}$~10^{-8} esu and the nonlinear refractive index of the dispersion ~10^{-5} cm^2 W^{-1}. In contrast to BN and TMDs, both antimonene and graphene display novel broadband nonlinear optical response from the visible to the near-infrared region. By changing the incident intensity, the relative variation in nonlinear refractive index of the antimony nanosheets can be tuned from ~14% to ~63%. These results will be helpful for the photonic applications of antimonene in a broadband wavelength range, such as an optical modulator and a switcher.

One part of work relative to this chapter have been published by the journal *Photonics Research* and another part is under peer reviews:

https://www.osapublishing.org/prj/abstract.cfm?uri=prj-3-2-A51

4. Comparative broadband NLO properties of $MoSe_2$/PVA composite thin films

---

In this chapter, a comparative study on the dependence of the nonlinear optical behavior of $MoSe_2$/PVA composites on wavelength, pulse duration and age was carried out systematically. Liquid-phase exfoliation was employed to fabricate few-layer $MoSe_2$ nanosheets in water using sodium cholate as the surfactant. Polyvinyl Acetate (PVA) powder was dissolved in the warm water to prepare the PVA solutions which was then used as a host to prepare $MoSe_2$/PVA composite thin films. By changing the concentration of $MoSe_2$ inside the PVA matrix, three composite thin films with different linear transmissions were fabricated. They are labelled by α, β and γ from high to low linear transmission respectively (see Figure 4.4). The nonlinear optical behavior of these composite thin films was investigated by the open-aperture Z-scan technique with laser pulses with a 6 ns duration at the center wavelength of 532 nm from a Q-switched Nd:YAG laser and ~ 100 femtosecond laser pulses at the wavelength of 400 nm, 500 nm and 800 nm. 400 nm and 500 nm ultrafast pulses were generated from a Coherent optical parametric amplifier (OPA 9800) that is driven by 800 nm pulses from a high repetition-rate, femtosecond Ti:Sapphire amplifier (Coherent Rega 9000). The pulse repetition-rates are 10 Hz for the nanosecond laser and 100 kHz for all femtosecond pulses. The results show that the embodiment of liquid-phase-exfoliated $MoSe_2$ within a host material, *i.e.*, PVA, is preferable not only for exploiting practical nonlinear optical devices but also for improving the stability of the 2D nanosheets. The $MoSe_2$/PVA thin films possess saturable absorption behavior in a wide wavelength region from 400 nm to 800 nm under femtosecond and nanosecond pulses.

This broadband saturable absorption of $MoSe_2$/PVA thin films shows an obvious dependence on both the linear absorption and irradiation laser wavelength. As the linear absorption increases from 12.8 cm^{-1} and 3.6 cm^{-1} to 36.2 cm^{-1} and 20.5 cm^{-1} for 550 nm and 800 nm respectively, the imaginary part of the third-order nonlinear optical susceptibility, $Im\chi^{(3)}$, increase from -0.88×10^{-13} esu and -0.38×10^{-13} esu to -7.2×10^{-13} esu and -23.8×10^{-13} esu respectively. Stronger saturable absorption was observed in the shorter wavelength region. The nonlinear absorption, α_{NL}, and the

third-order nonlinear optical susceptibility, $Im\chi^{(3)}$ are approximately three orders of magnitude larger under the irradiation of nanosecond pulses in comparison to femtosecond pulses.

The stability against aging of the composite thin films was studied by comparing the properties of fresh thin films with corresponding aged ones. It can be seen from the similarity of the linear absorption obtained by UV-vis spectroscopy that the alignment and orientation of the $MoSe_2$ nanosheets in the host stay the same for about half a year. The comparative optical nonlinearity between a fresh composite thin film and aged one was obtained from the same Z-scan set-up. Similar saturable absorption was observed in both samples.

As the carrier relaxation processes are important when a saturable absorber is used for mode-locking in a pulse laser, a degenerate pump-probe technique was employed to study the excited carrier dynamics of $MoSe_2$/PVA composites thin films. By studying the relationship between excitation carrier density and the pump-probe time, exciton-exciton annihilation was verified at the wavelength of 800 nm. This agrees with the ground-state absorption study on the composite thin films from the UV-vis spectroscopy.

4.1 Preparation and characterization of $MoSe_2$/PVA thin films

As a precursor to the fabrication of $MoSe_2$/PVA composite thin films, two dimensional $MoSe_2$ flakes were prepared from $MoSe_2$ bulks in the distilled (DI) water using sodium cholate as surfactant via a liquid-phase exfoliation technique.[55, 193] 1g $MoSe_2$ powder (Sigma-Aldrich) was dispersed in 20 ml aqueous surfactant solution with a concentration of sodium cholate of 10 mg/ml. This $MoSe_2$ dispersion was firstly sonicated using a flathead sonic tip for 90 min at 40% amplitude with a pulse of 2 s on and 4 s off. The sonication exfoliated the majority of the bulk into monolayer, bilayer and few-layer $MoSe_2$ flakes. To remove the bulk $MoSe_2$, the sonicated dispersion was centrifuged at 2000 rpm for 90 mins. The top ½ centrifuged dispersion was collected to prepare the $MoSe_2$/PVA composite thin films and the sediments on the bottom was recycled. The $MoSe_2$ flake dispersion are stable for about one month at a low temperature of ~2 ℃ in the fridge.

Before this dispersion was utilized to produce composite thin films, the state and quality of the 2D $MoSe_2$ flakes are characterized by transmission electron microscopy (TEM) and atom force microscopy (AFM). No $MoSe_2$ bulk was found in the TEM images of the centrifuged dispersions. Figure 4.1(a) shows a TEM image of two flakes stacked together, with the size of ~250 nm ×250 nm. The clear edges indicate that the two flakes are few-layer. A small $MoSe_2$ monolayer is shown

in Figure 4.1(a) in a relatively high resolution TEM image. Both TEM images indicate that the bulk $MoSe_2$ has been effectively exfoliated into 2D $MoSe_2$ flakes. These flakes are mainly composed of few-layer, bilayer and monolayer. This is also verified by the AFM study, see Figure 4.2.

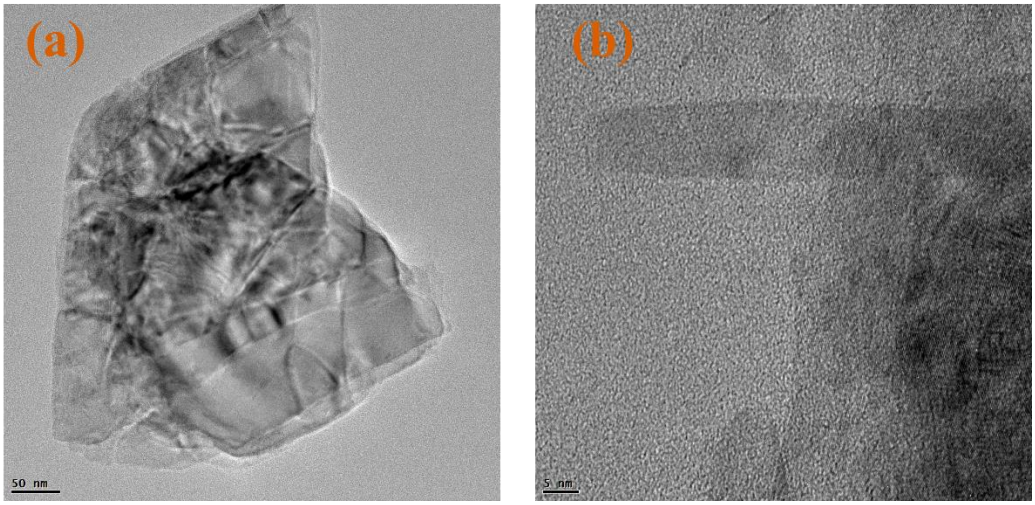

Figure 4.1. TEM images showing (a) a few-layer $MoSe_2$ flake and (b) a monolayer one in a relatively high resolution. The scale bar in (a) is 50 nm and 5 nm in (b).

To study the distribution of the number of the flake layers, AFM was employed to measure the sample in a large area of 2.5 μm × 2.5 μm, see Figure 4.2 (a). A great number of $MoSe_2$ nano-flakes are seen in the Figure 4.2 and only a few flakes stack together. To obtain the number of the flake layers, thickness profiles are plotted from the AFM image. For instance, a thickness versus the spatial length from the purple line in Figure 4.2 (a) is shown in Figure 4.2 (b). Since the thickness of $MoSe_2$ monolayer is ~0.67 nm,[194] the layer number of a flake with a thickness of, L, can be approximately calculated through the divide of L over 0.67 nm. Based on a number of thickness profiles from Figure 4.2 (a), a statistical distribution of the layer number of the flake was obtained, see Figure 4.2 (c). It can be seen that most of the flakes in the centrifuged dispersion are less than 15 layers. The flakes with the layer number between 3 and 15 account for more than 90% of the nanosheets. From statistics, the layer number of more than 25 was also calculated, as see in Figure 4.2 (c). It is likely to result from the stack of flakes, for example, see the green circle in Figure 4.2 (a).

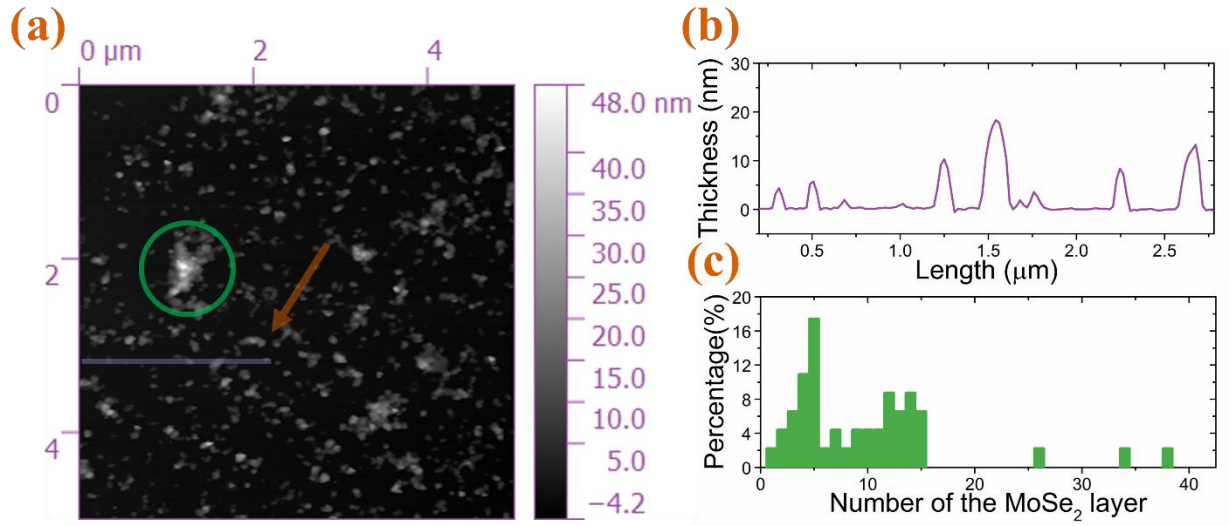

Figure 4.2. AFM image and corresponding analysis. (a) AFM image consist of a large amount of $MoSe_2$ flakes for thickness statistics in a 5 μm×5 μm area. (b) Thickness profile, *i.e.*, the thickness versus the spatial length. It is obtained from (a) at the purple line, as pointed by orange arrow. (c) The statistical percentage of the $MoSe_2$ flakes with different layers in dispersions.

These $MoSe_2$ flake dispersions consist of mainly 3-15 layers were subsequently utilized to fabricate composite thin films based on PVA. To prepare PVA solutions, 0.5 g PVA powder was dispersed into 10 ml DI water, following by heating in a water bath on a stirring hot plate (See Figure 4.3 (a)). After cooling down to room temperature, 10 ml resultant PVA solutions were mixed with 50 μl, 100 μl and 150 μl $MoSe_2$ flake dispersions respectively. These mixtures were stirred for one night using magnetic stir bars, subsequently sonicated for 5 mins at low power to achieve homogeneous mixed solutions. These mixed solutions were casted into petri dishes and dried in an oven at 60 °C for about 4 days. $MoSe_2$/PVA composite thin films with uniform surface were finally achieved, as shown in Figure 4.4. Pure PVA were also prepared via the same solution cast method to exclude the contribution to the optical nonlinearity of the composite thin films during the optical study.

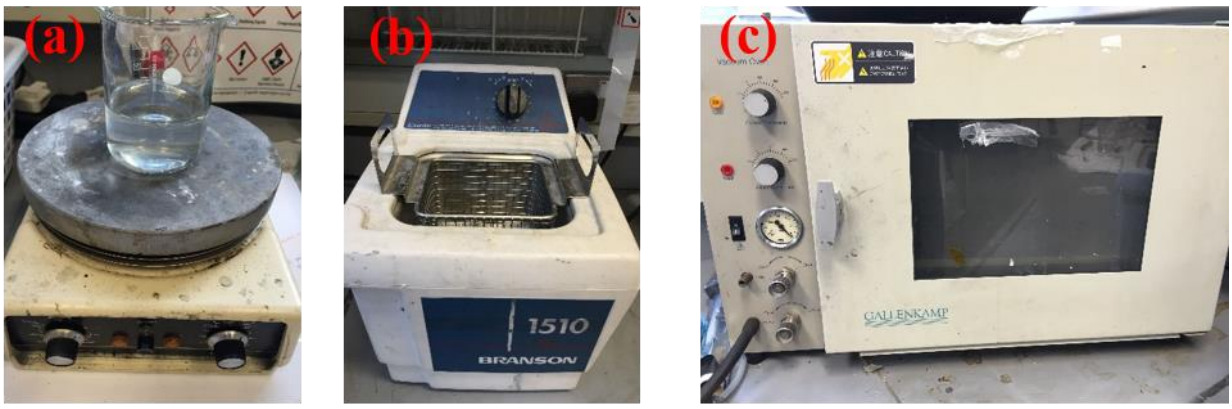

Figure 4.3. The equipment to fabricate the $MoSe_2$/PVA composite thin films. A stirring hot plate is utilized both to dissolve PVA powder (to prepare PVA solution) and to mix $MoSe_2$ dispersion and PVA solution.

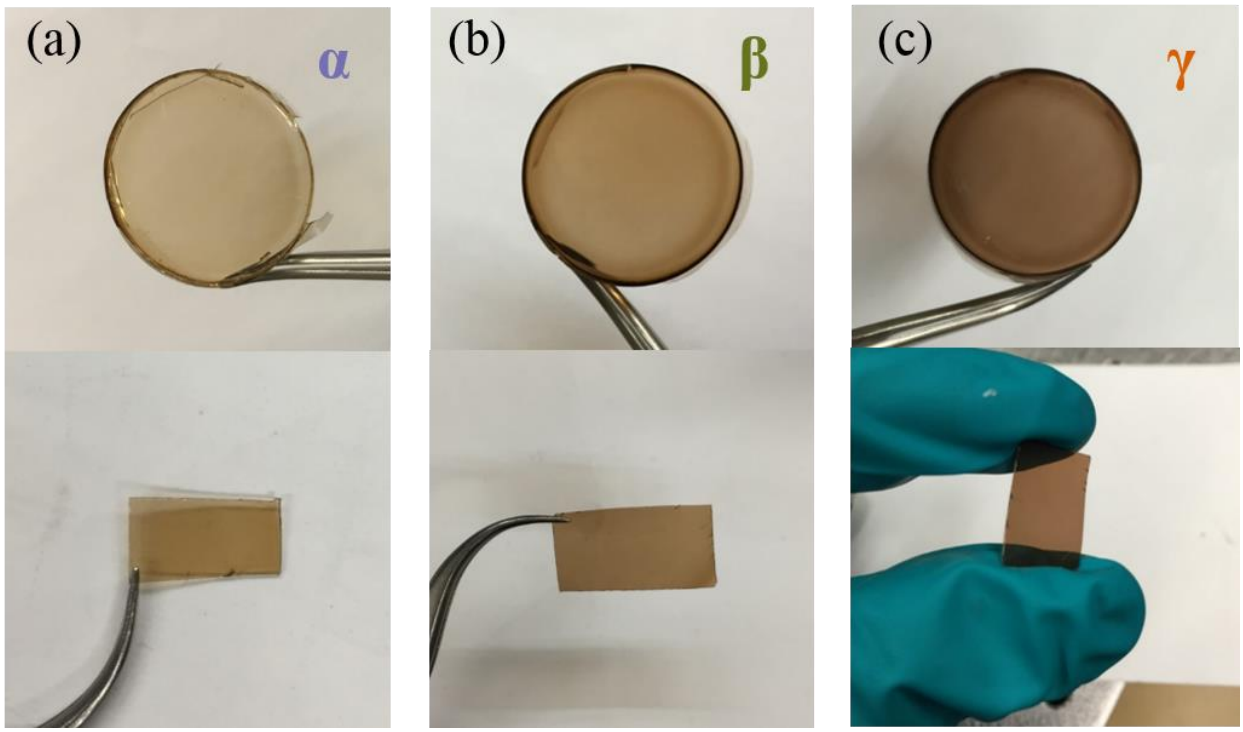

Figure 4.4. The photo of $MoSe_2$/PVA composite thin films with different linear transmission, *i.e.*, different content of $MoSe_2$ flakes in the composite thin films.

4.2 Saturable Absorption of $MoSe_2$/PVA thin films

4.2.1 Dependence of SA on pulse duration

By changing the concentration of $MoSe_2$ inside the PVA matrix, three composite thin films with different linear transmissions were fabricated. They are named by α, β and γ from high to low linear transmission respectively, see Figure 4.4. The optical nonlinear study of these thin films was then studied via an open-aperture Z-scan technique based nanosecond and femtosecond lasers. The results are plotted in Figure 4.5 and 4.6. Figure 4.5 (a)-(c) show the Z-scan results from laser pulses with the duration of 6 ns at the wavelength of 532 nm while Figure 4.5 (d)-(f) display the cases at the similar wavelength (550 nm) but different pulse width of ~100 fs. The results based on femtosecond lasers at the wavelength of 400 nm and 800 nm were shown in Figure 4.7 (a)-(c) and Figure 4.7 (d)-(f) respectively. The thin films at all the wavelengths and both pulse duration exhibit obvious saturable absorption, *i.e.*, the transmission of the composite thin films increase with the increase of the incident laser intensity and peaks at the focus point (Z=0). To theoretically analyze these results, the nonlinear optical theory was utilized to model the experimental Z-scan traces. According to Equation (2.3.1), the propagation equation in $MoSe_2$/PVA thin films is $\frac{dI}{dz} = -\alpha(I) \cdot I$, where I represents the excitation laser intensity, z is the propagating distance in the composite thin film, and $\alpha(I)$ is the total absorption that is consist of linear absorptive and nonlinear absorptive coefficients (α_0 and α_{NL} respectively): $\alpha(I) = \alpha_0 + \alpha_{NL} \cdot I$ (*i.e.*, Equation (2.2.2)) . This propagation equation was used to fit the experimental results and they all give favorable fits for all the wavelengths and pulse durations. The fitting curves are plotted in Figure 4.5 and 4.6. In the chapter, all the experimental results in nonlinear optical figures are shown using solid scatters and the modelling results using solid lines.

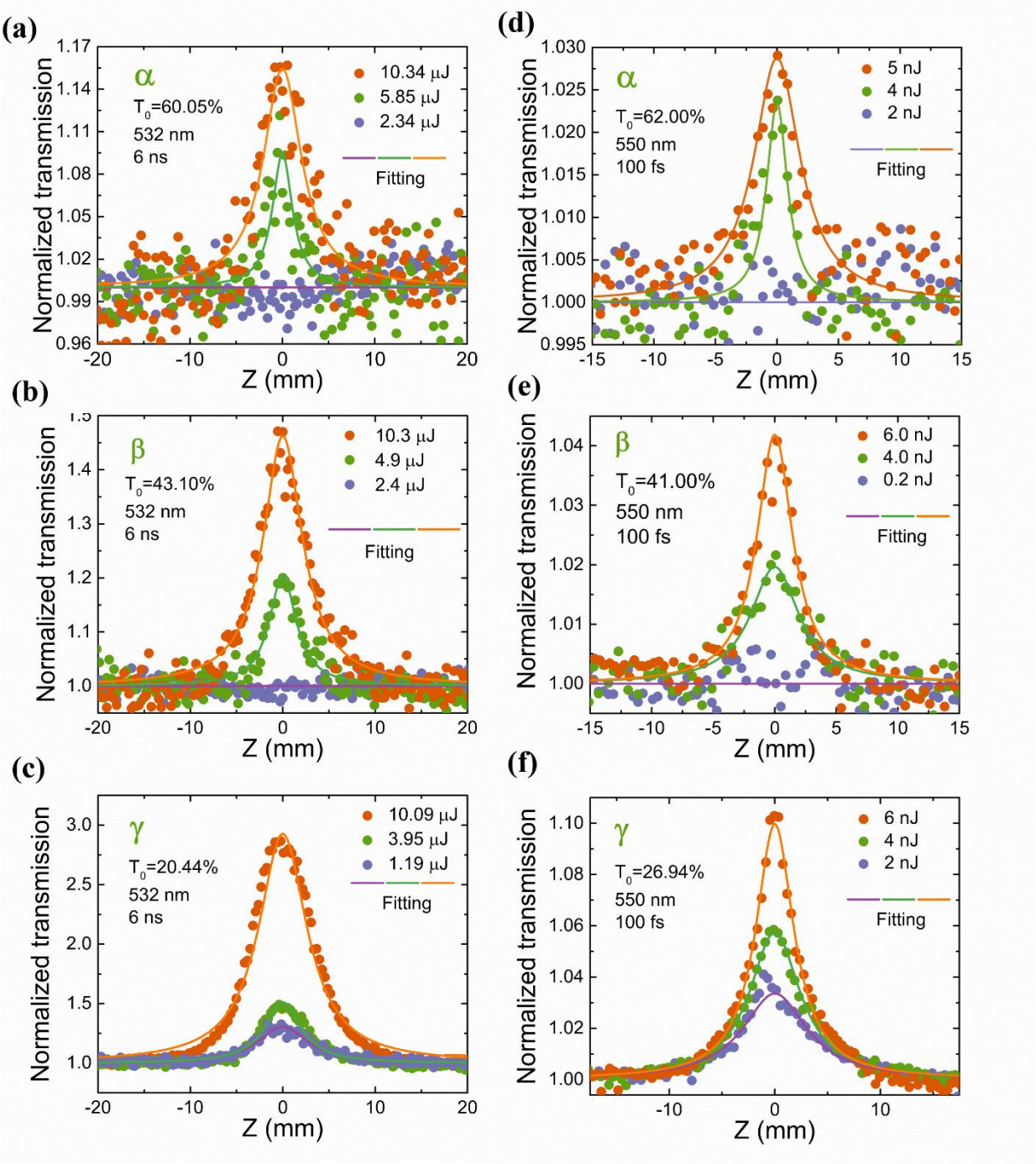

Figure 4.5. The experimental and fitting results of $MoSe_2$/PVA thin films based on nanosecond and femtosecond lasers at the center wavelength of 532 nm and 550 nm respectively. The measurements were carried out on three composite thin films (α , β and γ) with different linear transmission using variable energies.

The fitting linear and nonlinear optical parameters of the composite thin films α, β and γ are listed in Table 4.1 for 532 nm, 6 ns laser pulses and Table 4.2 for 550 nm, 100 fs laser pulses. Under irradiation of the laser with wavelength of 532 nm, pulse duration of 6 ns and repetition rate of 10

Hz, the linear transmission, T_0, of the composite thin films α, β and γ are measured to be 59.6%, 42.8% and 19.9% respectively. Based on these linear transmissions, the corresponding linear absorptions, α_0, were calculated to be 13.5 cm^{-1}, 25.0 cm^{-1} and 39.4 cm^{-1} respetively. As the linear absorption increase from 13.5 cm^{-1} to 39.4 cm^{-1}, the nonlinear absorption increase from -26.1 cm/GW to -960.0 cm/GW. That is to say, the $MoSe_2$/PVA composite thin films with lower linear absorption have smaller nonlinear absorption. This indicates that the saturable absorption increase with the increase in the content of $MoSe_2$ in the polymer host. This relationship between saturable absorption and linear absorption was also observed in other 2D nanosheets such as graphene.[24] As one of the most important nonlinear optical parameters, the imaginary part of the third-order nonlinear optical susceptibility related to α_{NL} can be calculated by:[24]

$$\mathrm{Im}\chi^{(3)} = \left(\frac{10^{-7} c\lambda n^2}{96\pi^2}\right)\alpha_{NL} \tag{4.1}$$

Here c represents the light speed, λ is the irradiation wavelength and n is the refractive index. $\mathrm{Im}\chi^{(3)}$ were calculated to be -1.0×10^{-11} esu, -33.6×10^{-11} esu and -37.2×10^{-11} esu for samples α, β and γ respectively. It is clear that $\mathrm{Im}\chi^{(3)}$ increases with the linear absorption. This is consistent with that the dependence of saturable absorption on the concentration of the nonlinear materials. The Figure of Merit (FOM) is defined as the $\mathrm{Im}\chi^{(3)}$ value per 1/cm to eliminate the discrepancy of different linear absorption:

$$\mathrm{FOM} = \left|\frac{\mathrm{Im}\chi^{(3)}}{\alpha_0}\right| \tag{4.2}$$

The calculated parameters from Equation (4.2) are also shown in Table 4.1. They were calculated to be 1.020 $\times 10^{-12}$ esu cm, 13.475 $\times 10^{-12}$ esu cm and 9.458$\times 10^{-12}$ esu cm, which are almost in the same order of magnitude.

Table 4.1 The fitting parameters of Z-scan results and optical nonlinearities of the composite thin films α, β and γ with linear transmission of 59.6%, 42.8% and 19.9% respectively at 532 nm. The pulse duration of the laser is 6 ns and the pulses repetition rate is 10 Hz.

Laser pulse	Sample	T_0 (%)	α_0 (1/cm)	Energy	ω_0 (μm)	NLO	α_{NL} (cm/GW)	Im$\chi^{(3)}$ ($\times10^{-13}$ esu)	FOM ($\times10^{-14}$ esu cm)
532 nm 6 ns 10 Hz	α		13.5	2.34 μJ					
				5.85 μJ	15.4	SA	-26.1	-101.4	75.3
				10.34 μJ	21.6	SA	-44.7	-173.6	128.8
	Average			-			-35.4	-137.5	102.0
	β	42.8	24.9	2.4 μJ					
				4.9 μJ	18.4	SA	-119.2	-462.6	185.5
				10.3 μJ	23.9	SA	-1612.6	-6257.0	2509.4
	Average			-			-865.9	-3359.8	1347.5
	γ	19.9	39.4	1.19 μJ	25.7	SA	-1612.6	-6257.0	1588.7
				3.95 μJ	23.0	SA	-535.4	-2077.3	527.4
				10.09 μJ	34.3	SA	-732.0	-2840.4	721.2
	Average			-			-960.0	-3724.9	945.8

Table 4.2 Linear and nonlinear optical parameters of the composite thin films α, β and γ based on a pulse laser with the center wavelength of 550 nm, pulses duration of ~100 fs and duration of 100 kHz. The linear transmission of the samples α, β and γ at 550 nm are 61.9 %, 41.0% and 26.9% respectively.

Laser pulse	Sample	T_0 (%)	α_0 (1/cm)	Energy	ω_0 (μm)	NLO	α_{NL} (cm/GW)	Im$\chi^{(3)}$ ($\times10^{-13}$ esu)	FOM ($\times10^{-14}$ esu cm)
550 nm ~100 fs 100 kHz	α	61.9	12.8	2 nJ					
				4 nJ	13.6	SA	-0.1	-0.6	0.4
				5 nJ	20.2	SA	-0.3	-1.2	0.9
	Average						-0.2	-0.9	0.7
	β	41.0	25.9	2 nJ					
				4 nJ	20.6	SA	0.4	-1.5	0.6
				6 nJ	17.8	SA	0.4	-1.6	0.6
	Average						0.4	-1.6	0.6
	γ	26.9	36.2	2 nJ	25.8	SA	-2.3	-9.8	2.7
				4 nJ	23.1	SA	-1.6	-6.5	1.8
				6 nJ	20.2	SA	-1.3	-5.5	1.5
	Average						-1.7	-7.2	2.0

For comparison, the wavelength of the femtosecond laser was tuned to be 550 nm, the closest wavelength I can have in the lab to that of the nanosecond laser. The linear and nonlinear parameters for this wavelength are listed in Table 4.2. The linear absorption at 550 nm were measured to be 12.8 cm^{-1}, 25.9 cm^{-1} and 36.2 cm^{-1} for samples α, β and γ respectively, which are

all slightly lower than that at 532 nm, *i.e.*, 13.5 cm^{-1}, 25.0 cm^{-1} and 39.4 cm^{-1}. This agrees with $MoSe_2$ possessing higher linear absorption at shorter wavelength.[195] It also indicates the accuracy of the method to measure the linear absorption. Similar to the nanosecond laser, strong saturable absorption was also observed under the irradiation of the femtosecond laser at the similar wavelength. At the same time, the nonlinear parameters including α_{NL} and $\mathrm{Im}\chi^{(3)}$ rise with the content of $MoSe_2$ in the host. This is consistent with the case for the nanosecond laser that is shown Table 4.1. α_{NL} were fitted to be -0.2 cm/GW, -0.4 cm/GW and -1.7 cm/GW, and $\mathrm{Im}\chi^{(3)}$ were calculated to be -0.884×10^{-13} esu, -1.6×10^{-13} esu and -7.2×10^{-13} esu for samples α, β and γ respectively. Both α_{NL} and $\mathrm{Im}\chi^{(3)}$ for the femtosecond laser are two magnitudes lower than that for the nanosecond laser. The similar results were also reported in the graphene/PVA thin films at the wavelength of 1030 nm (340 fs) and 1064 nm (6 ns). [24]

This dependence of saturable absorption on the pulse duration can be explained by excited carrier dynamics. Few-layer $MoSe_2$ is an indirect bandgap semiconductor and its relaxation process of excited carriers is plotted in Figure 4.6. The incident light injects excited carriers into the conduction and valence band, see Figure 4.6(a). Initially these carriers are in non-equilibrium state and will be a thermalized rapidly to a quasi-thermal state via carrier-carrier scattering in a very short time of ~10 - 200 fs, as seen in Figure 4.6(b). As shown in Figure 4.6(c), these quasi-thermal carriers are subsequently cooling down via intraband carrier-photon scattering at τ_1 ~1.9 ps (Obtained from pump-probe experiments, see Table 4.6. Finally these excited carrier annihilated in τ_2~49.5 ps. Hence the recovery time (τ_r) of the excited carrier in the composite thin films can be approximately calculated to be $\tau_r = \tau_1 + \tau_2 \approx 52$ ps. It is obvious that the pulse duration ($\tau_p = 6$ ns) of the nanosecond laser is much longer than the recovery time ($\tau_p \gg \tau_r$). As a nonlinear material with saturable absorption property, the conduction band of $MoSe_2$ can be fully filled by the accumulation of the excited carrier and no long accepts more incoming carriers before the relaxation. Consequently, the density of the excited carrier (N) can be approximately calculated by:

$$N = \alpha \frac{I\tau_r}{h\upsilon} \tag{4.3}$$

Here α is the interband absorption coefficient and $h\upsilon$ represents the energy of a single incident photon. For femtosecond laser, pulse duration ($\tau_p = 100$ fs) is much shorter than the recovery time of the composite thin films and N can be expressed as:

$$N = \alpha \frac{I\tau_p}{h\upsilon} \tag{4.4}$$

For the same composite thin films, the density of the excited carrier at saturable state are always the same. Therefore the saturable intensity (I_{sn}) for the nanosecond laser is smaller than that (I_{sf}) for femtosecond laser, *i.e.*, $I_{sn} < I_{sf}$. By combining Equation(2.2.2), $\alpha(I) = \alpha_0 + \alpha_{NL} \cdot I$, and Equation(2.2.5), $\alpha(I) = \frac{\alpha_0}{1+I/I_S}$, one can obtain

$$\alpha_0 + \alpha_{NL} \cdot I = \frac{\alpha_0}{1+I/I_S} \tag{4.5}$$

Since the sign of the nonlinear optical coefficient, α_{NL}, of a saturable absorption material is negative, the absolute value of α_{NL} is larger for a smaller saturable intensity. As a result, the nonlinear optical coefficient of the composite thin film obtained by the nanosecond laser is much larger than that by the femtosecond laser.

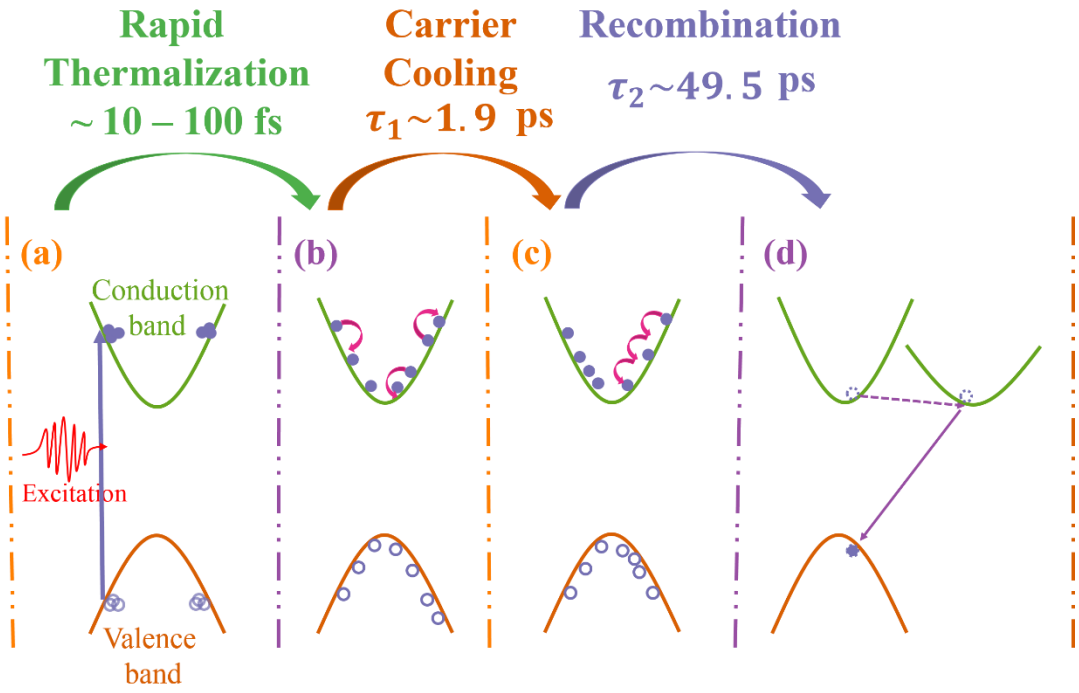

Figure 4.6. The relaxation processes of excited carrier of $MoSe_2$/PVA composite thin films.

4.2.2 Broadband SA of $MoSe_2$/PVA thin films

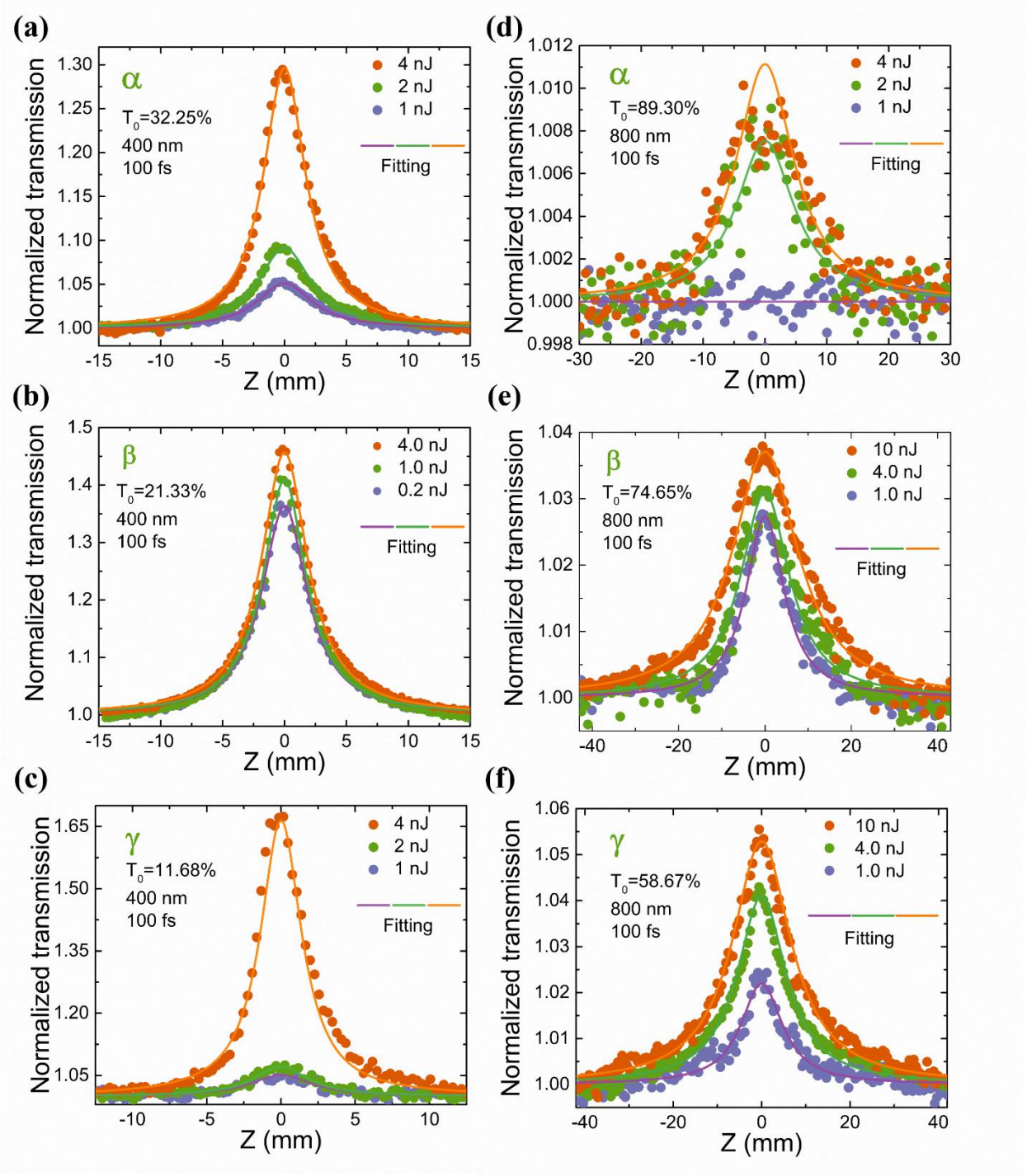

Figure 4.7. The Z-scan results of $MoSe_2$/PVA thin films (α , β and γ) under femtosecond pulses laser radiation at the wavelengths of 400 nm and 800 nm.

The nonlinear optical response of the $MoSe_2$/PVA thin films at the center wavelength of 400 nm and 800 nm were also studied. Saturable absorption was observed for the three samples at the both

wavelengths. All the experimental and fitting Z-scan curves at 400 nm and 800 nm are plotted in Figure 4.7.

The fitting parameters from the propagation Equation in nonlinear mediums for 400 nm and 800 nm are listed in Table 4.3 and 4.4 respectively. α_{NL} for samples α, β and γ at the wavelength of 400 nm were modelled to be -2.3 cm/GW, -35.6 cm/GW and -4.2 cm/GW, and $\mathrm{Im}\chi^{(3)}$ were calculated to be -2.9×10^{-13} esu, -45.5×10^{-13} esu and -5.3×10^{-13} esu respectively. It is easy to notice that the nonlinear optical parameters for the composite thin film β are one order of magnitude lager than that of thin films α and γ. α_{NL} for the thin film β under the pulse energy of 0.2 nJ is -84.0 cm/GW, which is about dozens times that of the thin films α (-2.5 cm/GW) and γ (-3.7 cm/GW), see Table 4.4. It introduces a larger error in the average values. This is likely to be caused by experimental inaccuracy due to the very low transmission of the composite thin film at 400 nm. The linear transmission of the thin film β is 74.5% for 800 nm but as low as 21.0% for 400 nm. In contrast, the dependence of the optical nonlinearities of $MoSe_2$/PVA thin films on the $MoSe_2$ concentration is very clear at 800 nm where their linear transmission is relatively higher. At this wavelength, α_{NL} is -0.06 cm/GW, -0.98 cm/GW and -3.8 cm/GW and $\mathrm{Im}\chi^{(3)}$ is -0.4×10^{-13} esu, -6.1×10^{-13} esu and -23.8×10^{-13} esu for the composite thin films α, β and γ respectively.

Table 4.3. Linear and nonlinear optical parameters of the thin films α, β and γ obtained from 100 fs pulse laser with a center wavelength of 400 nm and a duration of ~100 fs. The linear absorption of the samples α, β and γ at 800 nm are 22.9 cm^{-1}, 34.5 cm^{-1} and 43.7 cm^{-1} respectively.

Laser pulse	Sample	T_0 (%)	α_0 (1/cm)	Energy	ω_0 (μm)	NLO	α_{NL} (cm/GW)	$\mathrm{Im}\chi^{(3)}$ ($\times 10^{-13}$ esu)	FOM ($\times 10^{-14}$ esu cm)
400 nm ~100 fs 100 kHz	α	32.2	22.9	1 nJ	18.9	SA	-2.5	-3.2	1.4
				2 nJ	18.5	SA	-2.1	-2.7	1.2
				4 nJ	17.7	SA	-2.4	-3.1	1.3
	Average						-2.3	-3.0	1.3
	β	21.0	34.5	0.2 nJ	18.7	SA	-84.0	-107.4	31.2
				1 nJ	18.5	SA	-17.6	-22.5	6.5
				4 nJ	19.4	SA	-5.2	-6.6	1.9
	Average						-35.6	-45.5	13.2
	γ	11.7	43.725	1 nJ	18.2	SA	-3.7	-4.8	1.1
				2 nJ	17.2	SA	-2.3	-2.9	0.7
				4 nJ	16.6	SA	-6.5	-8.3	1.9
	Average						-4.2	-5.3	1.2

Table 4.4. Linear and nonlinear optical parameters of the thin films α, β and γ at the wavelength of 800 nm.

Laser pulse	Sample	T_0 (%)	α_0 (1/cm)	Energy	ω_0 (μm)	NLO	α_{NL} (cm/GW)	$Im\chi^{(3)}$ ($\times 10^{-13}$ esu)	FOM ($\times 10^{-14}$ esu cm)
800 nm ~100 fs 100 kHz	α	89.2	3.6	10 nJ					
				20 nJ	38.3	SA	-0.06	-0.4	1.1
				30 nJ	38.3	SA	-0.06	-0.4	1.1
	Average						-0.06	-0.4	1.1
	β	74.5	11.1	4 nJ	37.3	SA	-1.4	-9.1	8.2
				10 nJ	42.3	SA	-0.8	-5.3	4.7
				20 nJ	49.2	SA	-0.7	-4.2	3.8
	Average						-1.0	-6.2	5.6
	γ	58.6	20.5	1 nJ	38.4	SA	-6.0	-38.0	18.6
				4 nJ	41.8	SA	-3.3	-20.7	10.1
				10 nJ	45.8	SA	-2.0	-12.7	6.2
	Average						-3.8	-23.8	11.6

4.2.3 Dependence of SA on linear transmission

From both Figure 4.7 (a)-(c) and Figure 4.7 (d)-(f), we can also see that maximum normalized transmission rises with the linear absorption for both wavelengths. It is more obvious when the comparative Z-scan curves of samples α, β and γ for the same experimental parameters are plotted together, as seen in Figure 4.8. Figure 4.8 (a) shows the Z-scan results of the three samples under the irradiation of pulses with the duration of 6 ns at the center wavelength of 532 nm at ~ 5 nJ. Lager saturable absorption exists in the composite thin films with higher linear absorption. This dependence of optical nonlinearity of the $MoSe_2$/PVA thin films on the $MoSe_2$ concentration is also true for the ~100 fs pulses at the wavelength of 400 nm, 550 nm and 800 nm, as shown in Figure 4.8 (c), (b) and (d) respectively. Hence it is clear that the broadband saturable absorption of $MoSe_2$/PVA composite thin films can be tuned through changing the percentage of $MoSe_2$ in the polymer host.

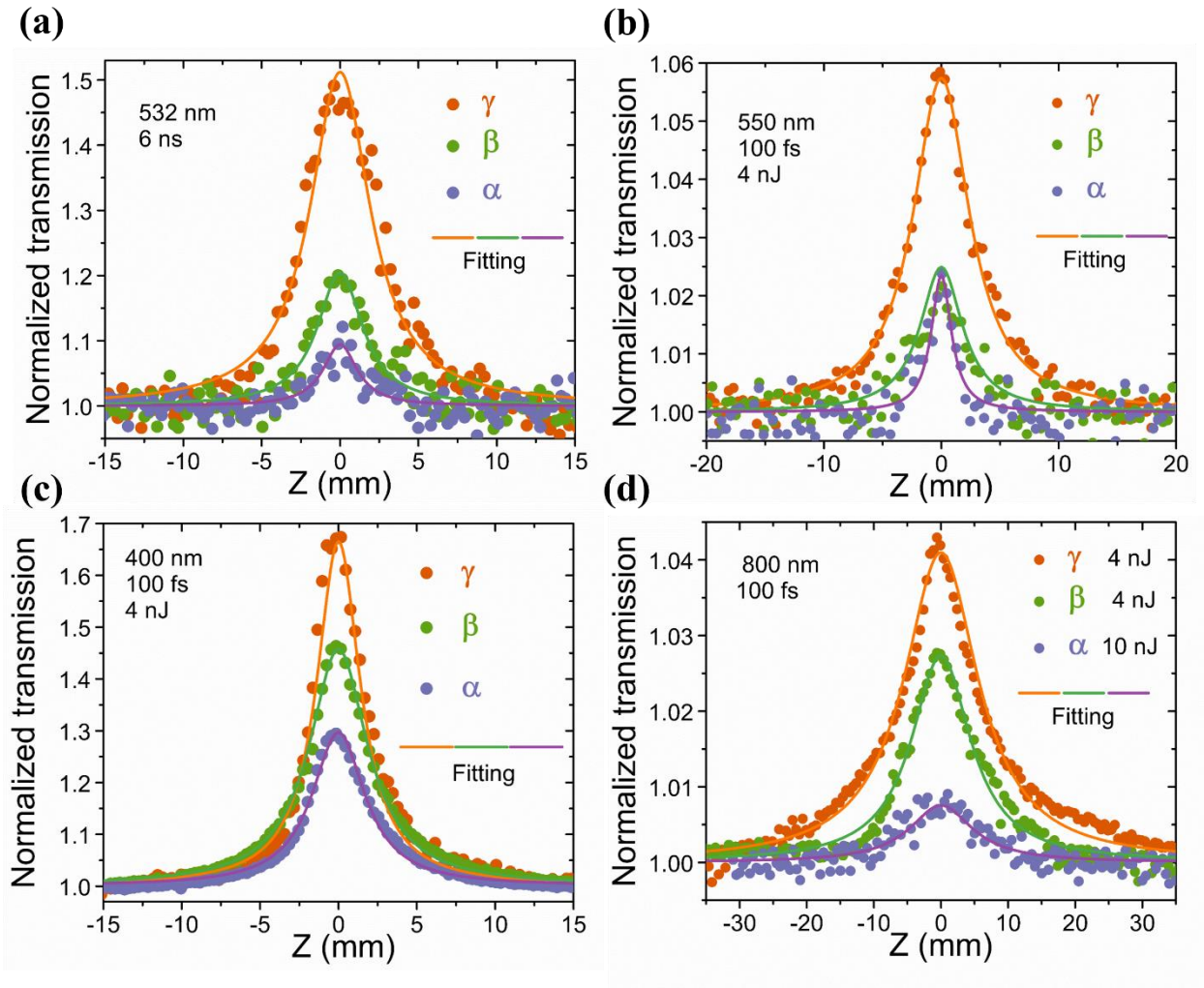

Figure. 4.8. (a) The Z-scan results of the samples α , β and γ under the irradiation of pulses with the duration of 6 ns at the center wavelength of 532 nm at ~ 5 nJ. The cases for the ~100 fs pulses at the wavelength of (b) 550 nm, (c) 400 nm and (d) 800 nm.

4.2.4 Dependence of SA on wavelength

The dependence of nonlinear optical behavior on wavelength is very obvious. Based on the above results, the experimental and fitting Z-scan curves for the thin film γ that were obtained from the laser pulses with duration of ~ 100 fs and wavelength of 400 nm, 550 nm and 800 nm are plotted together, see Figure 4.10. The pulse energies for the three wavelengths are all 4 nJ. It can be seen from Figure 4.10 (a) that the maximum normalized transmission at 400 nm is higher than that at 500 nm, which is higher than that at 800 nm. This is very clear when a zoom-in image of Figure 4.10 (a) is plotted, as seen in Figure 4.10 (b). This relationship is also related to the linear

absorption. From Table 4.2, 4.3 and 4.4, it can be seen that the linear transmission of the thin film γ is 11.7%, 26.9% and 58.6% at the wavelength of 400 nm, 550 nm and 800 nm, with a corresponding linear absorption of 43.7 cm^{-1}, 36.2 cm^{-1} and 20.5 cm^{-1} respectively.

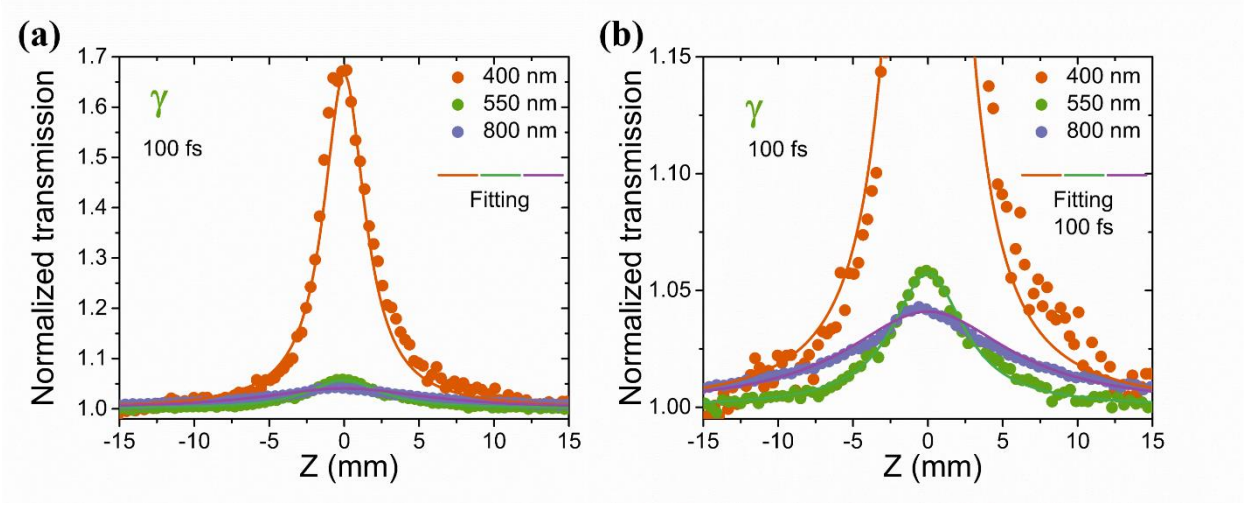

Figure 4.9. (a) Z-scan curves based on the laser pulses with duration of ~ 100 fs and wavelength of 400 nm, 550 nm and 800 nm. (b) A zoom-in image of Figure (a). The solid scatters stand for the experimental data and the solid line for fitting results.

4.3 Laser induced damage

When the laser beam was focused at the position of Z=0, the heat would accumulate inside the composite thin films due to the absorption of $MoSe_2$ resulting in laser induced damage of the composite thin films. In order to make sure all the experimental results were achieved at the laser intensity lower than the damage threshold, the damage caused by heat from the laser were studied under high intensity using both femtosecond laser and nanosecond lasers. As the pulse energy goes up to 400 nJ, an asymmetrical Z-scan curve which is different from the typical open-aperture Z-scan one was observed. As seen in Figure 4.10 (a), the normalized transmission increase when the composite thin film move toward the laser focus point along Z axis. This is the general saturable absorption as that was observed in previous section. However, the transmission dropped dramatically at the focus point of the laser (Z=0). This abnormal phenomenon on the $MoSe_2$/PVA composite thin films is attributed to the laser induced damage that result in a change of the thickness of sample. According to Lambert-Beer law, the transmission can be expressed as:

$$T = 10^{-A} = 10^{-\varepsilon c l} \quad (4.6)$$

Where ε is the molar attenuation coefficient, c is the light speed and l represents the thickness of the sample. When the composite thin films were melted by the heat from the laser as the focus point, the thickness of the thin film at the location and surrounding where the laser is irradiating becomes larger due to the stack of melted polymer. This leads to a decrease in the transmission according to Equation (4.6). This is also more obvious on the nanosecond laser pulses, as seen in Figure 4.10(b). As the pulse energy of 6 ns laser went to 35.5 μJ, the transmission decreased rapidly and had a slight increase in at Z=~4 mm. In comparison to the femtosecond laser, the pulse duration of the nanosecond laser is much longer and hence likely to accumulate heart through the absorption in $MoSe_2$. This caused a larger damage in nanosecond lasers than in femtosecond lasers.

All the nonlinear optical measurements were carried out bellow 400 nJ for femtosecond laser pulses and 35.5 μJ for nanosecond ones. Meanwhile, all the Z-scan results in Figure 4.5 and 4.6 are symmetrical. Therefore, all the experimental results in this chapter are reliable and believable.

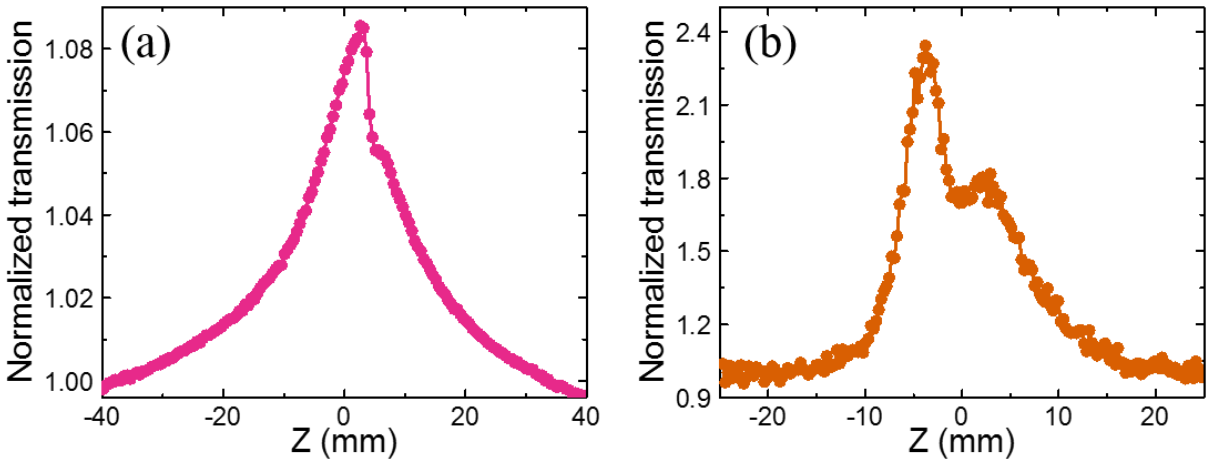

Figure 4.10. The Z-scan curves with laser induced damage under the irradiation of femtosecond (a) and nanosecond (b) lasers. The pulse energy 400 nJ for (a) with the repetition rate of 100 kHz while 35.5 μJ for (b) with the repetition rate of 10 Hz. The corresponding heat absorbed by the composite thin films are 100 nJ and 13.5 μJ respectively. The experienced temperature of damaging the composite thin films is ~90 °C.

4.4 Long-time stability of SA

The broadband nonlinear optical response of $MoSe_2$/PVA thin films has been verified via a laser wavelength range from 400 nm to 800 nm with both nanosecond and femtosecond pulse duration. These composite thin films were made from liquid-phase-exfoliated 2D $MoSe_2$ in solutions. Liquid-phase exfoliation is an effective and low-cost way to fabricate 2D materials in a large yield

and has be widely used. But the 2D flakes that are produced by this method are likely to aggregate and deposit from the solution after a month, resulting in the change in the 2D properties. It is significant to enhance the stability of the liquid-phase-exfoliated 2D materials for the practical applications. This section is going to carry out an aging study on the $MoSe_2$/PVA thin films and their saturable absorptive behavior.

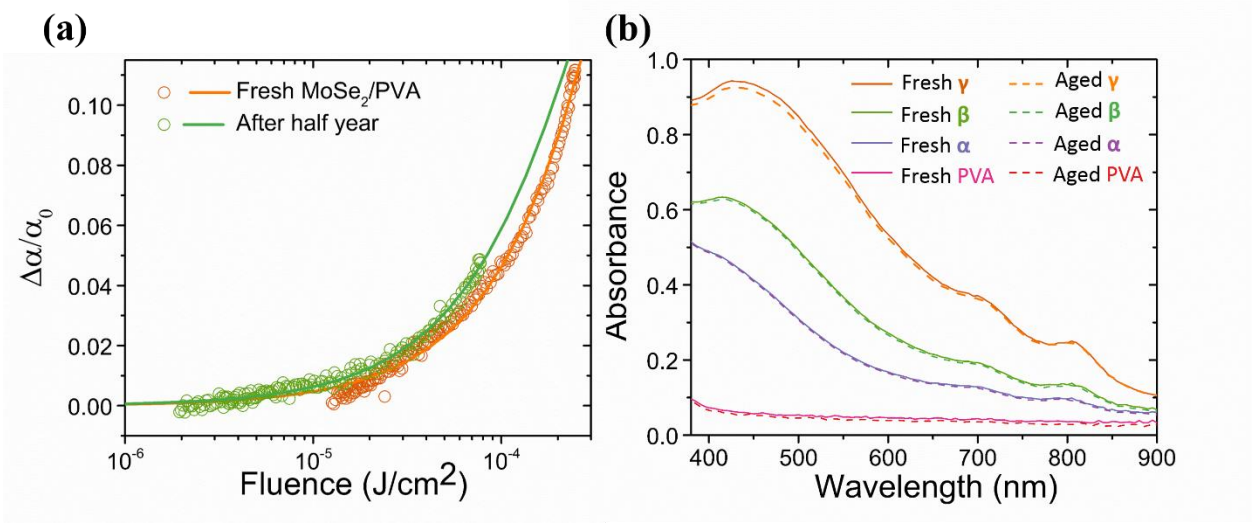

Figure 4.11. (a) The differential absorption of a fresh and corresponding aged composite thin film as a function of fluence. They are converted from the Z-scan results. The solid lines represent the Slow-absorber fitting.

In order to study the stability against time, the $MoSe_2$/PVA composite thin film was left in the air at room temperature for about half a year. No difference from the fresh one can be distinguished by eyes and one can infer that the properties of the composite thin film has not changed. For comparison in more accuracy, the stability against aging was verified by a ground-state absorption study using UV-vis spectroscopy. The UV-vis absorption of the above fresh and corresponding aged thin films (α, β and γ) are tested from 380 nm to 900 nm, which is shown in Figure 4.11(b). The absorption curves of fresh samples are plotted in solid lines and the aged ones in dash lines. It is clear that the total absorption keep stable for all thin films with different concentrations. Assume that the transmission of $MoSe_2$ single layer at the wavelength of is $T_{s\lambda}$, the total absorption, A_{total}, of a thin film with the total effective layer number of N can be expressed as:

$$A_{total} = log\frac{1}{T_{total\lambda}} = log\frac{1}{T_{s\lambda}^{N}} = -NlogT_{s\lambda} \tag{4.7}$$

Where $T_{total\lambda}$ represents the transmission of a composite thin film. As A_{total} stays almost the same for a long time and $logT_{s\lambda}$ is a constant for a certain wavelength, the total effective layer number of $MoSe_2$ monolayer stays the same. This indicates the alignment and orientation of $MoSe_2$ nanosheets inside the composites is stable for a long time. The same measurements were also carried out on a fresh pure PVA thin film and an equivalent aged one. They are also shown in Figure 4.11(b) in solid and dash lines respectively. This proves that the optical properties of pure PVA are stable for half a year. Since the absorption of the PVA from 400 nm to 900 nm is close to zero, one can claim that the absorption and nonlinear optical response of $MoSe_2$/PVA composites thin films at the wavelength range mainly originate from $MoSe_2$.

The nonlinear optical behavior of a fresh $MoSe_2$/PVA thin film was studied via an open-aperture Z-scan based on an ultrafast laser with a wavelength of 800 nm and a pulse duration of ~100 fs. Its linear transmission was measured to be 58.7%. Saturable absorption was observed at three different energies (1.0 nJ, 4.0 nJ and 10 nJ). As the increase in the energy from 1.0 nJ to 10 nJ, the transmission increased. All the Z-scan curves are symmetrical which guarantees that all the measurements were carried out at the intensity bellow the damaged threshold. These provide evidence that saturable absorption is reproducible and reliable.

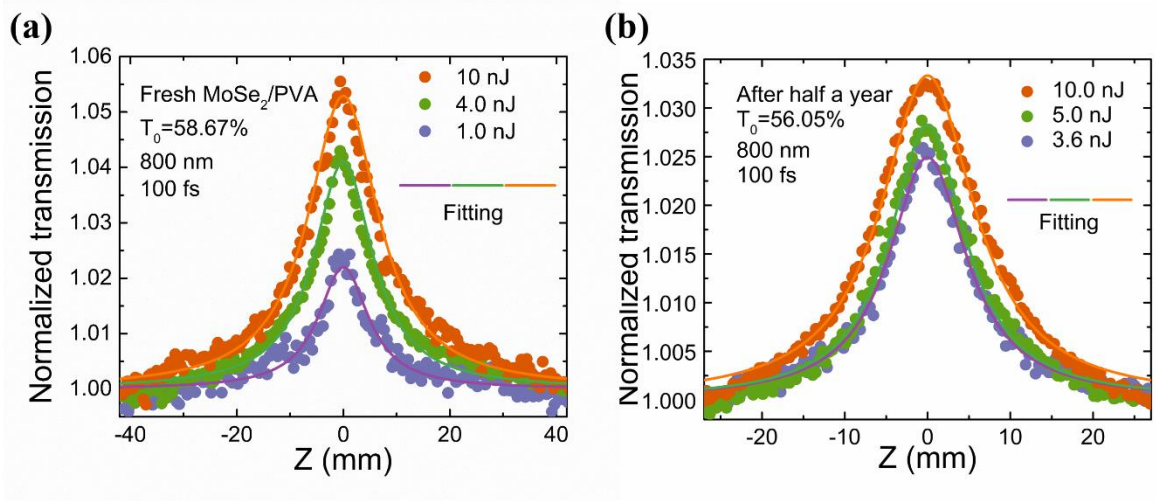

Figure 4.12. (a) Experimental and fitting Z-scan results of a fresh $MoSe_2$/PVA thin film with a linear transmission of 58.7%. (b) The same measurement and analysis on the $MoSe_2$/PVA thin film about half a year under using the same Z-scan set-up.

For comparison, the linear transmission of the aged composites thin film was measured at the same wavelength using the same method. It was 56.1%, very slightly different from that (58.7%) of the

fresh one. From the almost equivalent linear transmission, one can furtherly verify that no aggregation of 2D $MoSe_2$ flakes occurred inside the composite thin films during the six months. This agrees well with the UV-vis on both fresh and aged composite films. The slight difference might be caused by different measured points on the sample and it is totally acceptable. Most importantly, saturable absorption similar to the fresh sample was also observed on the aged thin film. This nonlinear measurements on the aged thin film were also carried out based on the same set-up using energies of 3.6 nJ, 5 nJ and 10 nJ. The measured results were shown in Figure 4.12 (b) using circle solid scatters. By converting both refresh and aged Z-scan data to the differential absorption as a function energy fluence which is seen in Figure 4.11(a), one can have an initial view that both films possess the same trend of change in the differential absorption, indicating the similar optical nonlinearity. The Z-scan modelling Equation (2.2.1) and (2.2.1) were utilized fit results of fresh and aged results. The fitting curves are plotted in Figure 4.12(a) and (b) in solid lines. The fitting results agree well with experimental results.

To give an extract view on the change, comparative linear and nonlinear optical parameters of the fresh and aged composite thin film are listed in Table 4.5. The linear absorption is 20.5 cm^{-1} for the fresh thin film and 21.7 cm^{-1} for aged one after about half a year. The slight difference are like to be the experimental error instead of variation, *i.e.*, the linear optical properties stay the same after about half a year. The nonlinear absorption was measured by Z-scan using the same laser source, which are -3.8 cm/GW for fresh sample and -1.5 cm/GW. The same order of magnitude of α_{NL} implies the stability of the nonlinear optical properties against the age.

Table 4.5. Comparative linear and nonlinear optical parameters of a fresh and aged composite thin film.

Laser pulse	Sample	T_0 (%)	α_0 (1/cm)	Energy	ω_0 (μm)	NLO	α_{NL} (cm/GW)	Im$\chi^{(3)}$ (×10^{-13}esu)	FOM (×10^{-14}esu cm)
800 nm				1 nJ	38.4	SA	-6.0	-38.0	18.6
~100 fs	Fresh	58.6	20.5	4nJ	41.8	SA	-3.3	-20.7	10.1
100 kHz				10 nJ	45.8	SA	-2.0	-12.7	6.2
	Average						-3.8	-23.8	11.6
800 nm				3.6 nJ	38.4	SA	-1.9	-11.9	5.8
~100 fs	Aged	56.1	21.7	5nJ	38.0	SA	-1.5	-9.4	4.6
100 kHz				10 nJ	42.4	SA	-1.1	-6.9	3.4
	Average						-1.5	-9.4	4.6

4.5 Carrier dynamics of $MoSe_2$/PVA thin films

The excitation carrier dynamics play a significant role in the saturable absorber used in a mode-locking pulse laser. The carrier lifetime of the saturable absorber is a key factor to limit the pulse duration. The above results have indicate the broadband SA response of $MoSe_2$/PVA thin films and this section is going to study their exited carrier behaviors via a degenerate pump-probe technique. The schematic of the degenerate pump-probe set-up based on the ultrafast laser with the wavelength of 800 nm, pulse duration of ~100 fs and repeat rate of 100 kHz is plotted in Figure 4.13. Both pump and probe beams were achieved from a 800 nm Ti:Sapphire femtosecond laser (Coherent RegA 9000). A beam splitter (~8/92) was employed to divide the initial 800 nm laser into two beams. One with relatively low intensity was delayed by a motorized linear translation stage and then used for probing. The other main beam was focused into the sample for pumping and was block by an aperture before the detector. An optical chopper was employed to modulate probe and pump beams at 422 Hz and 733 Hz respectively.

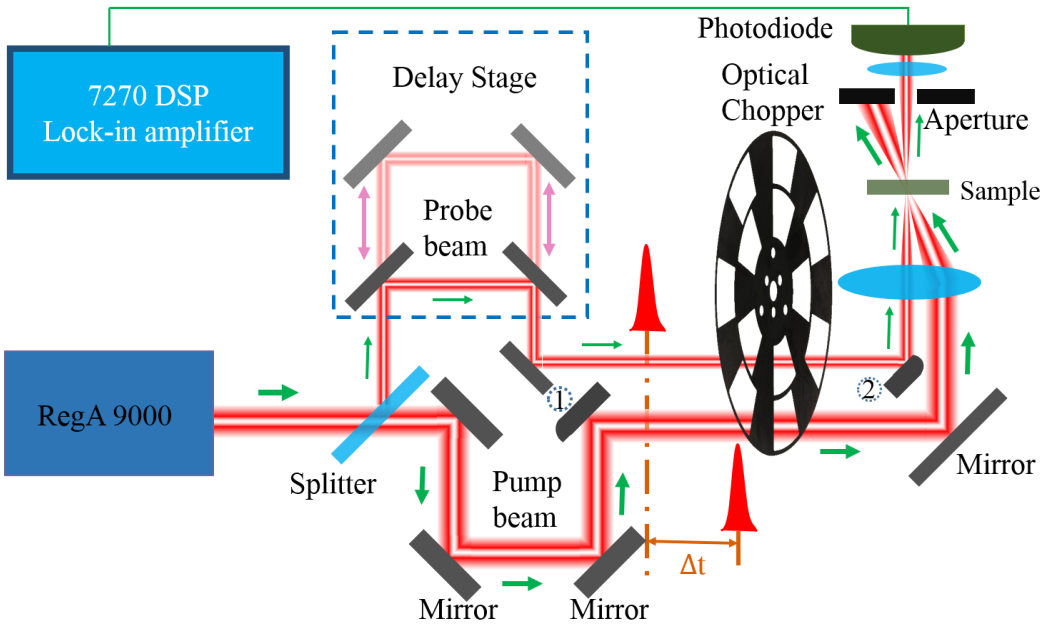

Figure 4.13. The degenerate pump-probe set-up based on a 800 nm femtosecond laser and 7270 DSP lock-in amplifier.

Based on the above pump-probe set-up, the excitation carrier dynamics of two $MoSe_2$/PVA thin film (γ, $T_{0,\ 800\ nm}$=58.7%) was investigated at the wavelength of 800 nm and the pump energy fluence spanning from 10 nJ to 80 nJ with an interval of 10 nJ. Both pump and probe pulses were obtained from the same laser source and they have a pulse duration of ~ 100 fs. Note that all the

measurements were carried out at room temperature and under the damage threshold which guarantee the validity of the experimental results. Figure 4.14 Plots the carrier dynamics traces for different pump energy fluence using solid scatters and circles with center dot in different color. Photoinduced bleaching signal (*i.e.*, positive $\Delta T/T$) were observed for all the pump energy fluence. The increase in the transmission at the early delayed time region right after excitation indicates the saturable absorption of the composites thin films due to the Pauli-blocking, which agrees the results of Z-scan that were introduced previously.

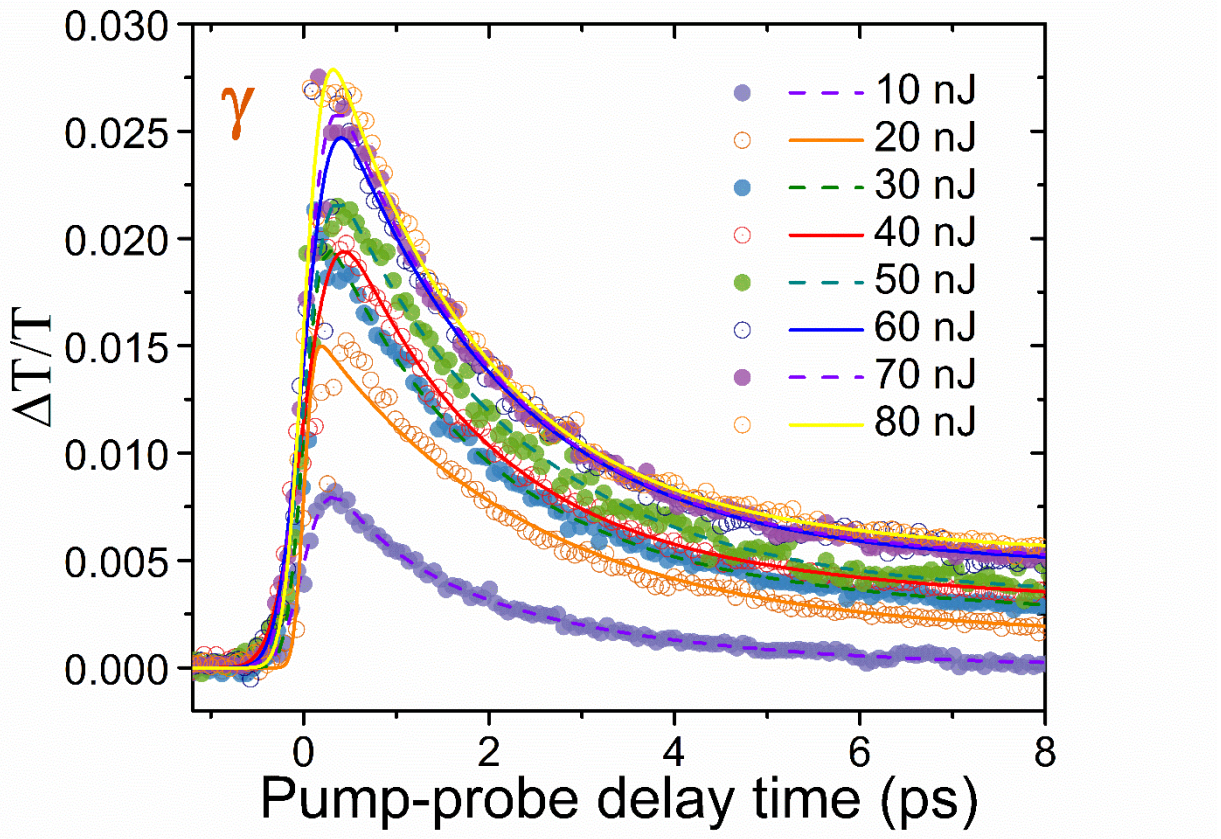

Figure 4.14. The differential transmission of $MoSe_2$/PVA thin films at different pump pulse energy is obtained from the degenerate pump-probe technique based on a 800 nm, ~100 fs and 100 kHz ultrafast laser.

From these experimental pump-probe data, we can easily see that the excited carrier of $MoSe_2$/PVA exist two exponential decay components with two characteristic carrier lifetimes. In order to figure

out the lifetime, a bi-exponential exponential decay model, *i.e.*, Equation (2.4.13), was employed to model the carrier dynamics traces:

$$g(t) = \sum_{i=1}^{N} D_i \exp\left(-\frac{t}{\tau_i}\right) erfc\left(\frac{\sigma}{\sqrt{2}\tau_i} - \frac{t}{\sqrt{2}\sigma}\right) \quad (4.8)$$

Here g(t) is equal to the differential transmission, $\Delta T/T$, and N is the number exponential decays. Therefore the bi-exponential decay model with autocorrelation to fit the pump-probe traces of $MoSe_2$/PVA thin films can be expressed as:

$$\Delta T/T = D_1 \exp\left(-\frac{t}{\tau_1}\right) erfc\left(\frac{\sigma}{\sqrt{2}\tau_1} - \frac{t}{\sqrt{2}\sigma}\right) + D_2 \exp\left(-\frac{t}{\tau_2}\right) erfc\left(\frac{\sigma}{\sqrt{2}\tau_2} - \frac{t}{\sqrt{2}\sigma}\right) \quad (4.9)$$

Where τ_1 and τ_2 ($\tau_1 < \tau_2$) represent the short and the relatively long carrier lifetime, D_1 and D_2 are the corresponding relative amplitudes, σ is the fitting laser pulse duration. To obtain a desirable fit on the experimental data, a nonlinear least-squares algorithm was employed during the modelling. The fitting results are shown in the same figure as the experimental results using solid lines and dash dot. All the fits are favorable and the fitting parameters are listed in Table 4.6.

Table 4.6.The fitting parameters obtained from the biexponential decay Equation to model pump-probe traces of $MoSe_2$/PVA.

Energy	D_1 (%)	D_2 (%)	$\boldsymbol{\tau_1}$ (ps)	$\boldsymbol{\tau_2}$ (ps)	$\boldsymbol{\sigma}$ (ps)
10 nJ	0.173	0.106	2.382	28.21	0.194
20 nJ	0.372	0.037	2.325	32.15	0.075
30 nJ	0.473	0.102	1.707	20.799	0.140
40 nJ	0.522	0.123	1.577	21.950	0.257
50 nJ	0.574	0.085	2.028	44.893	0.195
60 nJ	0.642	0.129	1.846	114.202	0.219
70 nJ	0.666	0.131	1.798	55.129	0.197
80 nJ	0.686	0.155	1.666	62.734	0.163
Average	0.513	0.108	1.916	47.508	0.180

Both the fitting values of D_1 and D_2 at all the pump fluence energy are in the same order of magnitude with average values of 0.5% and 0.1%. This also confirms the validity of the fittings. The average values of τ_1 and τ_2 were fitted to be 1.9 ps and 47.5 ps respectively. It should be pointed out that neither the short time part nor the long-time part of the relaxation process gives obvious independence on the pump fluence.

4.6 Exciton-exciton annihilation

Many studies on carrier dynamics have indicated that the relaxation rate of the excited carrier is helpful to understand the recombination mechanisms.[125, 196, 197] To develop a clear insight into the recombination processes, the recovery traces of the photoinduced carrier from excited states to the valence band are commonly described by a three-term rate equation:[150, 196, 197]

$$-dn/dt = \alpha n + \beta n^2 + \gamma n^3 \quad (4.10)$$

Where n is the excited carrier density and t is the relaxation time. α, β and γ are constants. The first, second and third terms in the right-hand side of the equation represent first-order Shockley-Read-Hall (SRH) recombination, free-carrier recombination/exciton-exciton annihilation and Auger recombination respectively.[150, 197] By employing this rate equation to study the experimental data, one is able to figure out relaxation process of the excitation carrier.

SRH recombination is also called trap state-mediated recombination which assumes an extra level between the exited state and the ground state.[73] The hot carrier would relax to the trap state before to the ground state. In a case which is dominated by SRH recombination, the rate equation can be obtained by eliminating the second- and third-order term:

$$-dn/dt = \alpha n \quad (4.11)$$

Similarly, a rate equation that is obtained from Equation (4.10) to describe the free-carrier recombination or exciton-exciton annihilation can be written as:[125, 150]

$$-dn/dt = \beta n^2 \quad (4.12)$$

In Auger recombination, the excited electrons recombine with the corresponding holes and release energy that is transferred to another electron in the conduction band. This results higher energy of the electron in question. Therefore, Auger recombination is a three-body behavior and related to the third-order term of Equation (4.10). In the configuration where Auger recombination dominates the carrier relaxation, the rate equation can be expressed as:

$$-dn/dt = \gamma n^3 \quad (4.13)$$

In the experiments, one can directly measure the pump energy instead of carrier density. To correlate the pump energy to the initial carrier density, one can employ the equation:

$$n_0 = j\alpha_0 \quad (4.14)$$

Here α_0 is the absorption coefficient of the $MoSe_2$/PVA composites thin films and j represents the pump photon fluence whose unit is photon per square centimeter, *i.e.*, photon/cm^2. Since the energy of a single photon, E_0, is equal to $h\frac{c}{\lambda}$, the pump photon fluence can be calculated via the rate equation:

$$j = \frac{F}{E_0} = \frac{\lambda I}{w_0^2 \pi h c} \tag{4.15}$$

Where F is the pump energy fluence, I is the pump intensity and w_0 is the beast waist which have been obtained from the above Z-scan experiments, see Table 4.4. Based one Equation (4.14) and (4.15), one can calculate the initial excited carrier density. Furtherly, a bridge linking the excited carrier density and the different transmission is needed to build to study the relationship between carrier density and pump-probe decay time. According to Equation (2.5.14): $\Delta OD = -log(e) \cdot \frac{\Delta T}{T}$ and the definition of the differential optical density: $\Delta OD = A(\lambda, t)_p - A(\lambda, t)_0$, the differential transmission can be expressed as:

$$\frac{\Delta T}{T} = -\frac{\Delta \mathrm{A}}{log(e)} \tag{4.16}$$

A phenomenological expression to describe the maximum differential absorption as a function of the pump photon fluence can be written as[196, 198]

$$\left[\frac{\Delta A}{A}\right]_{max} = \frac{\delta n_0}{\zeta + n_0^{\eta}} \tag{4.17}$$

Here, δ, ζ and η are fitting parameters, which are constants for a certain sample. Since the absorbance A of a certain sample at a wavelength is a constant, $\frac{\Delta T}{T}$ can be expressed as follow after a simple derivation from Equation (4.16) and (4.17):

$$\left[\frac{\Delta T}{T}\right]_{max} = \frac{\varepsilon n_0}{\zeta + n_0^{\eta}} \tag{4.18}$$

Where $\varepsilon = -\frac{\delta A_{max}}{log(e)}$ is a fitting parameter. This expression builds a relationship between $\Delta T/T$ and excited carrier density. The pump-probe traces in Figure 4.14 show that the maximum differential transmission increases continuously from ~0.8% to ~2.8% as the pump energy fluence increases from 10 nJ to 80 nJ. The pump energy fluence can be converted to pump photon fluence through Equation (4.14) and (4.15). As a result, the experimental $[\Delta T/T]_{max}$ versus the initial photoinduced carrier density can be obtained, which was plot in Figure 4.15. (a) using solid

hexagon scatters. By employing Equation (4.18) to model the experimental data, the fitting parameter, ε, ζ and η, can be achieved. The modelling result was plotted in 4.13 using solid line, indicating a favorable fit with the experimental results. After having the fitting parameter, ε, ζ and η, the differential transmission as a function of excited carrier density at the pump-probe delay time, t, can be expressed as:

$$\frac{\Delta T}{T}(t) = \frac{\varepsilon n_t}{\zeta + n_t^{\eta}} \tag{4.19}$$

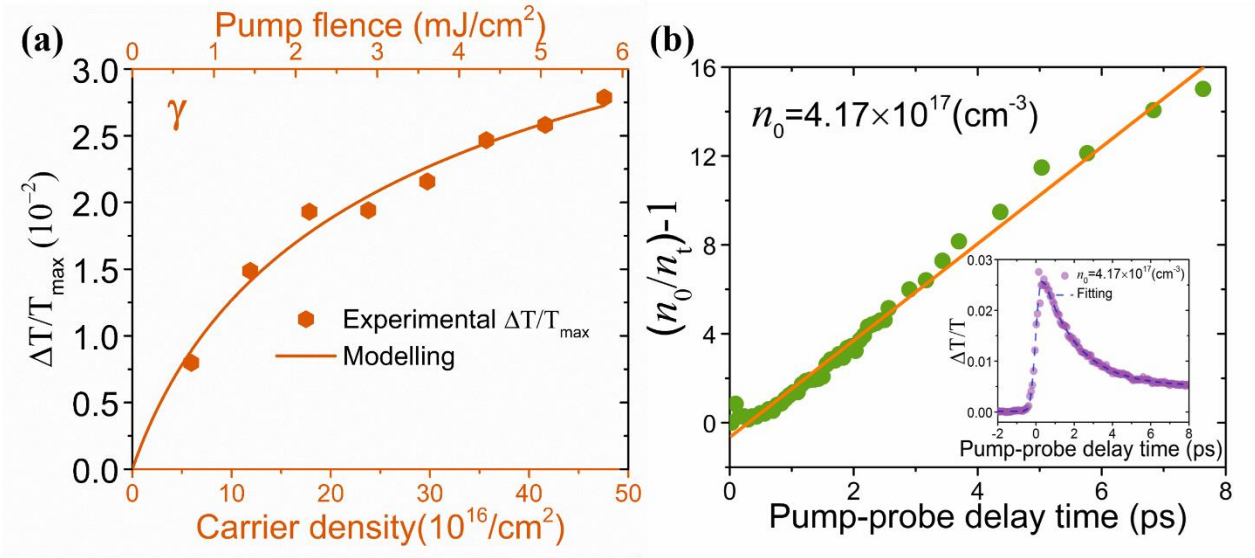

Figure 4.15. (a) Maximum differential transmission as a function of initial photoinduced carrier density. It is modelled by Equation (4.15). (b) $n_0/n_t - 1$ as a function of the pump-probe delay time at initial photoinduced carrier density, n_0, of 4.17×10^{17} cm^{-3}. The inset is the corresponding carrier dynamics trace.

Based on Equation (4.19), one can convert the differential transmission at t to photoinduced carrier density, n_t, and hence obtain n_t as a function of t from initial pump-probe traces. The inset of Figure 4.15(b) shows a measured pump-probe trace of $MoSe_2$/PVA composites thin film with an initial excited photons of 4.17×10^{17} cm^{-3}. By employing Equation (4.19) to transform the differential transmission as to the excited carrier density, the mechanism of recombination of excited carrier in $MoSe_2$/PVA can be investigated via the rate equation. To qualify if it was dominated by second-order kinetics, Equation (4.12), *i.e.*, $-dn/dt = \beta n^2$, was employed to analyze the converted data. By assuming the numbers of the photoinduced electrons and holes are equivalent and using an integral on this equation, the rate equation to describe a second-order carrier dynamics can be achieved as:[125, 150, 196, 197]

$$\frac{n_0}{n_t} - 1 = \upsilon n_0 t \quad (4.20)$$

Here υ is the second-order recombination rate constant. The experimental $[n_0/n_t - 1]$ as a function of the pump-probe delay time at initial photoinduced carrier density of 4.17×10^{17} cm^{-3} are plotted Figure 4.15(b) using green solid circle scatters. From the experimental data, $[n_0/n_t - 1]$ is proportional to the pump-probe delay time. This agrees with the rate equation of the second-order carrier dynamics. As no photoluminescence was observed from the few-layer, here I exclude the free-carrier recombination. Consequently, this second-order recombination can be attributed to exciton-exciton annihilation. From linear fit from Equation (4.20) to the converted excited carrier density, see the solid line in Figure 4.15(b), the exciton-exciton annihilation rate was obtained to be $(5.22 \pm 0.089) \times 10^{-6}$ cm^3/s.

4.7 Conclusion

In summary for this chapter, a comparative study on the dependence of NLO properties of $MoSe_2$/PVA composites on laser wavelength, pulse duration, linear absorption and aging was carried out systematically. The NOL study was carried out by the open-aperture Z-scan technique with laser pulses with a 6 ns duration at the center wavelength of 532 nm and ~ 100 femtosecond laser pulses at the wavelength of 400 nm, 500 nm and 800 nm. 400 nm and 500 nm. The $MoSe_2$/PVA thin films possess broadband saturable absorption behavior in a wavelength region from 400 nm to 800 nm under femtosecond, and nanosecond pulses. This saturable absorption is stronger in a composite thin film with higher linear absorption. An aging study shows that the embodiment of liquid-phase-exfoliated $MoSe_2$ within a host material, *i.e.*, PVA, is helpful for improving the stability of the 2D nanosheets. Exciton-exciton annihilation was observed by the pump-probe study on the relationship between excitation carrier density and the pump-probe delay time at the wavelength of 800 nm, and their annihilation rate was obtained to be $(5.22 \pm 0.089) \times 10^{-6}$ cm^3/s. This agrees with the ground-state absorption study on the composite thin films from the UV-vis spectroscopy.

5. NOL performance of a GSAM in the mid-infrared region

Benefiting from the inherent advantages of large core-size and an eye-safe spectrum, ultrafast fibre lasers operating at 2 μm have the potential to possess higher raw power than the 1 μm technology and are becoming a promising platform for laser manufacturing, optical medical procedure, free-space telecommunications and optical sensing.[199-205] Moreover, ultrafast 2 μm lasers have potential as a pump source that can efficiently generate infrared femtosecond pulses beyond 5 μm via optical parametric process. This can overcome the power limitation of current difference-frequency generation technology. To obtain ultrashort pulses, a mode-locking element must be introduced into the laser cavity.[200] The most common mode-locking technology are based on semiconductor saturable absorber mirrors (SESAMs), which are fabricated via complicated epitaxial deposition[206]. Such devices suffer from narrow operating wavelengths (<100 nm), slow-relaxation time, difficult fabrication and high-cost.[206] Additionally, as the wavelength goes beyond 3 μm, unconventional semiconductors are needed and further fabrication difficulties arise for SESAMs.[207] It is these limitations that have bottlenecked the development of high power, high repetition rate and stable ultrafast mid-infrared laser sources.

Due to the tuneable bandgap, 2D materials have emerged as promising materials for passive mode-locking in fibre laser system due to their broadband saturable absorption and ultrafast carrier relaxations.[60, 62, 178, 195, 204, 207-212] Widely-tuneable or multiple wavelength ultrafast laser sources can also be envisioned with the help of 2D material saturable absorbers.[213] Although a variety of works have reported on the success of mode-locking with 2D materials including transition metal dichalcogenides (TMDs) and phosphorene,[51, 208, 211, 212, 214-218] pure graphene is still irreplaceable at 2 μm range and above due to the zero bandgap and thermal stability.[24, 214, 219-227] While most investigations have focused on verifying the feasibility of mode-locking by 2D materials, only few have reported the nonlinear absorptive properties of the as-fabricated graphene saturable absorber mirror (GSAM).[29, 207, 209, 228-232] Particularly missing is a systematic comparison with the commercial SESAM at 2 μm.

To address this gap, a multi-layer GSAM was fabricated via liquid phase exfoliation dispersion of graphene using vacuum filtration and measured the nonlinear optical properties utilizing I-scan and pump-probe techniques with a 2 μm femtosecond laser in this chapter. The carrier absorptive cross-sections were obtained by a slow-absorber-mirror model modified from the Frantz-Nodvik equation. A commercial SESAM designed for 2 μm with similar linear optical reflection was compared with the GSAM. The results directly show the significant advantages of graphene with ~28% less absorptive cross-section ratio of excited-state to ground-state σ_e/σ_g and ~50 times faster carrier relaxation time to the commercial SESAM. These advantages make graphene a promising material for next generation mid-infrared mode-lockers, which can be used to fabricate saturable mirror with much better modulation depth, non-saturable loss and recovery time than the current commercial SESAM.

5.1 Fabrication of the GSAM

The large-area GSAM was fabricated by vacuum filtration methods using liquid-phase exfoliated graphene nanoflakes.[50, 233, 234] Graphite powder (Sigma Aldrich) was exfoliated in distilled water (5 mg/mL) by liquid-phase exfoliation with sodium cholate (0.1 mg/mL) utilised as surfactant. The dispersion was centrifuged at 3000 rpm to remove large flakes. After this, a graphene membrane was fabricated from vacuum filtration of the graphene dispersion using a nitrocellulose porous membrane (Millipore, Φ_m = 100 nm). The wet membrane was then attached onto a silver mirror (Thorlabs, PF05-03-P01) with a 1 kg weight applied for 12 hours to ensure firm contact between the nanoflakes and the mirror. Finally, the nitrocellulose membrane was removed from the GSAM surface using acetone. After which the GSAM was ready for characterization. Figure 5.1 (a) presents the optical image of the as-fabricated GSAM, showing a large high-quality graphene film on the surface of the silver mirror. The comparative SESAM was purchased from BATOP (SAM-2000-44-10ps, see Figure 5.1(c). The nominal working wavelength, absorption and relaxation time are 2000 nm, 44%, and 10 ps respectively.

To furtherly investigate the geometry of the fabricated GSAM, scanning electron microscopy (SEM) and atomic force microscopy (AFM) were employed. Figure 5.1 (b) shows a low magnification SEM image on the GSAM. The clear boundary of graphene on the mirror and flat surface implies a homogeneous deposition. As it went to higher magnification in Figure 5.1 (d), the graphene film was found to be consist of many small graphene flakes around ~500 nm size.

Figure 5.1 (e) shows an AFM image of a 10 μm × 10 μm area. Most area has a height variation below 100 nm (dark colour), while the others with large height is presented in bright (>240 nm). From AFM measurements, a surface roughness, R_a, of the fabricated GSAM was obtained to be 57.42 nm. Raman spectroscopy is a useful way to investigate thickness of graphene nanoflakes. With the thickness increasing from monolayer, to bilayer, to bulk, the 2D peak shifts from ~2680, ~2700 to ~2720 cm^{-1} respectively.[235] Figure 5.1 (g) shows the mapping of 2D peak using 514 nm excitation. The blue area (> 2700 cm^{-1}) represents multi-layer flakes, whereas the red (< 2700 cm^{-1}) indicates the mono- and bi-layers. It is revealed that the graphene film is composed of mixture of monolayers and few-layers. Mono- and bi-layer flakes cover the most area in the mapping. To investigate the average thickness of the graphene film, the Raman spectra of a large area 200 μm × 100 μm was averaged, which is presented in Figure 5.1 (f). The G and 2D peaks were found at 1580.3 and 2695.6 cm^{-1} respectively. This corresponds to an average thickness of ~1.7 layers of graphene flakes composing the graphene film.

As predicted by the GSAM optical image as well as the AFM roughness in Figure 5.1(a) and (e), unneglectable surface scattering may exist on the fabricated GSAM. To subtract the effect of scattering from the NLO parameters, the surface scattering was measured by a UV-Vis-NIR spectrophotometer equipped with an integrating sphere. Figure 5.6 (a) presented the reflection, scattering and the absorption of the GSAM from 1.6 μm to 2.4 μm. The solid lines are linear fittings as a visual guide. The exact values of scattering, linear reflection and absorption at 2 μm for the GSAM are determined to be 13.8%, 65.3% and 20.9% respectively. With the absorption of monolayer graphene equal to ~2.3%, the average number of layers on the GSAM sample was estimated to be ~5 when considering light passes twice through the graphene film.[236]

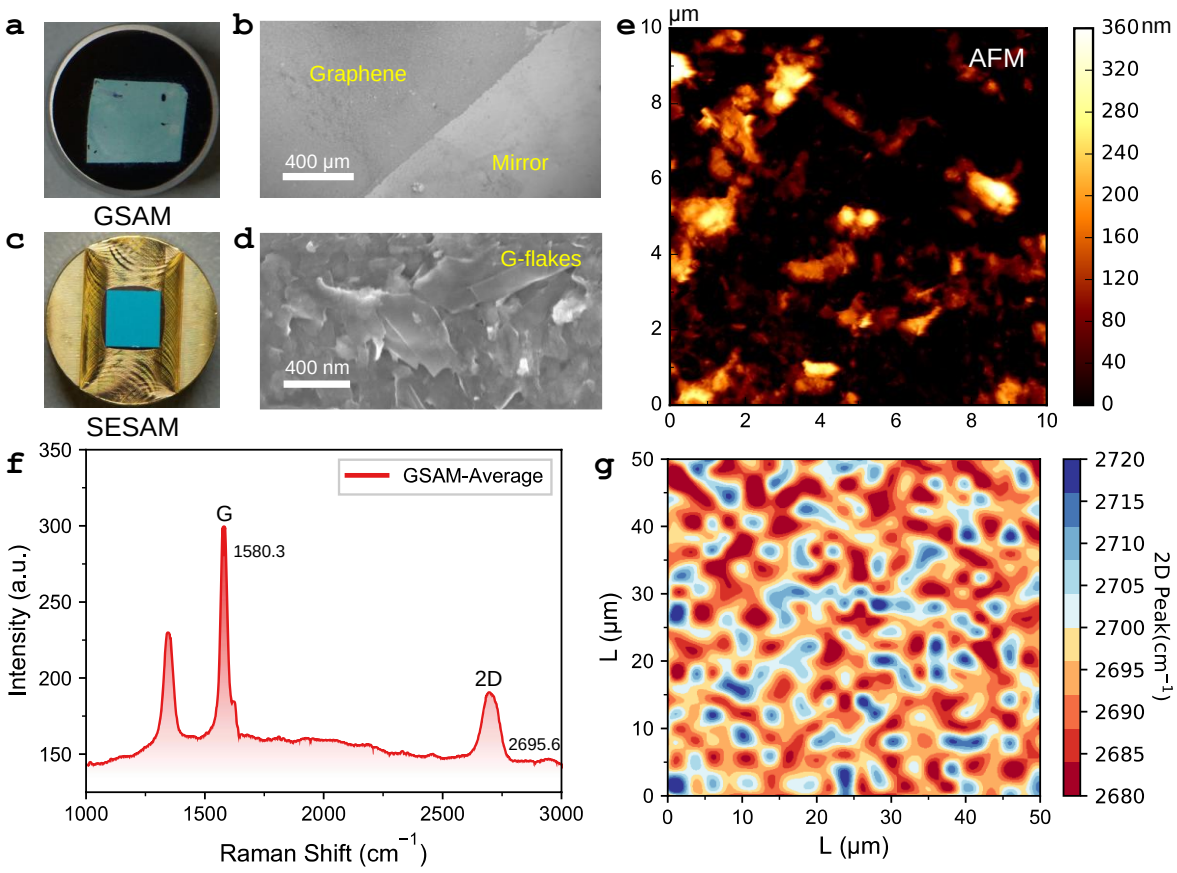

Figure 5.1 Characterizations of graphene saturable mirror (GSAM). The GSAM image taken by camera (a), low magnification SEM (b) and higher one (d). The commercial SESAM (BATOP, SAM-2000-44-10ps) for comparison is showed in (c). (e)AFM image of graphene film on GSAM. (f) is the average Raman spectra from a 200 μm × 100 μm Raman mapping of the graphene film. (g) Raman mapping representing the shift of the graphene 2D peak. The blue area (> 2700 cm^{-1}) represents multi-layer flakes, whereas the red (< 2700 cm^{-1}) indicates the mono- and bi-layers.

5.2 Methods of NLO Characterization

The ultrafast mid-infrared laser pulses (2 μm, 100 kHz, ~150 fs) for nonlinear-optical (NLO) measurements were generated by an optical parametric amplifier (Coherent OPA9800) pumped by a 800 nm Ti:Sapphire femtosecond laser (Coherent RegA 9000). The 2 μm laser wavelength was confirmed by a spectrometer (Ocean Optics, NIR Quest).

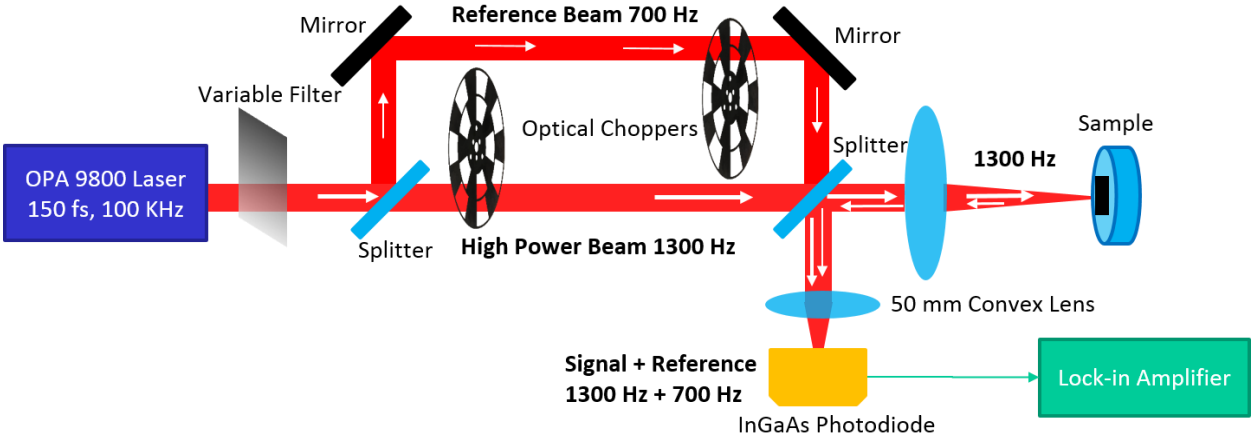

Figure 5.2 Reflective I-scan Scheme using a single photodiode. The lock-in amplifier works in a two references mode which can measure the signal and reference simultaneously.

The NLO responses were characterised by reflective I-scan technique, whose set-up schematic can be seen in Figure 5.2. The femtosecond beam power was controlled by a variable filter which was installed on a linear motorised translation stage. Then it was split into one main beam and another reference beam. Both beams were modulated by two optical choppers with different frequencies, *i.e.*, the reference beam was modulated at 700 Hz while high power beam was chopped at 1300 Hz. A convex lens was used to focus the main beam and collect the reflective light simultaneously. The sample was placed at the focal point of the lens. The reflected back signal and reference beam were combined by a beam splitter and direct onto a single 3 mm diameter InGaAs photodiode. A two-channel lock-in amplifier (Signal Recovery, SR7270) was employed to collect both the reflected and reference signal. The beam diameter was measured using a razor blade controlled by a motorised stage. By moving the razor blade, a function of laser power versus position of the blade was obtained, see Figure 5.3 (a). The beam profile was then obtained after applying a 1^{st}-order differential to these data points, as seen in Figure 5.3 (b).

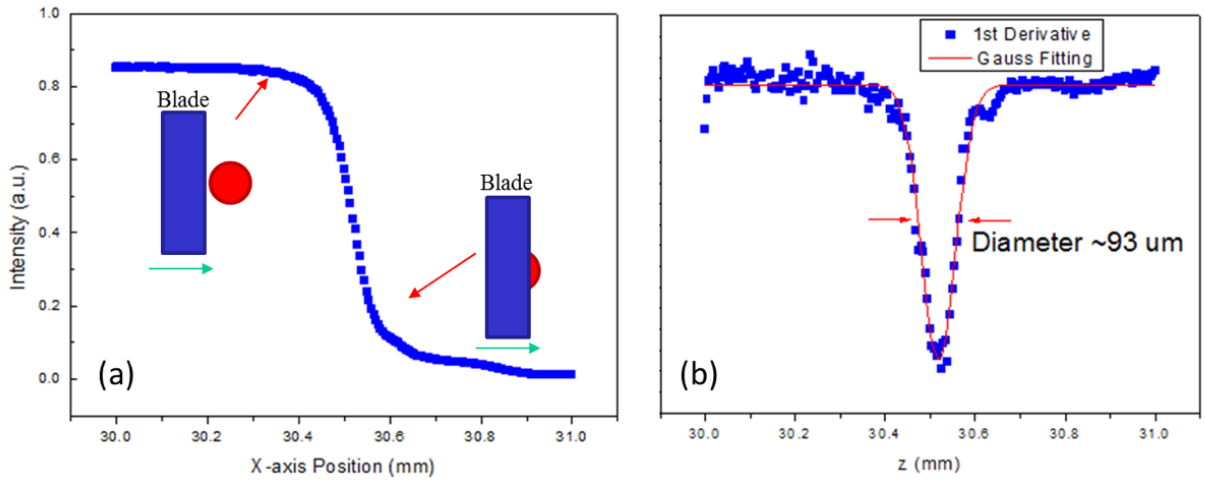

Figure 5.3 Experimental curve about beam-size measurement for I-scan. (a) The laser power as a function of the distance of blade position. (b) the result after applying 1st-order differential on (a). Solid lines: The Gaussian fitting.

A reflective degenerate pump-probe technique was utilized to study the carrier dynamics. The 2 μm femtosecond beam was split into one main pump beam and another probe (8%) one, as seen in Figure 5.4. Both beams were modulated using an optical chopper with frequencies of 733 Hz and 442 Hz respectively. The probe beam was delayed by a computer controlled linear stage. Then the pump and probe beams were combined non-collinearly and parallel incident into a convex lens (f = 10 cm). The pump and probe beams overlapped at the focal point of the lens, where the sample was placed. The reflected probe was then collimated by the convex lens and sent to an InGaAs photodiode while the reflected pump was stopped before the detector by an aperture. The amplitude of the sum frequency of pump and probe beam (1175 Hz) was measured by a lock-in amplifier. The polarisations of both beams were kept linear and horizontal in all measurements.

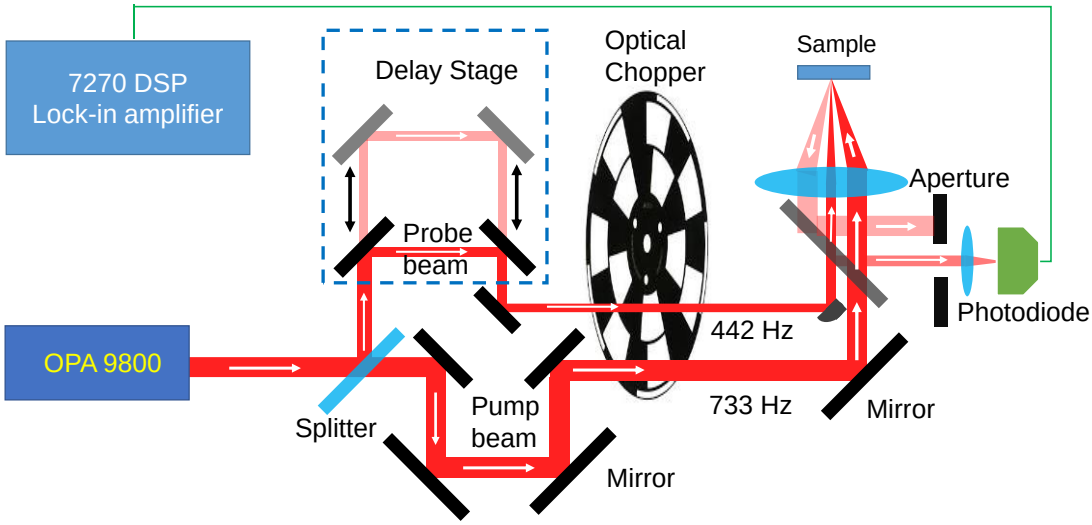

Figure 5.4 Pump-probe Scheme. The lock-in amplifier measures the sum frequency of pump and probe pulses (1175 Hz).

It should be noticed that the probe beam had a smaller probe spot size than that of the pump beam in the measurements, as seen in Figure 5.5.

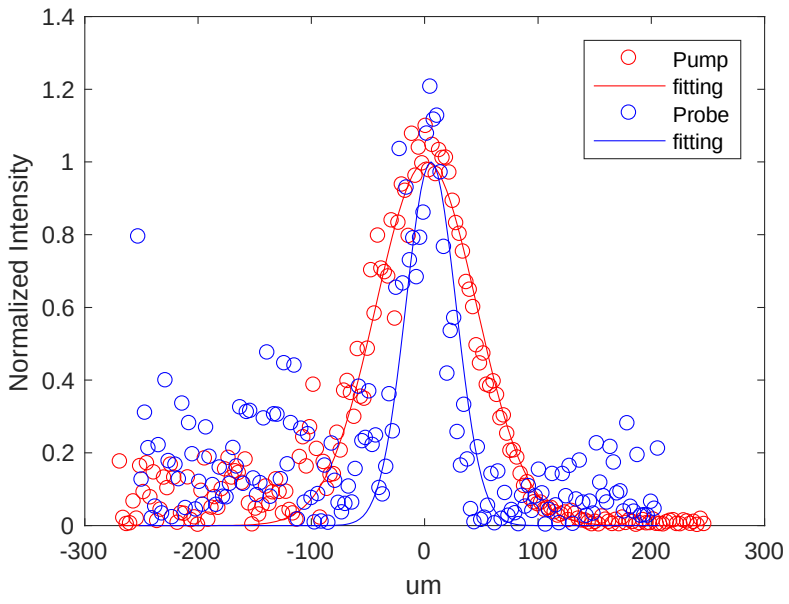

Figure 5.5 Beam profile measurements of pump and probe pulse on the focal plane of the focusing lens. Scatters are normalized experimental curves and solid lines are fitting results by a Gaussian function.

5.3 NOL response of the GSAM

The reflective I-scan technique was utilized to measure the nonlinear response of the GSAM and the SESAM with 2 μm femtosecond pulses. (~150 fs, 100 kHz, see Figure 5.1). The primary technique involves placing the sample on the focus of a convex lens to obtain high laser intensity. By changing the incident laser intensity with a variable filter, the sample transmission or reflection as a function of laser intensity can be measured. In one I-scan measurement, the laser spot is focused at a single position of the sample. This gives I-scan the obvious advantage of avoiding the noise created by moving samples when comparing to similar NLO techniques, such as Z-scan. A blank mirror was also measured throughout all optical experiments. The blank mirror gave no nonlinear responses during the measurements. To calculate the power intensity for the I-scan, the laser beam diameter on the sample surface was measured to be 93.5 ± 1.7 μm. (See Figure 5.3)

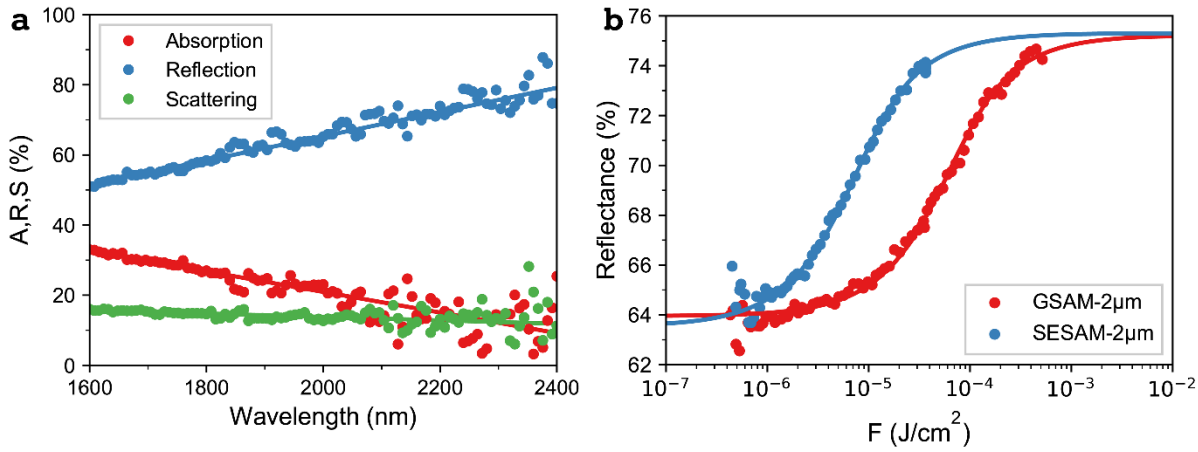

Figure 5.6. Optical responses of graphene saturable absorber mirror. (a) Absorption, reflection and scattering responses of the GSAM with a wavelength range from 1.6 to 2.4 μm using an integrating sphere. The scattering at 2 μm is shown be 13.8 % for GSAM. Solid lines are for visual guide. (b) Scatters represent the nonlinear reflectance of GSAM and SESAM as a function of laser fluence with 2 μm 100 fs pulses. Solid Lines show the fitting curves by a slow-absorber model with nonlinear regression algorithm.

Figure 5.6 (b) presents the experimental I-scan curve of GSAM and SESAM. Both samples exhibited typical saturable absorption behavior, *i.e.*, reflectance increasing with incident laser power. To further analyse the NLO response of the samples, a modified slow-absorber model was employed to fit the results. (Equation (5.2)) The fitting curves are presented in solid lines in Figure 5.6 (b), displaying a favourable fit with experimental results. Both samples showed very similar linear reflectivity, R_0, of~ 64%, maximum reflectivity, R_{max}, of ~76% and a modulation depth, ΔR,

of ~13%. Note that the R_0 value of the GSAM obtained via I-scan, 63.7%, approximates to the 65.3% that was got from integrating sphere, which implies strong coherence of the measurements. The saturated fluence, F_s, is defined as the laser intensity when a saturable absorber reaches its half modulation depth. The measurements revealed a saturated fluence at 52.4 and 6.9 μJ/cm^2 for the GSAM and the commercial SESAM respectively. These correspond to saturated intensities, I_s, of 349.3 and 46.0 MW/cm^2 respectively. All parameters are summarised in Table 5.1. The I-scan results imply the GSAM has a comparable performance to the SESAM at 2 μm wavelength except for the F_s value. However, it should be noted that the GSAM has a much broader wavelength response. During measurements, it is observed that even a small wavelength drift to 1.9 μm eliminated the saturable absorption response of the commercial SESAM. Furthermore, if the surface roughness can be reduced for graphene films, then GSAMs have excellent potential to outperform standard SESAM designs.

Table 5.1 Parameters of the GSAM and SESAM obtained via I-scan measurements. R_0, R_{max} and ΔR denote for the linear reflectivity, maximum reflectivity and modulation depth respectively. A_0 and A_{ns} are the linear and non-saturable absorption respectively. S is the scattering loss caused by the surface roughness.

Sample	R_0(%)	R_{max}(%)	ΔR(%)	A_0(%)	A_{ns}(%)	S(%)	F_s (μJ/cm^2)
GSAM	63.7	76.3	12.6	20.9	9.9	13.8	52.4
SESAM	63.6	76.8	13.2	36.4	23.2	-	6.9

5.4 Carrier dynamics of the GSAM

Carrier dynamics play a pivotal role in the NLO response of saturable absorbers. Degenerate pump-probe measurements were carried out on the GSAM and the SESAM using reflection geometry. Both the pump and the probe pulses were at 2 μm or 800 nm with linear and horizontal polarisation. Figure 5.7 (a) and (b) present the GSAM differential reflectivity, ΔR/R, as a function of probe delayed time t with 2 μm and 800 nm wavelength pulses respectively. The variations around zero delay are believed to be due to the coherent artefact. [237] As shown in Figure 5.7 (a) and (b), the GSAM exhibited typical saturable absorption from 800 nm to 2 μm, *i.e.*, the reflectivity immediately increased after pump pulse excitations. I also measured the SESAM for comparison at 2 μm in Figure 5.7(c). To get the excited carrier lifetime, a two-exponential model with autocorrelations was utilized to fit the experimental results: [238]

$$\frac{\Delta R}{R} = \left\{ D_1 \exp\left(-\frac{t}{\tau_1}\right) \operatorname{erfc}\left(\frac{\sigma}{\sqrt{2}\tau_1} - \frac{t}{\sqrt{2}\sigma}\right) + D_2 \exp\left(-\frac{t}{\tau_2}\right) \operatorname{erfc}\left(\frac{\sigma}{\sqrt{2}\tau_2} - \frac{t}{\sqrt{2}\sigma}\right) \right\} \quad (5.1)$$

where t is delayed time, D_1 and D_1 are relative amplitudes, τ_1 and τ_2 are two relaxation times, 'erfc' represents the integral error function and σ is the laser pulse duration. All fitted pump-probe curves are presented as the solid lines in Figure 5.7, displaying a favourable fit to the experimental results. The fitting parameters and carrier lifetimes are summarized in Table 5.2.

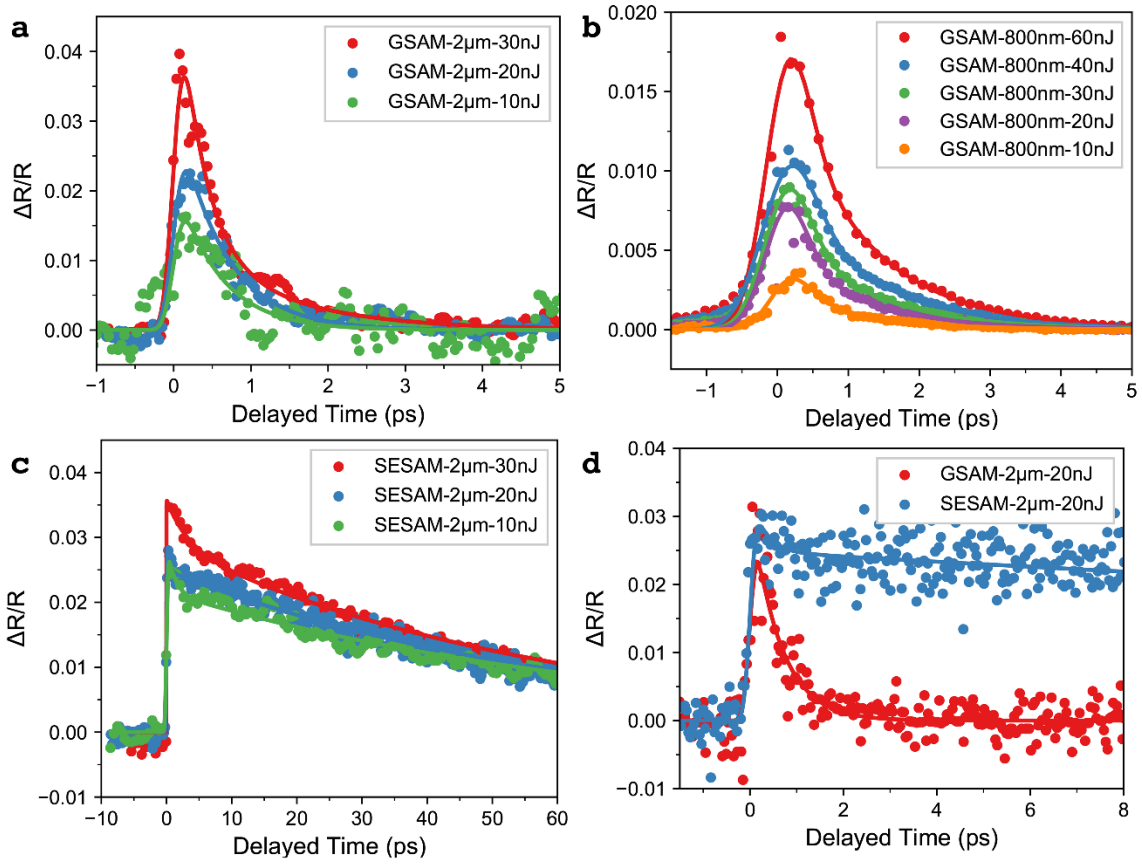

Figure 5.7 Time-dependent reflectivity of the GSAM and the commercial SESAM with fs pulses excitation (~150 fs, 100 kHz). 1 nJ corresponds to the laser fluence of ~0.106 mJ/cm^2 and ~12.0 μJ/cm^2 for 800 nm and 2 μm respectively. All scatters are from experiments while solid lines are fitting results using a two-exponential model. (a)-(b) GSAM differential reflectivity as a function of delayed time measured at 2 μm and 800 nm. (c) The same measurements from SESAM at 2 μm. (d) Comparison of the GSAM and the SESAM up to 8 ps delay time, where the carrier life-time in GSAM and SESAM were measured to be 1.2 and 63 ps respectively. The polarization of the pump and probe are linear and in the same direction.

From the measurements, the carrier relaxations of GSAM are seen to be very fast, *i.e.*, τ_2 is 1.15 ps for 800 nm and 1.19 ps for 2 μm. These agree well with previous reports in liquid-phase exfoliated dispersions.[60] However, the SESAM carrier relaxation, τ_2, is slower at ~63 ps for 2 μm pulses, which is significantly longer than GSAM. This becomes more obvious when comparing the GSAM and the SESAM curves together in Figure 5.7 (d), where the GSAM recovered within 3 ps whereas

the SESAM seemed to be unchanged even after 8 ps. The results imply that the GSAM is significantly faster as a saturable absorber than the commercial SESAM at 2 μm wavelength.

Table 5.2 Fitting Parameters for time-dependent reflectivity measurements of the GSAM and SESAM using Equation 5.1. E is the laser pulse energy. D_1 and D_2 are relative amplitudes. τ_1 and τ_2 represent the carrier relaxation times. The long part of carrier relaxation τ_2 at 2 μm is measured to be 1.19 ps in the GSAM, much faster than that 63 ps in the commercial SESAM.

λ (nm)	Sample	E (nJ)	F (mJ/cm^2)	D_1 (%)	D_2 (%)	τ_1(ps)	τ_2(ps)	Pulse Width (ps)
800	GSAM	10	1.06	0.276	0.161	0.193	1.036	0.255
	GSAM	20	2.12	14.070	0.338	0.093	1.063	0.288
	GSAM	30	3.18	16.644	0.378	0.102	1.141	0.312
	GSAM	40	4.24	20.135	0.517	0.115	1.224	0.367
	GSAM	60	6.36	27.267	0.795	0.107	1.269	0.329
	Average					0.122	1.1466	0.310
2000	SESAM	10	0.12	0.109	1.091	1.083	67.14	0.259
	SESAM	20	0.24	0.023	1.252	1.011	64.02	0.104
	SESAM	30	0.36	0.130	1.500	1.233	57.85	0.110
	Average					1.109	63.00	0.158
2000	GSAM	10	0.12	1.397	0.751	0.091	1.397	0.274
	GSAM	20	0.24	1.744	0.910	0.159	0.996	0.155
	GSAM	30	0.36	2.143	0.866	0.253	1.177	0.096
	Average			0.276	0.161	0.168	1.190	0.175

In Table 5.2, the short part, τ_1, of the GSAM and SESAM was determined to be 168 fs and 1.11 ps respectively at 2 μm wavelength. This process may be explained by carrier-carrier scattering after laser excitation.[63, 239, 240] The long part of SESAM carrier relaxation, τ_2, was measured to be ~63.0 ps while that of GSAM was only ~1.19 ps. This implies that the GSAM is a much faster saturable absorber than the commercial SESAM. The observed τ_2 values were attributed to carrier-photon scattering.[63, 239, 240]

Faster carrier relaxation times means that the absorber can recover from 'bleached' with less time. This recovery time is very important for determining the laser pulse-duration when it works as a mode-locker. It is known that the saturable absorber has two modes when they are used as passive mode-locker, *i.e.*, fast and slow mode-locking,.[233] In the fast-absorber mode locking, the absorber recover time is about equal to the output laser pulse duration. Even in a slow-absorber mode-locking, the minimum pulse duration is still limited to ~τ_p/30, where τ_p is absorber recovery time.[28] Because the carrier-photon scattering process is strong and slow as shown in Figure 5.7, τ_2 was taken as absorber recovery time τ_p. Thus, the pulse duration limit is ~2 ps for SESAM and

~37 fs for graphene, showcasing the advantage of utilising graphene in producing ultrafast pulses <100 fs.

5.5 GSAM as a slow-absorber

Because the carrier decay lifetimes of the GSAM and the commercial SESAM (1.19 ps and 63 ps) are much longer than the laser pulse width (~0.15 ps) in Figure 5.7, both samples can be treated as slow-absorbers. Note that the slow-absorber model is still very useful for real mode-locking application, in which the saturable absorber interacts with several-hundred-fs pulses. The response of a slow-absorber, achieved with a modified Frantz-Nodvik solution, is given by:[241]

$$T(F) = T_0 + \frac{T_{FN} - T_0}{1 - T_0}(T_{max} - T_0) \tag{5.2}$$

Where $T_0 = \mathrm{e}^{-\sigma_g NL}$, $T_{max} = \mathrm{e}^{-\sigma_e NL}$ and $T_{FN} = \ln\left[1 + T_0\left(\mathrm{e}^{\frac{\sigma_g F}{\hbar\omega}} - 1\right)\right]/(\sigma_g F/\hbar\omega)$. σ_g and σ_e are the ground state and excited state cross-section respectively. N is the absorber atom density and L is the absorber length. F represents the laser energy fluence and ω is the photon angular frequency. Note that N always accompanies with L. To avoid the difficulty of getting the exact effective thickness of both saturable absorber mirrors, the absorber density per area k was employed instead of N and L, where k = NL. Equation (5.2) describes the transmission when the absorber carriers are in a thermal equilibrium state.

In the experiments, the laser is vertically incident onto the mirrors and actually passes the saturable absorber twice in a very short time in the saturable absorber mirror (SAM) configuration. On the first pass of photons through the saturable absorber, the light transmission can be described by the Equation (5.2), *i.e.*, T(F). Then the photons are reflected by the mirror and pass through the absorber for the second time. Because the time between the first and second pass is very short, the carriers do not recover from the first-pass excitation. In other words, the photons sense the 'as-bleached' absorber on the second pass. Upon the approximation of slow absorber, the transmission sensed by the second-pass photons can be written as T(F+F·T(F)). The F in the brackets is for the remaining effect of the first pass photons and the F·T(F) is the second-pass light intensity. Therefore, the reflection of a SAM using a slow-absorber model can be derived as:

$$R = T(F) \cdot T(F + F \cdot T(F)) \tag{5.3}$$

Here the loss was neglected from mirror imperfection. The modulation depth of SAM is then as follows:

$$\Delta R = R_{max} - R_0 = T_{max}^2 - T_0^2 \tag{5.4}$$

And the non-saturable loss of the SAM is:

$$A_{ns} = 1 - R_{max} = 1 - T_{max}^2 \tag{5.5}$$

Here the T_0 and T_{max} stand for the same expressions as in Equation (5.2).

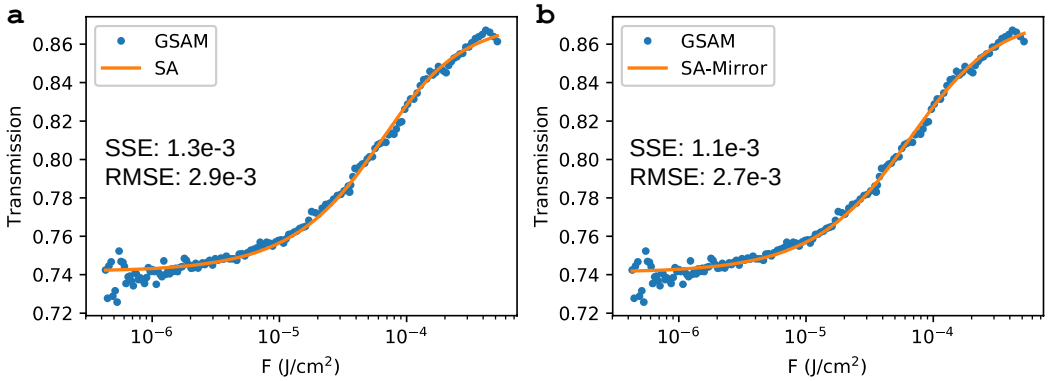

Figure 5.8 Comparison of curve-fitting using slow-absorber model (a) and slow-absorber mirror (b) model. The sum of squares due to error (SSE) and root mean squared error (RMSE) are used to determine the quality of curve fitting. Values closer to 0 indicate a better fit.

Both models mentioned previously were utilized to fit the I-scan results, *i.e.*, Equation (5.2) SA model and SA mirror model Equation 5.3 for both SAMs. Both models show excellent fitting whereas Equation 5.3 exhibited less errors than Equation (5.2). The sum of squares due to error (SSE) using Equation 5.3 was 1.1×10^{-3}, while SSE using Equation (5.2) was 1.3×10^{-3}. (See Figure 5.8). A lower SSE implies better fitting, indicating Equation 5.3 is a better model than Equation (5.2) for a SAM. To better show the nonlinear optical extinction, the Equation 5.3 fitted curves are plotted in Figure 5.6 after converting the reflectance to normalized differential absorption $\Delta\alpha/\alpha_0$.[60] The representation by differential absorption $\Delta\alpha/\alpha_0$ has an advantage over reflectance because sample thickness has no effect on the differential absorption $\Delta\alpha/\alpha_0$. This can help us to better understand the pristine NLO properties of materials. The solid scatters are the original data while the red hollow data points are for the real NLO response excluding the 13.8% surface scattering effect showed in Figure 5.6. It is obvious that although the graphene has a larger saturated

fluence F_s, it also has a larger $\Delta\alpha/\alpha_0$. This implies that graphene has a better modulation depth and non-saturable loss than the commercial SESAM used in this study.

Table 5.3 NLO parameters of the graphene and SESAM derived from I-scan at 2 μm. The σ_g and σ_e are the cross-section of ground state and excited state respectively. The k represents the absorber density per area.

Nano-structure	SA Model (Equation (5.2))				SA Mirror Model (Equation (5.3))			
	σ_g ($\times10^{-15}$cm^2)	σ_e ($\times10^{-15}$cm^2)	σ_e/σ_g	k ($\times10^{13}$cm^2)	σ_g ($\times10^{-15}$cm^2)	σ_e ($\times10^{-15}$cm^2)	σ_e/σ_g	k ($\times10^{13}$cm^2)
Graphene	3.19	1.44	0.451	9.357	2.12	0.936	0.442	7.067
SESAM	29.9	18.7	0.625	1.517	20.04	12.32	0.615	1.140

The obtained NLO parameters of both nanostructures from fitting are summarized in Table 5.3. It can be seen that the cross-sections obtained from Equation (5.3) are much smaller than that from Equation (5.2). This is because the carriers absorb twice in the SA mirror model while only once in the SA model. The ground state cross-section, σ_g, and excited state cross-section, σ_e, of graphene were measured to be 2.12×10^{-15} cm^2 and 0.936×10^{-15} cm^2 respectively. These are one-order smaller than that of SESAM, which are 20.04×10^{-15} cm^2 and 12.32×10^{-15} cm^2. Note that the cross-section ratio of the excited states to the ground state, σ_e/σ_g, are measured to be 0.442 and 0.615 for graphene and SESAM respectively. The graphene σ_e/σ_g at 2 μm is close to the previous reported 0.41-0.48 at 1030 nm.[211] The smaller σ_e/σ_g in graphene implies that there are less non-saturable losses when compared with the SESAM.

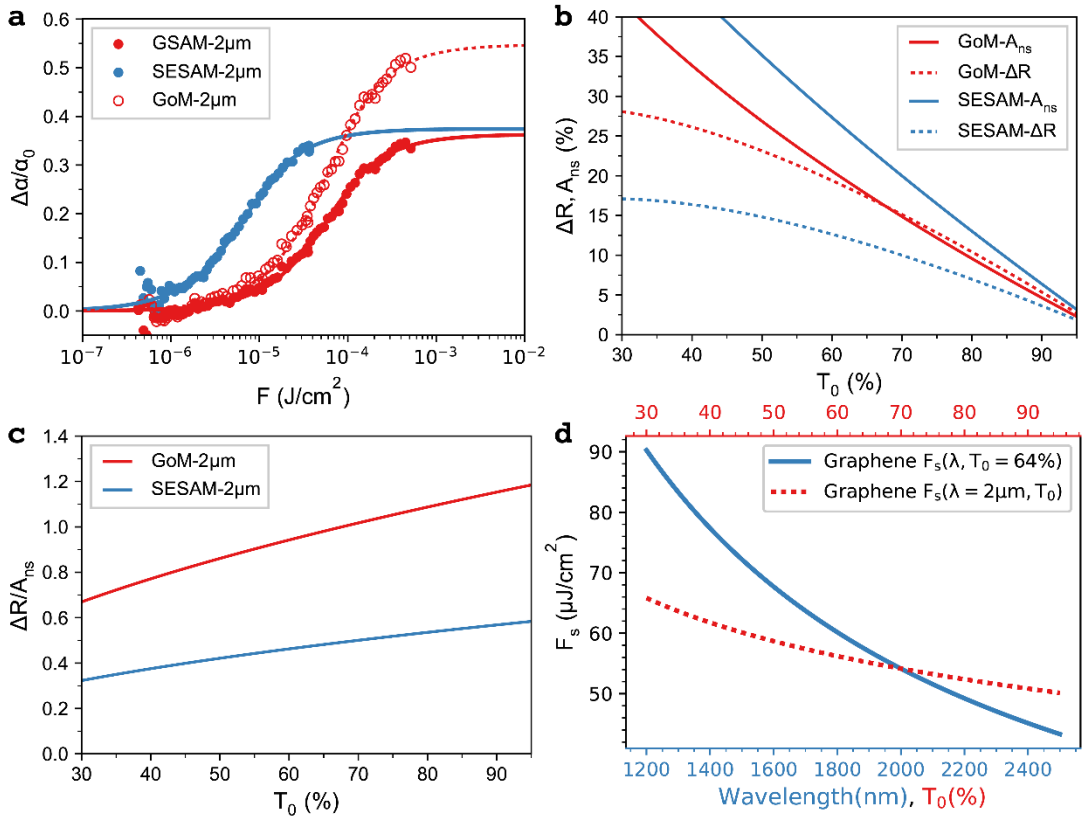

Figure 5.9 (a) Solid circles and lines: NLO performances of the GSAM and the commercial SESAM at 2 μm. Hollow circles: the response of graphene on mirror (GoM) after subtracted the 13.8% surface scattering from the GSAM. (b) Simulated modulation depth ΔR (dash lines) and non-saturated loss A_{ns} (solid lines) as a function of linear optical transmission at 2 μm for both saturable absorptive nanostructures. (c) The $\Delta R/A_{ns}$ ratio as a function of linear transmission calculated from (b), showing better performance of the graphene over SESAM. (d) Saturated laser fluence F_s of graphene as a function of wavelength (bottom axis, blue solid line) and linear optical transmission T_0 (top axis, red dashed line) respectively when a slow-absorber model is applied, *i.e.,* pulse width << τ_2 (1.19 ps).

As a design guideline for a practical SAM with varying linear optical transmission, the theoretical performance of both nanostructures were calcualated. Figure 5.9 (b) plotted theoretical modulation depth ΔR and non-saturable loss, A_{ns}, as a function of sample linear transmission T_0 from 30% to 95%. The calculation parameters are shown in Table 5.3. The solid lines are for the non-saturable absorption A_{ns} and the dashed lines are for the modulation depth, ΔR. From the Figure 5.9 (b), for the same linear transmission, the commercial SESAM nanostructure always has a larger non-saturable absorption, A_{ns}, and less modulation depth, ΔR, comparing to those of graphene. Furthermore, the modulation depth, ΔR, of the SESAM nanostructure is always less than that of graphene. The ratio, $\Delta R/A_{ns}$, in Figure 5.9 (c) display the advantage of graphene over the nanostructure of SESAMs more clearly, where graphene always has a higher $\Delta R/A_{ns}$, value. This

means a well-designed GSAM may produce much less absorptive heat than SESAM if both operate at the same ΔR. This is quite important because light absorption is one of the main reasons for device failure as well as the limitation of laser output power. It should be noted that despite material properties playing an important role in the damage of SAM, its threshold also strongly depends on the device design. [242, 243] However, with a better material like graphene, it is still possible to expect a mode-locker of higher damage threshold than that of traditional SESAMs in the mid-infrared.

The saturated fluence, F_s, and the saturable intensity, I_s, are key parameters for a mode locker. They are defined by the light fluence or intensity when the absorption coefficient decreased by a half. F_s of an ideal absorber can be also defined by the light intensity when the total absorption coefficient, α, decreased to half of linear absorption coefficient, α_0, *i.e.*, $\alpha(F_s) = \alpha_0/2$. Since the linear optical transmission $T_0 = e^{-\alpha_0 L} = e^{-\sigma_g N L}$, the transmission at saturated fluence F_s can be derived as $T(F_s) = e^{-\alpha_0 L/2} = \sqrt{T_0}$. For slow-absorber model, T_{FN} represents the contribution of ideal saturable absorber: [241]

$$T_{FN}(F) = \ln\left[1 + T_0\left(e^{\frac{\sigma_g F}{\hbar\omega}} - 1\right)\right]/(\sigma_g F/\hbar\omega) \tag{5.6}$$

Therefore let $T_{FN} = \sqrt{T_0}$ to get the saturated fluence F_s. Then one can obtain:

$$E^{x\sqrt{T_0}} - T_0 e^x = 1 - T_0 \tag{5.7}$$

where $x = F_s\sigma_g/(\hbar\omega)$. The x in the Equation (5.7) can be solved numerically in region $T_0 = [0.01,\ 0.99]$and the result is shown as scatters in Figure 5.10. To make it easier to use, a simple power function is utilized to fit (solid lines in Figure 5.10) and then the x is approximately expressed to be:

$$x = 5.038T_0^{-0.08223} - 3.449 \tag{5.8}$$

Finally, the F_s with $T_0 = [0.01,\ 0.99]$ can be written as:

$$F_s = (5.038T_0^{-0.08223} - 3.449)\hbar\omega/\sigma_g \tag{5.9}$$

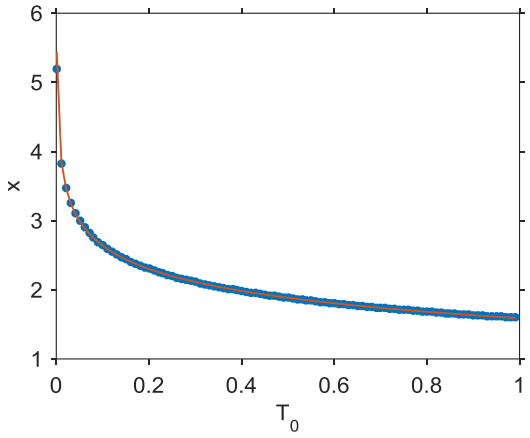

Figure 5.10 Scatters are the numerical solution of Equation $e^{x\sqrt{T_0}} - T_0 e^x = 1 - T_0$. Solid line represents

For slow-absorbers (pulse width << τ_p, where τ_p is the absorber recovery time), the F_s in the region $T_0 = [0.01,\ 0.99]$ can be expressed as an analytical form derived from Equation (5.2):

$$F_s = (5.038T_0^{-0.08223} - 3.449)\hbar\omega/\sigma_g \tag{5.10}$$

Figure 5.9 (d) displays the calculated F_s from Equation (5.10), where the blue dashed line is for the fixed 64% T_0 and the red solid line is for the constant 2 μm wavelength. The decreasing F_s implies an easier saturation of graphene as the wavelength goes to mid-infrared and the transmission increases. This explains wavelength-dependent results reported on graphene as well as other 2D materials such as MoS_2 and black phosphorus in previous investigations.[211, 244, 245]

For fast-absorbers, the saturated intensity I_s can be derived from the steady-state solution of three-state rate equation (pulse width >> τ_p): [246]

$$I_s = (\hbar\omega)/(\sigma_g\tau_p) \tag{5.11}$$

The saturated fluence, F_s, is used for slow-absorber and saturated intensity, I_s, for fast-absorber because the laser pulse-width will not be effective and the whole expression can be simplified. However, the simple relationship of $F_s = I_s\delta$ is required if one wishes to convert saturated fluence/intensity to another in a slow-/fast- absorber model, where δ is laser pulse width. Table 5.4 presents the typical F_s and I_s for both materials in slow-/fast-absorber models at 2 μm. Note that a pulse width of δ = 100 fs is utilized for slow-absorber and δ = 1 ns to calculate the asterisked I_s and F_s respectively. The graphene value for I_s is 542 MW/cm^2 for 100 fs pulses whereas it is 26.2 MW/cm^2 for 1 ns pulses. This has been observed in our previous investigations in MoS_2, $MoSe_2$

and black phosphorus. [60, 178, 195, 211, 215] A similar effect on F_s was observed. Table 5.4 shows how much the laser pulse width can affect the NLO measurement results.

Table 5.4 Saturated fluence and intensity with slow- and fast-absorber models. The I_s for the slow-absorber model and F_s for the fast-absorber model are calculated based on a pulse duration of 100 fs and 1 ns respectively.

Nanostructure	Slow-absorber (pulse width << τ_p)		Fast-absorber (pulse width >> τ_p)	
	F_s (μJ/cm^2)	I_s (MW/cm^2)	F_s (mJ/cm^2)	I_s (MW/cm^2)
Graphene	54.2	542	26.2	26.2
SESAM	6.9	69.2	0.527	0.527

5.6 Conclusion

In this chapter, the performance of a multi-layered GSAM device was systematically compared with a commercial SESAM at a wavelength of 2 μm. The GSAM was fabricated via the transfer of a vacuum-filtrated graphene film onto a silver-coated mirror. The nonlinear optical performance and carrier dynamics at the 2 μm wavelength were investigated by I-scan and pump-probe techniques with mid-infrared 2 μm, 100 fs laser pulses. With a similar linear optical reflection of ~64%, the GSAM exhibited comparable modulation depth of 13% and non-saturable loss of 9.9%. Moreover, after subtracting the 13.8% surface scattering loss, the pristine graphene possesses much better NLO properties than the nanostructures in the comparing SESAM. The cross-section ratio of the excited-state over ground state, σ_e/σ_g, is fitted to be 0.442 and 0.615 for graphene and SESAM respectively, implying graphene based SAM may produce less loss and heat than SESAM when operating as a mode-locker in a laser cavity. Additionally, graphene has been shown to be a much faster saturable absorber than the commercial SESAM in the pump-probe experiment. The graphene displayed carrier relaxation times of 1.14 ps and 1.2 ps at 800 nm and 2 μm respectively, while the SESAM was slower at ~63 ps at 2 μm. This advantage of graphene is very favourable for generating high repetition and short-pulse laser. The results imply that with proper design, graphene based saturable mirror can be superior than the current commercial SESAM in modulation depth, non-saturable loss and carrier relaxation for future mid-infrared lasers.

The work in this chapter has been published by *laser & photonics reviews* as a journal-cover paper.

6. Transient absorption spectroscopy

Atomically thin, layered crystals offer a platform for designing optoelectronic devices and exploring exciting new physics in the field of photonics, spintronics, valleytronics,[247] carrier dynamics. Recently layered platinum diselenide ($PtSe_2$) comes to the spotlight of research as a new member of 2D ilk in its monolayer limit. It has been theoretically proven that $PtSe_2$ has an emergent band gap in the monolayer limit.[248-250] It was initially experimentally obtained by directly selenizing a Pt(111) substrate at ultra-high-vacuum conditions and its photocatalytic performance was observed.[251] As a new semiconducting transition metal dichalcogenide, monolayer $PtSe_2$ emerged as a promising potential material for valleytronics devices due to its circular polarization in momentum. [251] Experimental studies also provided evidence that $PtSe_2$ has three dimensional type-II Dirac Fermions, which breaks Lorentz invariance.[252]

Most importantly, $PtSe_2$ was found to be of use as a photodiode and solar cells when it is vertically stacked on a Si substrate.[253] In solar cells system, non-equilibrium carrier thermalization is one major loss of conversion efficiency.[122] By harvesting the hot carriers before cooling down, the Shockley-Queisser limit can be stepped over and hence conversion efficiency of solar cells can be significantly improved.[122, 254, 255] The study of carrier dynamics relative to hot carrier lifetime on $PtSe_2$ thin films would provide the necessary physical insight into the hot carrier transport properties, and therefore help to achieve higher conversion efficiency when designing solar cells.

This chapter is going to introduce a time- and spectra- resolved study of ultrafast excitation carrier dynamics of layered $PtSe_2$ with different thicknesses using a degenerate pump probe technique and a transient absorption spectroscopy. Three decays were observed in both degenerate pump probe curves and transient absorption spectroscopy. Both photoinduced bleaching, *i.e.*, positive $\Delta T/T$, and absorption, *i.e.*, negative $\Delta T/T$, were observed in the thinnest $PtSe_2$ film. These analyses allow for insights into the hot carrier relaxation mechanisms of layered atomically thin $PtSe_2$ films with guides for designing their photovoltaic and photonic devices.

6.1 CVD fabrication and characterization of layered $PtSe_2$

6.1.1 CVD of layered $PtSe_2$ thin films

The $PtSe_2$ films were synthesized by thermally assisted selenization of platinum films as previously reported. Briefly, platinum was deposited onto fused silica substrates via sputtering using a Gatan precision etching and coating system. A quartz-crystal microbalance was used to monitor the deposition process. The Pt-deposited substrates were then placed in a quartz-tube vacuum furnace and heated up to 450 ℃. Se powder was heated to 220 ℃ in an independently controlled heating zone upstream of the Pt samples and its vapor was carried to the Pt films under a 150 sccm flow of forming gas (10%H_2/Ar). The Pt samples were previously deposited on the quartz substrates with the initial Pt atom layer thicknesses of 0.5 nm, 1 nm and 3 nm respectively. The photos of the corresponding layered $PtSe_2$ thin films are shown in Figure 6.1 (a) from left to right respectively.

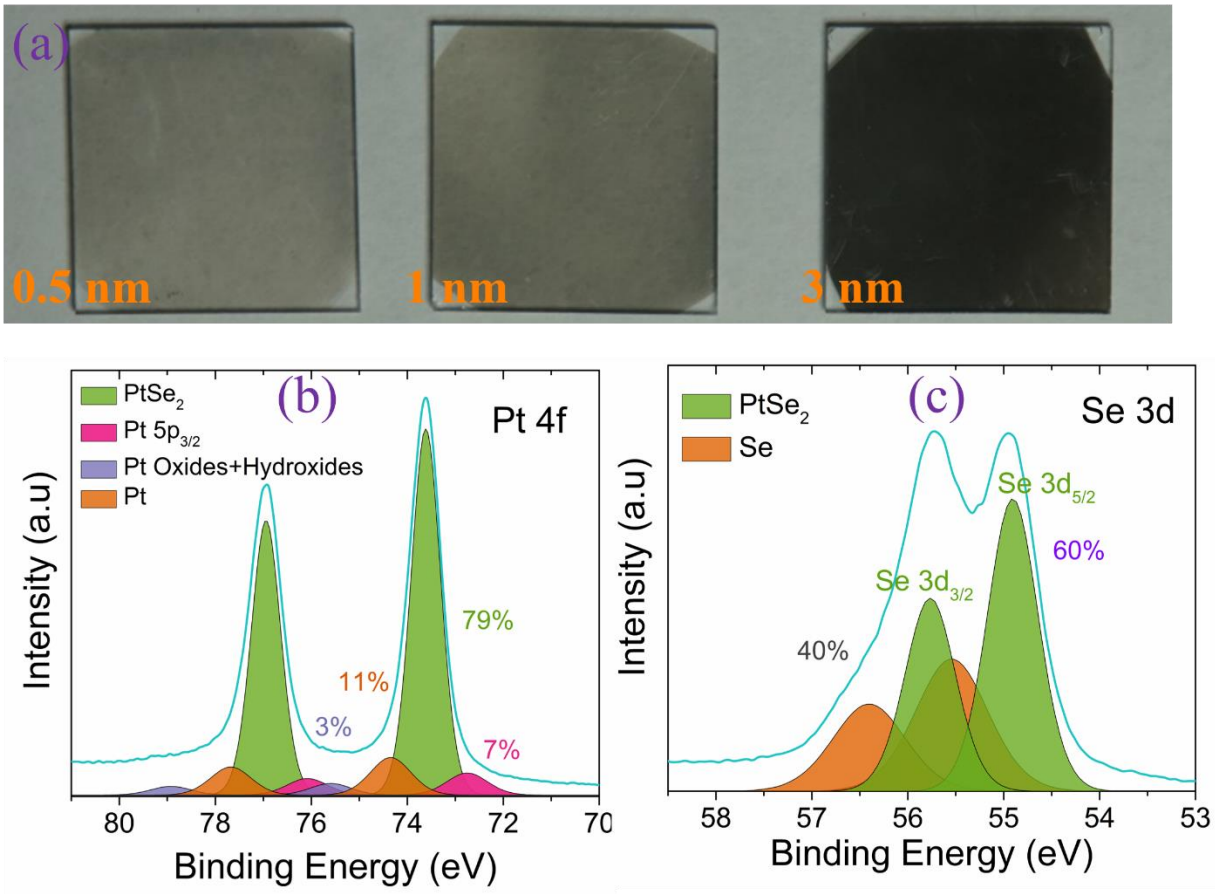

Figure 6.1 (a) Photos of $PtSe_2$ thin films with the initial Pt atom layer thicknesses of 1 nm, 2 nm and 3 nm from left to right respectively. XPS spectra showing the binding states for (a) Se 3d and (b) Pt 4f region of a $PtSe_2$ thin film acquired by selenizing a 1 nm thick Pt atom film.

6.1.2 Characterizations of $PtSe_2$ thin films

X-ray photoelectron spectroscopy (XPS) was carried out to study the composition of the thin films. The XPS spectrum in figure 6.1(b) shows the binding states of Pt 4f region for $PtSe_2$ thin film prepared of '1 nm' $PtSe_2$ film. The spin orbit interaction of the 4F states splits the peak into two major peaks locate at 76.9 eV and 73.6 eV respectively, corresponding to ~79% $PtSe_2$. This result agrees well with previous studies.[253] They are attributed to $PtSe_2$ and account for ~79% of the thin films, *i.e.*, the majority of Pt layer has been reacted into selenide.

There also exist two small peaks at the binding energy of ~75.6 eV and ~74.4 eV, which originate from Pt Oxides+Hydroxides and unreacted Pt, respectively. These two peaks occupy in total ~14% of the whole relative atomic percentages. The remaining ~7% of components coming from Pt $5p_{3/2}$ spin-orbit is not taken into account in this preparation. In terms of anions, two primary peaks for Se were observed in the XPS Se 3d region, see Figure 6.1 (c), of which one is attributed to Se $3d_{3/2}$ (~55.8 eV) and another to Se $3d_{5/2}$ (~54.9 eV). It then can be confirmed as Se^{2-} state and also indicates that the most of the Pt atoms have be transformed into $PtSe_2$. A smaller percentage of atoms located at the binding energy of ~55.5 eV are likely to attributable to amorphous or edge Se.

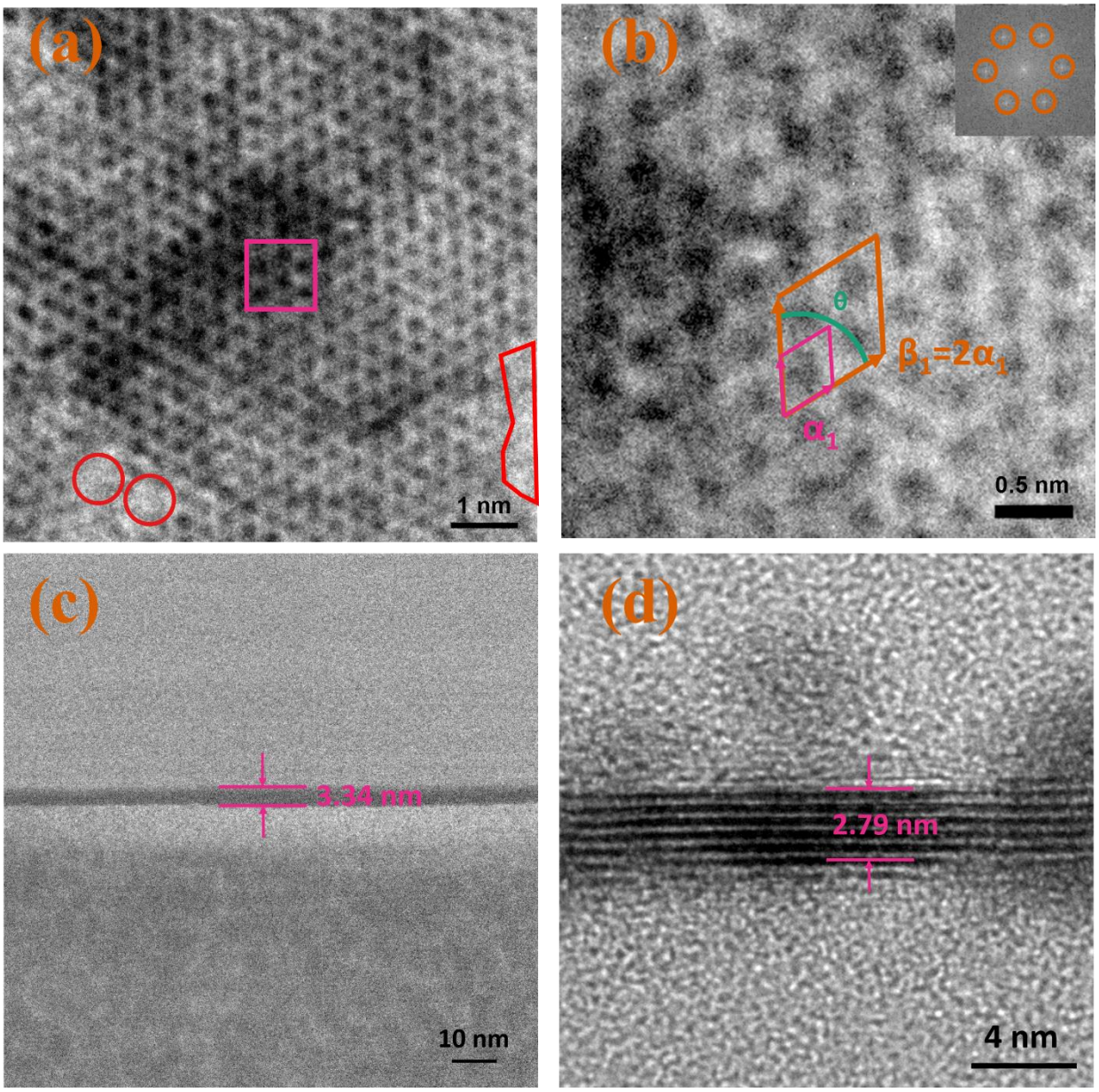

Figure 6.2 Atomic-resolution in-plane TEM images showing (a) the hexagonal structure of $PtSe_2$, and (b) unit cell lattice (light red rhombi) and (2×2) superlattice of $PtSe_2$. The red areas indicate some defects. TEM images of profiles of '0.5 nm' $PtSe_2$ thin film in (c) low and high (d) resolution.

To verify the atomic structure of layered $PtSe_2$ crystals, high revolution transmission electron microscopy (TEM) was performed to photograph their in-plane and cross section, see Figure 6.2. The TEM samples are prepared by transferring the $PtSe_2$ film onto holey-carbon grid with the help of PMMA. The $PtSe_2$ grown on SiO_2 coated silicon wafer with the same synthesizing conditions as other samples on quartz were used for the prepare of TEM samples. Briefly, the $PtSe_2$ film was spin-coated by a PMMA layer as a support. Then the SiO_2 was etched away by KOH solution bath and the $PtSe_2$/PMMA floated up. A holey-carbon TEM grid was then used to 'fish' the films and dried in the air for TEM measurements.

An in-plane TEM image in Figure 6.2 (a) shows the hexagonal structure of Pt atoms in $PtSe_2$ sandwich-type structure. A zoom-in atomic-resolution image from Figure 6.2 (b) clearly indicates the lattice structure of one $PtSe_2$ unit cell in light red rhombi and its (2×2) superlattice in light green rhombi. The average lattice constant of α_1 was measured to be 0.371 nm, which is in agreement with the interatomic distance of Se atoms in both monolayer and bulk $PtSe_2$.[251] The angle between two light red arrows was measured to be 60º, which is the supplementary angle (60º=180º−120º) of one hexagonal angle. This verifies the hexagonal structure of Se atoms in $PtSe_2$. The light green rhombi shows a (2×2) regular moiré superlattice with a periodicity of $\beta_1 = 2\alpha_1 = 0.742\ nm$. Its orientation agrees well with that of FFT observed image in inset of Figure 6.2 (b). The cross-sectional TEM image of the thinnest $PtSe_2$ thin film shown in Figure 6.2 (d) suggests that it has a thickness of about 2.79 nm. This indicates that the 0.5nm $PtSe_2$ film contains about six layers.

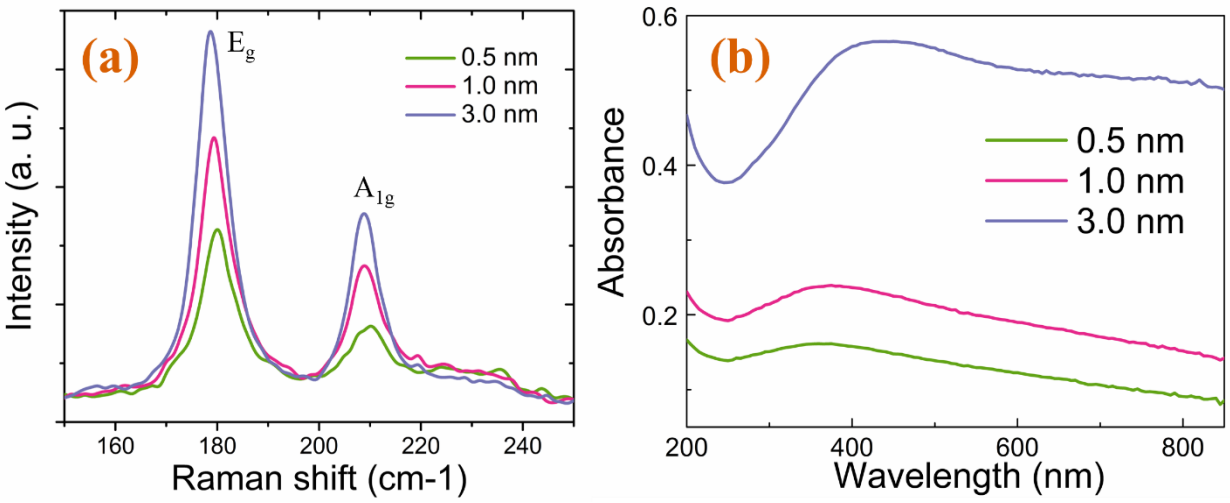

Figure 6.3 (a) Raman spectrum and (b) UV-vis absorbance from 250 nm to 850 nm of '0.5 nm', '1 nm' and '3 nm' $PtSe_2$ thin films.

Raman spectroscopy was carried out to study the states of the thin films. [250] Figure 6.3 (a) presents the in-plane E_g mode (~175 cm^{-1}) and out-of-plane mode, A_{1g}, in the three $PtSe_2$ samples. As the nominal thickness increases from '0.5 nm' to '3 nm', there is an obvious increase in the relative intensity of A_{1g} mode vibration. This results from stronger out-plane interaction of a larger number of layers. It was also observed that the E_g peaks blue shift with the increase in the thickness of the samples. To be specific, the A_{1g} peaks of the '0.5 nm', '1 nm' and '3 nm' thin films sit at 208.7 cm^{-1}, 209.0 cm^{-1} and 210.1 cm^{-1}, which are in good agreement with the previous samples. Figure 6.3(b) shows the optical absorption of the $PtSe_2$ thin films on quartz substrate. All $PtSe_2$ thin films exhibited broadband ground state absorptions from 380nm to 850 nm. The broadband absorption can be explained both by the narrow bandgap of mono- and bi-layered $PtSe_2$ and semi-metallic band structure of few-layered nanostructures. [10]

6.2 Transient absorption

6.2.1 Methods to study carrier dynamics

Transient Spectroscopy is based on 800 nm pulses with a ~100 fs pulse width that are generated by a mode-locked Ti:sapphire laser (Coherent RegA 9000, repetition rate 100 kHz). Then the beam was split into two, see Figure 6.4. One beam went into a BBO crystal to generate 400 nm femtosecond pulses for pumping. This pump beam was then modulated by an optical chopper at 50 Hz. The other 800 nm beam was focused onto a 3 mm sapphire to obtain a supercontinuum white light for probing. These pulses were then filtered by 750 nm short-pass (~470-750nm) and then delayed by a motorized stage. Both pump and probe were combined collinearly by a dichroic mirror (450 nm) and focused onto the samples by a f =10 cm convex lens. Then the 400 nm pump was blocked by a 425 nm long-pass filter. Transient spectra were collected by a CCD spectrometer (Ocean Optics, USB 2000+) and then extracted the signal via a computer program.

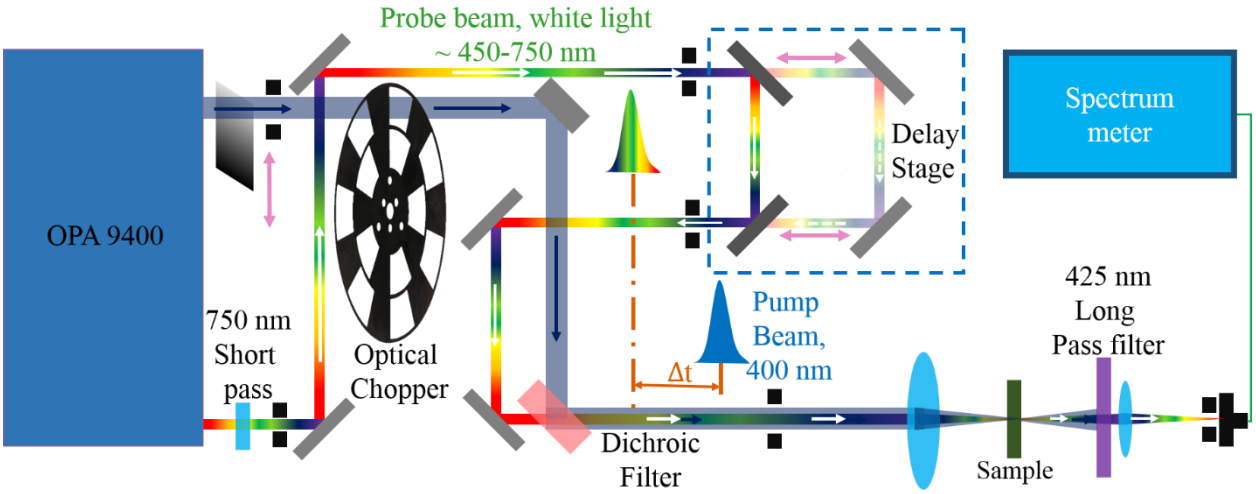

Figure 6.4. The schematic of the transient absorption spectroscopy.

In the degenerate pump-probe configuration, femtosecond pulses at 800 nm were split into two beams for pump and probe respectively, as shown in Figure 6.5. The probe pulses were delayed by a motorized stage and their polarization was rotated by 90-degrees with respect to the pump pulses to eliminate coherent artefacts. The pump and probe beams were modulated by a chopper at different frequencies. Then both beams were non-collinearly combined and focused on the samples. The light transmitted through the sample was filtered by a polarizer to block the pump beam. The final signal was detected by a single Si photodiode with a lock-in amplifier (Signal Recovery, SR7270) locked at 1157 Hz, the sum frequency of pump and probe beams.

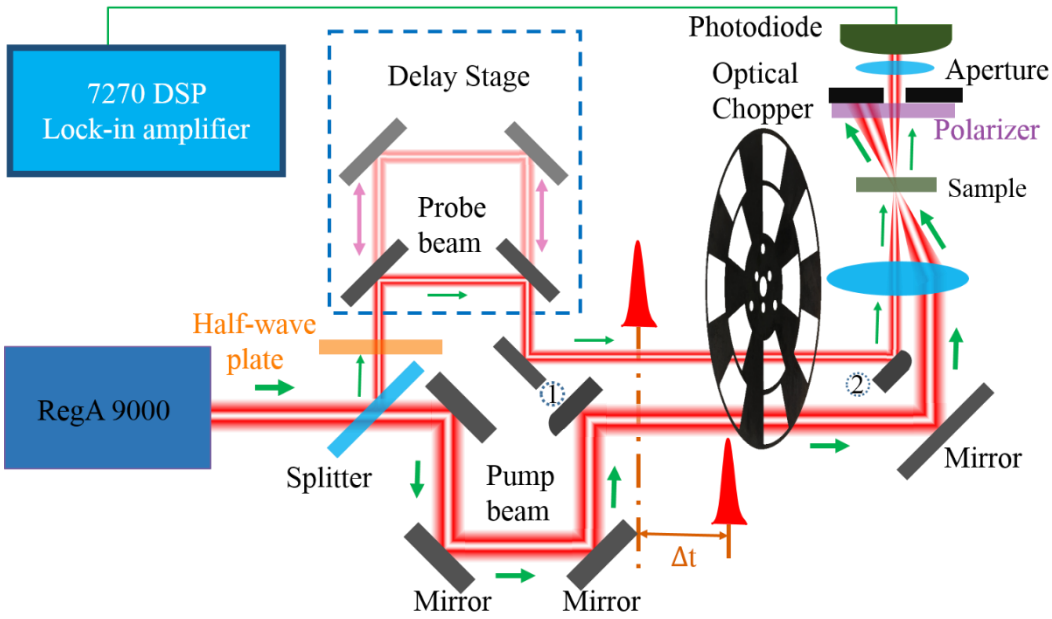

Figure 6.5. The schematic of the degenerate pump-probe based on 800 nm femtosecond pulses.

6.2.2 Transient absorption in the visible region

The ultrafast carrier dynamics of the layered $PtSe_2$ films were investigated by optical transient absorption spectroscopy pumped with 400 nm (3.1eV) femtosecond laser pulses. By probing with a white light from 1.72 eV (720nm) to 2.64 eV (470nm), the mapping of the optical differential transmission ($\Delta T/T$) as a function of delayed time are showed in Figure 6.6. The fluence of 3.1eV pump pulse was fixed at 7.18 uJ/cm^2 for all three samples in this figure, *i.e.,* '3 nm', '1 nm' and '0.5 nm'. It is clear shown that after the 3.1eV photon excitation at zero delayed-time, all the three $PtSe_2$ samples immediately exhibited a broadband optical bleaching in the first few hundred femtosecond across the whole probing wavelength range, implying strong excited-state absorptions. It is obvious that the recovery of $\Delta T/T$ can be separated by two distinct processes, *i.e.*, the deep color areas (~1 ps) and light color ones (>1 ps) in Figure 6.6 (a)-(c). These two areas correspond to a fast- and slow-decay process respectively. The maxima of $\Delta T/T$ show a decreasing from '3nm', nm' to '0.5nm'. This trend may be attributed to the $PtSe_2$ thickness changes in these three samples, see Figure 6.6 (d)-(i).

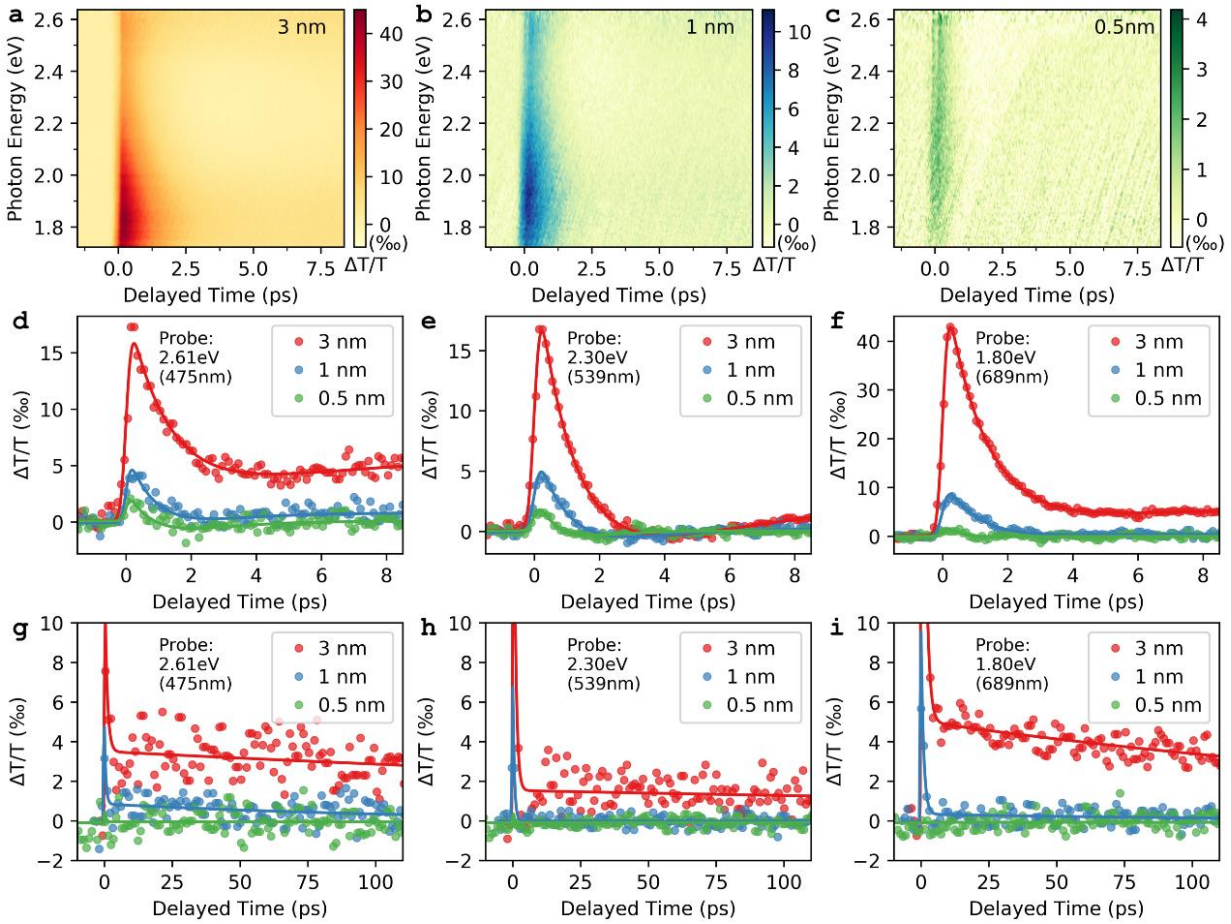

Figure 6.6. Time- and spectral-resolved carrier dynamics of layered PtSe2 nanostructures with 3.1 eV (400 nm) pump pulses. The pump fluence was 7.18 uJ/cm2 for all three $PtSe_2$ samples. (a)-(c) Transient absorptive mapping in the visible range from 1.72 eV (720nm) to 2.64 eV (470nm) for '3 nm', '1 nm' and '0.5 nm' $PtSe_2$ samples. (d)-(f) Scatters are transient absorptive spectra for 2.61 eV, 2.30 eV and 1.80 eV photons from (a)-(c). Lines are the fitting results by triple exponential model employing nonlinear regression algorithm. The first two fast (within ~10 ps) carrier life times, τ_1 and τ_3, were estimated to be ~1.2 ps and ~6 ps. (g)-(i) transient absorptive spectra show long (~100 ps) carrier relaxations, τ_2. Here two-exponential model (τ_1 and τ_2) was employed to obtain the fitting lines because the τ_3 process is weak in these long-time scale measurements ($\tau_1 \leq \tau_3 \leq \tau_2$). The polarizations of pump and probe beams were parallel.

To better compare the variation of ΔT/T as different delays, the transient absorptive mapping of $PtSe_2$ are sliced at 2.61 eV, 2.3 eV and 1.8 eV and presented in Figure 6.6 (d)-(f) respectively. For the probe photons with same energies, the carrier decays look similar for '3nm', '1nm' and '0.5nm' samples, although the strength of ΔT/T is stronger for thicker samples due to larger absorption. Additionally, corresponding transient absorptions in a time scale up to 100 ps are exhibited in Figure 6.6 (g)-(i). These figures show the long-time behaviors of excited carriers. For the '3 nm' sample, a very slow and strong decay >100 ps has been observed at all wavelengths. For the '1nm' film, similar slow relaxation was also found at 2.61 eV and 1.8 eV photon energy, but much weaker

compared to '3nm' sample. No long-time scale decay in 0.51nm' sample was observed in the solution of the transient absorptive spectroscopy due to the small absorption. To analyze the time-resolved experimental results, a multi-exponential decay Equation that is modified from biexponential decay model was employed:[60]

$$g(t) = \sum_{i=1,2,..,n} D_i \exp\left(-\frac{t}{\tau_i}\right) erfc\left(\frac{\sigma}{\sqrt{2}\tau_i} - \frac{t}{\sqrt{2}\sigma}\right) \quad (6.1)$$

where $g(t)$ is the differential transmission signal at one wavelength, t is the probe delayed time, D_i and τ_i are relative amplitude and relaxation time respectively. '$erfc$' represents the integral error function and σ is the laser pulse duration. The 'n' is the number of decay process, *i.e.*, the number of independent exponential decays. This Equation has already taken into account the convolution of the pump and probe pulses.

According to the analyses about Figure 6.6 (d)-(e) in the previous paragraph, the carrier relaxations of $PtSe_2$ compose three distinct processes, namely τ_1 (~1.2 ps), τ_3 (~6 ps) and τ_2 (~100 ps). A tri-exponential model was employed for the fitting of the transient absorption mapping for '3nm' $PtSe_2$ sample, *i.e.*, n = 3. However, for '1 nm' and '0.5 nm' samples, only bi- and mono-exponential model for were employed for fitting, *i.e.*, n = 2 and 1 respectively, because of the weak amplitude of long relaxations. A nonlinear regression algorithm was employed to find the best fitting parameters for Equation (6.1). This algorithm needs a set of initial parameters to start fitting and improper initial values will fail the calculation. Because of the large number of wavelengths in the Figure 6.6 (a)-(c), there are too much work to specify the initial values for each curve. Here a shortcut that only designate the initial values of the first wavelength was employed, then used the results of the previous fitting as the initial values of the next neighboring wavelength. As this process iterated, all the wavelengths in a mapping can be easily fitted. The fitting parameters (D_i and τ_i) for different thicknesses samples are plotted in Figure 6.7.

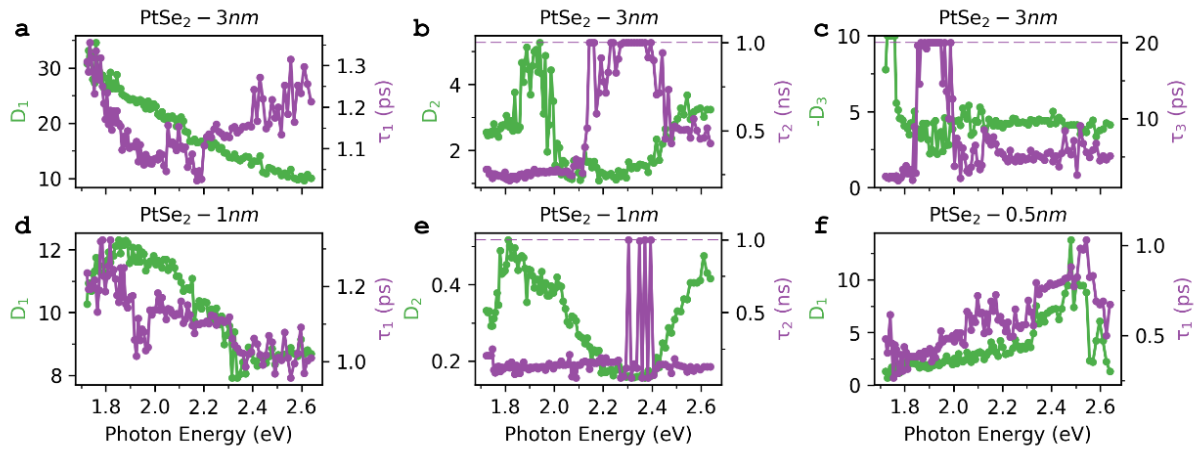

Figure 6.7. The fitting results of transient absorption mapping of $PtSe_2$ superlattice films. Carrier relaxation times, τ_i, and corresponding relative amplitudes, Di, as a function of the probe photon energy for '3 nm', '1 nm' and '0.5 nm' samples are exhibited in (a)-(c), (d) and (e) respectively. Noted that the numbers of independent exponential decays for the curve fittings (Equation (6.1)) are three, two and one for '3 nm', '1 nm' and '0.5 nm' samples respectively. Hollow scatters represent the parameters at the fitting bounds, which may be caused by the small strength of corresponding process.

As shown in Figure 6.7 (a), the first fast relaxation time (τ_1) indicates dependence on the probe photon energy. For '3 nm' thick sample, τ_1 is shortest at ~2.3 eV and becomes longer and longer with the increase or decrease in probe phonon energy. With the decrease of probe photon energy, τ_1 shows a decreasing trend for '1 nm' sample and a slight increase for '0.5 nm', see Figure 6.7 (d) and (f) respectively. However, the similar values of τ_1~0.5-2ps in differential thickness samples indicate that they originate from the same relaxation process: carrier-carrier scattering. What follows the first fast decay is a gentle rise with a relaxation time τ_3 of 1-10 ps. This rise signal (τ_3) cannot be observed in both '1 nm' and '0.5 nm' samples in long-time scale transient absorptive mapping, which is likely due to the small strength of corresponding process. For the same reason, the long-time relaxation (τ_2) was not captured in the thinnest sample, while the average value of this carrier lifetime was measured be ~5 ns for '3 nm' sample and ~0.2 ns for '1 nm' sample. It should be pointed out that all the fitting relative amplitudes D_i are close to their average values except for D_3 overflow the boundary condition in '3 nm' at two probe wavelength, see Figure 6.7. This implies the validity of the fitting carrier lifetimes.

6.2.3 Degenerate pump-probe study at 800 nm

To develop further insight into the carrier dynamics in $PtSe_2$ thin films at near-infrared range, a degenerate pump-probe experiment was carried out. Both pump and probe beams were at the center wavelength of 800 nm. The experimental results for the three samples at 5 various pump fluence from 10 nJ to 40 nJ are presented in Figure 6.8 (a)-(c) using solid scatters. These measurements were carried out at the pump-probe delay time range from -1.8 ps to 6.5 ps, clearly indicating a slight rise signal after about 2 ps in all the three samples. Figure 2(d)-(f) plot the same pump-probe measurements in a long delayed time scale, which aims to obtain the long carrier lifetime. As the pump fluence increase, the maximum differential transmission $(\Delta T/T)_{max}$ increases nearly linearly for all the samples. This indicates that the optical transitions in the measurements were not saturable and confirms that the results at the experimental energy fluence are valid. The changing trend of the differential transmission trace for "3 nm" and "1 nm" sample is similar. It rose transiently at "zero point" within ~100 fs and then decayed dramatically in ~2 ps, followed by a slight ~2 ps rise and a final relatively long time decay. In comparison to the "3 nm" thin film, the ~2 ps rise in "1 nm" sample is stronger and more obvious. In contrast, the signal in "0.5 nm" thin film is more interesting with photoinduced Bleaching (PB), *i.e.*, negative $\Delta T/T$, at the first ~ 1 ps and photoinduced Absorption (PA) *i.e.*, positive $\Delta T/T$, after 1 ps.

The fitting parameters as a function of pump fluence for the three samples are plotted in Figure 6.8 (g)-(i). For the "3 nm" samples, the first short characteristic relaxation time in average, τ_1, was fitted to be ~2 ps, very close to the second short time (τ_3 ~ 3 ps), while the third one (τ_2) is estimated to be 0.25 ns, far longer than the previous two. Similarly, the three characteristic relaxation components for "1 nm" sample, were calculated to be ~2.3 ps, ~2.5 ps and ~0.1ns, respectively. It is very interesting for "0.5 nm" sample that an optically induced absorption, *i.e.*, positive $\Delta T/T$, was observed after the first decay at ~1 ps.

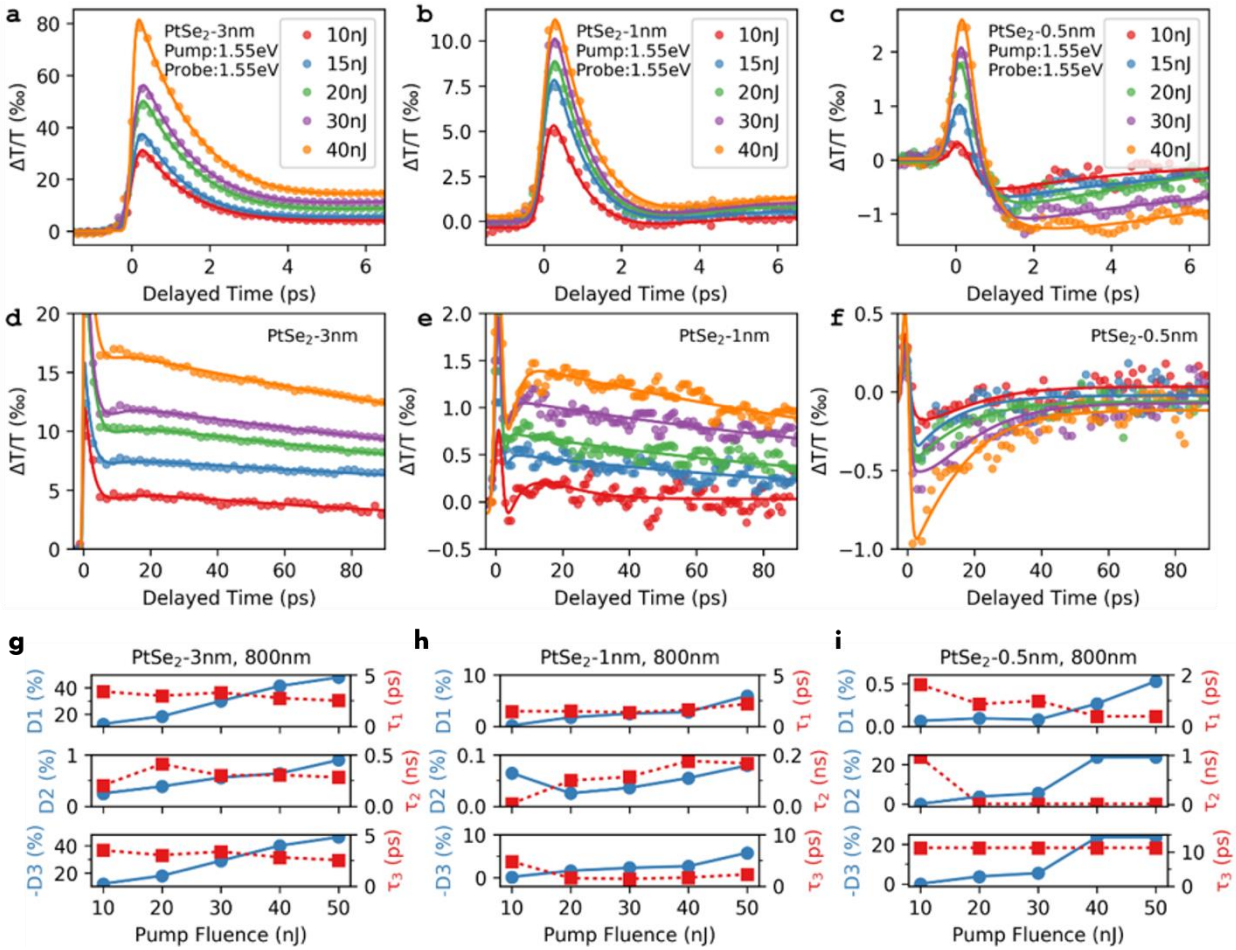

Figure 6.8. (a)-(c) Carrier dynamics of layered $PtSe_2$ samples with 1.55 eV (800 nm) pump and probe pulses. Solids are experimental results and lines are fitted curves using tri-exponential model. Every 10 nJ laser pulse energy corresponds to 3.59 uJ/cm^2 intensity here. The polarizations of pump and probe pulses were orthogonal to each other. (d)-(h) are same measurements as (a)-(c) but showing the carrier relaxations over a long time scale. Fitting carrier lifetimes (τ_1, τ_2 and τ_3) and corresponding relative amplitudes (D_1, D_2, and D_3) as a function of pump fluence for (g) '3 nm', (h) '1 nm' and (i) '0.5 nm' $PtSe_2$ thin film. All the parameters are extracted by fitting the degenerate pump-probe results based on 800 nm pulse lasers.

6.2.4 Carrier relaxation processes and distribution

Based on the above results of transient absorptive mapping and degenerate pump probe, here I are going to discuss the possible mechanism contributing to the corresponding dynamics. The thermal effects can be neglected in the processes since no resolvable dependence of carrier relaxation lifetimes on the pump energy fluence was observed. That is to say, no hot photons play a role in these excited carrier dynamics. The whole processes can be summarized to be the initial excitation, rapid thermalization, cooling and recombination, see Figure 6.9 and 6.10.

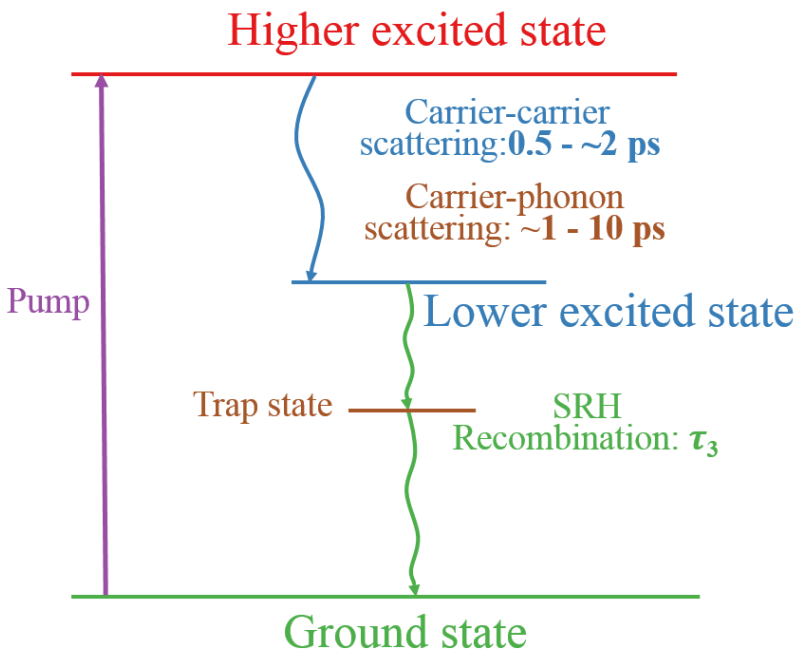

Figure 6.9. The schematic of carrier relaxation processes in layered $PtSe_2$ thin films

Both monolayer and bilayer $PtSe_2$ are semiconductors with a bandgap of 1.20 and 0.21 eV respectively while $PtSe_2$ is semimetallic starting from trilayer.[251] Since 400 nm and 800 nm pulses have a photon energy of 3.10 eV and 1.55 eV respectively that are far larger than the bandgap, a large amount of hot carriers were pumped to higher excited states under the irradiation of the pump pulse. The processes of the carrier excitation are generally in the time scale of ~10 fs to 200 fs,[29] which can be seen as a swift rise around zero delay before the first fast decay in both transient absorptive and degenerate pump-probe traces, see Figure 6.6(d)-(f) and Figure 6.8 (a)-(c). This rise time is measured to be ~150 fs in both case, at which pump-probe delay time (~150 fs) a great number of hot carrier stay in the higher excited state. Note that no coherent spike was observed in degenerate pump probe traces during the swift rise since the pump and probe beam polarizations were set to be orthogonal. These carriers in a non-thermal regime cannot be described using any thermal distribution functions, *e.g.*, Maxwell-Boltzman or Fermi-Dirac equation.[29] A schematic of the distribution of these carriers (Initial excited electrons and holes) can be seen in Figure 6.10 (a). It is clear that they cannot be characterized by a temperature as they are far from any thermal equilibrium. These non-equilibrium electrons and holes are thermalized rapidly to a to a quasi-thermal equilibrium state via carrier-carrier, as seen From 6.10 (a) to (b). The carriers in the quasi-thermal equilibrium state can be characterized by the Fermi-Dirac distribution, see Figure

6.10 (b). As this process occurred in the time region of ~10 fs -100 fs that are out of resolution of the set-ups in the lab, the signal could not be distinguished in neither transient absorptive nor degenerate pump-probe curves.

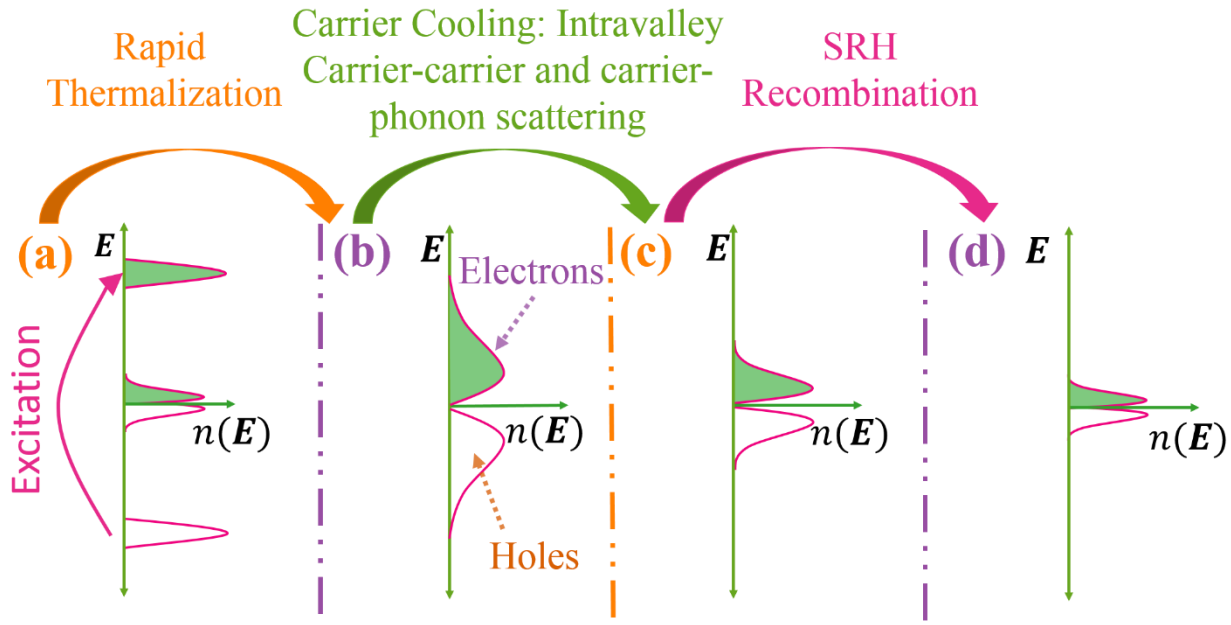

Figure 6.10. A schematic showing the carrier distribution right after their excitation, rapid thermalization, cooling and recombination.

These carriers were subsequently cooling via the intravalley scattering paths, which include carrier-carrier scattering and carrier-phonon scattering, as seen from Figure 6.10 (b) to (c) and Figure 6.9. These two processes are reflected as a fast decrease that followed by a slight rise in both transient absorptive and degenerate pump-probe traces. The fast decrease signal is related to the first fast decay via the carrier-carrier scattering path with a carrier lifetime (τ_1) of ~0.5 ps – 2 ps, while the slightly rising signal is related to the second decay via intravalley carrier-phonon scattering a carrier lifetime (τ_3) of ~1 ps – 10 ps. It should be noticed that photoinduced bleaching is observed in both the '3 nm' and '1 nm' $PtSe_2$ thin films but the second and third decays are photoinduced absorption in '0.5 nm' sample. The change in sign of this signal might be due to the bandgap energy renormalization and/or surface bound excitons, which were observed in $MoSe_2$ and WS_2 respectively.[69, 70, 256]

The electrons in the lower excited state finally recombined with corresponding holes, which is attributed to an indirect recombination with the assistance of a trap state. The relaxation path is shown in Figure 6.9 and the carrier distribution is seen from Figure 10 (c) to (d). A trap state can

be introduced by defects and/or dopants. The XPS spectrum in Figure 6.1 shows that the samples are pure, and therefore the trap state in these $PtSe_2$ thin films must be generated by defects. The defects can be seen from the TEM images, such as Figure 6.2 (a). For '3 nm' and '1 nm' $PtSe_2$ thin films, these relaxation times are calculated to be in the range of ~0.1 ns to ~0.3 ns. Interestingly, this time for '0.5 nm' $PtSe_2$ thin film is much shorter of ~40 ps. This is likely to be caused by much more defects in the thinner thin films. It is easy to understand that more rifts between the atoms were created during the CVD fabrication in thinner films, which leads to more defects. This results in the trap state closer to the middle of lower excited state and ground state and hence enhance the recombination rate of electrons and holes with via the trap state.

6.3 Conclusion

In summary, the excited carrier dynamics of layered $PtSe_2$ thin films were studied by femtosecond lasers. Transient absorption spectroscopy and degenerate pump probe measurements indicate that excited carrier in $PtSe_2$ exhibits two fast and one slow relaxation processes. The favourable fits of a three-dimensional triexponential and biexponential decay model on the carrier dynamic traces calculated out the corresponding relaxation times. The first fast decay process is attributed to carrier-carrier scattering while the second fast relaxation was dominated by intraband carrier-phonon scattering. The slowest relaxation is attributable to an indirect recombination of electron-hole pair via a trap state which is introduced by the defects. This relaxation is slower in the thinner samples due to more defects.

7. Conclusion and outlook

7.1 Conclusion

The third-order NLO response and ultrafast excited carrier dynamics of some 2D Materials, including liquid-phase-exfoliated antimonene, $MoSe_2$/PVA composite thin films, a graphene saturable absorber mirror (GSAM) and layered $PtSe_2$ have be studied.

Firstly, antimonene was exfoliated from antimony bulk in CHP. UV-visible spectroscopy, Raman spectroscopy and TEM of the exfoliated flakes indicate that the exfoliated dispersion consists mainly of few-layers. The NLO properties of the antimonene dispersion were then studied by continuous wavelength (CW) lasers at the center wavelengths of 405 nm, 785 nm and 1064 nm. Spatial self-phase modulation of the antimonene dispersion was observed under the irradiation of lasers at the three wavelengths, implying a broadband NLO response of the antimonene from visible to near-infrared region. By analyzing the SSPM diffraction rings pattern that generated in the far field, the nonlinear refractive index of the antimonene dispersion and the third-order nonlinear optical susceptibility of the antimony monolayer were obtained to be ~10^{-5} cm^2 W^{-1} and ~10^{-8} esu respectively. In addition, the relative variation in nonlinear refractive index of the antimonene dispersion can be tuned from ~14% to ~63% by changing the incident laser intensity.

Secondly, a systematically comparative study on the dependence of the NLO behaviors of $MoSe_2$/PVA composite thin films on laser wavelengths, pulse durations and aging was carried out based home-made Z-scan set-ups. Few-layer $MoSe_2$ nanosheets were prepared in DI water using sodium cholate as the surfactant. By dissolving PVA powder into warm water, PVA solutions were obtained as a host to fabricate $MoSe_2$/PVA composite thin films. Three thin films with different linear optical transmissions were prepared by tuning the content of $MoSe_2$ nanosheets in PVA. This aims to study the dependence of the NLO properties $MoSe_2$/PVA composite thin film on the linear absorption. The NLO studies were carried out using the open-aperture Z-scan techniques based on laser pulses with a duration of ~ 100 fs at the center wavelength of 400 nm, 500 nm an

800 nm and another wider duration of 6 ns at 532 nm. The pulse repetition-rates are 100 kHz for all femtosecond lasers and 10 Hz for the nanosecond pulses. Saturable absorption behavior in a wide wavelength region from 400 nm to 800 nm were observed in $MoSe_2$/PVA thin films with linear absorption from ~3.6 cm^{-1} to ~43.0 cm^{-1}. The broadband saturable absorption possesses an interesting dependence on laser wavelengths and linear absorption. Saturable absorption of $MoSe_2$/PVA composite thin films are stronger in the shorter wavelength. As the linear absorption increases from 12.8 cm^{-1} and 3.6 cm^{-1} to 36.2 cm^{-1} and 20.5 cm^{-1} for 550 nm and 800 nm respectively, the NLO coefficient increases from -0.2 cm/GW and -0.06 cm/GW to -1.7 cm/GW and -3.8 cm/GW. The corresponding imaginary part of the third-order nonlinear optical susceptibility, $Im\chi^{(3)}$, increases from -0.9 $\times 10^{-13}$ esu and -0.4×10^{-13} esu to -7.2×10^{-13} esu and -23.8×10^{-13} esu respectively. The nonlinear absorption, α_{NL}, and the third-order nonlinear optical susceptibility, $Im\chi^{(3)}$ are approximately three order magnitude larger under the irradiation of nanosecond pulses in comparison to femtosecond pulses. By comparing the properties of a fresh thin film with the corresponding aged one, the stability against aging of the composite thin films in regard to both linear and nonlinear properties was studied. The UV-vis spectroscopy shows that both thin films possess similar linear absorption indicating that the alignment and orientation of the $MoSe_2$ nanosheets in the host stay the same for about half a year. The same Z-scan set-up was employed to study the comparative optical nonlinearity between the fresh composite thin film and the corresponding aged one after half a year. Both samples show the similar saturable absorption. This proves that the embodiment of liquid-phase-exfoliated $MoSe_2$ within a host material, *i.e.*, PVA, guarantees the stability of both linear and nonlinear properties. Since the excited carrier relaxation mechanism is important when a saturable absorber is used for mode-locking in a pulse laser, a degenerate pump-probe experiments based on a femtosecond laser was employed to study the excited carrier dynamics of $MoSe_2$/PVA composites thin films. The study demonstrates the exciton-exciton annihilation at the center wavelength of 800 nm by analyzing the relationship between excitation carrier density and the pump-probe time. This is in agreement with the study of the ground-state absorption on the composite thin films using the UV-vis spectroscopy.

Thirdly, the NLO performance of a GSAM device was systematically compared with a commercial SESAM at a wavelength of 2 μm. A GSAM was fabricated by transferring a vacuum-filtrated and liquid-phase-exfoliated graphene film onto a silver-coated mirror. The NLO performance and carrier dynamics of the two SAMs at a center wavelength of 2 μm were investigated by I-scan and

degenerate pump-probe techniques based on laser pulses with duration of ~100 fs. For comparison, the linear optical reflection of the GSAM (64%) was chosen to be similar to that of the SESAM. The GSAM possesses a desirable non-saturable loss of ~9.9% and a modulation depth of ~13%. It shows much better NLO properties than SESAM when subtracting the GSAM's surface scattering loss of ~13.8%. A slow-absorber-mirror model modified from the Frantz-Nodvik equation was employed to analyse the I-scan results and obtain cross-sections of the ground-state and the excited state. The cross-section ratio of the excited-state over ground state, σ_e/σ_g, is calculated to be 0.442 for the GSAM and 0.615 for the SESAM. This ~28% less carrier absorptive cross-section ratio indicates the advantage of the GSAM when it is used as a mode-locker in a laser cavity. Because it produces much less loss and heat than SESAM under the irradiation of the same intense light. The carrier lifetime at the wavelength of 2 μm was measured to be 1.2 ps for the GSAM and ~63 ps for the SESAM. This means that a mode-locked laser based the GSAM are able to generate the ultrashort pulses with duration of ~40 fs while that of the SESAM is limited up to ~2 ps. These advantages make graphene a promising material for next generation mid-infrared mode-lockers, which can be used to fabricate saturable mirror with much better modulation depth, non-saturable loss and recovery time than the current commercial SESAM.

Thirdly, the excited carrier dynamics of layered $PtSe_2$ thin films were studied by femtosecond lasers. Transient absorption spectroscopy shows that $PtSe_2$ thin films possess broadband excited states absorption in the wavelength region from ~470 to ~750 nm. The transient absorptive mapping and degenerate pump probe traces imply that excited carriers in $PtSe_2$ relaxed to the ground state via two fast and one slow processes. The triexponential and biexponential decay model were employed to fit the carrier dynamic traces and figured out the corresponding relaxation times, which are ~0.5 ps - 2 ps, ~1 ps - 10 ps and ~35 – 300 ps respectively. The first fast decay process within 2 ps is dominated by carrier-carrier scattering, while the second fast relaxation is attributed to the intraband carrier-phonon scattering. The slowest relaxation is an indirect recombination of electron-hole pairs with the assistance of a trap state introduced by the defects.

These results show that antimonene, graphene, $MoSe_2$ and $PtSe_2$ possess novel nonlinear optical properties and various relaxation processes of excited carrier. The third-order nonlinear optical susceptibilities of antimonene and graphene are remarkably large, up to 10^{-8} and 10^{-7} esu respectively. This implies their promising nonlinear optical applications. Since the recovery time of graphene as a saturable absorber is very short, it has several advantages during the mode-locking to generate ultrafast laser pulses. The $MoSe_2$ has relatively small third-order nonlinear optical

susceptibility of ~10^{-13} esu and longer relaxation time of excited carrier in comparison to graphene, but its nonlinear optical property shows observable dependence on pulse width and wavelength of lasers. $PtSe_2$ indicates broadband ground state and excited state absorption. The results provide a clear insight into different nonlinear optical applications of the above 2D materials.

7.2 Outlook

The study on the excited carrier dynamics of layered $PtSe_2$ thin films with different thicknesses in Chapter 6 shows that the relaxation of these carriers possess sensible three processes. This was confirmed by both the degenerate pump-probe (p-p) experiments and the transient absorption (TA) spectroscopy. The $PtSe_2$ thin films were prepared by thermally assisted selenization of previously-deposit platinum films using the CVD method. The XPS spectroscopy shows that ~80% of the thin films are composed by $PtSe_2$, hence the p-p and TA signals were mainly resulting from $PtSe_2$. The remaining ~20 percent components contain some platinum atoms, which were not totally reacted with diselenide. This might play a role in both linear and nonlinear optical performance of the thin films. It could also have an influence on the diffusion of the excited carrier due the strong ability of transporting electrons of metals. To reduce these possibilities, one method in the future is to enhance the purity of the thin films during the fabrication. From the optical point of view, it would be effective to guarantee the preciseness by locating the focus points of laser beams at the area of the thin films where the majority of $PtSe_2$ lies. TEM images of the thin films in Figure 6.2 indicates that most part of the thin films are successive $PtSe_2$ with large size. By focusing the laser beams into smaller diameters using a microscope lens and controlling the sample under the monitoring of the microscopy, one can study excited carrier dynamics at even nano scale during p-p and TA experiments.

The results in Chapter 6 also indicates that the relaxation process contain two short- and one long-time behaviours, which were attributed to be dominated by carrier-carrier scattering, intraband carrier-phonon scattering and Shockley-Read-Hall recombination respectively. The corresponding excited carrier distribution has been qualitatively plotted in Figure 6.10. A quantitative analysis can be done by calculating the Fermi-distribution and DOS of the layered $PtSe_2$, as introduced in section 1.2. As 2D $PtSe_2$ has just been experimentally obtained recently, very little research on both its excited carrier dynamics and DOS was reported except for a paper published by *Nano Letters*.[251] The simulation of band structure in this work shows that the monolayer $PtSe_2$ is an

indirect semiconductor while its bulk is semimetal. In this thesis, the thinnest $PtSe_2$ that was utilized to study the excited carrier dynamics is 6 layers. A calculation on the band structure and DOS of 6 layers $PtSe_2$ using density function theory could provide a more clear insight into the relaxation processes of the excited carriers.

Bibliography:

1. Lohne, J.A., *Isaac Newton: The Rise of a Scientist 1661-1671*. Notes and Records of the Royal Society of London, 1965. **20**(2): p. 125-139.
2. Maiman, T.H., *Stimulated optical radiation in ruby.* nature, 1960. **187**(4736): p. 493-494.
3. Boyd, R.W., *Nonlinear optics*. 2003, Academic press. p. 1.
4. Franken, e.P., et al., *Generation of optical harmonics.* Physical Review Letters, 1961. **7**(4): p. 118.
5. Moulton, P., *Ti-doped sapphire: tunable solid-state laser*. Optics News, 1982. **8**(6): p. 9-9.
6. Moulton, P.F., *Tunable solid-state lasers.* Proceedings of the IEEE, 1992. **80**(3): p. 348-364.
7. Holler, M., et al., *Attosecond electron wave-packet interference observed by transient absorption.* Physical review letters, 2011. **106**(12): p. 123601.
8. Bækhøj, J.E. and L.B. Madsen, *Attosecond transient-absorption spectroscopy on aligned molecules.* Physical Review A, 2016. **94**(4): p. 043414.
9. Pabst, S., et al., *Theory of attosecond transient-absorption spectroscopy of krypton for overlapping pump and probe pulses.* Physical Review A, 2012. **86**(6): p. 063411.
10. Lee, K.J., et al., *Charge-transfer dynamics and nonlocal dielectric permittivity tuned with metamaterial structures as solvent analogues.* Nature Materials, 2017: p. 722-729.
11. Hong, X., et al., *Ultrafast charge transfer in atomically thin MoS_2/WS_2 heterostructures.* Nature nanotechnology, 2014. **9**(9): p. 682-686.
12. Jonas, D.M., et al., *Pump− Probe Polarization Anisotropy Study of Femtosecond Energy Transfer within the Photosynthetic Reaction Center of Rhodobacter sphaeroides R26.* The Journal of Physical Chemistry, 1996. **100**(30): p. 12660-12673.
13. Kühn, O. and V. Sundström, *Pump–probe spectroscopy of dissipative energy transfer dynamics in photosynthetic antenna complexes: a density matrix approach.* The Journal of chemical physics, 1997. **107**(11): p. 4154-4164.
14. Boyd, R.W., *Nonlinear optics*. 2003, Academic press. p. 10 - 21.
15. Lind, R.C. and D.G. Steel, *Demonstration of the longitudinal modes and aberration-correction properties of a continuous-wave dye laser with a phase-conjugate mirror.* Optics letters, 1981. **6**(11): p. 554-556.
16. Yakymyshyn, C.P., J.F. Pinto, and C.R. Pollock, *Additive-pulse mode-locked NaCl: OH− laser.* Optics letters, 1989. **14**(12): p. 621-623.
17. Svelto, O. and D.C. Hanna, *Principles of lasers*. 1998, Springer. p. 164.
18. Svelto, O. and D.C. Hanna, *Principles of lasers*. 1998, Springer. p. 341.
19. Svelto, O. and D.C. Hanna, *Principles of lasers*. 1998, Springer. p. 340.
20. Haus, H.A., *Mode-locking of lasers.* IEEE Journal of Selected Topics in Quantum Electronics, 2000. **6**(6): p. 1173-1185.

21. Huber, R., M. Wojtkowski, and J. Fujimoto, *Fourier Domain Mode Locking (FDML): A new laser operating regime and applications for optical coherence tomography.* Optics express, 2006. **14**(8): p. 3225-3237.

22. Bouma, B., et al., *Hybrid mode locking of a flash-lamp-pumped Ti: Al_2O_3 laser.* Optics Letters, 1994. **19**(22): p. 1858-1860.

23. Pittoni, F., M. Gioannini, and I. Montrosset, *Time-domain analysis of fiber grating semiconductor laser operation in active mode-locking regime.* IEEE Journal of Selected Topics in Quantum Electronics, 2001. **7**(2): p. 280-286.

24. Feng, Y., et al., *Saturable absorption behavior of free-standing graphene polymer composite films over broad wavelength and time ranges.* Optics Express, 2015. **23**(1): p. 559-569.

25. Wang, G., et al., *Ultrafast Nonlinear Optical Properties of a Graphene Saturable Mirror in the 2 μm Wavelength Region.* Laser & Photonics Reviews, 2017. **11**(5): p. 1700166-1700175.

26. Yang, L.-z., et al., *Ytterbium-doped fiber ring laser in multi-pulse operation.* Optoelectronics Letters, 2007. **3**(6): p. 401-403.

27. Schröder, W., et al., *Effect of Pauli blocking on exchange and dissipation mechanisms operating in heavy-ion reactions.* Physical Review Letters, 1980. **44**(5): p. 308.

28. Paschotta, R. and U. Keller, *Passive mode locking with slow saturable absorbers.* Applied Physics B: Lasers and Optics, 2001. **73**(7): p. 653-662.

29. George, P.A., et al., *Ultrafast optical-pump terahertz-probe spectroscopy of the carrier relaxation and recombination dynamics in epitaxial graphene.* Nano letters, 2008. **8**(12): p. 4248-4251.

30. Koch, S., N. Peyghambarian, and M. Lindberg, *Transient and steady-state optical nonlinearities in semiconductors.* Journal of Physics C: Solid State Physics, 1988. **21**(30): p. 5229.

31. Wildberger, K., et al., *Fermi-Dirac distribution in ab initio Green's-function calculations.* Physical Review B, 1995. **52**(15): p. 11502.

32. Yacobi, B.G., *Semiconductor materials: an introduction to basic principles*. 2003, Springer Science & Business Media. p. 63.

33. Arkhipov, V., et al., *Charge carrier mobility in doped semiconducting polymers.* Applied Physics Letters, 2003. **82**(19): p. 3245-3247.

34. Yacobi, B.G., *Semiconductor materials: an introduction to basic principles*. 2003, Springer Science & Business Media. p. 62.

35. Delerue, C., G. Allan, and M. Lannoo, *Electron-phonon coupling and optical transitions for indirect-gap semiconductor nanocrystals.* Physical Review B, 2001. **64**(19): p. 193402.

36. Sanderocock, J., *Light scattering from surface acoustic phonons in metals and semiconductors.* Solid State Communications, 1978. **26**(8): p. 547-551.

37. Harb, M., et al., *Excitation of longitudinal and transverse coherent acoustic phonons in nanometer free-standing films of (001) Si.* Physical Review B, 2009. **79**(9): p. 094301.

38. Kushwaha, M.S., et al., *Acoustic band structure of periodic elastic composites.* Physical review letters, 1993. **71**(13): p. 2022.

39. Achtstein, A.W., et al., *p-State Luminescence in CdSe Nanoplatelets: Role of Lateral Confinement and a Longitudinal Optical Phonon Bottleneck.* Physical review letters, 2016. **116**(11): p. 116802.

40. Kuik, M., et al., *Trap-assisted recombination in disordered organic semiconductors.* Physical review letters, 2011. **107**(25): p. 256805.

41. Shen, Y., et al., *Auger recombination in InGaN measured by photoluminescence.* Applied Physics Letters, 2007. **91**(14): p. 141101.

42. Geim, A.K. and K.S. Novoselov, *The rise of graphene.* Nature Materials, 2007. **6**(3): p. 183-191.

43. Wang, J., et al., *Broadband Nonlinear Optical Response of Graphene Dispersions.* Advanced Materials, 2009. **21**(23): p. 2430-2435.

44. Dean, J.J. and H.M. van Driel, *Second harmonic generation from graphene and graphitic films.* Applied Physics Letters, 2009. **95**(26): p. 261910.

45. Balandin, A.A., et al., *Superior thermal conductivity of single-layer graphene.* Nano Letters, 2008. **8**(3): p. 902-907.

46. Kim, K.S., et al., *Large-scale pattern growth of graphene films for stretchable transparent electrodes.* Nature, 2009. **457**(7230): p. 706-710.

47. Lee, C., et al., *Measurement of the elastic properties and intrinsic strength of monolayer graphene.* Science, 2008. **321**(5887): p. 385-388.

48. Van Der Zande, A., *The structure and mechanics of atomically-thin graphene membranes*. 2011, Cornell University.

49. Katsnelson, M.I., *Graphene: carbon in two dimensions.* Materials today, 2007. **10**(1): p. 20-27.

50. Coleman, J.N., et al., *Two-dimensional nanosheets produced by liquid exfoliation of layered materials.* Science, 2011. **331**(6017): p. 568-571.

51. Wang, K., et al., *Ultrafast Nonlinear Excitation Dynamics of Black Phosphorus Nanosheets from Visible to Mid-Infrared.* ACS nano, 2016.

52. Hanlon, D., et al., *Liquid exfoliation of solvent-stabilized few-layer black phosphorus for applications beyond electronics.* Nature communications, 2015. **6**.

53. Gorbachev, R.V., et al., *Hunting for monolayer boron nitride: optical and Raman signatures.* Small, 2011. **7**(4): p. 465-468.

54. Cunningham, G., et al., *Solvent exfoliation of transition metal dichalcogenides: Dispersibility of exfoliated nanosheets varies only weakly between compounds.* Acs Nano, 2012. **6**(4): p. 3468-3480.

55. Wang, G., et al., *Tunable nonlinear refractive index of two-dimensional MoS_2, WS_2, and $MoSe_2$ nanosheet dispersions.* Photonics Research, 2015. **3**(2): p. A51-A55.

56. Gordon, R., et al., *Structures of exfoliated single layers of WS_2, MoS_2, and $MoSe_2$ in aqueous suspension.* Physical Review B, 2002. **65**(12): p. 125407.

57. Tongay, S., et al., *Thermally driven crossover from indirect toward direct bandgap in 2D semiconductors: $MoSe_2$ versus MoS_2.* Nano letters, 2012. **12**(11): p. 5576-5580.

58. Xia, F., et al., *Two-dimensional material nanophotonics.* Nature Photonics, 2014. **8**(12): p. 899-907.

59. Dean, C.R., et al., *Boron nitride substrates for high-quality graphene electronics.* Nature nanotechnology, 2010. **5**(10): p. 722-726.

60. Wang, K., et al., *Ultrafast nonlinear excitation dynamics of black phosphorus nanosheets from visible to mid-infrared.* ACS nano, 2016. **10**(7): p. 6923-6932.

61. Yang, H., et al., *Giant two-photon absorption in bilayer graphene.* Nano letters, 2011. **11**(7): p. 2622-2627.

62. Bao, Q., et al., *Atomic‐layer graphene as a saturable absorber for ultrafast pulsed lasers.* Advanced Functional Materials, 2009. **19**(19): p. 3077-3083.

63. Kumar, S., et al., *Femtosecond carrier dynamics and saturable absorption in graphene suspensions.* Applied physics letters, 2009. **95**(19): p. 191911.

64. Du, J., et al., *Ytterbium-doped fiber laser passively mode locked by few-layer Molybdenum Disulfide (MoS_2) saturable absorber functioned with evanescent field interaction.* Scientific reports, 2014. **4**.

65. Malard, L.M., et al., *Observation of intense second harmonic generation from MoS_2 atomic crystals.* Physical Review B, 2013. **87**(20): p. 201401.

66. Li, Y., et al., *Probing symmetry properties of few-layer MoS_2 and h-BN by optical second-harmonic generation.* Nano letters, 2013. **13**(7): p. 3329-3333.

67. Zhang, S., et al., *Direct observation of degenerate two-photon absorption and its saturation in WS_2 and MoS_2 monolayer and few-layer films.* ACS nano, 2015. **9**(7): p. 7142-7150.

68. Sotor, J., et al., *Black phosphorus saturable absorber for ultrashort pulse generation.* Applied Physics Letters, 2015. **107**(5): p. 051108.

69. Singh, A., et al., *Trion formation dynamics in monolayer transition metal dichalcogenides.* Physical Review B, 2016. **93**(4): p. 041401.

70. Gao, F., et al., *Valley trion dynamics in monolayer $MoSe_2$.* Physical Review B, 2016. **94**(24): p. 245413.

71. Sie, E.J., et al., *Valley-selective optical Stark effect in monolayer WS_2.* Nature materials, 2015. **14**(3): p. 290-294.

72. Sie, E.J., et al., *Large, valley-exclusive Bloch-Siegert shift in monolayer WS_2.* Science, 2017. **355**(6329): p. 1066-1069.

73. Shi, H., et al., *Exciton dynamics in suspended monolayer and few-layer MoS_2 2D crystals.* ACS nano, 2013. **7**(2): p. 1072-1080.

74. Wang, K., et al., *Ultrafast Saturable Absorption of Two-Dimensional MoS_2 Nanosheets.* Acs Nano, 2013. **7**(10): p. 9260-9267.

75. Wang, Y., et al., *Ultrafast recovery time and broadband saturable absorption properties of black phosphorus suspension.* Applied Physics Letters, 2015. **107**(9): p. 091905.

76. Zhu, B., X. Chen, and X. Cui, *Exciton Binding Energy of Monolayer WS_2.* Scientific Reports, 2014. **5**: p. 5.

77. Jones, A.M., et al., *Optical Generation of Excitonic Valley Coherence in Monolayer WSe_2.* Nature nanotechnology, 2013. **8**: p. 634–638.

78. Singh, A., et al., *Long-Lived Valley Polarization of Intravalley Trions in Monolayer WSe_2.* Physical review letters, 2016. **117**(25): p. 257402.

79. Lui, C., et al., *Trion-induced negative photoconductivity in monolayer MoS_2.* Physical review letters, 2014. **113**(16): p. 166801.

80. Hanamura, E., *Theory of the High Density Exciton. I.* Journal of the Physical Society of Japan, 1970. **29**(1): p. 50-57.

81. Thilagam, A., *Two-dimensional charged-exciton complexes.* Physical Review B, 1997. **55**(12): p. 7804.

82. Chen, H., et al., *Ultrafast formation of interlayer hot excitons in atomically thin MoS_2/WS_2 heterostructures.* Nature Communications, 2016. **7**: p. 12512.

83. Kou, L., et al., *Structural and Electronic properties of Layered Arsenic and Antimony Arsenide.* The Journal of Physical Chemistry C, 2015.

84. Aktürk, O.Ü., V.O. Özçelik, and S. Ciraci, *Single-layer crystalline phases of antimony: Antimonenes.* Physical Review B, 2015. **91**(23): p. 235446.

85. Backes, C., et al., *Production of Highly Monolayer Enriched Dispersions of Liquid-Exfoliated Nanosheets by Liquid Cascade Centrifugation.* ACS nano, 2016.

86. Wu, R., et al., *Purely Coherent Nonlinear Optical Response in Solution Dispersions of Graphene Sheets.* Nano Letters, 2011. **11**(12): p. 5159-5164.

87. Durbin, S.D., S.M. Arakelian, and Y.R. Shen, *Laser-Induced Diffraction Rings from a Nematic-Liquid-Crystal Film.* Optics Letters, 1981. **6**(9): p. 411-413.

88. Karimzadeh, R., *Spatial self-phase modulation of a laser beam propagating through liquids with self-induced natural convection flow.* Journal of Optics, 2012. **14**(9): p. 095701.

89. Ji, W., et al., *Gravitation-dependent, thermally-induced self-diffraction in carbon nanotube solutions.* Opt. Express, 2006. **14**(20): p. 8958-8966.

90. Wang, G., et al., *Tunable effective nonlinear refractive index of graphene dispersions during the distortion of spatial self-phase modulation.* Applied Physics Letters, 2014. **104**(14): p. 141909.

91. Lam, S.K., M.A. Chan, and D. Lo, *Z-scan measurements of the nonlinear absorption and refractive index for fluorescein 548-doped organically modified sol–gel silica films.* Optical Materials, 2001. **18**(2): p. 235-241.

92. Ono, H. and Y. Harato, *Anisotropic diffraction pattern formation from guest host liquid crystals.* Optics Communications, 1999. **168**(1-4): p. 251-259.

93. Pu, S.L., et al., *Threshold-tunable optical limiters based on nonlinear refraction in ferrosols.* Optics Communications, 2009. **282**(5): p. 908-913.

94. Sathiyamoorthy, K., C. Vijayan, and M.P. Kothiyal, *Low power optical limiting in ClAl-Phthalocyanine due to self defocusing and self phase modulation effects.* Optical Materials, 2008. **31**(1): p. 79-86.

95. Brugioni, S. and R. Meucci, *Self-phase modulation in a nematic liquid crystal film induced by a low-power CO_2 laser.* Optics Communications, 2002. **206**(4-6): p. 445-451.

96. Sheik-Bahae, M., A.A. Said, and E.W. Van Stryland, *High-sensitivity, single-beam n_2 measurements.* Optics letters, 1989. **14**(17): p. 955-957.

97. Sheik-Bahae, M., et al., *Sensitive measurement of optical nonlinearities using a single beam.* IEEE journal of quantum electronics, 1990. **26**(4): p. 760-769.

98. Eilers, H., et al., *Saturation of 1.064 μm absorption in Cr, Ca: Y3Al5O12 crystals.* Applied physics letters, 1992. **61**(25): p. 2958-2960.

99. Sheik-Bahae, M., D.J. Hagan, and E.W. Van Stryland, *Dispersion and band-gap scaling of the electronic Kerr effect in solids associated with two-photon absorption.* Physical review letters, 1990. **65**(1): p. 96.

100. Zhao, W. and P. Palffy‐Muhoray, *Z‐scan measurement of $\chi^{(3)}$ using top‐hat beams.* Applied physics letters, 1994. **65**(6): p. 673-675.

101. Xia, T., et al., *Eclipsing Z-scan measurement of λ/10 4 wave-front distortion.* Optics letters, 1994. **19**(5): p. 317-319.

102. Liu, Z.-B., et al., *Ultrafast dynamics and nonlinear optical responses from sp2-and sp3-hybridized domains in graphene oxide.* The Journal of Physical Chemistry Letters, 2011. **2**(16): p. 1972-1977.

103. Elim, H.I., et al., *Observation of saturable and reverse-saturable absorption at longitudinal surface plasmon resonance in gold nanorods.* Applied physics letters, 2006. **88**(8): p. 083107.

104. Wei, T.-H., T.-H. Huang, and T.-C. Wen, *Mechanism of reverse saturable absorption in chloro-aluminum phthalocyanine solution studied with Z-scan.* Chemical physics letters, 1999. **314**(5): p. 403-410.

105. Fang, G., et al., *Z-scan of excited-state nonlinear materials with reverse saturable absorption.* Optics communications, 2000. **183**(5): p. 523-527.

106. Firester, A.H., M. Heller, and P. Sheng, *Knife-edge scanning measurements of subwavelength focused light beams.* Applied Optics, 1977. **16**(7): p. 1971-1974.

107. de Araújo, M.A., et al., *Measurement of Gaussian laser beam radius using the knife-edge technique: improvement on data analysis.* Applied optics, 2009. **48**(2): p. 393-396.

108. Khosrofian, J.M. and B.A. Garetz, *Measurement of a Gaussian laser beam diameter through the direct inversion of knife-edge data.* Applied Optics, 1983. **22**(21): p. 3406-3410.

109. O'Connell, R.M. and R.A. Vogel, *Abel inversion of knife-edge data from radially symmetric pulsed laser beams.* Applied optics, 1987. **26**(13): p. 2528-2532.

110. Behnia, K., *Condensed-matter physics: Polarized light boosts valleytronics.* Nature nanotechnology, 2012. **7**(8): p. 488-489.

111. Kim, J., et al., *Ultrafast generation of pseudo-magnetic field for valley excitons in WSe_2 monolayers.* Science, 2014. **346**(6214): p. 1205-1208.

112. Malajovich, I., et al., *Persistent sourcing of coherent spins for multifunctional semiconductor spintronics.* Nature, 2001. **411**(6839): p. 770-772.

113. Wang, Q., et al., *Valley carrier dynamics in monolayer molybdenum disulfide from helicity-resolved ultrafast pump–probe spectroscopy.* ACS nano, 2013. **7**(12): p. 11087-11093.

114. Bauer, C., et al., *Ultrafast relaxation dynamics of charge carriers relaxation in ZnO nanocrystalline thin films.* Chemical physics letters, 2004. **387**(1): p. 176-181.

115. Ikeda, S., et al., *Photocatalytic activity of transition-metal-loaded titanium (IV) oxide powders suspended in aqueous solutions: Correlation with electron–hole recombination kinetics.* Physical Chemistry Chemical Physics, 2001. **3**(2): p. 267-273.

116. Krauter, C.M., et al., *Ultrafast branching in the excited state of coumarin and umbelliferone.* Physical Chemistry Chemical Physics, 2013. **15**(41): p. 17846-17861.

117. Cahill, D.G., et al., *Nanoscale thermal transport.* Journal of applied physics, 2003. **93**(2): p. 793-818.

118. Prasankumar, R.P. and A.J. Taylor, *Optical techniques for solid-state materials characterization*. 2016: CRC Press.

119. Kumar, N., et al., *Spatially resolved femtosecond pump-probe study of topological insulator Bi_2Se_3.* Physical Review B, 2011. **83**(23): p. 235306.

120. Cui, Q., et al., *Transient absorption microscopy of monolayer and bulk WSe_2.* ACS nano, 2014. **8**(3): p. 2970-2976.

121. Chen, Y.-C., et al., *Ultrafast optical switching properties of single-wall carbon nanotube polymer composites at 1.55 μm.* Applied Physics Letters, 2002. **81**(6): p. 975-977.

122. Guo, Z., et al., *Long-range hot-carrier transport in hybrid perovskites visualized by ultrafast microscopy*. Science, 2017. **356**(6333): p. 59-62.

123. Jundt, C., et al., *Exciton dynamics in pentacene thin films studied by pump-probe spectroscopy.* Chemical physics letters, 1995. **241**(1-2): p. 84-88.

124. Mai, C., et al., *Exciton valley relaxation in a single layer of WS_2 measured by ultrafast spectroscopy.* Physical Review B, 2014. **90**(4): p. 041414.

125. Kumar, N., et al., *Exciton-exciton annihilation in $MoSe_2$ monolayers.* Physical Review B, 2014. **89**(12): p. 125427.

126. Soavi, G., et al., *Exciton-exciton annihilation and biexciton stimulated emission in graphene nanoribbons.* Nature communications, 2016. **7**: p. 1-7.

127. Haran, G., et al., *Femtosecond polarized pump− probe and stimulated emission spectroscopy of the isomerization reaction of rhodopsin.* The Journal of Physical Chemistry A, 1999. **103**(14): p. 2202-2207.

128. Mathies, R., W. Pollard, and C.B. Cruz, *Direct observation of the femtosecond excited-state cis-trans isomerization in bacteriorhodopsin.* 4BEdited, 1988: p. 584.

129. Hell, S.W. and J. Wichmann, *Breaking the diffraction resolution limit by stimulated emission: stimulated-emission-depletion fluorescence microscopy.* Optics letters, 1994. **19**(11): p. 780-782.

130. Koetke, J. and G. Huber, *Infrared excited-state absorption and stimulated-emission cross sections of Er3+-doped crystals.* Applied Physics B, 1995. **61**(2): p. 151-158.

131. Guyot-Sionnest, P., et al., *Intraband relaxation in CdSe quantum dots.* Physical Review B, 1999. **60**(4): p. R2181.

132. Woutersen, a., U. Emmerichs, and H. Bakker, *Femtosecond mid-IR pump-probe spectroscopy of liquid water: Evidence for a two-component structure.* Science, 1997. **278**(5338): p. 658-660.

133. De Ninno, G., et al., *Chirped seeded free-electron lasers: self-standing light sources for two-color pump-probe experiments.* Physical review letters, 2013. **110**(6): p. 064801.

134. Shen, Y., *Optical second harmonic generation at interfaces.* Annual Review of Physical Chemistry, 1989. **40**(1): p. 327-350.

135. Luo, C., et al., *Eliminate coherence spike in reflection-type pump-probe measurements.* Optics express, 2009. **17**(14): p. 11321-11327.

136. Eichler, H., D. Langhans, and F. Massmann, *Coherence peaks in picosecond sampling experiments.* Optics communications, 1984. **50**(2): p. 117-122.

137. Prasankumar, R.P. and A.J. Taylor, *Optical techniques for solid-state materials characterization*. 2016, CRC Press. p. 337.

138. Prasankumar, R.P. and A.J. Taylor, *Optical techniques for solid-state materials characterization*, in *Optical techniques for solid-state materials characterization*. 2016, CRC Press. p. 338.

139. Prasankumar, R.P. and A.J. Taylor, *Optical techniques for solid-state materials characterization*, in *Optical techniques for solid-state materials characterization*. 2016, CRC Press. p. 339.

140. Prasankumar, R.P. and A.J. Taylor, *Optical techniques for solid-state materials characterization*, in *Optical techniques for solid-state materials characterization*. 2016, CRC Press. p. 340.

141. Wang, L., et al., *Ultrafast dynamics of a new class of highly fluorescent boron difluoride dyes.* Physical Chemistry Chemical Physics, 2015. **17**(4): p. 2349-2351.

142. Imanbaew, D., et al., *Pump‐Probe Fragmentation Action Spectroscopy: A Powerful Tool to Unravel Light‐Induced Processes in Molecular Photocatalysts.* Angewandte Chemie International Edition, 2017.

143. Gabriel, M.M., et al., *Direct imaging of free carrier and trap carrier motion in silicon nanowires by spatially-separated femtosecond pump–probe microscopy.* Nano letters, 2013. **13**(3): p. 1336-1340.

144. Dani, K.M., et al., *Subpicosecond optical switching with a negative index metamaterial.* Nano letters, 2009. **9**(10): p. 3565-3569.

145. Beschoten, B., et al., *Spin coherence and dephasing in GaN.* Physical Review B, 2001. **63**(12): p. 121202.

146. Andreakou, P., et al., *Influence of magnetic quantum confined Stark effect on the spin lifetime of indirect excitons.* Physical Review B, 2016. **93**(11): p. 115410.

147. Andreakou, P., et al., *Nonlinear optical spectroscopy of indirect excitons in coupled quantum wells.* Physical Review B, 2015. **91**(12): p. 125437.

148. Lui, K. and F. Hegmann, *Ultrafast carrier relaxation in radiation-damaged silicon on sapphire studied by optical-pump–terahertz-probe experiments.* Applied Physics Letters, 2001. **78**(22): p. 3478-3480.

149. Edamatsu, K., et al., *Transient absorption due to self-trapped excitons in NaBr and NaI.* Physical Review B, 1993. **47**(11): p. 6747.

150. Sun, D., et al., *Observation of rapid exciton–exciton annihilation in monolayer molybdenum disulfide.* Nano letters, 2014. **14**(10): p. 5625-5629.

151. Walker, B.J., et al., *Singlet exciton fission in solution.* Nature chemistry, 2013. **5**(12): p. 1019-1024.

152. Wu, X., M.T. Trinh, and X.-Y. Zhu, *Excitonic many-body interactions in two-dimensional lead iodide perovskite quantum wells.* The Journal of Physical Chemistry C, 2015. **119**(26): p. 14714-14721.

153. Guo, Z., et al., *Exciton Structure and Dynamics in Solution Aggregates of a Low-Bandgap Copolymer.* The Journal of Physical Chemistry B, 2015. **119**(24): p. 7666-7672.

154. Guo, Z., et al., *Relationship between interchain interaction, exciton delocalization, and charge separation in low-bandgap copolymer blends.* Journal of the American Chemical Society, 2014. **136**(28): p. 10024-10032.

155. Wan, Y., et al., *Cooperative singlet and triplet exciton transport in tetracene crystals visualized by ultrafast microscopy.* Nature chemistry, 2015. **7**(10): p. 785-792.

156. Yoon, S.J., et al., *Direct Imaging of Long-Range Exciton Transport in Quantum Dot Superlattices by Ultrafast Microscopy.* ACS nano, 2016. **10**(7): p. 7208-7215.

157. Nah, S., et al., *Spatially segregated free-carrier and exciton populations in individual lead halide perovskite grains.* Nature Photonics, 2017. **11**(5): p. 285-288.

158. Korovyanko, O., et al., *Ultrafast spectroscopy of excitons in single-walled carbon nanotubes.* Physical review letters, 2004. **92**(1): p. 017403.

159. Grancini, G., et al., *Hot exciton dissociation in polymer solar cells.* Nature materials, 2013. **12**(1): p. 29-33.

160. Yamaguchi, S. and H.-O. Hamaguchi, *Convenient method of measuring the chirp structure of femtosecond white-light continuum pulses.* Applied spectroscopy, 1995. **49**(10): p. 1513-1515.

161. Hamm, P., R.A. Kaindl, and J. Stenger, *Noise suppression in femtosecond mid-infrared light sources.* Optics letters, 2000. **25**(24): p. 1798-1800.

162. Bellini, M. and T.W. Hänsch, *Phase-locked white-light continuum pulses: toward a universal optical frequency-comb synthesizer.* Optics letters, 2000. **25**(14): p. 1049-1051.

163. Liaros, N., et al., *Ultrafast Processes in Graphene Oxide during Femtosecond Laser Excitation.* The Journal of Physical Chemistry C, 2016. **120**(7): p. 4104-4111.

164. Born, M. and E. Wolf, *Principles of optics: electromagnetic theory of propagation, interference and diffraction of light*. 2013: Elsevier.

165. Harvey, K. and C. Myatt, *External-cavity diode laser using a grazing-incidence diffraction grating.* Optics letters, 1991. **16**(12): p. 910-912.

166. Aarnio, H., et al., *Recombination studies in a polyfluorene copolymer for photovoltaic applications.* Synthetic metals, 2005. **155**(2): p. 299-302.

167. Wurtz, G.A., et al., *Designed ultrafast optical nonlinearity in a plasmonic nanorod metamaterial enhanced by nonlocality.* Nature nanotechnology, 2011. **6**(2): p. 107-111.

168. Swinehart, D., *The beer-lambert law.* J. Chem. Educ, 1962. **39**(7): p. 333.

169. Singh, D., et al., *Antimonene: a monolayer material for ultraviolet optical nanodevices.* Journal of Materials Chemistry C, 2016. **4**(26): p. 6386-6390.

170. Lu, L., et al., *Broadband Nonlinear Optical Response in Few‐Layer Antimonene and Antimonene Quantum Dots: A Promising Optical Kerr Media with Enhanced Stability.* Advanced Optical Materials, 2017. **5**: p. 1700301.

171. Gibaja, C., et al., *Few‐Layer Antimonene by Liquid‐Phase Exfoliation.* Angewandte Chemie International Edition, 2016. **55**(46): p. 14345-14349.

172. Ares, P., et al., *Mechanical Isolation of Highly Stable Antimonene under Ambient Conditions.* Advanced Materials, 2016. **28**(30): p. 6332-6336.

173. Zhang, Y., et al., *Direct observation of the transition from indirect to direct bandgap in atomically thin epitaxial $MoSe_2$.* Nature nanotechnology, 2014. **9**(2): p. 111-115.

174. Mak, K.F., et al., *Atomically thin MoS_2: a new direct-gap semiconductor*. Physical Review Letters, 2010. **105**(13): p. 136805.

175. Splendiani, A., et al., *Emerging photoluminescence in monolayer MoS_2.* Nano letters, 2010. **10**(4): p. 1271-1275.

176. Dong, N., et al., *Optical limiting and theoretical modelling of layered transition metal dichalcogenide nanosheets.* Scientific reports, 2015. **5**.

177. Wang, S., et al., *Broadband Few‐Layer MoS_2 Saturable Absorbers.* Advanced materials, 2014. **26**(21): p. 3538-3544.

178. Wang, K., et al., *Ultrafast saturable absorption of two-dimensional MoS_2 nanosheets.* ACS nano, 2013. **7**(10): p. 9260-9267.

179. Li, Y., et al., *Giant two‐photon absorption in monolayer MoS_2.* Laser & Photonics Reviews, 2015. **9**(4): p. 427-434.

180. Zhang, J., et al., *Broadband spatial self-phase modulation of black phosphorous.* Optics letters, 2016. **41**(8): p. 1704-1707.

181. Zhang, S., et al., *Atomically Thin Arsenene and Antimonene: Semimetal–Semiconductor and Indirect–Direct Band‐Gap Transitions.* Angewandte Chemie, 2015. **54**(10): p. 3155-3158.

182. Lei, T., et al., *Electronic structure of antimonene grown on Sb_2Te_3 (111) and Bi_2Te_3 substrates.* Journal of Applied Physics, 2016. **119**(1): p. 015302.

183. Huo, C., et al., *Few-layer Antimonene: Large Yield Synthesis, Exact Atomical Structure and Outstanding Optical Limiting.* Journal of the American Chemical Society, 2016.

184. Wu, Y., et al., *Emergence of electron coherence and two-color all-optical switching in MoS_2 based on spatial self-phase modulation.* Proceedings of the National Academy of Sciences, 2015. **112**(38): p. 11800-11805.

185. Wang, K.P., et al., *Ultrafast Saturable Absorption of Two-Dimensional MoS_2 Nanosheets.* Acs Nano, 2013. **7**(10): p. 9260-9267.

186. Wu, Y., et al., *Electronic origin of spatial self-phase modulation: Evidenced by comparing graphite with C_{60} and graphene.* Applied Physics Letters, 2016. **108**(24): p. 241110.

187. Wang, Z., *Alignment of graphene nanoribbons by an electric field.* Carbon, 2009. **47**(13): p. 3050-3053.

188. Singh, D., et al., *Antimonene: a monolayer material for ultraviolet optic nanodevices.* Journal of Materials Chemistry C, 2016. **4**(26): p. 6386-6390.

189. Ci, L., et al., *Atomic layers of hybridized boron nitride and graphene domains.* Nature materials, 2010. **9**(5): p. 430-435.

190. Karimzadeh, R., *Spatial self-phase modulation of a laser beam propagating through liquids with self-induced natural convection flow.* Journal of Optics, 2012. **14**(9): p. 095701/1-095701/9.

191. Wang;, G., et al., *Tunable effective nonlinear refractive index of graphene dispersions during the distortion of spatial self-phase modulation.* Appl. Phys. Lett. , 2014. **104**: p. 141909.

192. Vest, C.M. and M.L. Lawson, *Onset of convection near a suddenly heated horizontal wire.* Inl. 3. Heat Mass Transfer., 1972. **15**: p. 1281-1283.

193. Lotya, M., et al., *Liquid phase production of graphene by exfoliation of graphite in surfactant/water solutions.* Journal of the American Chemical Society, 2009. **131**(10): p. 3611-20.

194. Shaw, J.C., et al., *Chemical vapor deposition growth of monolayer $MoSe_2$ nanosheets.* Nano Research, 2014. **7**(4): p. 511-517.

195. Wang, K., et al., *Broadband ultrafast nonlinear absorption and nonlinear refraction of layered molybdenum dichalcogenide semiconductors.* Nanoscale, 2014. **6**(18): p. 10530-10535.

196. Manser, J.S. and P.V. Kamat, *Band filling with free charge carriers in organometal halide perovskites.* Nature Photonics, 2014. **8**(9): p. 737-743.

197. Ghanassi, M., et al., *Time‐resolved measurements of carrier recombination in experimental semiconductor‐doped glasses: Confirmation of the role of Auger recombination.* Applied physics letters, 1993. **62**(1): p. 78-80.

198. Robel, I., et al., *Exciton recombination dynamics in CdSe nanowires: bimolecular to three-carrier Auger kinetics.* Nano letters, 2006. **6**(7): p. 1344-1349.

199. Jackson, S.D., *Towards high-power mid-infrared emission from a fibre laser.* Nature photonics, 2012. **6**(7): p. 423-431.

200. Rudy, C.W., M.J. Digonnet, and R.L. Byer, *Advances in 2-μm Tm-doped mode-locked fiber lasers.* Optical Fiber Technology, 2014. **20**(6): p. 642-649.

201. Theisen, D., et al. *Cw high power IR-laser at 2μm for minimally invasive surgery*. in *European Conference on Biomedical Optics*. 2003. Optical Society of America.

202. Tittel, F.K., D. Richter, and A. Fried, *Mid-infrared laser applications in spectroscopy*, in *Solid-state mid-infrared laser sources*. 2003, Springer. p. 458-529.

203. Cho, W.B., et al., *Passive mode-locking of a Tm-doped bulk laser near 2 μm using a carbon nanotube saturable absorber.* Optics express, 2009. **17**(13): p. 11007-11012.

204. Cheng, Z., et al., *Progress on mid-IR graphene photonics and biochemical applications.* Frontiers of Optoelectronics, 2016. **9**(2): p. 259-269.

205. Sugioka, K. and Y. Cheng, *Ultrafast lasers—reliable tools for advanced materials processing.* Light: Science & Applications, 2014. **3**(4): p. e149.

206. Keller, U., *Recent developments in compact ultrafast lasers.* Nature, 2003. **424**(6950): p. 831-838.

207. Wang, F., *Two-dimensional materials for ultrafast lasers.* Chinese Physics B, 2017. **26**(3): p. 034202.

208. Yu, S., et al., *2D Materials for Optical Modulation: Challenges and Opportunities.* Advanced Materials, 2017.

209. Martinez, A. and Z. Sun, *Nanotube and graphene saturable absorbers for fibre lasers.* Nature Photonics, 2013. **7**(11): p. 842-845.

210. Bao, Q., et al., *Monolayer graphene as a saturable absorber in a mode-locked laser.* Nano Research, 2011. **4**(3): p. 297-307.

211. Zhang, S., et al., *Slow and fast absorption saturation of black phosphorus: experiment and modelling.* Nanoscale, 2016. **8**(39): p. 17374-17382.

212. Lu, S., et al., *Broadband nonlinear optical response in multi-layer black phosphorus: an emerging infrared and mid-infrared optical material.* Optics express, 2015. **23**(9): p. 11183-11194.

213. Sun, Z., et al., *A stable, wideband tunable, near transform-limited, graphene-mode-locked, ultrafast laser.* Nano Research, 2010. **3**(9): p. 653-660.

214. Liu, X., Q. Guo, and J. Qiu, *Emerging Low‐Dimensional Materials for Nonlinear Optics and Ultrafast Photonics.* Advanced Materials, 2017.

215. Zhang, S., et al., *Size-dependent saturable absorption and mode-locking of dispersed black phosphorus nanosheets.* Optical Materials Express, 2016. **6**(10): p. 3159-3168.

216. Chen, Y., et al., *Mechanically exfoliated black phosphorus as a new saturable absorber for both Q-switching and mode-locking laser operation.* Optics express, 2015. **23**(10): p. 12823-12833.

217. Zhang, H., et al., *Molybdenum disulfide (MoS_2) as a broadband saturable absorber for ultra-fast photonics.* Optics express, 2014. **22**(6): p. 7249-7260.

218. Xu, Y., et al., *Quantum Dots: Solvothermal Synthesis and Ultrafast Photonics of Black Phosphorus Quantum Dots.* Advanced Optical Materials, 2016. **4**(8): p. 1222-1222.

219. Ferrari, A.C., et al., *Science and technology roadmap for graphene, related two-dimensional crystals, and hybrid systems.* Nanoscale, 2015. **7**(11): p. 4598-4810.

220. Sun, Z., et al., *Graphene mode-locked ultrafast laser.* ACS nano, 2010. **4**(2): p. 803-810.

221. Husaini, S. and R. Bedford, *Graphene saturable absorber for high power semiconductor disk laser mode-locking.* Applied Physics Letters, 2014. **104**(16): p. 161107.

222. Zhang, H., et al., *Z-scan measurement of the nonlinear refractive index of graphene.* Optics letters, 2012. **37**(11): p. 1856-1858.

223. Zheng, Z., et al., *Microwave and optical saturable absorption in graphene.* Optics express, 2012. **20**(21): p. 23201-23214.

224. Bao, Q., et al., *Broadband graphene polarizer.* Nature Photonics, 2011. **5**(7): p. 411-415.

225. Murray, A.A. and W. Blau, *Nonlinear Properties of Graphene Dispersions and Thin Films at a Wavelength of 1.2 μm.* Journal of Nanoelectronics and Optoelectronics, 2013. **8**(1): p. 23-27.

226. Zhang, L., et al., *Graphene incorporated Q-switching of a polarization-maintaining Yb-doped fiber laser.* Laser Physics Letters, 2012. **9**(12): p. 888.

227. Zhang, L., et al., *Linearly polarized 1180-nm Raman fiber laser mode locked by graphene.* Photonics Journal, IEEE, 2012. **4**(5): p. 1809-1815.

228. Hader, J., et al., *Microscopic analysis of saturable absorbers: Semiconductor saturable absorber mirrors versus graphene.* Journal of Applied Physics, 2016. **119**(5): p. 053102.

229. Zhang, H., et al., *Graphene mode locked, wavelength-tunable, dissipative soliton fiber laser.* Applied Physics Letters, 2010. **96**(11): p. 111112/1-111112/3.

230. Ma, J., et al., *Wavelength-versatile graphene-gold film saturable absorber mirror for ultra-broadband mode-locking of bulk lasers.* Scientific reports, 2014. **4**: p. 5016.

231. Lagatsky, A., et al., *2 μm solid-state laser mode-locked by single-layer graphene.* Applied Physics Letters, 2013. **102**(1): p. 013113.

232. Miao, L., et al., *Broadband ultrafast nonlinear optical response of few-layers graphene: toward the mid-infrared regime.* Photonics Research, 2015. **3**(5): p. 214-219.

233. Haus, H.A., *Theory of mode locking with a fast saturable absorber.* Journal of Applied Physics, 1975. **46**(7): p. 3049-3058.

234. Hernandez, Y., et al., *High-yield production of graphene by liquid-phase exfoliation of graphite.* Nature nanotechnology, 2008. **3**(9): p. 563-568.

235. Ferrari, A.C. and D.M. Basko, *Raman spectroscopy as a versatile tool for studying the properties of graphene.* Nature nanotechnology, 2013. **8**(4): p. 235-246.

236. Dawlaty, J.M., et al., *Measurement of the optical absorption spectra of epitaxial graphene from terahertz to visible.* Applied Physics Letters, 2008. **93**(13): p. 131905.

237. Vardeny, Z. and J. Tauc, *Picosecond coherence coupling in the pump and probe technique.* Optics Communications, 1981. **39**(6): p. 396-400.

238. Prasankumar, R.P. and A.J. Taylor, *Optical techniques for solid-state materials characterization*. 2011: CRC Press.

239. Breusing, M., C. Ropers, and T. Elsaesser, *Ultrafast carrier dynamics in graphite.* Physical review letters, 2009. **102**(8): p. 086809.

240. Shah, J., *Ultrafast Spectroscopy of Semiconductors and Semiconductor Nanostructures*. 2013: Springer Berlin Heidelberg.

241. Burshtein, Z., et al., *Excited-state absorption studies of Cr/sup 4+/ions in several garnet host crystals.* IEEE journal of quantum electronics, 1998. **34**(2): p. 292-299.

242. Zaugg, C., et al., *Ultrafast and widely tuneable vertical-external-cavity surface-emitting laser, mode-locked by a graphene-integrated distributed Bragg reflector.* Optics express, 2013. **21**(25): p. 31548-31559.

243. Saraceno, C.J., et al., *SESAMs for high-power oscillators: design guidelines and damage thresholds.* IEEE Journal of Selected Topics in Quantum Electronics, 2012. **18**(1): p. 29-41.

244. Husaini, S., et al., *Broadband saturable absorption and optical limiting in graphene-polymer composites.* Applied Physics Letters, 2013. **102**(19): p. 191112.

245. Woodward, R., et al., *Few-layer MoS_2 saturable absorbers for short-pulse laser technology: current status and future perspectives.* Photonics Research, 2015. **3**(2): p. A30-A42.

246. Keller, U., et al., *Semiconductor saturable absorber mirrors (SESAM's) for femtosecond to nanosecond pulse generation in solid-state lasers.* IEEE Journal of selected topics in QUANTUM ELECTRONICS, 1996. **2**(3): p. 435-453.

247. Schaibley, J.R., et al., *Valleytronics in 2D materials.* Nature Reviews Materials, 2016. **1**: p. 16055.

248. Zhuang, H.L. and R.G. Hennig, *Computational search for single-layer transition-metal dichalcogenide photocatalysts.* The Journal of Physical Chemistry C, 2013. **117**(40): p. 20440-20445.

249. Miró, P., M. Ghorbani‐Asl, and T. Heine, *Two Dimensional Materials Beyond MoS_2: Noble‐Transition‐Metal Dichalcogenides.* Angewandte Chemie International Edition, 2014. **53**(11): p. 3015-3018.

250. O'Brien, M., et al., *Raman characterization of platinum diselenide thin films.* 2D Materials, 2016. **3**(2): p. 021004.

251. Wang, Y., et al., *Monolayer $PtSe_2$, a New Semiconducting Transition-Metal-Dichalcogenide, Epitaxially Grown by Direct Selenization of Pt.* Nano letters, 2015. **15**(6): p. 4013-4018.

252. Zhang, K., et al., *Experimental evidence of type-II Dirac fermions in $PtSe_2$.* Physical Review B, 2017. **96**: p. 125102.

253. Yim, C., et al., *High-performance hybrid electronic devices from layered $PtSe_2$ films grown at low temperature.* ACS nano, 2016. **10**(10): p. 9550-9558.

254. Ross, R.T. and A.J. Nozik, *Efficiency of hot‐carrier solar energy converters.* Journal of Applied Physics, 1982. **53**(5): p. 3813-3818.

255. Nozik, A.J., *Spectroscopy and hot electron relaxation dynamics in semiconductor quantum wells and quantum dots.* Annual review of physical chemistry, 2001. **52**(1): p. 193-231.

256. Luo, Z., et al., *Two-dimensional material-based saturable absorbers: towards compact visible-wavelength all-fiber pulsed lasers.* Nanoscale, 2016. **8**(2): p. 1066-1072.